Subcellular control of cAMP microdomain signaling using targeted optogenetics

Dissertation

zur

Erlangung des Doktorgrades (Dr. rer. nat.)

der

Mathematisch-Naturwissenschaftlichen Fakultät

der

Rheinischen Friedrich-Wilhelms-Universität Bonn

vorgelegt von

Berivan Mansuroglu

aus

Berlin, Deutschland

Bonn 2025

Angefertigt mit der Genehmigung der Mathematisch-Naturwissenschaftlichen Fakultät der
Rheinischen Friedrich-Wilhelms-Universität Bonn

Gutachter/Betreuer: Prof. Dr. Philipp Sasse
Gutachterin: Prof. Dr. Evi Kostenis

Tag der Promotion: 09.09.2025
Erscheinungsjahr: 2025

Die vorliegende Arbeit wurde vom Oktober 2019 bis Februar 2024 am Institut für Physiologie I der Rheinischen Friedrich-Wilhelms-Universität Bonn unter Anleitung von Prof. Dr. Philipp Sasse erstellt.

Acknowledgments

I sincerely thank Prof. Philipp Sasse for his guidance and supervision throughout my doctoral studies. His support during this work, particularly as my thesis advisor and first reviewer, has been much appreciated.

I am also grateful to Prof. Evi Kostenis for her role as co-supervisor and member of the expert committee, alongside Prof. Pfeifer and Prof. Wachten, whose expertise contributed to the successful evaluation of this thesis.

I gratefully acknowledge the financial and academic support from the German Research Foundation (DFG) and the Graduate School 1873, under the direction of Prof. Pfeifer. Special thanks go to Dr. Elisabeth Mies-Klomfass, coordinator of RTG 1873, for her consistent support and encouragement throughout the project.

This work was strongly supported by optogenetic tools provided by Prof. Peter Hegemann's lab, including the bPAC, bPAC-S27A, and TpPAC plasmids. I also wish to thank the virus core facility at the UKB, especially Dr. Anne Quatraccioni and Pia Trebing, for their expert assistance.

I deeply thank Dr. Daniela Malan and Dr. Vanessa Dusend for their invaluable scientific and technical contributions. Their highly valuable support was instrumental in the project's success. I would also like to thank Frank Holst for his reliable supply of primary cells, as well as our former technical assistants, Mehwish Salamat and Isabell Blameuser, for their contributions to earlier phases of this work.

A very warm thank you goes again to Daniela, Yoke, and Vanessa for not only their input as colleagues but also for the many shared experiences, support, and friendship they have provided throughout this time. Our moments in the lab, at conferences, and on field trips made this journey truly memorable.

I would also like to thank Sophie Hartmann for her initiative and help in mastering the GA3 software, which has been a valuable tool for our lab work.

Finally, I am deeply grateful to my friends and family for their encouragement, patience, and emotional support throughout this journey.

Contents

Abbreviations

Å Ångström
°C Degrees Celsius
µL Microliter
µm Micrometer
µM Micromolar
µmol/l Micromole/Liter
AAV Adeno-associated virus
AC Adenylyl cyclase
ACh Acetylcholine
aCM Adult cardiomyocyte
AKAPs A-kinase anchoring proteins
ANOVA Analysis of variance
AP Action potential
ATP Adenosine triphosphate
ATPase Adenosintriphosphatase
AVN Atrioventricular node
ß-AR Beta-adrenergic-receptor
BCA Bicinchoninic acid
BLUF-domain Blue-light sensing domain
ß-ME ß-Mercapto Ethanol
bmp Beats per minute
BP Band-pass
bPAC Photoactivatable adenylyl cyclase from the bacterium *Beggiatoa*
bPAC-S27A Red-shifted Photoactivatable adenylyl cyclase from the bacterium *Beggiatoa*
BSA Bovine serum albumin
ca. Circa
Ca^{2+} Calcium
$CaCl_2$ Calcium chloride
CAG-promoter Cytomegalovirus immediate-early enhancer/chicken β-actin promoter
CaMKII Ca^{2+}/calmodulin kinase II
cAMP Cyclic adenosine monophosphate
Casq2 Calsequestrin 2
Cav1.2, CACNA1C, I_{CaL} Voltage-gated L-type calcium channels / current
cDNA Complementary desoxyribonucleic acid
cGMP Cyclic guanosine monophosphate
CICR Ca^{2+}-induced Ca^{2+} release
CMV-promoter Human cytomegalovirus promoter

CO_2 Carbon dioxide
CPVT catecholaminergic polymorphic ventricular tachycardia
Cyt. Cytosolic
DADs Delayed afterdepolarizations
DAG Diacylglycerol
DAPI 4',6-diamidino-2-phenylindole
Db Diabetic
ddH_2O Deionized distilled water
DHPR Dihydropyridine receptors
DMEM Dulbecco's Modified Eagle Medium
DMSO Dimethyl sulfoxide
DNA Desoxyribonucleic acid
DPBS Dulbecco's Phosphate Buffered Saline
DTT Dithiothreitol
EADs Early afterdepolarizations
E.g., Exempli Gratia
EBs Embryonic bodies
ECG Electrocardiogram
EDTA Ethylenediaminetetraacetic acid
ELISA Enzyme-linked immunosorbent assay
Epac Exchange protein directly activated by cAMP
ESC Embryonic stem cells
et al. And others ("et alii")
EtOH Ethanol
EYFP Basic (constitutively fluorescent) green/yellow fluorescent protein
FAD Flavin adenine dinucleotide
FCS Fetal calf serum
Fig. Figure
FKBP12.6 FK506 binding protein
FMN Flavin mononucleotide
FRET Förster resonance energy transfer
FSK Forskolin
FW Forward
g Gravity
GA3 General analysis 3
GFP Green fluorescent protein
GIRK G-protein coupled inwardly rectifying potassium channel
GPCR G protein-coupled receptor
G protein Guanine nucleotide-binding protein

GRK G protein-coupled receptor kinases
h Hour
HCl Hydrochloric acid
HCN Hyperpolarization-activated cyclic nucleotide-gated
HEK293 Human embryonic kidney 293 cells
HFpEF Heart Failure with Preserved Ejection Fraction
HFrEF Heart failure with reduced ejection fraction
HRP Horseradish peroxidase
IBMX 3-isobutyl-1-methylxanthine
I_f Inward current
IgG Immunoglobulin G
IMEM Iscove's Modified Dulbecco's Medium
InsP3R Inositol triphosphate receptor
IP Prostacycline receptor
IP_3 Inositol trisphosphate
K^+ Potassium
KCl Potassium chloride
kDA Kilodalton
kg Kilogram
KO Knockout
LB Lysogeny broth
LED Light-Emitting Diode
LOV-domain Light-oxygen-voltage-sensing domain
LOV-PKI Photoactivated protein kinase A inhibitor
LP Long-pass
LV Left ventricle
LTCC L-type Ca^{2+} channels
LQTS Long-QT syndrome
M2/3 Muscarinergic
mAKAP/AKAP6 Muscle selective A-kinase anchoring protein
MEM Minimum Essential Media
Mg^{2+} Magnesium
$MgCl_2$ Magnesium chloride
$MgSO_4$ Magnesium sulfate
min Minute
mM Millimolar
mol/L Mol/Liter
msec Millisecond
mV Millivolt

MW Molecular weight
Na^+ Sodium
Na_2HPO_4 Sodium hydrogen phosphate
NaCl Sodium chloride
$NaHCO_3$ Sodium bicarbonate
$NaIO_3$ Sodium iodate
Na^+/K^+-ATPase pump Sodium-potassium adenosine triphosphatase
NaOH Sodium hydroxide
nCM Neonatal cardiomyocyte
NCX Na^+/Ca^{2+} exchanger
NEAA Nonessential amino acids
ng Nanogram
nM Nanomolar
nm Nanometer
O_2 Oxygen
OH Overhang
p Passage
PAC Photoactivatable adenylyl cyclase
PBS Phosphate-buffered saline
PCR Polymerase chain reaction
PDE Phosphodiesterase
PenStrep Penicillin-Streptomycin
PFA Paraformaldehyde
PIP_2 Phosphatidylinositol-4,5-bisphosphate
PIP_3 Phosphatidylinositol (3,4,5)-trisphosphate
PKA Protein kinase A
PKC Protein kinase C
PKG Protein kinase G
PKI PKA inhibitor
PLN Phospholamban
PLC Phospholipase C
PLC-β Phospholipase C-β
pmol Picomole
pmol/µL Picomole per microliter
PPi Inorganic pyrophosphate
PSS Physiological salt solution
PVDF Polyvinylidene fluoride
RIPA Radioimmunoprecipitation assay buffer
rpm Rounds per minute

RT Room temperature
RV Right ventricle
RV Reverse
RyR2 Ryanodine receptors 2
s Second
sAC Soluble adenylyl cyclase
SEM Standard error of the mean
S.O.C. Super optimal broth with catabolite repression
SD Standard deviation
SDS Sodium dodecyl sulfate
SERCA Sarco(endo)plasmic reticulum Ca^{2+}-ATPase
SAN Sinoatrial node
SN Sinus node
SR Sarcoplasmic reticulum
T2D Type 2 diabetes
TBS Tris-buffered saline
TBST Tris-buffered saline + 0.1% tween20
TEMED N,N,N', N'-Tetramethyl ethylenediamine
tmAC Transmembrane adenylyl cyclase
TpPAC Photoactivatable adenylyl cyclase from the bacterium *Turneriella parva*
Tris Tris(hydroxymethyl)aminomethane
TTCC Transient-type Ca^{2+} channel
T-tubule Transverse tubule
U International units
UCR1 Upstream Conserved Region 1
V Volt
VGKC Voltage-gated potassium channels
Vs. Versus
WB Western blot

1. Introduction

The heart's complex function relies on the precise interplay between electrical and mechanical processes. Cardiovascular dysfunctions are the most common diseases in Western societies. Understanding the physiological function of contractility and its regulation is crucial for diagnosing and treating cardiovascular diseases, which have high individual consequences for affected patients and result in high medical expenses.

1.1 Cardiac contractility

The heart is a muscular organ in the chest that pumps blood through the body, delivering oxygen and nutrients to tissues and organs.[1] The mammalian heart consists of four chambers: two atria and two ventricles, which work together to ensure efficient blood flow.[1]

A heartbeat, or cardiac cycle, has two phases: diastole and systole. Diastole lasts 600-700 ms, while systole lasts about 300 ms in resting humans. During diastole, the heart relaxes and fills with blood, while atrial contraction moves blood into the ventricles.[1] In systole, the ventricles contract, pumping blood to the lungs and the rest of the body. The right atrium receives deoxygenated blood and transfers it to the right ventricle, which sends it to the lungs via the pulmonary artery for oxygenation.[1] Oxygen-rich blood then enters the left atrium, moves to the left ventricle, and is pumped through the aorta to the systemic circulation, delivering oxygen and nutrients.[1, 2]

The heart is composed of various specialized tissues, including the endocardium, which is the innermost layer of the heart chambers; the epicardium, which forms the outermost layer; and the myocardium, the thickest layer of the heart responsible for the rapid and continuous mechanical work.[3] It comprises striated, glycogen- and fibrillar-rich cardiomyocytes, which generate the force necessary for heart contractions.[3]

The cardiac muscle corresponds to a “single motor unit,” in which cardiomyocytes are arranged to exhibit electrical coupling between cells, allowing action potentials (APs) to propagate from cell to cell.[2]

Cardiac myofibrils are composed of sarcomeres, which are highly ordered parallel arrays of actin and myosin filaments, along with various regulatory proteins.[2] Myosin is the motor protein responsible for generating the force during muscle contraction. The myosin molecule comprises two heavy chains and four light chains, forming a thick filament.[2] Each myosin head contains an actin-binding site and ATPase activity.[2] When ATP binds, the myosin heads detach from actin, causing the cross-bridges to dissociate. ATP hydrolysis by myosin ATPase energizes the myosin heads, preparing them for the next contraction cycle.[2] Actin filaments comprise globular actin monomers and serve as binding sites for myosin cross-

bridges.[2] Regulatory proteins, tropomyosin and troponins, control the interaction between actin and myosin during contraction and relaxation.[2] When the Ca^{2+} concentration rises above 1 µM, Ca^{2+} binds to troponin C, and the troponin-tropomyosin complex undergoes a conformational change, exposing myosin-binding sites on actin filaments.[2] This interaction enables the formation of cross-bridges between actin and myosin, promoting sarcomere shortening and muscle contraction.[2] During the relaxation phase, when the Ca^{2+} concentration decreases below 1 µM/L, Ca^{2+} dissociates from troponin C, causing the rearrangement of the tropomyosin molecule. This rearrangement blocks the availability of the high-affinity myosin-binding side at the actin filaments.[2] Ca^{2+} sensitivity can be modulated through troponin I, which has a phosphorylation site for protein kinase A (PKA) and can be modulated via cyclic adenosine monophosphate (cAMP).[2] Phosphorylation of the cardiac troponin I subunit accelerates the dissociation of Ca^{2+} from troponin C, resulting in faster relaxation.[2]

1.2 Electrical excitation in the heart

The cardiac conduction system begins at the sinoatrial node (SAN), which serves as the pacemaker, initiating the contraction of the atria.[3] The electrical excitation is then conducted to the atrioventricular node (AVN) in the right atrium, which delays the excitation to allow the ventricles to fill with blood. The activation propagates to the right and left ventricles via the His bundle and Purkinje fibers, activating ventricular cardiomyocyte contraction (**Fig. 1 A**).[3] The conduction velocity, which describes the speed of an electrical signal called dromotropy, indicates how quickly electrical impulses travel through the AV node and His-Purkinje system. The dromotropy is regulated by the autonomic nervous system and ion channel activity. The heart's electrical conduction can be measured using an electrocardiogram (ECG), which records the electrical potential changes in the heart through electrodes placed on the body's surface (**Fig. 1 B**).[3]

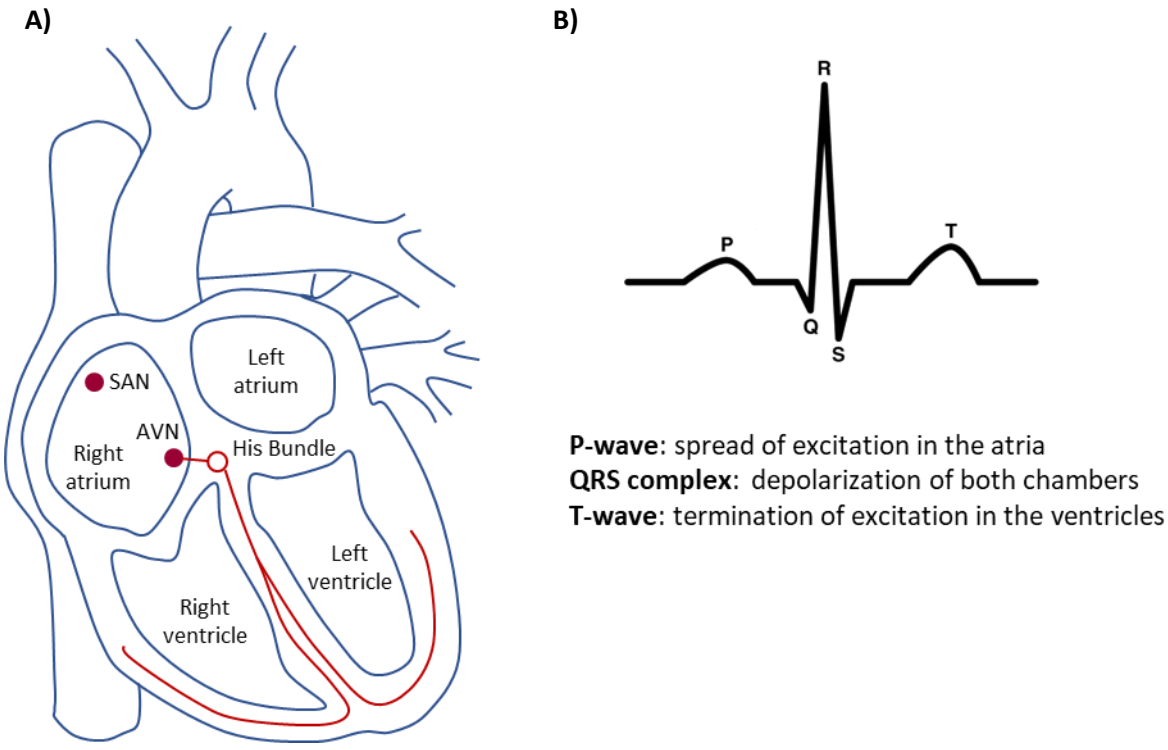

Fig. 1: Scheme of the cardiac electrical conduction system
A) *Overview of the cardiac electrical conduction system. The electrical impulse starts at the SAN and is delivered to the AVN. From there, it is transferred to the His bundle and subsequently to the right and left ventricles.*[3] ***B)*** *Electrocardiogram (ECG) of a sinus beat leading to the excitation of the whole heart.*[3]

The ECG curve is divided into sections, each corresponding to a particular electrophysiological event in the heart (**Fig. 1 B**).[3] The P-wave is caused by the spread of excitation in the atria, followed by the QRS complex, which corresponds to the depolarization of both chambers.[3] The PQ interval is the duration that measures the time from the start of the P-wave to the beginning of the QRS complex. It reflects the delay at the AVN.[3] The following QRS complex indicates ventricular depolarization (contraction). The duration of ventricular depolarization until repolarization is measured in the QT interval. A prolonged QT interval can be associated with arrhythmias. The ST segment reflects the phase with complete activation, and changes in the ST segment can indicate myocardial ischemia. Finally, the T-wave represents ventricular repolarization. Abnormal T-waves may suggest electrolyte imbalances or other cardiac pathologies.[3]

1.2.1 Action potential in pacemaker cells

The cardiac AP originates in specialized cells known as pacemaker cells, primarily located in the SAN, and is propagated through the cardiac conduction system to ventricular cardiomyocytes, initiating synchronized cardiac contractions. Unlike ventricular cardiomyocytes (**1.2.2**), pacemaker cells exhibit unique electrophysiological properties that allow them to depolarize and generate regular, rhythmic APs spontaneously.[4] This automaticity is driven by a combination of ion currents, including the "funny" current (I_f) and Ca^{2+} currents ($I_{Ca,\ L}$), which are crucial for setting the heart rate and maintaining rhythmic contractions.[3] Pacemaker cells in the SAN are characterized by a hyperpolarization-activated inward current, known as the "funny" current (I_f), mediated by hyperpolarization-activated cyclic nucleotide-gated (HCN) channels.[3] These channels open in response to membrane hyperpolarization (unlike most other ion channels, which open upon depolarization) and allow the influx of Na^+ and K^+ ions.[3] The I_f current slowly depolarizes the membrane, initiating the next AP, thereby contributing to the intrinsic pacemaker activity and regulating the heart rate.[3]

Modulation of HCN channel activity by intracellular cyclic nucleotides, particularly cAMP, can increase the I_f current, resulting in a higher pacemaker firing rate. Autonomic neurotransmitters such as acetylcholine and noradrenaline modulate cAMP levels, allowing the parasympathetic and sympathetic nervous systems to fine-tune heart rate by modulation of HCN channel activity for changing requirements (resting state or exercise).[3]

Another crucial regulator in the generation and propagation of APs in pacemaker cells is the influx of Ca^{2+}. The depolarization phase of the pacemaker cell AP is mainly driven by the L-type Ca^{2+} current ($I_{Ca,\ L}$), mediated by the L-type Ca^{2+} channel (LTCC).[4] These channels open in response to moderate depolarization, allowing a significant influx of Ca^{2+} ions into the cell, which leads to further depolarization and initiates the AP upstroke in SAN cells. Additionally, T-type Ca^{2+} channels (TTCC), which activate at lower membrane potentials, contribute to the late diastolic depolarization phase, bringing the membrane potential closer to the threshold for LTCC activation. The coordinated activity of these channels ($I_{Ca,\ L,}$ and $I_{Ca,\ T}$) provides the key Ca^{2+} influx necessary for AP initiation in pacemaker cells.[3]

Ca^{2+} plays a central role in cardiomyocytes´ AP generation and excitation-contraction coupling. In pacemaker cells, the Ca^{2+} influx via LTCC during each AP contributes to intracellular Ca^{2+} cycling (see Chapter **1.3**), which is critical for maintaining rhythm and force in subsequent APs. Moreover, the sarcoplasmic reticulum (SR) can release Ca^{2+} spontaneously during late diastole, which helps depolarize the cell membrane and contributes to the "Ca^{2+}-clock" mechanism, in which rhythmic Ca^{2+} release helps modulate heart rate. The released Ca^{2+} is then extruded from the cell by the Na^+/Ca^{2+} exchanger (NCX), which exchanges 1 Ca^{2+} out for 3 Na^+ in.

This inward Na^+ current is electrogenic (net positive charge enters the cell), causing a depolarizing current that helps push the membrane potential toward the threshold for AP firing. The NCX translates the internal Ca^{2+} signal (from SR release) into a membrane depolarization, helping synchronize the Ca^{2+} -clock with the "membrane clock" (M-clock). The M-clock, driven by the activity of ion channels in the plasma membrane, generates the I_f, Ca^{2+}, and K^+ currents that contribute to diastolic depolarization, gradually bringing the membrane potential to threshold and initiating the next AP. In parallel, the Ca^{2+}-clock promotes automaticity through rhythmic intracellular Ca^{2+} cycling, mainly via spontaneous Ca^{2+} release from the SR. Both clocks work synchronously, forming the coupled-clock mechanism; the M-clock ensures rhythmic firing, while the Ca^{2+}-clock fine-tunes depolarization timing and regulates firing frequency, ensuring the regular and robust pacing of cardiac pacemaker cells.[2, 3, 4, 5]

In addition to Ca^{2+}, other critical ion currents contribute to the AP dynamics in pacemaker cells. The repolarization phase of the pacemaker AP is mediated by delayed rectifier K^+ currents, particularly through $K_v7.1$ and $K_v11.1$ channels, which generate I_{Ks} (slow) and I_{Kr} (rapid) currents, respectively. These currents contribute to the outward K^+ flow, repolarizing the cell membrane and allowing the cell to reset for the next AP. This process is slower in SAN cells than in ventricular cells, enabling the gradual diastolic depolarization that defines pacemaker activity.[3, 4]

K^+ channels such as $K_{ir}3.x$ contribute to the acetylcholine-activated K^+ current (I_KACh), which is critical in the parasympathetic regulation of heart rate. I_KACh is activated by acetylcholine released from the vagus nerve, leading to a hyperpolarizing K^+ outflow that slows the heart rate by prolonging diastolic depolarization. This parasympathetic modulation enables heart rate adjustment during various physiological states, such as rest or exercise.[3, 4]

Dysfunction in these ion channels can lead to arrhythmias or irregular heartbeats. For instance, cardiac arrhythmias, such as SAN dysfunction and atrial fibrillation, have been linked to dysfunction of cardiac HCN channels.[3] Genetic mutations, alterations in cyclic nucleotide signaling, and changes in HCN channel expression levels can cause these pathological conditions.[3] Similarly, mutations in LTCC or disruptions in Ca^{2+} handling can disrupt the Ca^{2+} cycling essential for pacemaker cell automaticity, thereby affecting cardiac rhythm and contractility. Additionally, disruptions in I_KACh, typically caused by changes in parasympathetic tone, can lead to abnormal bradycardia or tachycardia responses.[3]

The importance of Ca^{2+} release and the role of LTCC and RyR2 on pacemaker activity were shown in different species and developmental stages of cardiomyocytes. A study by Sasse et al. (2007) showed that Ca^{2+} oscillations serve as intrinsic pacemakers in mouse embryonic heart cells by inducing contractions directly through Ca^{2+} release and indirectly by depolarizing the membrane via the NCX, thereby orchestrating rhythmic contractions during early heart development.[8] A second study by Lakatta et al. (2010) investigated rabbit sinoatrial nodal pacemaker cells (SANC).[9] They showed that

normal automaticity is regulated by constitutive Ca^{2+} activation of the cAMP/PKA signaling pathway and dependent protein phosphorylations, which govern a complex clock system comprising intracellular SR and surface membrane molecules that regulate intracellular Ca^{2+} cycling. G protein-coupled receptor (GPCR) signaling (see Chapter **1.4**) also ensures pacemaker flexibility, affecting rate regulation by impacting these factors that regulate coupled-clock Ca^{2+} cycling to guarantee basal state pacemaker stability and robustness.[9]

1.2.2 Action potential of ventricular cardiomyocytes

The cardiac ventricular AP coordinates the cyclic elevation of intracellular Ca^{2+} and contraction of ventricular cardiomyocytes, effectively pumping blood from the heart to the body and lungs. The AP duration in ventricular cardiomyocytes lasts around 300 ms, approximately 100 times longer than the AP of skeletal muscle (2-4 ms) or neurons (1 ms), due to its characteristic long plateau phase (**phase 2**). The ventricular AP involves the opening and closing of specific ion channels in different phases (**Fig. 2**): **phase 0** (rapid depolarization), **phase 1** (early repolarization), **phase 2** (plateau phase), **phase 3** (rapid repolarization), and **phase 4** (resting membrane potential).[2]

During depolarization, the initial stimulus from neighboring cardiomyocytes, transmitted through gap junctions, rapidly increases the membrane potential to approximately +20 mV. This is due to the opening of fast voltage-gated Na^+ channels ($Na_v1.5$, I_{Na}), allowing a rapid influx of Na^+ into the cell, leading to rapid membrane depolarization (**phase 0**). The depolarization is further enhanced by the block of $K_{ir}2.1$ at membrane potentials above -50 mV by the biogenic amine spermine.[3] Shortly after depolarization, during early repolarization (**phase 1**), the cell undergoes initial repolarization due to the activation of transient voltage-gated outward K^+ channels (K_v4), resulting in the efflux of K^+ ($I_{to,\,f}$ and $I_{to,\,s}$). When the membrane potential reaches approximately -40 mV, LTCC ($Ca_v1.2$, I_{Ca}) open, allowing Ca^{2+} ions to enter the cell. This long influx of Ca^{2+} is responsible for the characteristic plateau phase (**phase 2**), which lasts 200-300 ms. The prolonged elevation of intracellular Ca^{2+} contributes to cardiac muscle contraction. During the plateau phase, the intracellular Ca^{2+} concentration peaks at around 1.5 µmol/L, compared to 0.1 µmol/L at rest. During repolarization (**phase 3**), delayed outward rectifying K^+ channels ($K_v7.1$, $K_v11.1$) open, which allow the outward flow of K^+ (I_{Kr}, rapid, and I_{Ks}, slow), and the $Ca_v1.2$ channels close, thereby restoring the resting membrane potential. This allows K^+ to exit the cell, causing the membrane potential to return to its negative resting state. Additionally, the NCX, which is activated by increased Ca^{2+} in the cytosol, transports one Ca^{2+} out of the cell in exchange for three Na^+, generating a depolarizing current in the cell, thereby balancing intracellular Ca^{2+} levels. During the resting membrane potential (**phase 4**), the cardiomyocyte membrane maintains a negative charge inside the cell relative to the outside, typically around -85 mV in ventricular cardiomyocytes.[3] This negative charge is primarily determined by the balance of K^+ and Na^+ concentrations, with Na^+ and Cl^- as the primary extracellular ions and K^+ as the main intracellular ion. The inward rectifier K^+ channel ($K_{ir}2.1$, KCNJ2) conducts K^+ more effectively into the cell (inward rectifier current (I_K1)) at hyperpolarized potentials, helping to maintain a stable resting membrane potential and protecting the cell from excessive depolarization.[2, 3]

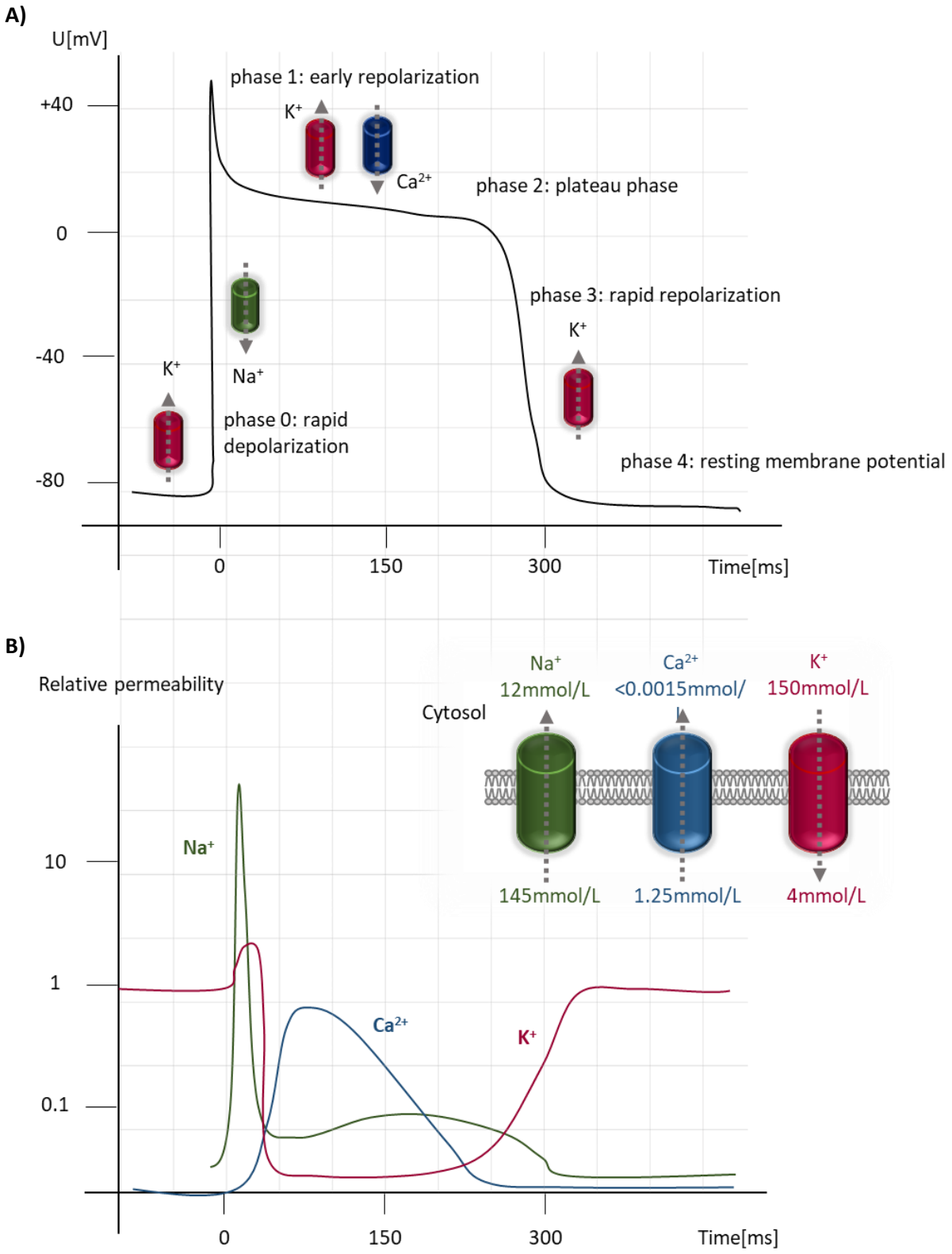

Fig. 2: Phases of the ventricular action potential

A) *the ionic basis for forming the AP of a cardiac muscle cell from the working myocardium. It describes the phases of a ventricular AP, including rapid depolarization (phase 0), early repolarization (phase 1), plateau phase (phase 2), rapid repolarization (phase 3), and resting membrane potential (phase 4).* ***B)*** *explains the temporal changes in permeability for Na^+, Ca^{2+}, and K^+ that are assigned to the individual phases of the AP. Finally, it notes that intra- and extracellular Na^+, Ca^{2+}, and K^+ concentrations are highly regulated. Figure adapted from Cardiac Electrophysiology: From Cell to Bedside, 7th edition, 2018, Elsevier, by Zipes, Jalife, and Stevenson.*[3]

The Na^+/K^+-ATPase pump also plays a critical role by pumping three Na^+ ions out of the cell and moving two K^+ ions into the cell, using ATP to maintain the ion concentration gradients.[3] Na^+ channels rapidly become inactivated and remain in that state during the plateau and early repolarization phases, creating an absolute refractory period during which the cell cannot propagate another AP. This refractory period has been reported to last 220-260 ms in humans and only 30-80 ms in mice. The refractory period protects the heart from early depolarization before the AP is complete, ensuring functional diastole and systole.[2, 3]

1.3 The role of Ca^{2+} in ventricular cardiomyocytes in the modulation of contractility

Excitation-contraction coupling is the process that links the cardiac AP to myofilament contraction.[3] This process is initiated by the depolarization of the cardiac cell membrane, which opens the LTCC, allowing Ca^{2+} to enter the cell, which triggers the release of Ca^{2+} from the intracellular store - the SR- through the activation of the RyR2. This mechanism is called Ca^{2+}-induced Ca^{2+} release (CICR).[5] Cardiac LTCCs and RyR2 are crucial in regulating Ca^{2+} dynamics within cardiomyocytes like described in **1.2.1** and **1.2.2**.[5]

LTCCs are abundantly expressed in cardiac tissues. They belong to the family of voltage-gated Ca^{2+} channels and are mainly distributed in T-tubules and the surface sarcolemma, facilitating their role in linking electrical signals to mechanical contraction.[3] LTCCs are multi-subunit protein complexes consisting of five subunits: the pore-forming subunit, α_1 (170 kDa), and four auxiliary subunits, α_2 (150 kDa), β (50–78 kDa), δ (17–25 kDa), and γ (32 kDa).[3] LTCCs are further divided by variations in the α_1 subunit into subclasses $Ca_V1.1$-1.4.[3] The α_1 subunit contains the voltage-sensing domains and the Ca^{2+}-selective pore, while the auxiliary subunits modulate channel activity and localization.[3] The α_1 subunit consists of approximately 2000 amino acid residues and has four repeating domains (I-IV).[3] Each domain has six transmembrane segments (S1-S6) with a pore located between S5 and S6. This pore contains negatively charged glutamate residues and is responsible for Ca^{2+} selectivity.[3] The voltage sensitivity is regulated by S4.[3] LTCC can be blocked by dihydropyridines, phenylalkylamines, and benzothiazepines.[3] Regulatory mechanisms involve the protein-protein interaction motifs found in the C-terminus of the α1C subunit.[3]

The influx of Ca^{2+} through LTCCs is tightly regulated by factors such as membrane potential, Ca^{2+}-induced inactivation, and phosphorylation. Various factors, including sympathetic and parasympathetic neurotransmitters, hormones, and intracellular signaling pathways, can modulate cardiac LTCCs. These modulatory influences can affect heart rate, contractility, and cardiac function.[4] PKA phosphorylation of the LTCC after sympathetic activation enhances I_{Ca} by making the LTCC more sensitive (more likely to open and allow Ca^{2+} entry) due to modifying its gating properties (see Chapter **1.2**).[4] This increases their activity in response to depolarization and boosts cardiac contractility during sympathetic stimulation. CICR is the mechanism responsible for amplifying Ca^{2+} signals during cardiac excitation-contraction coupling.[3] The mechanism involves the release of Ca^{2+} from the SR through RyR2, which is triggered by the influx of Ca^{2+} via LTCCs.[5]

The RyR2 is a high-conductance Ca^{2+} release channel composed of a large homo-tetrameric protein complex. Each subunit consists of over 5.000 amino acids.[3] The 565 kDa RyR2 monomers contain distinct domains, including the cytoplasmic N-terminal, central, and transmembrane domains.[3] The

RyR2 activity is tightly regulated by various binding partners/proteins, including calmodulin, FK506-binding proteins (FKBP), protein kinases, phosphatases, Ca^{2+}, $Mg^{2+,}$ and ATP.[3]

A key regulator of RyR2 activity is the phosphorylation by PKA, which increases its open probability and sensitivity towards Ca^{2+}. PKA primarily phosphorylates RyR2 on serine (Ser) residues, with major sites including Ser2808 (or Ser2809 in some species), Ser2814, Ser2815, and Ser2030. Additionally, CaMKII phosphorylates RyR2 primarily at Ser2814. Previous studies have identified RyR2-S2030 as a key site for PKA phosphorylation in response to ß-AR activation.[6, 7] Hyperphosphorylation of the RyR2 lead to SR Ca^{2+} leak through the RyR2, which leads to cardiac arrythmias (see Chapter **1.6.1**) and promotes the Ca^{2+}-clock mechanism.

The FKBP12.6 protein is a vital regulator and stabilizer of the RyR2. FKBP12.6 binds to RyR2 with a high affinity and stabilizes its closed state, preventing excessive Ca^{2+} leakage from the SR.[1] Disruption of FKBP12.6-RyR2 interactions by heperphosphorylation has been implicated in cardiac arrhythmias and heart failure through Ca^{2+} leakage from the SR.[5] RyR2 dysfunction is associated with several cardiac disorders, such as catecholaminergic polymorphic ventricular tachycardia (CPVT), arrhythmogenic cardiomyopathy, and heart failure.[3, 7, 50] These disorders are caused by genetic mutations, post-translational modifications such as phosphorylation, and alterations in RyR2 regulation such as FKBP12.6 binding, which contribute to abnormal Ca^{2+} release (Ca^{2+} leak), and arrhythmogenesis (see Chapter **1.6.1**).[5, 6, 7, 10, 121]

Phospholamban (PLN) plays a crucial role in modulating the activity of the SR Ca^{2+} ATPase (SERCA2a), which is responsible for Ca^{2+} reuptake into the SR.[3] SERCA2a is mainly responsible for the lusitropy (cardiac relaxation), the rate and efficiency of myocardial relaxation during diastole. PLN inhibits SERCA2a activity, and upon PKA phosphorylation, PLN unbinds SERCA2a, which can transport Ca^{2+} with a higher affinity into the SR.[3] In humans, around 70% of the cytosolic Ca^{2+} during the systole is transported into the SR, whereas in mice, the proportion can reach up to 90%. This highlights the importance of modulating SR Ca^{2+} overall in contraction. Disruption of the PLN interaction has been associated with altered Ca^{2+} handling and cardiac dysfunction.[2, 3]

Furthermore, the Na^+/Ca^{2+} exchanger (NCX), an integral membrane protein in the sarcolemma, is crucial in maintaining Ca^{2+} homeostasis in cardiac myocytes, particularly during diastole. NCX operates as a bidirectional antiporter that exchanges three Na^+ for one Ca^{2+}, harnessing the Na^+ gradient generated by the Na^+/K^+-ATPase to drive Ca^{2+} transport. Under normal physiological conditions, NCX primarily functions in a "forward mode" to export Ca^{2+} out of the cell, thereby balancing Ca^{2+} influx and facilitating diastolic relaxation by reducing cytosolic Ca^{2+} levels. This process is critical in preventing Ca^{2+} overload.[2, 3]

1.4 Vegetative modulation of cardiac contractility and pacemaking

The active forces of the myocardium can be adapted to changing needs by the autonomous nervous system. This system comprises the parasympathetic and sympathetic branches, which have opposing effects on heart function. The parasympathetic nervous system decreases heart rate, while the sympathetic nervous system increases it. These adjustments are mediated by neurotransmitters, which act as signaling molecules by binding to specific G protein-coupled receptors (GPCRs).[2, 5, 11]

GPCRs are seven-transmembrane proteins that respond to extracellular ligands and initiate intracellular signaling cascades.[11] They are ubiquitous in living organisms, with over 1000 members, and are one of the largest protein superfamilies. Approximately 800 GPCRs have been identified in humans, playing a crucial role in diverse signaling processes.[12] GPCRs can modulate cellular function through multiple downstream signaling pathways, making them targets for approximately 50% of currently available drugs, such as ß-blockers, against heart arrhythmia. GPCRs can form homo- or heterodimers, which increases their functional diversity.[2, 11]

Their signaling pathway involves the activation of guanine nucleotide-binding (G) proteins and downstream effectors, producing second messengers that regulate various cellular responses. G-proteins are a family of proteins that act as molecular switches in cellular signaling pathways. They are either present as guanosine diphosphate (GDP) in the inactive state or guanosine triphosphate (GTP) in the active state. Upon binding to a ligand (e.g., a hormone or neurotransmitter), GPCRs undergo conformational changes that activate the heterotrimeric G-proteins consisting of α, ß, and γ subunits, causing the α subunit (now with GTP) to dissociate from the βγ dimer. Both can now activate different downstream targets. The α subunit can hydrolyze GTP to GDP, turning itself off, leading to a reassociation with the βγ dimer, reforming the inactive G protein.[2, 11, 12]

The two prominent signaling pathways activated by GPCRs in the heart are associated with the Gs and Gi protein families. Specifically, the ß1- and ß2-adrenergic receptors (ARs) subtypes belong to the Gs family and play a critical role in regulating heart function. In humans, the heart expresses ß1-AR at a ratio of approximately 4:1 compared to ß2-AR, while the ß3-AR subtype is expressed at comparatively low levels.[13] ß1-AR in the heart are located throughout the sarcolemma and T-tubuli. These receptors are activated by the sympathetic nervous system through the neurotransmitters norepinephrine and epinephrine, initiating the Gs pathway, which subsequently activates the cAMP/PKA signaling cascade.[14] Gs proteins activate adenylate cyclases (ACs), which produce cAMP from ATP. Cardiomyocytes express two primary membrane-bound AC isoforms, AC5 and AC6. AC5 facilitates its interaction with both the ß1-AR and ß2-AR, while AC6 is primarily associated with the ß1-AR.[13, 14, 15, 16] AC activation leads to cAMP production, which in turn activates PKA, resulting in the phosphorylation of several target proteins, including LTCC, RyR2, PLN, and troponin I (**Fig. 3**).[2, 17] As a result, cardiac

contractility (inotropic response, the strength of myocardial contraction) and heart rate (chronotropy, the frequency of contraction) and lusitropy (myocardial relaxation during diastole) are enhanced (**Fig.3**).[2] Inotropy is mainly dependent on intracellular Ca^{2+} availability and myofilament sensitivity, while chronotropy is determined by the firing rate of the SAN.[2] Lusitropy is mainly dependent on the rate and extent of Ca^{2+} removal from the cytosol after contraction, by SERCA2a, NCX (see Chapter **1.3**), and troponin I, which reduces the Ca^{2+} sensitivity of troponin C, enhancing the relaxation.[2]

In the inactive state, PKA exists as a tetrameric holoenzyme composed of two catalytic (C) subunits and two regulatory (R) subunits (**Fig. 3**). Each regulatory subunit contains two cAMP-binding domains. When cAMP levels increase, cAMP molecules bind to the regulatory subunits, causing a conformational change that releases the catalytic subunits, which become active kinases. These catalytic subunits can phosphorylate serine and threonine residues on target proteins by transferring the phosphate from ATP to the protein substrate, leading to changes in their activity.[17]

Gs stimulation has positive chronotropic effects on pacemaker activity. The activation of HCN channels contributes to faster depolarization, and the LTCC accelerates the AP upstroke through cAMP. The enhanced activity of IKs contributes to faster repolarization by the PKA-mediated phosphorylation of the hERG channel (KCNH2), allowing for higher heart rates without loss of diastolic filling time.[3, 4]

On the contrary, Gi proteins inhibit AC activity, which reduces cAMP levels and downstream PKA-mediated signaling.[3] They are activated by receptors like M_2 muscarinic receptors when stimulated by the parasympathetic neurotransmitter acetylcholine (ACh).[16] The inhibition of AC activity reduces cAMP levels and counteracts Gs-mediated effects, like reduced LTCC and HCN-channel activity. In addition, the βγ subunits of Gi activate G-protein-gated inwardly rectifying potassium (GIRK) channels, causing hyperpolarization of the membrane potential, which increases the time required for pacemaker cells to reach the threshold for AP generation.[3, 15, 16] These processes lead to a decreased heart rate known as negative chronotropy.[3]

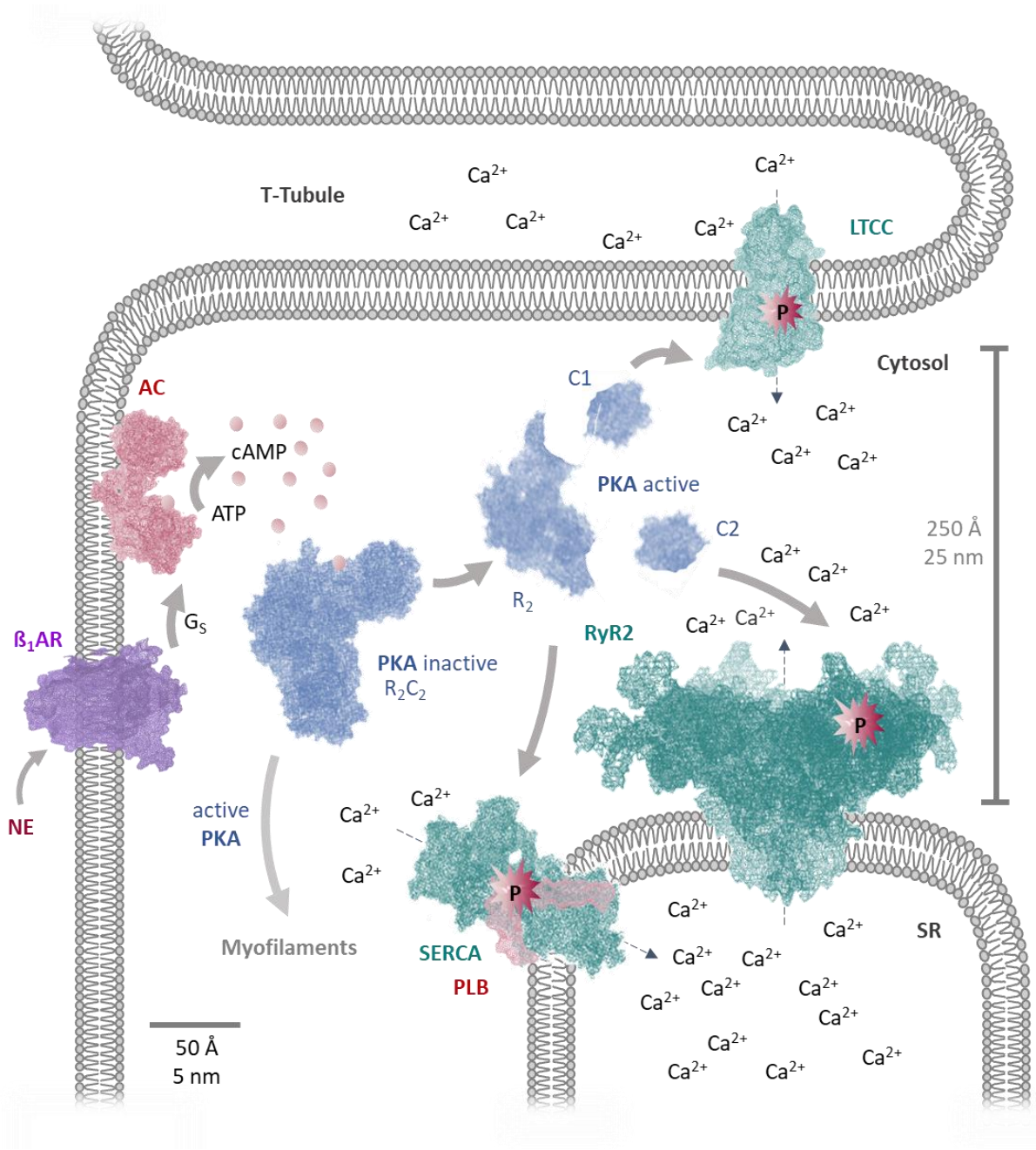

Fig. 3: Gs-coupled sympathetic signaling pathway

The sympathetic system can further enhance the contraction-excitation coupling process. When stimulated, the sympathetic system releases norepinephrine (NE) onto cardiomyocytes, activating ß1-adrenergic receptors (ß1-ARs) and triggering the second messenger cAMP by AC via the Gs protein. Subsequently, the second messenger, cAMP, activates PKA, which phosphorylates various channels and proteins in the cardiomyocyte. The figure illustrates the phosphorylation of the LTCC, RyR2, and PLN and their effect on the myofilament. The protein structures were generated using PyMol, with the following PDB numbers LTCC (8E5B), RyR2 (5GOA), ß1-AR (7BTS), PKA (6NO7), SERCA with PLN (4Y3U), and adenylyl cyclase (AC) (2AR7). Protein sizes and distances are accordingly.

1.5.1 Signaling microdomains

A multitude of signaling pathways are subject to regulation by a shared set of second messengers, including cAMP and cyclic guanosine monophosphate (cGMP). Consequently, cells are equipped with regulatory mechanisms that distinguish between signals that share the same second messengers. This can be accomplished by confining specific signals to a designated microdomain location.[14, 18, 20]

Microdomains are unique subcellular regions that contain distinct protein assemblies and signaling complexes. Phosphodiesterases (PDEs) and A-kinase anchoring proteins (AKAPs) play a critical role in these regions by terminating signals and facilitating the precise localization of regulatory proteins.[18, 19] PDEs terminate cyclic nucleotide signals by hydrolysing the cyclic structure, and AKAPs anchor key signaling molecules (e.g., PDEs, PKA), ensuring spatially restricted signal transduction.[13-19]

Cardiac PDEs, including PDE1, PDE2, PDE3, PDE4, PDE5, PDE8, and PDE9, exhibit isoform-specific substrate selectivity and subcellular localization, enabling the fine-tuned regulation of cyclic nucleotide levels in different cardiac compartments and ensuring spatially restricted signaling.[18] The most important PDEs in cardiac regulation are PDE1, PDE2, PDE3, PDE4 and PDE8 (**Table 1**).[18, 29] PDE1 is activated by Ca^{2+} and hydrolyzes cAMP and cGMP, but is more relevant to cGMP regulation. While PDE2 primarily degrades cAMP, it is activated by cGMP, allowing the cGMP-cAMP crosstalk. PDE3 hydrolyzes cAMP, but its activity is competitively inhibited by cGMP, modulating cAMP availability. PDE4 is phosphorylated and activated by PKA, forming a negative feedback loop; in contrast, PDE8 contributes to sustained cAMP degradation but is not regulated by PKA. In cardiomyocytes, distinct PDE isoforms compartmentalize signaling to maintain precise control over cAMP dynamics, ultimately modulating the phosphorylation of RyR2 and LTCC, which influence Ca^{2+} handling and excitation-contraction coupling.[15, 16, 18, 29]

AKAPs refine signaling specificity by tethering regulatory proteins within microdomains, thereby impacting cardiac contractility, ion channel function, and gene expression, as well as interactions with PDEs (**Table 2**).[18, 19] Cardiomyocytes express multiple AKAP isoforms, including AKAP5, AKAP6, AKAP7, AKAP9 (Yotiao), and AKAP12.[19, 20, 21] Important AKAPs in cardiomyocytes are AKAP5 (also known as AKAP150/79)[22] and AKAP15/18α (Gravin)[23], they interact with the LTCC by anchoring PKA, PDEs (PDE4D3/5) and other signaling molecules to regulate LTCC activity, Ca^{2+} influx, and cardiac excitation-contraction coupling. Similarly, muscle-selective AKAP (mAKAP/AKAP6)[25-27] forms a complex with RyR2, PDE4D3, and PKA, modulating Ca^{2+} dynamics.[22] RyR2 microdomains involve mAKAP and PDE4D3, which co-immunoprecipitate with RyR2 in human and rat hearts.[14, 44, 45] The disruption of PKA-mAKAP interactions has decreased PDE4D3 activity, impairing the feedback regulation. PDE4D knockout models display RyR2 hyperphosphorylation, abnormal Ca^{2+} release (leak), and increased arrhythmic

susceptibility.[24, 25, 26, 27] At SERCA, AKAP15/18 δ forms a signaling complex with PKA, PDE3A, PDE4D and PP2B, coordinating the PLN phosphorylation and thus ensuring Ca^{2+} reuptake into the SR during the diastole. [23] It was shown that PDE3A inhibition increased PLN phosphorylation, thereby enhancing Ca^{2+} handling. [14, 28, 29] Furthermore, ß1-AR-cAMP signaling is four times higher in SERCA2a microdomains compared to the cytosol, underscoring the significance of compartmentalized regulation. [14, 28, 29]

Table 1: Human cyclic nucleotide phosphodiesterase isozymes: from Essayan et al., 2001[29]

Family (no. of genes)	**Characteristics**	**Km (µmol/L) cAMP; cGMP**	**Primary tissue distribution**	**Examples of Inhibitors**
PDE1 (3)	Ca^{2+}/calmodulin-stimulated	1-30; 3	Heart, brain, lung, smooth muscle	KS-505a, Vinpocetine
PDE2 (1)	cGMP-stimulated	50; 50	Adrenal gland, heart, lung, liver, platelets	EHNA (MEP-1)
PDE3 (2)	cGMP-inhibited, cAMP-selective	0.2; 0.3	Heart, lung, liver, platelets, adipose tissue, immunocytes	Cilostamide, Enoxamone, Milrinone, Siguazodan
PDE4 (4)	cAMP-specific, PKA-activated	4; >3000	Heart, Sertoli cells, kidney, brain, liver, lung, immunocytes	CDP840, Rolipram, SB 207499, Tibenelast
PDE8 (2)	cAMP-selective, IBMX insensitive	0.06; N/A	Heart, testes, eye, liver, skeletal muscle, kidney, ovary, brain, T lymphocytes	None selective

Table 2: Distinct AKAP localization

Channel	**AKAPs**	**Anchored regulatory proteins**
LTCC	AKAP15/18α[23]	PKA, PDE4D3/5, AC5, calcineurin
LTCC	AKAP5[22]	PKC, PP2B, PKA, AC5, calcineurin
RyR2	mAKAP (AKAP6)[25, 26, 27]	PP2A, PDE4D3, PKA
SERCA	AKAP15/18 δ[28]	PKA, PP2B, PDE3A, PDE4D

1.5.2 Dysregulation of microdomains in the context of impaired cardiac function

The autonomic nervous system plays a crucial role in regulating signaling pathways in the heart (see Chapters **1.4** and **1.5.1**), and disruptions in any of these signaling pathways that are maintained by microdomains can contribute to impaired cardiac function and heart failure.[33, 40]

It has been shown that disruption of the microdomains of the ß-AR signaling pathway due to PDE downregulation leads to cardiomyocyte apoptosis, hypertrophy, and heart failure.[13, 14, 30-33] Dysregulation of PDE-mediated cAMP compartmentalization is closely linked to cardiac dysfunction in hypertrophied myocytes, where the activities of PDE3A, PDE4A, and PDE4B were reduced, which alters Ca^{2+} handling via RyR2 and LTCC.[29] This disruption contributes to impaired excitation-contraction coupling and arrhythmic potential.

In heart failure with reduced ejection fraction (HFrEF), Ca^{2+} signaling is impaired due to the disruption of microdomains around the LTCC by increased PDE2 activity, and around the RyR2 by PDE4 uncoupling.[14, 22, 38, 39-48] PDE4 disregulation leads to higher cAMP levels leading to increased PKA activity and thus to hyperphosphorylation of the RyR2 and following abnormal Ca^{2+} release (leak), which increased arrhythmic susceptibility.[14, 42, 44, 45, 46] In addition, in HFrEF, the SERCA2a expression is decreased. [14, 47, 48] The restoration of SERCA2a function has been demonstrated to enhance cardiac performance in models of heart failure. [14, 42,45,47]

In heart failure with preserved ejection fraction (HFpEF), where reduced T-tubule density and increased diastolic SR Ca^{2+} leak occur, PDE2 and PDE3 activities increase, resulting in enhanced cAMP degradation and impaired ß2-AR signaling. Additionaly, PDE4 downregulation disrupts the integrity of the RyR2 microdomain, contributing to abnormal Ca^{2+} handling and diastolic dysfunction by abnormal Ca^{2+} release (leak).[14, 27, 45, 46]

Given the established role of dysregulated signaling within microdomain compartments in the development of heart failure and arrhythmias, targeting specific regulators, such as PDE isoforms and microdomain components, might lead to promising therapeutic approaches for restoring cardiac function.[24] UCR1C (Upstream Conserved Region), a novel activator of PDE4 in cardiomyocytes, is particularly interesting for therapeutic applications. The expression of UCR1C has been shown to decrease PKA activity and prevent hypertrophy when subjected to chronic ß-AR stimulation.[24,, 29] Another not yet approved but promising group of drugs are Rycals, which stabilize the RyR2 and prevent Ca^{2+} leak (see Chapter **5.7**).[60]

1.6.1 Cardiac arrhythmias

Cardiac arrhythmias, defined as deviations from the heart's regular beating rhythm, affect millions worldwide.[50] The most prevalent form of cardiac arrhythmia is atrial fibrillation (AF), affecting over 33 million individuals. According to estimates by the World Health Organization (WHO), ischemic heart disease, which can cause heart arrhythmia, resulted in 123.1 deaths per 100,000 individuals worldwide in 2021, with Germany experiencing a higher rate of 176.11 deaths per 100,000 population.[49] The overall burden of arrhythmias varies depending on factors such as age, comorbidities, underlying causes such as coronary heart disease, heart failure, electrolyte imbalance, and genetic predispositions/mutations. A comprehensive understanding of the molecular mechanisms underlying cardiac arrhythmias and analyzing the various components implicated in the disease, such as the role of PKA/cAMP microdomains in different cardiomyocyte subtypes, is imperative for developing targeted therapies and enhancing management strategies.[50]

The development of cardiac arrhythmias is associated with complex molecular processes that disrupt normal electrical signaling and rhythm in the heart (see Chapter **1.2**). Key mechanisms include abnormalities in ion channels, impaired intracellular Ca^{2+} handling, conduction system dysfunction, and structural remodeling, which are often exacerbated by genetic mutations, myocardial ischemia, and underlying heart disease.[51]

Distinct subpopulations of cardiomyocytes contribute to the initiation and maintenance of arrhythmias.[50] Abnormalities in pacemaker cells can lead to bradycardia (< 60 beats per min [bpm]) or tachycardia (> 100 bpm) and can predispose patients to arrhythmias such as AF.[50] Dysfunction in working cardiomyocytes, like metabolic dysfunction (e.g., ATP deficiency), ischemia, electrolyte imbalances, or abnormal Ca^{2+} handling (Ca^{2+} leak), can lead to ectopic activity that fires a premature beat (extrasystole). When the extrasystole finds one path blocked (still refractory) and another path conducting slowly, the impulse may circle back via the recovered tissue, forming a reentrant circuit, where a wave of excitation reenters and re-excites the same tissue repeatedly. Depending on the location and scale, this can cause and maintain tachycardias or fibrillation. [50, 51] Anatomical reentry occurs around obstacles like fibrotic or necrotic tissue, as seen in heart failure or post-myocardial infarction.[51]

Ca^{2+} dysregulation plays a pivotal role in arrhythmogenesis. Dysfunctional RyR2 channels have been linked to abnormal Ca^{2+} leaks, which are associated with conditions such CPVT. [50, 52, 53, 121] This condition arises due to mutations in the RyR2 gene, leading to impaired binding of the FKBP12.6 protein, increasing the sensitivity of the RyR2 to Ca^{2+} within the cell, or unzipping of the RyR2 protein. The net result of this process is the occurrence of a Ca^{2+} leak through RyR2 during diastole, which activates the NCX. The NCX attempts to extrude the excess Ca^{2+} and, in the process, transports three Na^{+} into the

cell in electrogenic exchange. This process can generate a depolarizing current, which, in turn, can lead to delayed afterdepolarizations (DADs). DADs have the potential to reach a threshold that triggers premature atrial or ventricular contractions. These extrabeats can propagate through the heart, disrupting normal rhythm and potentially leading to arrhythmias, such as ventricular tachycardia (VT) or atrial fibrillation (AF).[52, 53]

Prolonged Ca^{2+} leak can lead to ventricular tachycardia (VT), which increases transporter activity and contributes to ATP depletion. This energy deficiency, combined with abnormal calcium handling, can contribute to the development of cardiomyopathy, a condition characterized by weakened heart muscle and reduced pumping capacity. Over time, these changes can contribute to the onset of heart failure and elevate the risk of sudden cardiac death.[3, 50, 51]

Similarly, dysregulation of LTCC function can lead to arrhythmias associated with genetic mutations resulting in Long-QT syndrome and early afterdepolarizations (EADs). EADs develop during the repolarization phase of the cardiac AP, often prolonging the plateau phase and reactivating Ca^{2+} channels. This can result in life-threatening arrhythmias, such as Torsades de Pointes. LTCC blockers, such as verapamil and diltiazem, are frequently used to mitigate these effects by reducing excessive Ca^{2+} influx (see Chapter **1.6.2**).[52, 57]

1.6.2 Treatments for cardiac arrhythmias

Cardiac arrhythmias are a significant clinical challenge, requiring effective pharmacological interventions to restore normal heart rhythm.[50] Molecular and genetic research advances have identified potential targets for novel antiarrhythmic therapies, including ion channels, gap junction proteins, and intracellular signaling pathways. Approved antiarrhythmic drugs are classified into four main classes using the Vaughan Williams classification system based on the different mechanism of action: class I are Na^+ channel blockers, class II consists of ß-blockers, class III are K^+ channel blockers and class IV are Ca^{2+} channel blockers.[3, 52-59]

For example, Flecainide primarily blocks voltage-dependent Na^+ channels, preventing the influx of Na^+. This prevents the formation of premature ventricular contractions (PVCs), reduces and slows the overall heart rate.[53, 55] Additionally, Flecainide inhibits the activity of RyR2 when it is in the open state. Thus, it reduces the occurrence of arrhythmogenic Ca^{2+} leak and serves as a protective measure against CPVT in both mice and humans.[56, 121] Another example is Verapamil, an LTCC blocker, which is mainly used to treat cardiac arrhythmia, hypertension, and angina pectoris. It has a negative dromotropic effect (slowing down conduction at the AVN), a negative chronotropic effect (reducing the heart rate), and a negative inotropic effect (reducing the force of contraction). Additionally, it leads to vasodilation, resulting in a decrease in blood pressure.[57] K^+ channel blockers, such as Amiodarone, are also widely used to prolong the refractory period and maintain a stable rhythm.[58] Carvedilol, an effective ß-blocker, reduces heart rate and contractility and prevents reentry, among other effects.[54, 59] It blocks the Gs/cAMP/PKA signaling pathway and thus decreases the LTCC, RyR2, PLN, and troponin I activity, which leads to a reduced heart rate and contractility.[59]

However, antiarrhythmic drug therapies are often broad-spectrum medications (e.g., ß-blockers), and therefore have a wide range of side effects,[3, 54, 59] necessitating non-pharmacological interventions, such as catheter ablation or the use of an implantable cardioverter-defibrillator to prevent or rapidly terminate ventricular arrhythmias. Additionally, multiple studies have demonstrated that implantable cardioverter-defibrillators are more effective than antiarrhythmic drugs in reducing the risk of sudden cardiac death. However, using these devices has drawbacks, as they require an invasive procedure and have a limited lifespan. Moreover, the electrical shock delivered by the device can have psychological impacts on patients.[84] These challenges underscore the need for novel approaches and more research to identify specific drug targets for heart arrhythmias, with a focus on regulating LTCC and RyR2 in signaling microdomains and their role in Ca^{2+} cycling abnormalities, as Ca^{2+} leak through the RyR2 is almost always involved in heart arrhythmias. Currently, there are no clinically approved medications against Ca^{2+} leak trough the RyR2.

1.7 Optogenetic methods

Previous information on microdomain formation has provided valuable insights. However, this was mainly achieved through pharmacological approaches, such as the inhibition of PDEs, which resulted in global rather than local inhibition. Information from local FRET-sensor measurements was also available; however, the same local modulation issue persisted. This work employed targeted optogenetic tools to investigate the modulation of cAMP microdomains on LTCC and RyR2. Optogenetics is a rapidly advancing field that combines the tools of genetics and light to control and manipulate cellular processes with high spatiotemporal precision compared to pharmacological approaches. It involves using light-sensitive proteins, the best known of which are the opsins, to manipulate and control cellular activities with light. The mechanism is based on a conformational change that occurs in the light-sensing domains of these proteins upon exposure to specific light. These conformational changes then lead to a variety of functional modifications in different proteins, such as channel opening (e.g., channelrhodopsin)[67], GPCR activation (e.g., jellyfish opsin),[68] or AC activation (e.g., photoactivatable adenylate cyclases),[69, 70, 72] inhibitory tools (e.g., photoactivated PKA inhibitor)[71,] and many more. Light-sensitive proteins can be genetically expressed in specific cell types and subcellular compartments, allowing for targeted light-induced activation or inhibition of cellular processes. Several optogenetic tools were considered for this study for local and global activation and inhibition of the cAMP/PKA pathway. Increasing cAMP levels in response to light is possible using photoactivatable adenylate cyclases (PACs) (**Fig. 4 A**). For this study, PACs from the bacterium Beggiatoa bPAC,[69, 72] its red-shifted mutant bPAC-S27A,[69] and a PAC from the bacterium *Turneriella parva* TpPAC[70] which exhibits lower dark activity, were used.

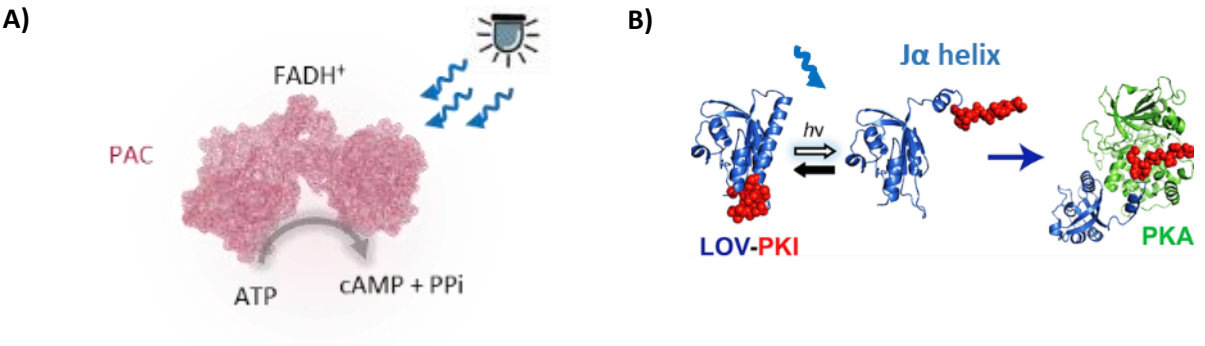

Fig. 4: Optogenetic tools to modulate cAMP and PKA
A) *3D structure/model of photoactivatable adenylyl cyclase (PAC) with BLUF domain containing the FAD chromophore that reacts to FADH⁺ after blue light illumination leading to a conformational change that activates the enzymatic function to generate cAMP from ATP in the catalytic domain* ***B)*** *The light oxygen voltage sensing (LOV) domain is fused to a PKA inhibitor (PKI) at the Jα helix building the LOV-PKI. The arm of the Jα helix in LOV-PKI opens upon illumination with blue light. It exposes the PKI to be active and bind to the catalytic subunit of PKA, inhibiting its catalytic function. Protein structures generated using PyMol. LOV-PKI construct from Yi et al., 2014. PDB number: 8QFE (OaPAC).*

PACs convert ATP into cAMP and inorganic pyrophosphate (PPi) upon light stimulation, activating downstream signaling pathways (see Chapter **1.4**). The process is driven by the blue light-sensing (BLUF) domain, which contains a photoreceptor that utilizes flavin adenine dinucleotide (FAD), a redox-active coenzyme, as its chromophore. The FAD molecule absorbs photons when exposed to blue light, specifically in the range of 450-470 nm. It is formed into $FADH^+$, resulting in a conformational change in the overall shape of the BLUF domain by rearrangement of hydrogen bonds within the protein. In its resting state, in the dark, without light activation, PAC activity remains unchanged. One of the advantages of PAC is that its activation is reversible and can be induced many times. The BLUF domain can return to its original conformation when the blue light stimulus is removed. This light-driven enzyme is a valuable tool for studying cellular processes and cAMP signaling pathways in a highly controlled manner.[69, 70, 71]

To locally reduce PKA-dependent phosphorylation by light, the photoactivated protein kinase A inhibitor (LOV-PKI)[71] was used (**Fig. 7 B**). The Light-Oxygen-Voltage Sensing (LOV) domain is a light-sensing protein found in various organisms, including plants, bacteria, and fungi. It plays a critical role in photoreception and signal transduction in response to blue light. The LOV domain contains a flavin chromophore (flavin mononucleotide (FMN) or FAD) that undergoes a conformational change upon exposure to blue light. This flavin chromophore is non-covalently bound to the LOV domain within a binding site. The LOV domain responds to blue light, with an absorption peak typically at 450-470 nm. When the flavin chromophore absorbs blue light, it provides energy to excite an electron within the chromophore to a higher energy state. The formation of the covalent bond between flavin* and the cysteine adduct induces a conformational change in the LOV domain.[71] LOV-PKI is an optogenetic tool that combines the LOV domain, which undergoes conformational changes upon exposure to blue light, with a peptide inhibitor of PKA. Illumination-induced unfolding of the Jα helix exposes the dark-docked PKI peptide and triggers downstream reactions, in particular, binding of PKI to the catalytic subunit of PKA, thereby preventing its phosphorylation activity.[71]

2. Aim of the Thesis

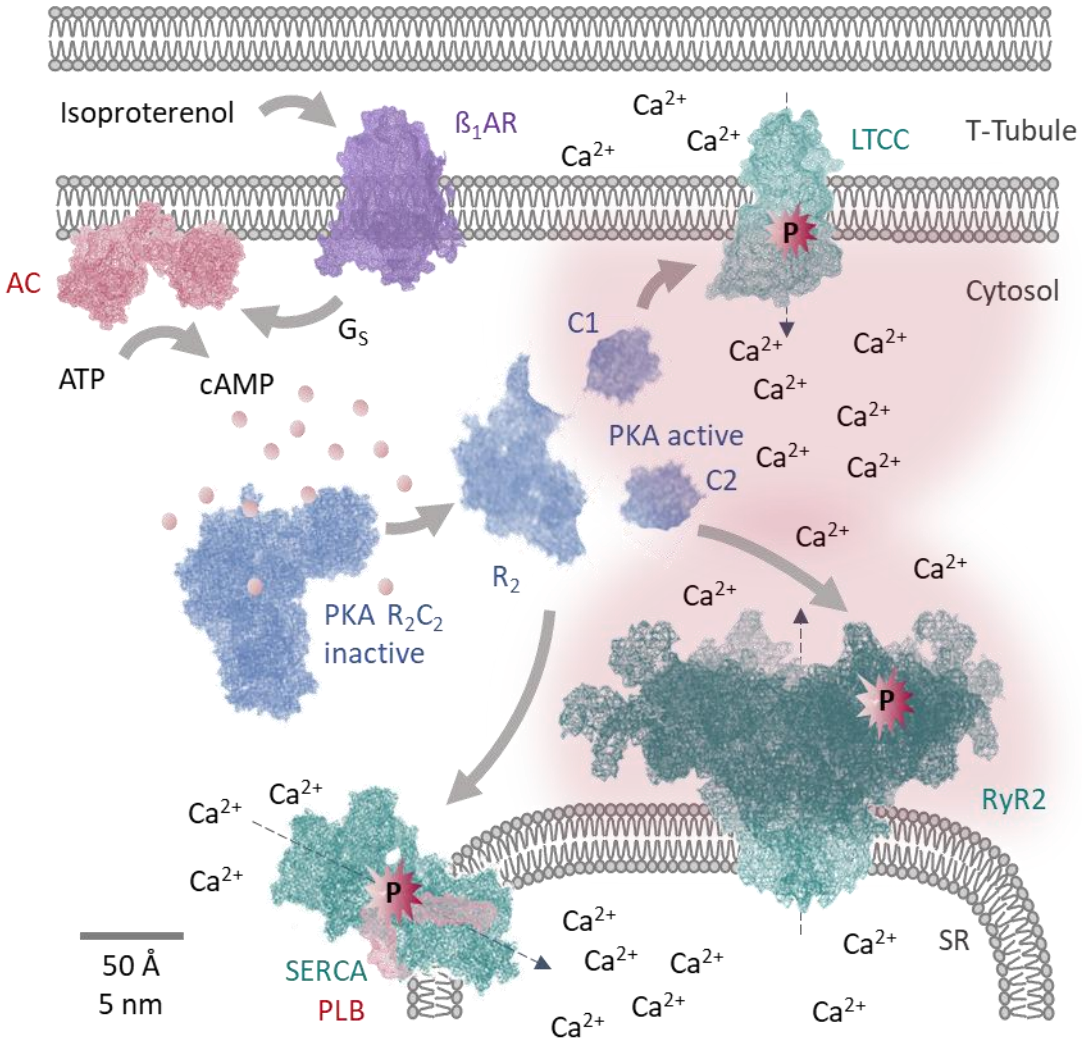

Fig. 5: Are LTCC and RyR2 controlled by the same cAMP pool or by separated cAMP pools
The sympathetic activation of LTCC and RyR2 is both mediated by the cAMP/PKA pathway, raising the question of whether they are controlled by independent cAMP microdomains or functionally cross-talk. This should provide further insight into their contribution to cardiac arrhythmias and possible therapeutic approaches. Protein structures were created using PyMol with the following PDB numbers: LTCC (8E5B), RyR2 (5GOA), ß1-AR (7BTS), PKA (6NO7), SERCA (4Y3U).

Hypothesis: Cardiac LTCC and RyR2 are controlled by independent cAMP microdomains.

This study investigates whether independent cAMP microdomains control cardiac LTCCs and RyR2 or if they functionally cross-talk. The ß-AR Gs/cAMP/PKA signaling pathway (see Chapter **1.4**) is a critical intracellular cascade regulating the heart's pacemaking, contractility, and arrhythmia.[12-19] It is well established that cAMP signaling is organized into microdomains composed of GPCRs, AKAPs, PDEs, and PKA (see Chapter **1.5**).[12-19, 66] During adrenergic stimulation, cAMP signaling mediates LTCC phosphorylation, which increases external Ca^{2+} entry and CICR from the SR (**Fig. 5**). However, the

relative contribution to the overall inotropic effect is difficult to predict. Furthermore, the close physical proximity between LTCCs and RyR2 (~100–200 Å) raises the question of whether these proteins are regulated by independent cAMP microdomains or engage in functional cross-talk. Indeed, a study by Wang and his colleagues investigated the Ca^{2+} signaling between LTCCs and RyR2s at the single-channel level and showed that a Ca^{2+} sparkle from a single LTCC triggers SR Ca^{2+} release from four to six RyR2s, indicating a direct and local control of SR Ca^{2+} release through LTCCs.[3, 17]

Most knowledge of microdomain signaling is based on fluorescence imaging techniques using FRET-based cAMP sensors.[13] However, such observational techniques often yield only correlative results, rather than providing direct mechanistic insights into direct local modulation. To address this limitation, this project uses optogenetic methods (see Chapter **1.7**). In particular, light-activated adenylyl cyclases were subcellularly targeted to the LTCC and RyR2 and globally expressed in the cytosol. The effect of local and global cAMP production was then analyzed concerning the beating rate, Ca^{2+} transients, and phosphorylation in cardiomyocytes (see Chapter **4**).

3. Material and Methods

3.1 Cloning strategy for PACs and LOV-PKI constructs

Table 3: Generated and used plasmids

Plasmid/DNA name	Origin	Size	Resistance
CMV_mVenus-LOV-PKI	Addgene	5176 bp	Kan.
pEGFP-h_bPAC_mCherry cMyc	Dr. Yinth Andrea Bernal Sierra*	5911 bp	Amp.
bPAC-S27A-SthK-P2A-TS-mKate-ER	Dr. Yinth Andrea Bernal Sierra*	5911 bp	Amp.
TpPAC-mCherry	Dr. Yinth Andrea Bernal Sierra*	7010 bp	Amp.
AAV CAG JellyOp EYFP	Philipp Makowka (AG Sasse)	6,6kB	Amp.
pCAG-bPAC_EYFP	Cloned	8311bp	Amp.
pCAG-bPAC-S27A_EYFP	Cloned	8311bp	Amp.
pCAG_TpPAC_EYFP	Cloned	8308 bp	Amp.
nb.F3 Fragment for PACs	GeneArt	423 bp	-
nb.F3 Fragment for LOV-PKI	GeneArt	425 bp	-
FKBP12.6 for PACs	GeneArt	1191 bp	-
FKBP12.6 for LOV-PKI	GeneArt	1122 bp	-
pCAG_nb.F3_bPAC-WT_EYFP	Cloned	8686 bp	Amp.
pCAG_nb.F3_bPAC-S27A_EYFP	Cloned	8686 bp	Amp.
pCAG_nb.F3_TpPAC_EYFP	Cloned	8683 bp	Amp.
pCAG_bPAC_mCitrine_FKBP12.6	Cloned	8644 bp	Amp.
pCAG_bPAC-S27A_mCitrine_FKBP12.6	Cloned	8644 bp	Amp.
pCAG_TpPAC_mCitrine_FKBP12.6	Cloned	8641 bp	Amp.
pCMV_nb.F3_mVenus_LOV-PKI	Cloned	5553 bp	Kan.
pCMV_FKBP12.6_mCitrine_LOV-PKI	Cloned	5512 bp	Kan.
AAV pCAG-TpPAC-EYFP-cyt	Cloned	6607 bp	Amp.
AAV pCAG-nb.F3-TpPAC-EYFP	Cloned	6982 bp	Amp.
AAV pCAG-TpPAC-mCitrine-FKBP12.6	Cloned	6940 bp	Amp.

*(Dr. Yinth Andrea Bernal Sierra: Experimental Biophysics Department of Biology Humboldt University Berlin)

The plasmid mVenus-PA-PKI (Kan^R) was ordered from Addgene (65456 ID, Yi et al., 2014). The plasmids pEGFP-N1-h_bPACwt_mCherry, pEGFP-N1-h_bPAC-S27A_mCherry and TpPAC-mCherry (h-TP-PAC_pManu) were provided by Dr. Yinth Andrea Bernal Sierra from the lab of Prof. Peter Hegemann and were used for PCR amplification of bPAC, bPAC-S27A and TpPAC with appropriate overhangs to the destination vector. The destination vector CAG_opto_b2AR_EYFP (AG Sasse) was cut with HindIII and NotI to excise the opto_b2AR. The fragments were obtained from the gel and purified. The

plasmids pCAG_bPAC_EYFP and pCAG_bPAC-S27A_EYFP were produced through homologous recombination of the bPAC and bPAC-S27A inserts into pCAG_EYFP backbone with GeneArt® Seamless Cloning and Assembly Enzyme Mix.

The nanobody nb.F3 sequence was obtained from Morgenstern et al. (2019) eLIFE and generated by GeneArt, along with overhangs for the PAC and LOV-PKI constructs. The fragments contain restriction sites for HindIII in PACs and AgeI in LOV-PKI for enzyme ligation.

FKBP12.6 was also synthesized by GeneArt, along with the fluorescent marker mCitrine and overhangs for the PAC and LOV-PKI constructs. The fragments contain restriction sites for PACs (HindIII and NotI) and for LOV-PKI (AgeI and BsrGI) for enzyme ligation.

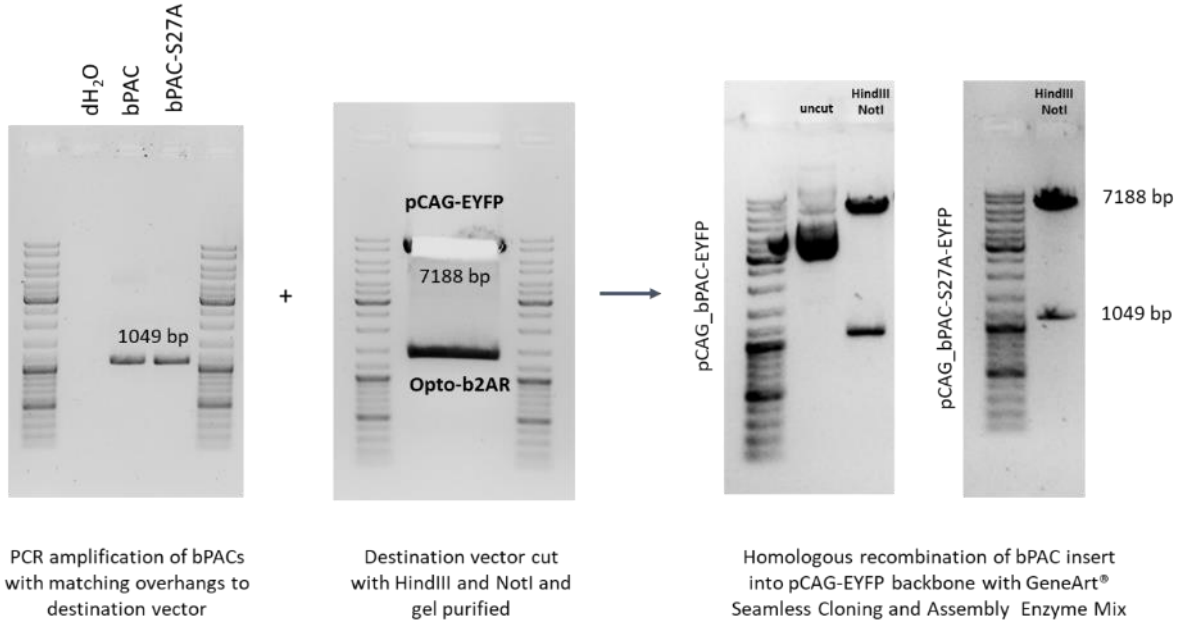

Fig. 6: Example of bPAC-EYFP and bPAC-S27A-EYFP cloning
bPAC and bPAC-S27A were PCR amplified using matching overhang primers for the destination vector containing the CAG promoter and EYFP. The Opto-ß2-AR was excised with HindIII and NotI from the destination vector, which was then replaced with bPACs in a ligation reaction. Test digestion of the newly ligated plasmid shows the vector's backbone and the insert fragment of the bPACs. DNA size was visualized in a 1% agarose gel using HD-Green for DNA staining.

3.1.1 Cloning protocol: 1 restriction cloning

3.1.1.1 Re-transformation

Approximately 50-100 ng of DNA was used to retransform the desired DNA into Mach1-competent bacterial cells for plasmid proliferation.

Mach1 cells were thawed on ice, and 50-100 ng of DNA was added. The cells were then incubated on ice for 30 min. The cells were then heat-shocked at 42°C for 45 s, incubated on ice for 2 min, and 250 µL of SOC medium was added. The cells were then incubated at 37°C for 1 h. The cells were then plated on LB plates containing the antibiotic and the plasmid resistance marker. The cells were diluted with 750 µL SOC medium, and 20 µL was taken per plate. The plates were incubated overnight, and the next day, 10 colonies were picked and incubated in 5 mL of LB with the appropriate antibiotic overnight to promote bacterial proliferation and facilitate the desired plasmid production. The next day, plasmid preparation was performed using the QIAprep® Spin Miniprep Kit (250) according to the manufacturer's instructions. After preparation, nucleic acid concentration and quality were measured using a Thermo Scientific NANODROP 2000C spectrometer, followed by digestion with the appropriate restriction enzymes, and then checked on a 1% agarose gel. If a large amount of plasmid is required for further cloning, a maxi plasmid preparation using the EndoFree® Plasmid Maxi Kit (10) is recommended per the user's manual.

Table 4: LB-medium

LB-Medium	
Trypton	1%
yeast extract	0.50%
NaCl	1%
in ddH_2O and autoclave	

Table 5: LB-Agar-plates medium

LB-Agar-Plates medium	
Trypton	1%
yeast extract	0.50%
NaCl	1%
Agar	1.5%
in ddH_2O and autoclave	

3.1.1.2 Digest insert and vector with same restrictions enzymes

Restriction enzymes were used to cut plasmids with specific overhangs at a specific site for subsequent ligation.

Table 6: Reaction mix for enzyme digestion

(e.g. HindIII and BamHI in BamHI-Buffer) run for 2h at 37°C	
DNA	
Enzyme 1	10 µg (5-10 µg)
Enzyme 2	5 µL HindIII (2x fold)
Buffer	2.5 µL BamHI
Add up to 80 µL with ddH_2O	8 µL BamHI Buffer

3.1.1.3 Test-gel

To check the fragments' size and degree of digestion, 1-2 µL were taken, applied to a 1% agarose gel, and imaged.

3.1.1.4 Inactivation of enzyme reaction

After correct and complete digestion, the enzymes were inactivated. The correct inactivation temperature and time for each enzyme were determined. For example, HindIII and BamHI are inactivated at 80°C for 20 min.

3.1.1.5 Dephosphorylation of vector plasmid with FASTAP

The vectors were dephosphorylated to avoid self-alignment, as described in **Table 7**.

Table 7: Reaction mix of dephosphorylation

(keep insert on ice)	
Vector	80 µL (10 µg DNA)
10x FASTAP-Buffer	10 µL
FASTAP (1U)	10 µL
Incubate for 10 minutes at 37°C and inactivate with 75°C for 5 min.	

3.1.1.6 Run big gel to cut out fragments (Insert and vector)

The total volume was added to a combined pocket of 2-3 wells to harvest the correct DNA fragments, and then, the gel was run very slowly. The gel was imaged, the desired fragments were excised, and a second image was taken to confirm that the correct pieces were removed.

3.1.1.7 Purify gel with QIAquick® Gel Extraction Kit (50)

Gel pieces were purified using the QIAquick® Gel Extraction Kit (50), and nucleic acid concentration and quality were measured using a Thermo Scientific NANODROP 2000C spectrometer.

3.1.1.8 Ligation of insert and vector

50 ng (30-100 ng) of the vector were taken and ligated at a 1:1, 1:5, and 1:0 ratio, respectively, as a negative control. The NEB ligation calculator (https://nebiocalculator.neb.com/#!/ligation) was used to determine the amount of insert.

Table 8: Reaction mix for ligation

Insert	x
Vector	50 ng
PEG	2 µL
10x Buffer	2 µL
T4 Ligase	1 µL
Add ddH_2O to a total volume of 20 µL	

Samples were incubated for 1 h at 22°C, and then 5 µL were collected for heat shock transformation into Mach1 cells for each of the 1:1, 1:5, and 1:0 samples.

3.1.1.9 Heat shock transformation

Bacterial Mach1 cells were thawed on ice, and 50-100 ng of DNA was added to the cells. The samples were then incubated on ice for 30 min. The cells were heat-shocked at 42°C for 45 s. The cells were then returned to ice and incubated for 2 min. Then 250 µL of pre-warmed SOC medium was added, and the cells were incubated at 37°C for 1 h at 200 rpm. Samples of 50 µL and 20 µL were taken and plated on pre-warmed plates with appropriate antibiotics. Cells were incubated overnight at 37°C to grow into colonies, which were then harvested the next day.

3.1.2.1 Pic 10 single colonies

The 1:0 negative sample should ideally be empty. Ten potential positive clones were selected and cultured overnight in 5 mL LB with appropriate antibiotics. The next day, plasmid preparation was performed using QIAprep® Spin Miniprep Kit (250), and nucleic acid concentration and quality were measured using a Thermo Scientific NANODROP 2000C spectrometer. This was followed by testing the digestion with appropriate restriction enzymes and verified on a 1% agarose gel. A positive clone was selected for sequencing.

3.1.2.2 Sending in plasmids for sequence verification to Eurofins

The Eurofins Genomics Over Night Mix2Seq Kit was used to sequence the newly created plasmids. The desired sequence (1 primer for approximately 700 bp) was selected for the primers. For each reaction with 1 primer, 50-100 ng/µL DNA was taken and made up to a total volume of 15 µL DNA (e.g., 2 µL DNA and 13 µL ddH_20). 2 µL primer was added at a concentration of 10 pmol/µL (1:10 from 100 pmol/µL stock). Tubes were sent to the Eurofins facility for sequencing.

3.2.1 Cloning protocol: 2 overhang cloning

3.2.2.1 Digest vector with corresponding restrictions enzymes

Restriction enzymes were used to cut plasmids with specific overhangs at a specific site for subsequent ligation.

Table 9: Reaction mix for enzyme digestion

(e.g., HindIII and NotI in R-Buffer) run for 2 h at 37°C	
DNA	10 µg (5-10 µg)
Enzyme 1	2.5 µL HindIII
Enzyme 2	2.5 µL NotI
Buffer	8 µL R-Buffer
Add up to 80 µL with ddH_2O	

3.2.2.2 PCR of insert with overhang-primer

The desired insert DNA was amplified by PCR using insert-specific forward and reverse primers with specific overhangs (15 bps) that matched the vector. The reaction mix for the PCR was prepared as described in **Table 10**, and the PCR program was described in **Table 11**.

Table 10: PCR reaction mix

PrimerStar Max Premium (2x) includes Buffer and enzyme (1x conc.)	25 µL
10 pmol FW-Primer	1 µL
10 pmol RV-Primer	1 µL
DNA template	< 200 ng
Add ddH_2O up to a total reaction volume of 50 µL	

Table 11: PCR-Program

98°C	10 s
55°C	5 s 30-35 cycles
72°C	5 s/kb
16°C hold ∞	

3.2.2.3 Digest vector with restrictions enzymes

Restriction enzymes were used to cut plasmids with specific overhangs at a specific site for subsequent ligation.

3.2.2.4 Test-gel

To check the size of the PCR fragments and the digestion of the vector, 1-2 µL were taken, applied to a 1% agarose gel, and imaged.

3.2.2.5 PCR purification with: QIAquick® Nucleotide Removal Kit (50)

PCR samples were purified using the QIAquick® Nucleotide Removal Kit (50) as directed, and nucleic acid concentration and quality were measured using a Thermo Scientific NANODROP 2000C spectrometer. Samples can be stored at -20°C.

3.2.2.6 Inactivate digestion vector

Look up the correct inactivation temperature and time for each enzyme. For example, HindIII and BamHI are inactivated at 80°C for 20 min.

3.2.2.7 Dephosphorylation of vector plasmid with FASTAP

The vectors were dephosphorylated to avoid self-alignment, as described in **Table 12**.

Table 12: Reaction mix of dephosphorylation

(Keep insert on ice)	
Vector	80 µL (10 µg DNA)
10x FASTAP-Buffer	10 µL
FASTAP (1U)	10 µL
Incubate for 10 min at 37°C and then inactivate by heating at 75°C for 5 min.	

3.2.2.8 Run big gel to cut out vector backbone

To harvest the vector backbone, the total volume was added in a combined pocket of 2-3 wells, and then the gel was run very slowly. The gel was imaged, and the desired fragments were excised from it, and a second image was taken.

3.2.2.9 Purify gel with QIAquick® Gel Extraction Kit (50)

Gel pieces were purified using the QIAquick® Gel Extraction Kit (50) as directed, and nucleic acid concentration and quality were measured using a Thermo Scientific NANODROP 2000C spectrometer.

3.2.3 Homologous recombination

50 ng of the linearized vectors were taken in 1 µL, and the amount of insert DNA was calculated using the NEB ligase calculator (https://nebiocalculator.neb.com/#!/ligation) for 1:2. The mixture was made up to 5 µL with ddH_2O. Finally, 5 µL of 2x GeneArt® Enzyme Mix was added. A negative control 1:0 was added in parallel. The Enzyme Mix has to be handled carefully, with no unnecessary thawing and mixing. Therefore, it has to be returned immediately to -80°C in the freezer. Samples were incubated for 15-30 min at RT and then placed on ice for 4-5 min. Then, 3 µL were collected for transformation into DH10B cells.

3.2.3.1 DH10B transformation

DH10B cells were thawed on ice, and 3 µL of recombinase mixture was added. The cells were then incubated on ice for 30 min. The mixture was transferred to 37°C for 10 min and then placed on ice for 2 min. 250 µL of pre-warmed SOC medium was added, and samples were incubated at 37°C for 1 h at 200 rpm. 100 µL and 200 µL were added to each pre-warmed plate with the appropriate antibiotic. Plates were incubated overnight at 37°C to allow single colonies to grow, which were then picked the following day.

3.2.3.2 Pic 10 single colonies

The 1:0 negative sample should ideally be empty. Ten potential positive clones were selected and cultured overnight in 5 mL LB with appropriate antibiotics. The next day, plasmid preparation was performed using QIAprep® Spin Miniprep Kit (250), and nucleic acid concentration and quality were measured using a Thermo Scientific NANODROP 2000C spectrometer. This was followed by test digestion with appropriate restriction enzymes and checking on a 1% agarose gel. A positive clone was selected for sequencing.

3.2.3.3 Sending in plasmids for sequencing to Eurofins

The Eurofins Genomics Over Night Mix2Seq Kit was used to sequence the newly created plasmids. Primers were selected for the desired sequence, with one primer designed to approximately 700 bp.

50-100 ng/µL DNA were taken for each reaction with 1 primer and filled up to a total volume of 15 µL DNA (e.g., 2 µL DNA and 13 µL ddH_20). 2 µL primer was added at a concentration of 10 pmol/µL (1:10 from 100 pmol/µL stock). Tubes were sent to the Eurofins facility for sequencing.

Table 13: Primer list

1	EGFP_FW2	CCACTACCAGCAGAACAC
2	EGFP_RV1	TCCATGCCGAGAGTGATCC
3	CAG_FW	TTCGGCTTCTGGCGTGTGAC
4	CMVfor	CGCAAATGGGCGGTAGGCGTG
5	pcDNA3_rev	GGCAACTAGAAGGCACAGTC
6	pEGFPN1rev	GTCCAGCTCGACCAGGAT
7	pEGFPC1rev	CATTTTATGTTTCAGGTTCAGGG
8	CAG_REV	CGGGCCATTTACCGTCATTG
9	IRES_FW	ATAAGGCCGGTGTGCGTTTG
10	IRES_RV	CGCTTGAGGAGAGCCATTTG
11	pEGFPC1for	GATCACTCTCGGCATGGAC
12	pEGFPN1for	GTCGTAACAACTCCGCCC
13	bPAC_Forward_OH	AATTGCTCGAGCTCAAGCTTGCCACCATGATGAAGCGGCTGGTG
14	bPAC_Reverse_OH	GCTCACCATGGTGGCGGCCGCGGCGTACGTCCGCGGCTTGTCG
15	TpPAC_Forward_OH	AATTGCTCGAGCTCAAGCTTGCCACCATGAAACGCCTGACTTACATTAG
16	TpPAC_Reverse_OH	GCTCACCATGGTGGCGGCCGCGGCTTGCTGCACTGGATGCTGTC
17	mCaRhAC_FW	TCGACAGCCTCGTCGAATGC
18	mCaRhAC_RV	ACCTCTGGTGCTCCAGTAAC
19	bPAC_FW1	AGGTGGTCATCCTGGTCAAC
20	bPAC_RV1	TCGCCGATGAACTTGGTCAC
21	TpPAC_FW1	CCGACATCTTCAGCAGTACC
22	TpPAC_RV1	ACTGAGCGGTTGGCAATATC

3.2.3.4 Cloning TpPACs into AAV6 vector plasmid 1292

First, the AAV TpPAC-PLN plasmid was cloned by cutting the vector AAV JellyOP EYFP and the insert TpPAC-PLN plasmids with XbaI and PmeI in B buffer (2x XbaI), followed by ligation of the fragments. The resulting plasmid AAV TpPAC-hPLN was used as a vector to clone TpPAC-cyt, -nb.F3 and -FKBP12.6 into the viral vector by cutting the vector AAV TpPAC-hPLN and the insert plasmids TpPAC-cyt, -nb.F3 and -FKBP12.6 with XhoI and PmeI in Tango buffer and then ligating the vector with each insert fragment.

3.3 Cell culture

3.3 General handling of cell culture

Cells were cultured under sterile conditions in HERA cell 240 chambers at 37°C, 100% humidity, and 5% CO_2. This work used two to five cell lines to characterize cAMP modulation by PAC and LOV-PKI constructs. HEK293 cells were cultured in Dulbecco's Modified Eagle's Medium (DMEM) supplemented with 10% fetal calf serum (FCS) and 1% penicillin-streptomycin (Pen-Strep) on gelatin-coated plates, flasks, or dishes. HL-1 cells were cultured in Claycomb's medium supplemented with 10% fetal calf serum (FCS) and 1% Pen-Strep on gelatin- or fibronectin-coated plates, flasks, or dishes. Cultivation of D3, EBs, and nCMs was performed in Iscove's modified Dulbecco's medium (IMEM) supplemented with 20% fetal calf serum (FCS) and 1% Pen-Strep on fibronectin-coated plates/flasks/dishes. ACMs were cultivated in minimum essential medium (MEM) supplemented with 2% fetal calf serum (FCS) and 1% Pen-Strep on laminin-coated plates, flasks, or dishes. Cells were passaged when grown to 90% confluence.

3.3.1 HEK 293 Ad with pGloSensor ™ 22 F Plasmid

The GloSensor DNA (40 µg) was linearized with the PstI restriction enzyme, and the DNA concentration was determined using a Thermo Scientific NanoDrop 2000C spectrometer (105.0 ng/µL). HEK 293 cells were cultured in 15% DEMEM and then transfected by lipofection using FuGENE® HD Transfection Reagent. Briefly, 1 million cells were plated onto a 35 mm cell culture dish and grown for 1 day. The next day, 2 µg of linearized GloSensor plasmid and 7.5 µL FuGene HD Transfection Reagent in 75 µL serum-free DMEM were added dropwise to the cells and incubated for 10 min at room temperature (RT). The medium was then replaced with 15% DMEM. The next day, the medium was replaced with a fresh 15% DEMEM medium. On day 3, the selection antibiotic hygromycin (150 µg/mL) was added. The medium was changed daily until colonies were detectable. To detach the cells, trypsin was added and incubated for 1-2 min at 37°C. To stop the enzymatic reaction, 15% DMEM medium was added (1:1), and the cell suspension was transferred to a Falcon. Samples were centrifuged at 200-300 x g for 5 min to remove trypsin. The pellet was resuspended in 1 mL of 15% DMEM, and the cells were passaged 1:10 for further cultivation.

Single-cell colonies were selected by transferring diluted cells (0.5 cells per 100 µL) to 24-well plates (100 µL per well) and cultured in 15% DMEM with 150 µg/mL hygromycin. The medium was changed daily until colonies were observed. 10 Colonies were picked and grown in T25 flasks. Their function was tested according to the Promega assay protocol by measuring the luminescence signal after

stimulation with forskolin (10 µM) and isoprenaline (1 µM). Cells were passaged for further experiments. Excess cells were frozen in 1 mL of freezing solution containing 0.5 mL: 80% FCS, 20% DMSO, and 0.5 mL cell solution containing approximately two million cells were transferred to a cryovial and then placed in a Nalgene freezing tube containing RT isopropanol and immediately placed in a -80°C freezer, which allowed the cells to freeze at a rate of -1°C/min. 6 to 12 h later, the cryovials were transferred to the -150°C freezer and stored.

Table 14: 15% DMEM medium for HEK 293 cells

15% DMEM for HEK 293 cells	
FCS (for ES-cells)	15%
NonEssentialAminoAcids (NEAA)	1%
Penicillin/Streptomycin (Pen-Strep)	1%
ß-Mercapto Ethanol (ß-ME)	0,2%
DMEM	82,8%
Stable for at least 2 weeks at 4°C	

3.3.1.1 Transfecting HEK 293 cells containing GloSensor from Promega with 12 constructs

Cells were transfected by nucleofection using the LONZA 4D NucleofectorTM System™ in 16-well strips with SF medium. For this purpose, HEK 293 cells were passaged as usual with GloSensor (already available in the laboratory) at approximately 90% confluence. 200,000-350,000 cells were resuspended in 20 µL SF medium per well, and the linearized DNA of interest was added. DNA was linearized: PACs were linearized with the PvuI restriction enzyme in R buffer, and LOV-PKIs were linearized with BstBI in Tango buffer, both at 37°C for 2 h. The reaction was stopped by inactivating the enzymes at 85°C for 20 min. Lonza's recommended amount of DNA was 0.4 µg per 20 µL cell suspension. Using 1-2 µg of DNA per 20 µL of cell suspension was more efficient for our constructs. Avoiding bubbles when transferring cells and DNA into the 16-well strips was important to avoid electrical pulse problems. After testing various pulse programs, the CM-130 program was used for further experiments. After the pulse, 70 µL of pre-warmed HEK medium was added to the wells. The cells were then plated in a precoated 24-well plate with prewarmed medium. 24 h after transfection, the cells were selected with the appropriate antibiotic neomycin, using the marker EYFP, which is expressed in the PAC and LOV-PKI constructs.

3.3.1.2 Measurement of cAMP kinetics in multi-plate reader

HEK293 cells containing the GloSensor and the different PACs were plated at 20,000 - 40,000 cells per well in 96-well plates (Greiner Bio-One 655094) coated with 10 µg/mL fibronectin (Sigma-Aldrich). After 20-24 h, 200 µL of equilibration medium containing 88% CO_2-independent medium, 10% fetal bovine serum, 2% GloSensor™ cAMP reagent stock solution (Promega) was added to each well. 2 h later, luminescence measurements (1 s integration, 90 s cycle time) were performed at room temperature in an Infinite® 200 plate reader (Tecan) modified with a light guide in the injector port for application of LED light (465 nm, LEDMOD, Omicron Laserage, Germany). After baseline measurements, cells were illuminated with increasing light durations (50 ms - 1 s). Finally, forskolin (10 µM, Sigma Aldrich) was applied as a control, and the increase in luminescence was monitored. As a control, experiments were also performed on HEK 293 cells containing only the GloSensor and on HEK 293 WT cells.

3.3.1.3 Transfecting and maintaining HL-1 cells

HL-1 cells that were frozen and stored at -150°C were thawed as follows and cultured for subsequent experiments. First, T25 flasks were coated with gelatin/fibronectin (0.02% gelatin/0.01 mg/mL) for at least 1 h at 37°C. The cells were maintained in a special medium, Claycomb's medium (**Table 17**), which is light-sensitive and wrapped in aluminum foil. The gelatin/fibronectin was then removed from the flasks, replaced with 4 mL of supplemented Claycomb's medium, and returned to the incubator. A 15 mL tube was filled with 5 mL of prewarmed medium. The HL-1 cells were quickly thawed in a 37°C water bath (approximately 2 min) and then transferred to a 15 mL tube containing a pre-warmed medium. The tube was centrifuged for 5 min at 500 × g or 1000 rpm to remove the freezing medium in which the cells were frozen. The medium was then removed, and the remaining cell pellet was gently resuspended in 1 mL of supplemented Claycomb's medium and then transferred to the T25 flask prepared with 4 mL of medium. After the cells were thawed, the medium was replaced with fresh, supplemented Claycomb's medium 4 h later, when the cells had adhered to the flask.

Table 15: Claycomb medium for HL-1cells

Claycomb Medium 100mL		
Ingredients	ml	Final Concentration
Claycomb Medium	87	
Fetal Bovine Serum	10	10%
Penicillin-Streptomycin (10^4 U/ml P and 10^4 µg/ml S)	1	100 U/mL:100 µg/mL
Norepinephrine (10 mM stock)	1	0.1 mM
L-Glutamine (200 mM stock)	1	2 mM
The medium is recommended not to be older than 2 weeks		

HL-1 cells were passaged 1:3 after reaching a confluence density of 90%. The medium was changed daily. Before passage, the cells were washed twice with 5 mL of phosphate-buffered saline (PBS) that had been warmed to 37°C by pipetting PBS onto the side of the flask, taking care not to hit the cells directly. Then 1 mL of pre-warmed 0.05% trypsin/EDTA was added per dish and incubated for 2 min at room temperature. The trypsin was removed, and 1 mL of fresh 0.05% trypsin/EDTA solution was added, followed by incubation at 37°C for 2-5 min. Cells were examined under the microscope, and if they were still adherent, the flasks were gently tapped on the benchtop to dislodge any remaining cells. Inactivation of the trypsin enzyme was achieved by the addition of an equal volume (1 mL per dish) of soybean trypsin inhibitor (**Table 16**). 1 mL of supplemented Claycomb's medium was added to resuspend the cells, and they were plated 1:3 in new gelatin/fibronectin-coated flasks. The cells not used for further cultivation were frozen 1:1 in a freezing medium containing 95% FCS and 5% DMSO. The resuspended cells were then pipetted into a cryovial and placed in a Nalgene freezing tube containing room-temperature isopropanol. The tube was immediately transferred to the -80°C freezer, allowing the cells to freeze at a rate of approximately -1°C/min. 6 to 12 h later, the cryovials were transferred to the -150°C freezer for storage.

Table 16: Soybean trypsin inhibitor

Soybean trypsin inhibitor	
Soybean trypsin inhibitor	25 mg
Dulbecco's phosphate-buffered saline (PBS)	100 mL
Filter-sterilize, using a 0.2 µm syringe filter (can be stored for 4 months at 4°C)	

Table 17: Norepinephrine (10 mM stock)

Norepinephrine (10 mM stock)	
Norepinephrine [(±)-arterenol] (MW: 319.3)	10 mM
Ascorbic acid	30 mM
Fill up to 100 mL with ddH_20 and filter-sterilize using a 0.2 µm Acrodisc syringe filter	

Aliquot to 1 mL and store at -20°C (10 mM stock norepinephrine); use 1 mL of stock per 100 mL of medium for a final concentration of 0.1 mM.

3.3.1.4 Transfecting D3 stem cells with 12 constructs

An early passage of D3 mouse embryonic stem cells, already available in the lab, was thawed and cultured on feeder-precultured flasks. After 2 passages, the D3 cells were plated on 10 cm petri dishes for 30 min to remove the feeder cells. The D3 cell suspension was then used for transfection by nucleofection using the LONZA 4D Nucleofector™ system. The desired DNA was then linearized: PACs were linearized with the restriction enzyme PvuI in R buffer, and PKI was linearized with BstBI in Tango buffer, both at 37°C for 2 h. Complete linearization was checked on 1% agarose gel. The reaction was stopped by incubation at 85°C for 20 min. For transfection, 10 µg of DNA was taken and added to 350,000 D3 cells resuspended in LONZA P3 buffer. The 4D-Nucleofector™ system from LONZA was used to transfect the cells with the specific CM-150 program. After nucleofection, the cells were transferred to 2x 10 cm petri dishes with feeder cells and grown in a 15% FCS medium with LIF. After 24-72 h, the selection antibody neomycin was added. The successfully transfected colonies expressing the marker EYFP were grown and subsequently picked. The colonies were then plated onto 24-well plates containing feeder cells for proliferation. Cells were further proliferated, and cryovials were made to freeze excess cells. Clones were differentiated using the hanging drop method and tested for contractility.

3.3.1.5 D3 differentiation via Hanging Drop method

To generate embryonic bodies (EBs) from mouse D3 embryonic stem cells, 400 cells were added per drop in 20% IMDM medium (200,000 cells per 10 mL for 5-6 10 cm dish lids). The cell suspension was formed into drops using a multi-pipette with a combi tip (1 = 10 µL) on the lid of a 10 cm dish filled with 5 mL PBS to provide a moist environment for the drops. Approximately 60 drops were formed per lid. The lid was then gently inverted, placed on the 10 cm dish, and transferred to the cell incubator. EBs were grown on the lids for 2 days before being collected and transferred (1:1) to a 10 cm dish containing 10 mL of 20% IMDM medium. The EBs were grown in suspension for 3-5 days on a horizontal shaker (80 to 85 rpm). The EBs were then plated individually in 24-well plates and scored for viability.

Table 18: 20% IMDM for D3 and EBs cells

20% IMDM for D3 and EBs	
FCS (for ES-cells)	20%
NonEssentialAminoAcids (NEAA)	1%
Penicillin/Streptomycin (Pen-Strep)	1%
ß-Mercapto Ethanol (ß-ME)	0,2%
IMDM	77,8%
Stable for at least 2 weeks at 4°C	

3.3.1.6 EB-dissociation

To dissociate EBs, approximately 20 beating EBs were transferred to a 1.5 mL Eppendorf tube and centrifuged at 1200 rpm for 5 min at 4°C to remove the supernatant. The EBs were then washed with 500 mL PBS without Ca^{2+} and Mg^{2+} and centrifuged again at 1200 rpm for 5 min at 4°C to remove the supernatant. To dissociate the cells from the EBs, they were resuspended in 800 µL collagenase B (1 mg/mL) and incubated at 37°C in an Eppendorf thermomixer with constant shaking (800-1200 rpm) for 30 min. The cells were resuspended twice and incubated for 30 min until the EBS were completely dissociated. The cell suspension was then centrifuged to remove the collagenase, resuspended in 1 mL of 20% IMDM medium, and plated on fibronectin-coated plates as desired.

3.3.1.7 Preparation, transfection, and maintenance of neonatal cardiomyocytes (nCMs)

The Neonatal Heart Dissociation Kit mouse and rat from Miltenyi for postnatal mouse day P0-3 was used to prepare neonatal hearts. Neonatal mice were killed by decapitation, and the hearts were removed and transferred to 10 cm dishes filled with PBS on ice. Enzyme Mix 1 (Enzyme P: 62.5 µL + Buffer X: 2300 µL preheated at 37°C) and Enzyme Mix 2 (Buffer Y: 25 µL + Enzyme A: 12.5 µL + Enzyme D: 100 µL) were mixed, and 600 µL were transferred into 1 mL Eppendorf tubes. The hearts were then divided into 4 hearts/600 µL enzyme mixes 1 and 2 for the enzymatic degradation of the extracellular matrix. The hearts were cut into small pieces with scissors, shaken at 37°C for 15 min at 700 rpm, and pipetted up and down. The shaking and pipetting steps were repeated a total of 3 times. To stop the enzyme reaction of the enzyme mixture, 600 µL of medium was added to the samples. The samples were then filtered through a MACS SmartStrainer (70 µm) pre-separation filter, and the supernatant was collected. The filter was washed with the collected medium, and the samples were centrifuged at 300 x g for 5 min. The pellet was resuspended in 300 µL PBS. Then 3 mL of red blood 1x cell lysis buffer (1:10 in Ampuwa ddH_2O) was added and incubated for 2 min at RT. The samples were then centrifuged at 300 × g for 5 min. The pellet was resuspended in 90 µL PEB, and 10 µL nCMs iso-mix was added. Cells were then magnetically filtered through the Miltenyi MS column (8 hearts/column), placed on a magnetic rack, and equilibrated with 500 µL PBS. The samples were then filtered, and the supernatant was collected. The filtration is based on negative depletion, meaning all other cells become trapped in the filter, while only the small cardiomyocytes pass through. The column was washed three times with 500 µL PBS, and the supernatant was centrifuged at 300 × g for 5 min. The cells were resuspended in 20% IMDM medium and counted before being plated.

Table 19: 20% IMDM for nCM cells

20% IMDM for nCMs	
FCS (for ES-cells)	20%
NonEssentialAminoAcids (NEAA)	1%
Penicillin/Streptomycin (Pen-Strep)	1%
ß-Mercapto Ethanol (ß-ME)	0,2%
IMDM	77,8%
Stable for at least 2 weeks at 4°C	

3.3.1.8 Preparation and maintenance of adult CM cells

Table 20: Ca^{2+}-free Tyrode solution

Ca^{2+}-free Tyrode solution	
NaCl	135 mM
KCl	4 mM
$MgCl_2$	1 mM
HEPES	2.5 mM
Glucose	5 mM
pH 7,4 with NaOH	

Table 21: Lysis solution

Lysis solution	
Collagenase B	25-35 (31) mg
Trypsin	1-4 (1,5) mg
Blebistatin	1:500 from a 10 mM stock solution
$CaCl_2$	50 µM
diluted in 30 mL Ca^{2+}-free Tyrode	

Table 22: Stop solution

Stop solution	
FCS	2.5 ml
Blebbistatin	1:500 from a 10 mM stock solution
$CaCl_2$	50 µM
diluted in 47.5 ml Ca^{2+}-free Tyrode	

Two 10 cm dishes were prepared with cold PBS, and one 6 mm dish with cold Ca^{2+}-free Tyrode solution had a cannula attached to the side to fix the heart with a silk thread, which would later be used to tie a knot around the aorta. The cannula was evacuated using a 1 mL syringe. Approximately 20 mL of Ca^{2+}- Free Tyrode solution with blebbistatin was then gassed with oxygen. To prevent cardiomyocytes from contracting and dying, blebbistatin was used by preparing a 10 mM stock solution and diluting it 1:500. Mice were killed by cervical dislocation and then pinned to a polystyrene plate and disinfected with alcohol. First, the fur was cut open, and the muscle layer was removed. Then, the thorax was opened on both the left and right sides, and the diaphragm was removed. The thorax was then folded up and pinned down. The heart was then carefully separated from the major vessels and the lungs

using forceps and placed in PBS. Under a dissecting loupe, the lung tissue, thymus, possibly the trachea, and fatty tissue were carefully removed. The heart was then transferred to a 60 mm dish with the cannula, where the aorta was pulled onto the cannula and secured with a suture. The heart was then perfused with the fumigated Ca^{2+}-free Tyrode's solution containing blebbistatin at a rate of 4.15 ml/min (pump) for approximately 3-5 min. During this time, the lysis solution was prepared (**Table 21**). The heart was then perfused with the lysis solution for 10-15 min until it became transparent and enlarged. It was then transferred to a dish with lysis solution, cut into small pieces, and filtered through a 100 µm cell filter. Five milliliters of stop solution containing FCS was added to stop the lysis enzymes. The mixture was centrifuged for 1 min at 700 rpm (approximately 80 x g). The supernatant was discarded, and the pellet was resuspended in a 10 mL stop solution. This step was repeated, and the cells were resuspended in 20 mL stop solution and transferred to two 10 cm dishes. Subsequently, Ca^{2+} tolerance was assessed by increasing the Ca^{2+} concentration with a 2 M $CaCl_2$ solution stepwise from 450 µM, 900 µM, and 1.35 mM to 1.8 mM, with a 10 min incubation time in between. Cell quality was then observed under a microscope.

3.3.1.9 Nucleofection of neonatal cardiomyocytes

After the nCMs were prepared, they were used for transfection. Lonza's 4D-Nucleofector™ system delivered the desired plasmids into nCMs by nucleofection. Specifically, the P3 Primary Cell 4D-Nucleofector® X Kit L with the X-unit (cuvettes) and the CM-150 or CM-120 program for cell suspension were used for nCM. The freshly prepared nCMs were resuspended in P3 buffer (1 million cells/100 µL P3 buffer). The resuspended cells were then transferred to the nucleofection cuvettes (100 µL per cuvette), and 10 µg DNA was added before the cuvettes were placed in the nucleofector and the program-specific electrical pulse was applied. Next, 100 µL of pre-warmed medium was added to the cuvettes, and cells were plated on fibronectin-coated wells with pre-warmed 20% IMDM medium.

Another nucleofection method was also tested for the Lonza 4D-Nucleofector™ System, the AD1 4D-Nucleofector™ Y Kit, using the Y-unit for adherent cell transfection. For this, freshly prepared nCMs were plated in specific 24-well plates (fibronectin-coated) at 20,000 cells/well, as provided in the kit, and transfected the next day. The 20% IMDM medium was removed for nucleofection, 350 µL of AD1 buffer was added, and 10 µg of plasmid DNA per well. The nucleofection lid of the 24-well plate was then placed on top. The plate was placed in the nucleofector, and the CD-142 program was applied. The nucleofection cap was carefully removed from the plate, and the AD1 buffer was replaced with 1 mL of 20% IMDM.

3.3.2 Cell fixation and staining

Cells grown on either glass or ibidi µ-well plates were washed 3 times with PBS to remove dead cells and serum before being fixed with 4% PFA for 30 min. During the procedure, the PFA waste was sorted into special waste containers. After 30 min of fixation, the cells were washed 3 times with PBS to remove PFA. To make the cells accessible to the antibodies, the cells were permeabilized with 0.2% Triton X-100 in PBS for 30 min and then washed three times with PBS. To block the cells from unspecific antibody binding, the cells were incubated in donkey serum (5% in PBS) for 1 h. Subsequently, the desired 1. antibodies were applied at specific concentrations in PBS containing 0.05% donkey serum and incubated overnight at 4°C. The next day, the cells were washed 3 times for 10 min with PBS to remove excess and unbind the first antibody. The corresponding secondary antibodies were prepared at specific concentrations in Hoechst solution (1:1000 in PBS) containing DAPI staining, and the cells were incubated for 2 h in the dark. The cells were washed 3 times with PBS for 10 min. Glass plates were then glued onto coverslips with Aqua-PolyMount and dried. Ibidi µ-wells were treated with an ibidi mounting medium to fix the cells in the wells.

3.4 Protein analysis

3.4.1 Protein extraction from cells

All protein extraction procedures were performed on ice.

Table 23: RIPA buffer

RIPA buffer for 500 mL			
EDTA	2 mM	0,3 g	Sigma Aldrich, #E4884
Trizma base	25 mM	1,5 g	Sigma Aldrich, #T1503
NaCl	150 mM	4,4 g	Sigma Aldrich, #S5586
Natriumdeoxycholat	0,1%	0,5 g	Sigma Aldrich, #D6750
SDS	0,1%	0,5 g	Carl Roth, CN30.2
Nonidet P40	1%	5 g	Sigma Aldrich, #I3021
Adjust pH to 7.5 and fill up to 500 ml with ddH_2O			

Protein extraction with RIPA buffer was performed as follows. Cultured cells were washed with ice-cold PBS containing a protease inhibitor before ice-cold RIPA buffer containing a protease inhibitor was applied. Cells were detached from the wells using a cell scraper. The cell lysate was collected in an Eppendorf tube and stored at -80°C if necessary. An ultrasonic rod was used for complete cell lysis, and the cell suspension was centrifuged for 10 min at 13000 rpm and 4°C. The supernatant was collected, and the cell debris pellet was discarded. The isolated proteins can be stored at -80°C.

Table 24: Titin-buffer

Titin-buffer	
Urea	8 M
Thiourea	2 M
SDS	3%
Triton X 100	1.5%
Tris base HCL (pH=6.8)	0.05 M
Serva blue	spoon tip
Glycerol	10%
DTT, Fresh to thawed aliquots	75 mM

Table 25: Phosphatase inhibitor (PI)

Phosphatase inhibitor (PI)		
Ingredients	g/mol	Concentration
Sodium orthovanadate	183.9	1 mM
Sodium fluoride	41.99	1 mM
Sodium pyrophosphate	446.06	10 mM
ß-glycerophosphate	216.04	1 mM

Table 26: PhosStop

PhosStop	
1 pill	Diluted in 1 mL ddH2O
Use it 1:10	

Table 27: cOmplete mini protease inhibitor

cOmplete mini protease inhibitor	
1 pill	Diluted in 1.5 mL ddH2O
Use it 1:100	

Protein extraction with Titin buffer for phosphorylation analysis and membrane protein extraction was performed as follows. Samples were washed with PBS, and DEMEM F12 was added. The cells were then incubated for 4 h to allow for medium exchange. Titin lysis buffer was prepared by adding PhosStop (1:10), phosphatase inhibitor (1:15), and complete (1:100). Cells were then treated with light, iso, or FSK, and the medium was carefully exchanged with the titin buffer solution containing PhosStop, phosphatase inhibitor, and complete. Cells were detached from the wells using a cell scraper. The cell lysate was collected in an Eppendorf tube and stored at -80°C.

3.4.1.1 Protein extraction from EBs

The beating area of EBs (20-25 pieces, up to 40) was collected and washed with ice-cooled PBS. Then, the supernatant was removed, and 300 µL ice-cooled lysis buffer was added to the EB pieces. The samples were mixed by pipetting, and complete lysis was performed using an ultrasonic rod. The cell suspension was centrifuged for 10 min at 13000 rpm and 4°C. The supernatant was collected, and the cell debris pellet was discarded. The isolated proteins can be stored at -80°C.

3.4.1.2 Protein concentration measurement

After the proteins were prepared, the concentration of the samples in RIPA buffer was determined using Pierce™ BCA Protein Assay Kits to ensure a consistent amount of protein for Western blot analysis and to compare the samples.

The assay is based on proteins reducing Cu^{2+} to Cu^{1+} in an alkaline medium. Bicinchoninic acid (BCA) selectively detects this.

A standard curve using bovine serum albumin (BSA) (**Table 28**) was generated as a reference to measure the protein concentration of the sample. The working solution was prepared by mixing reagents A and B 50:1, and 200 µL of the working reagent was mixed with 10 µL of samples and

standard. The standard and samples were added to a 96-well plate and incubated at 37°C for 30 min before being read on a TECAN plate reader at an absorbance of 562 nm.

The protein concentration of the samples with titin buffer was determined on Bio-Rad Stain-Free gels. Therefore, the same number of samples was loaded and run on a Stain-Free gel, followed by imaging.

Table 28: BSA Standards

BSA Standards			
	Buffer [µL]	BSA [µL]	Final BSA conc. [mg/mL]
A	0	300	2
B	125	375	1.5
C	325	325	1
D	175	175 from B	0.75
E	325	325 from C	0.5
F	325	325 from E	0.25
G	325	325 from F	0.125
H	400	100 from G	0.025
I	400	0	0

3.4.1.3 Western Blot with ECL Detection

After determining the protein concentrations, the quality and quantity of proteins were analyzed using Western blot. A total of 10 µg protein was used in a volume of 15 µL from each sample and was loaded and run on the gel. The samples were loaded with 4x Laemmli sample buffer containing BME in RIPA buffer. All samples were heated at 95°C for 5 min to denature proteins. 4 µL of protein standard marker was loaded onto the gel. Western blot was performed using the Mini-PROTEAN Tetra Cell System for protein separation and the Trans-Blot Turbo Transfer System for transfer. Gels with 7%, 10%, and 4-20% were used for different experiments with different protein sizes of interest and run in the run buffer. Gels were first run at 60V until the proteins passed through the capture gel and into the separating gel. Gels were then run at 120V until the loading cloud reached the black line at the bottom. The gels were removed from the chamber using a spatula, and a significant amount of liquid was applied to gently dislodge the gel from the chambers to prevent breaking. Stain-free gels were imaged to determine the total protein concentration in samples lysed in Titin buffer, and the protein concentration was then determined. A second gel was prepared with the desired protein concentrations, following the same procedure described above.

The Trans-Blot Turbo Transfer System, which included a pre-cast membrane and filters from the Trans-Blot Turbo Transfer Pack (with Mini and PVDF membranes), was used to transfer the proteins from the gel. Therefore, the bottom membrane was placed in the transfer chamber, the gel was placed on top,

and then the top membrane was placed on top of the gel. The stack was wetted, and air bubbles were removed with a roller. The programs for Turbo TGX gels, 7 min or standard 30 min, were used for the transfer. The stained membranes were scanned to verify the successful transfer. To avoid nonspecific antibody binding, the membranes were blocked in TBST with 5% milk powder for 1 h on a shaker at RT. Primary antibodies were prepared at antibody-specific concentrations (GFP 1:1000) in TBST with 5% milk powder, and the membranes were incubated overnight on a shaker at 4°C. The next day, the membranes were washed 3 times with TBST for 20 min under shaking. The secondary antibody (1:10,000 horseradish peroxidase (HRP)) was prepared in TBST with 5% milk powder, and the membrane was incubated in the secondary antibody solution for 1 h under shaking at RT. The membranes were washed 3 times with TBST for 20 min under shaking. ECL solution mixes 1 and 2 (1:1) were prepared (2 mL per membrane) and applied equally to the membrane for antibody detection. The ECL solution was incubated for 1 min, followed by imaging. Chemiluminescence was used to detect antibodies, and the standard was detected by calorimetric imaging. Gel documentation was performed using Li-COR Odyssey FC.

Table 29: 10x SDS-Running buffer

10x SDS-Running buffer (pH 8,3)			
Trizma base	0,25 M	30,285 g	Sigma Aldrich, #T1503
Glycin	1,92 M	144,1 g	Sigma Aldrich, #G8898
SDS	0.1%	10 g	Carl Roth, CN30.2
Adjust pH and add up to 1 L ddH_2O Use 1x running buffer			

Table 30: 10x TBS

To make TBST, add 0,5% of Tween 20 to TBS.

10x TBS (pH 7,5)			
Trizma base	0,5 M	60,57 g	Sigma Aldrich, #T1503
NaCl	1,5 M	87,66 g	Sigma Aldrich, #S5586
Adjust pH and add up to 1 L ddH_2O Use 1x running buffer			

3.5 Functional read-out experiments

3.5.1 cAMP measurement with GloSensor in TECAN plate reader

HEK 293 cells containing the GloSensor (from Promega) were transfected with the 12 constructs using nucleofection with the CM-130 program in SF medium. Stable lines were selected. 15,000 cells were transferred to each 96-well plate and grown overnight. They were then equilibrated in 100 µL GloSensor equilibration medium (**Table 32**) for 1-2 h until a stable baseline was reached. Cells were then exposed to different light durations: 50 ms, 150 ms, 500 ms, 1000 ms, and 2000 ms at 0.1015 mW/mm^2 and 5 V. Finally, 10 µM forskolin was added as a positive control. The experiment was conducted under RT.

Table 31: GloSensor™ cAMP Reagent stock solution

GloSensor™ cAMP Reagent stock solution	
GloSensor™ cAMP Reagent	25 mg
HEPES buffer	817 µL

Table 32: Equilibration medium

Equilibration-medium	
CO_2 -independent medium	88%
FCS	10%
GloSensor™ cAMP Reagent stock solution	2%

3.5.2 Prepare HL-1 cells for Ca^{2+} imaging with X-Rhod

Previously cultured HL-1 cells were transferred to square coverslips (150,000 cells/well), precoated with gelatin-fibronectin solution, and grown for 2 days.

Ca^{2+} imaging was performed using the Ca^{2+} dye X-Rhod, which was prepared in 1.5 mM X-Rhod aliquots diluted in DMSO and stored at -20°C. The 1.5 mM aliquots were used at 1:1000 in the DEMEM F12 medium. The cells were then incubated for 12-15 min at RT, washed 2-3 times with DMEM F12, and then 500 µL of DMEM F12 was added. The cells were incubated for another 12-15 min at 37°C. The coverslips were then transferred to the perfusion system on the microscope and perfused with DEMEM F12. The 527 nm filter was used at position 5 and LED 5 for X-Rhod imaging. Imaging was performed with 66 ms exposure time, 5% illumination, and one image was taken every 1 s, 2x2 binning.

3.5.3 Frequency measurements

Frequency was measured in embryoid bodies (EBs) and nCMs. Transfected D3 mouse embryonic stem cells were grown into EBs until day 14 and then analyzed. nCMS (P1-P3) were transfected by nucleofection, plated on precoated ibidi µ-24 well plates, and measured 3-5 days later. Cells transfected with the PAC and LOV-PKI constructs were maintained in the dark at all times to minimize background activation.

The effect of localized cAMP generation in microdomains was analyzed by observing changes in spontaneous beating frequency using video microscopy (Cell Frequency Analysis 4.9 software), with information transferred to LabChart. Imaging was performed under infrared light with a 500 nm filter to avoid activation of PACs. Blue light flashes were applied with increasing pulse durations (1.9 ms, 3.9 ms, 7.8 ms, 15.6 ms, 31 ms, 62.5 ms, 125 ms, 250 ms, 500 ms, and 1000 ms at 0.1015 mW/mm^2 and 5 V, 5% Omicron 465 nm) controlled by Ad-instruments, light flashes resulted in instantaneous acceleration of beating frequency in a dose-dependent manner, demonstrating cAMP-dependent chronotropy. The experiments were performed (**Fig. 7**) in a small cell chamber with 5% CO_2, 80% humidity, and a temperature of 37°C (Ibidi Stage Top Incubation System).

A) **B)**

Fig. 7: Experimental setup for frequency and Ca^{2+} imaging measurement
A) *Stage-top incubator from ibidi (https://ibidi.com/stage-top-incubators/230-ibidi-stage-top-incubation-system-universal-fit-for-1-chamber-co2.html) with gas conditioner and chamber heater.* ***B)*** *Stage-top incubator on a microscope with plated cells in a 24-well plate. A Nikon Eclipse Ti2 fluorescence microscope with a red-light imaging Fura/Fluo filter (380 nm) and an optogenetic stimulation system using blue light (465 nm) was combined with a 1% ND2.0 filter.*

3.5.4 Ca^{2+} Imaging measurements

Ca^{2+} transients were analyzed in nCMs using Ca^{2+} imaging with the red light Ca^{2+} dye Cal-630 (excitation, 600-620 nm) to record Ca^{2+} transients without PAC activation. Therefore, nCMs transfected with PAC constructs (TpPAC-EYFP-cyt, nb.F3-TpPAC-EYFP, and TpPAC-mCitrine-FKBP12.6) were plated on ibidi 24-µ-plates. Cells transfected with the PAC constructs were kept in the dark to avoid background activation. After 4-6 days, the cells were washed and incubated with the Ca^{2+} dye Cal-630 and Pluronic (to enhance dye uptake into the cells) for 2 h in DMEM-F12 medium. After incubation, the cells were washed 3 times with PBS, and 1 mL of DMEM-F12 was added. An Arduino code (**S.1**) was written to synchronize pacing, trigger imaging, and optogenetic stimulation, and minimize imaging time, thereby reducing bleaching (**Fig. 8**). Cells were paced at 0.5-2 Hz, depending on the individual cell's capacity, during the experiments. Blue light (465 nm) flashes were applied for 1 s at increasing intensities (0.5-23.4 µW/mm²). The experiments were performed (**Fig. 7**) in a small cell chamber with 5% CO_2, 80% humidity, and a temperature of 37°C (Ibidi Stage Top Incubation System).

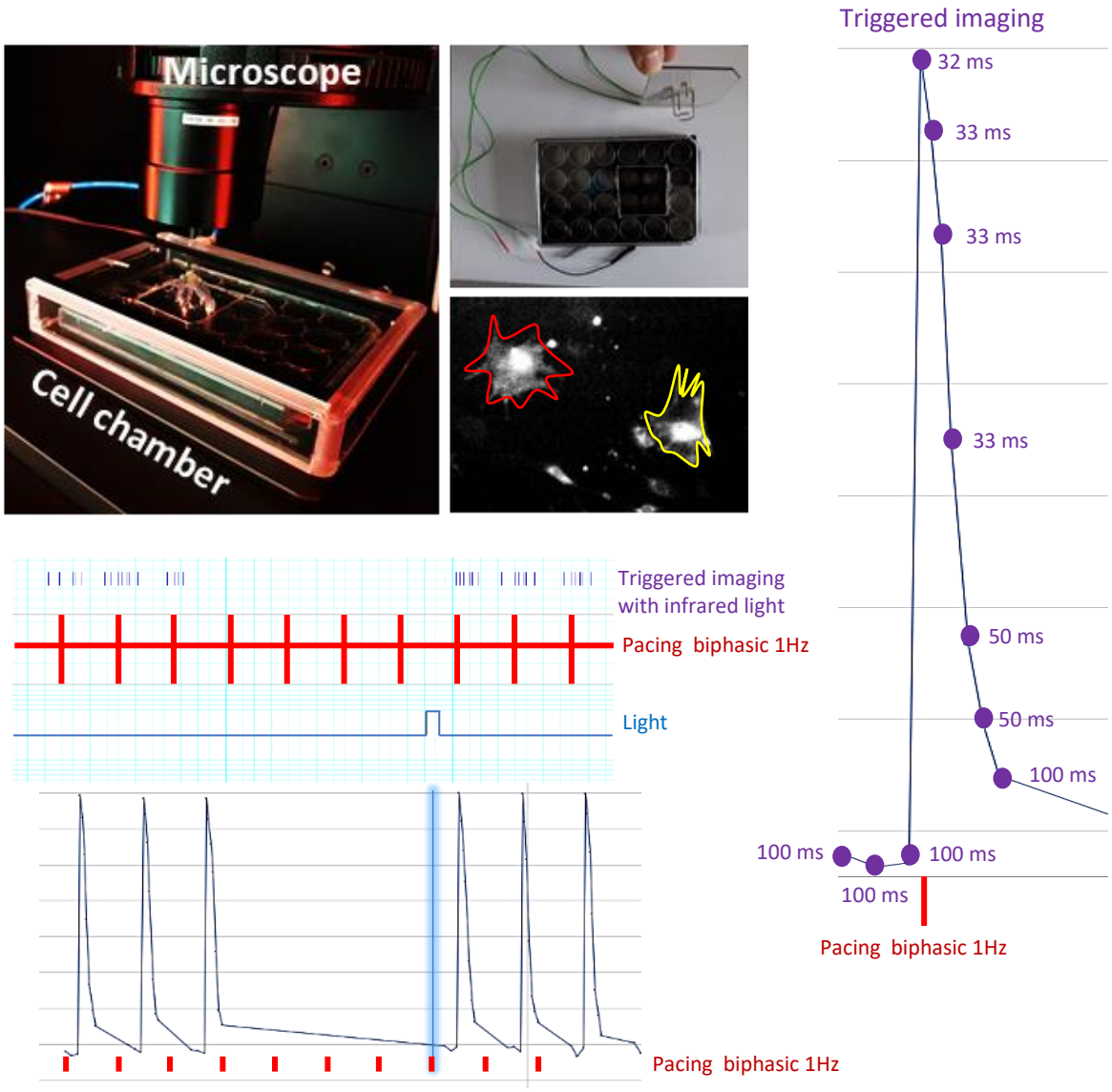

Fig. 8: Experimental setup for Ca^{2+} imaging measurement and triggered imaging system *nCMs were transfected and plated on ibidi 24-µ plates. 4-6 days after transfection, the cells were incubated with a Ca^{2+} dye and placed on the stage top incubator. A homemade 24-well platin pacer was built to pace the cells at a specific frequency. Imaging and optogenetic stimulation were triggered using an Arduino program and box pacing. To image a transient, ten images were taken, with three 100 ms images taken before pacing and three 33 ms images taken after pacing, followed by two 50 ms images and one 100 ms image in between. A Nikon Eclipse Ti2 fluorescence microscope with a red-light imaging Fura/Fluo filter (380 nm) and an optogenetic stimulation system using blue light (465 nm) was combined with a 1% ND2.0 filter.*

3.5.5 Pre-Analyzing phosphorylation

Pre-analyzing phosphorylation of samples for phospho-proteome analysis in Western Blots. The samples were washed with PBS, and DEMEM F12 was added. The cells were then incubated for 4 h to allow for medium exchange. Titin lysis buffer was prepared by adding PhosStop (1:10), phosphatase inhibitor (1:15), and complete (1:100). Cells were then treated with light, iso, or FSK, and the medium was carefully exchanged with the titin buffer solution containing PhosStop, phosphatase inhibitor, and complete. Cells were detached from the wells using a cell scraper. The cell lysate was collected in an Eppendorf tube and stored at -80°C.

Either nCMs were transfected by nucleofection or by the AAV6 virus.

Titin lysis buffer was prepared by adding PhosStop (1:10), phosphatase inhibitor (1:15), and complete (1:100). 1,000,000 nCMs were grown in 6-well plates and transfected with AAV6 one day later. Four days after transfection, they were washed with DMEM-F12 and incubated in DMEM-F12 for 4 h to recover from the medium change. They were then illuminated and immediately lysed in a lysis buffer. Illumination was performed under a macroscope using an illumination protocol of 1 s and 5 V light, repeated every 10 s for 1 min. The light intensity was 65 ms/mW. Omicron 100%, 460 nm filter 2. DEMEM F12 medium was carefully aspirated, and 200 µL titin buffer containing PhosStop, a phosphatase inhibitor, and complete was added. Cells were detached from the wells using a cell scraper. The cell lysate was collected in an Eppendorf tube and stored at -80°C.

Table 33: Lysis buffer used for Western Blot and Spectrometry

Substance	Final concentration	in 50 mL
Triton-X	1%	500 µL
Tris-HCl, pH 7,5	50 mM	0,3 g
NaCl	300 mM	0,89 g
EDTA	5 mM	0,09 g

Protein samples were then assayed by Western blot as described in **1.6.5**. To prepare samples for phospho-proteomic analysis, 4x ice-cooled acetone was added (360 µL sample with 1.44 mL acetone) and vortexed. Samples were then incubated overnight at -20°C. The next day, the samples were centrifuged at 18,000 x g for 30 min at 4°C. The supernatant was discarded, and the pellets were washed with 400 µL ice-cold acetone and centrifuged at 18,000 x g at 4°C for 10 min. Finally, the supernatant was discarded, and the pellet was air-dried for 5 min. The pallets were stored at a temperature of -20°C.

3.5.6 Protein generation in HEK293 cells and purification

Table 34: Lysis buffer

Lysis buffer	Final concentration
Tris/HCL, pH 7.5	10 mM
NaCl	150 mM
EDTA	0.5 mM
Nonidet P40 substrate	0.5%
pH was adjusted at 4°C	

Table 35: Dilution buffer

Dilution buffer	Final concentration
Tris/HCL, pH 7.5	10 mM
NaCl	150 mM
EDTA	0.5 mM
pH was adjusted at 4°C	

Table 36: Wash buffer

Wash buffer	Final concentration
Tris/HCL, pH 7.5	10 mM
NaCl	150 mM
EDTA	0.5 mM
Nonidet P40 substrate	0.05%
pH was adjusted at 4°C	

Table 37: Acidic elution buffer

Acidic elution buffer	Final concentration
Glycine, pH 2.5	200 mM
pH was adjusted at 4°C	

Table 38: Neutralization buffer

Neutralization buffer	Final concentration
Tris, pH 10.4	1 M
pH was adjusted at 4°C	

Proteins were generated in HEK293 cells and purified via immunoprecipitation of GFP-fusion proteins. HEK 293 cells were transfected by nucleofection using SF buffer and the CM-130 program and selected with the antibiotic neomycin. Cells were cultured in large 8 x 10 cm dishes per construct.

All subsequent steps were performed on ice and with pre-cooled solutions to avoid protein degradation. The supernatant can be saved after each step to check fluorescence intensity and, therefore, binding efficiency.

HEK293 cells with the desired construct were grown on 10 cm dish culture plates (8 dishes per construct). When they reached 90% confluence (approximately 106-107 cells), they were washed with ice-cold PBS and collected with 200-300 µL of lysis buffer. The lysate was transferred to an Eppendorf tube and placed on ice for 30 min, where it was vortexed every 10 min. The lysates were then centrifuged at 17,000 x g for 10 min at 4°C. The clarified lysate (supernatant) was transferred to a pre-cooled tube and frozen/stored at -80°C.

Immunoprecipitation of GFP fusion proteins from ChromoTek GFP-Trap® Magnetic Agarose, which is based on a nanobody to bind GFP, was used to capture the TpPAC constructs selectively. Lysates were thawed on ice, and 300 µL of dilution buffer containing 1 mM cOmplete was added.

Beads were gently mixed by pipetting. 25 µL of bead slurry was transferred to a 1.5 mL tube and washed three times with 500 µL to 1 mL of dilution buffer. The solution was removed, and the lysis solution was added to incubate for 1 h at 4°C with rotation.

The magnetic beads were separated with a magnet until the supernatant was clear. The beads were washed by resuspending them in 500 µL of Wash Buffer (3 times). The supernatant was removed. 100 µL of acidic elution buffer was added and pipetted up and down continuously for 30-60 s at 4°C or room temperature.

The beads were separated with a magnet until the supernatant was clear. The elution was transferred to a new tube and immediately neutralized with 10 µL of neutralization buffer. The elution step was repeated at least two times to increase elution efficiency.

3.6 Statistics

All statistical analyses were performed with GraphPad Prism (GraphPad Software, San Diego, CA, USA). The error bars show the average ± S.E.M or SD. P-values of statistical differences between groups are marked with asterisks as follows: *: $p<0.05$; **: $p<0.01$; ***: $p<0.001$; ****: $p<0.0001$.

3.7 Materials

Table 39: Substances

Substance	Order number	Company
10x Tris/Glycine/SDS buffer	1610732	Bio-Rad Laboratories (Feldkirchen, Germany)
2-Mercaptoethanol	31350010	Thermo Fisher Scientific (Waltham, USA)
2-Propanol	A0900	AppliChem (Darmstadt, Germany)
Agarose Low Melt	6351.5	Carl Roth (Karlsruhe, Germany)
Ampuwa®	B315475	Fresenius Kabi Germany (Bad Homburg, Germany)
Aqua Poly/Mount	18606	Polysciences Europe (Hirschberg an der Bergstrasse, Germany)
bis-Benzimid-H-33342-trihydrochloridtrihydrat, 98%	J62134.MC	Thermo Fisher Scientific (Waltham, USA)
Bovine Serum Albumin	A2153	Sigma Aldrich (Taufkirchen, Germany)
Calcium chloride (CaCl2)	C4901	Sigma Aldrich (Taufkirchen, Germany)
Claycomb Medium	51800C	Sigma-Aldrich (Taufkirchen, Germany)
cOmplete™ Protease Inhibitor Cocktail Tabletten	11873580001	Roche Germany Holding (Grenzach-Wyhlen, Germany)
Collagenase B	11088 815 001	Roche Germany Holding (Grenzach-Wyhlen, Germany)
Dimethyl sulfoxide (DMSO)	D8418	Sigma Aldrich (Taufkirchen, Germany)
DL-Dithiothreit (DTT)	DTT-RO	Roche Germany Holding (Grenzach-Wyhlen, Germany)
Donkey Serum	017-000- 121	Jackson ImmunoResearch Laboratories, INC.
Dulbecco`s Modified Eagle Medium (DMEM)	41965-039	Thermo Fisher Scientific (Waltham, USA)
Dulbecco`s Modified Eagle Medium F-12 Nutrient Mixture (DMEM)	11039-021	Thermo Fisher Scientific (Waltham, USA)
Dulbecco`s Phosphate-buffered saline (DPBS) no calcium, no magnesium	14190-094	Life Technologies (Darmstadt, Germany)
Ethanol (EtOH) 70 % (v/v)	27669	Fischer (Saarbrücken, Germany)
Ethanol absolute for molecular biology	A8075	AppliChem (Darmstadt, Germany)
Ethylenediaminetetraacetic acid disodium salt dihydrate (EDTA)	E4884	Sigma Aldrich (Taufkirchen, Germany)
FCS	FBS-11A	Capricorn scientific (Ebsdorfergrund, Germany)
Fibronectin (1 mg/ml)*	F1141	Sigma Aldrich (Taufkirchen, Germany)
Forskolin (Fsk)	F6886	Sigma Aldrich (Taufkirchen, Germany)
FuGENE® HD	E2311	Promega (Mannheim, Germany)
Gelatin from porcine skin	G1890	Sigma Aldrich (Taufkirchen, Germany)

GeneRuler™ DNA-ladder	SM0333	Thermo Fisher Scientific (Waltham, USA)
Glycerol	49767	Sigma Aldrich (Taufkirchen, Germany)
HEPES	H3375	Sigma Aldrich (Taufkirchen, Germany)
HDGreen™		Intas
Hoechst 33342	B2261	Sigma Aldrich (Taufkirchen, Germany)
IBMX	I5879	Sigma Aldrich (Taufkirchen, Germany)
Iscove´s Modified Dulbecco`s Medium (IMEM)	21980-032	Thermo Fisher Scientific (Waltham, USA)
Isopropanol	6752.4	Carl Roth (Karlsruhe, Germany)
Kanamycin sulfate from Streptomyces kanamyceticus	K1377	Sigma Aldrich (Taufkirchen, Germany)
L-Ascorbic Acid, Sodium Salt*	A7506	Sigma Aldrich (Taufkirchen, Germany)
L-Glutamine, 200 mM*	G7513	Sigma Aldrich (Taufkirchen, Germany)
Lipofectamine ™ 3000 Transfection reagent	L3000015	Thermo Fisher Scientific (Waltham, USA)
Mitomycin C	M4297-5X2MG	Sigma Aldrich/Merck
Norepinephrine [(±) -Arterenol]	A0937	Sigma Aldrich (Taufkirchen, Germany)
Non essentielle aminoacids	11140035	Gibco Life Technologies (Darmstadt, Deutschland)
Opti-MEM	31985-070	Thermo Fisher Scientific (Waltham, USA)
Paraformaldehyd ([CH2O]8-100) 4%	0002197124	AppliChem (Darmstadt, Germany)
PhosSTOP™ EASYpack	4906845001	Roche Germany Holding (Grenzach-Wyhlen, Germany)
ROTI Fair BPS 7.4	1112.2	Carl Roth (Karlsruhe, Germany)
Pen-Strep (Penicillin/Streptomycin)	15140-122	Life Technologies (Darmstadt, Germany)
Pierce™ ECL Western Blotting Substrate	32106	Thermo Fisher Scientific (Waltham, USA)
Precision Plus Protein™ Dual Color Standards	161-0374	BioRad Laboratories (Feldkirchen, Germany)
Precision Plus Protein™ All Blue Pre-Stained Protein Standard	1610373	BioRad Laboratories (Feldkirchen, Germany)
Roti®Block (10x)	A151.1	Carl Roth (Karlsruhe, Germany)
Serva Blue R	35051.02	Serva
Skim Milk Powder	70166	Sigma Aldrich (Taufkirchen, Germany)
S.O.C.	15544034	Thermo Fisher Scientific (Waltham, USA)
Sodium Chloride (NaCl)	S5586	Sigma Aldrich (Taufkirchen, Germany)
Sodium dodecyl sulfate (SDS)	L4390	Sigma Aldrich (Taufkirchen, Germany)
Sodium hydroxide (NaOH)	S8045	Sigma Aldrich (Taufkirchen, Germany)
Taq DNA-polymerase (5 E/µL), with 10x PCR buffer, MgCl2 (50 mM)	10342-020	Invitrogen

Thiourea (NH2CSNH2)	T7875	Sigma Aldrich (Taufkirchen, Germany)
Triton X-100	T8787	Sigma Aldrich (Taufkirchen, Germany)
Tritrack 6x DNA loading dye	R1161	Thermo Fisher Scientific (Waltham, USA)
Trizma® Base (TRIS base)	93352	Sigma Aldrich (Taufkirchen, Germany)
Tween 20	P9416	Sigma Aldrich (Taufkirchen, Germany)
0.05% Trypsin-EDTA	25300054	Life Technologies (Darmstadt, Germany)
Trypsin Inhibitor Type I-S, Soybean	T6522	Sigma Aldrich (Taufkirchen, Germany)
Urea (NH2CONH2)	U5128	Sigma Aldrich (Taufkirchen, Germany)

Table 40: Consumables

Consumables	**Company**
15 mL tubes	Greiner bio-one (Frickenhausen, Germany)
50 mL tubes	Greiner bio-one (Frickenhausen, Germany)
4–20% Mini-PROTEAN® TGX Stain-Free™ Protein Gels, 10 well, 30 µL	Bio-Rad Laboratories (Feldkirchen, Germany)
4–20% Mini-PROTEAN® TGX Stain-Free™ Protein Gels, 15 well, 15 µL	Bio-Rad Laboratories (Feldkirchen, Germany)
BD Micro-Fine™ insulin syringe	BD (Heidelberg, Germany)
Cell culture flask Falcon® (25 & 75 cm2)	VWR (Langenfeld, Germany)
Cell culture plate Falcon® (35 mm, 24 well, 6 well)	Corning (Kaiserslautern, Germany)
Cellstar® Cell culture dish 60/15mm	Greiner bio-one (Frickenhausen, Germany)
Combitips advanced® 0,5mL, 5mL	Eppendorf (Hamburg, Germany)
Corning® Thermowell™ GOLD 0.2 mL Polypropylene PCR Tubes with Flat Cap	Corning (Kaiserslautern, Germany)
Cover slips (24x 50 mm, 12 mm, 30 mm)	VWR International (Darmstadt, Germany)
Cryotubes 1,8 mL	Thermo Fisher Scientific (Waltham, USA)
Histobond® microscope slides	Marienfeld
Immersol™ 518F	Carl Zeiss (Oberkochen, Germany)
Leukosilk®	BSN medical (Hamburg, Germany)
Microscope slides	VWR (Langenfeld, Germany)
Parafilm	M Bemis Company Inc. (Oshkosh, USA)
Pasteur pipettes (1 & 3 mL)	VWR (Darmstadt, Germany)
Pipette tips	Sarstedt (Nümbrecht, Germany)
razor blades	Wilkinson (Solingen, Germany)
Reaction tubes (0,2 & 0,5 mL)	VWR (Darmstadt, Germany)
Reaction tubes (2 & 1,5 mL)	Sarstedt (Nümbrecht, Germany)
Reaction tubes 1,5 mL Safe-lock	Eppendorf (Hamburg, Germany)
Syringe (2 & 5 mL)	BD (Heidelberg, Germany)
Sterile filter: 0.2 µm	Whatman GmbH (Maidstone, Großbritannien)
Trans-Blot Turbo Mini 0.2 µm PVDF Transfer Packs	Bio-Rad Laboratories (Feldkirchen, Germany)

Table 41: Laboratory instruments and equipment

Instrument/Equipment	Company
Agarose gel chamber Mini-Sub Cell GT	Bio-Rad Laboratories (Feldkirchen, Germany)
Analytical balance	Mettler Toledo, (Gießen, Germany)
Autoclave	HSP steriltechnik AG
Centrifuge Rotana 460R	Hettich (Stuttgart, Deutschland)
Centrifuge MICRO STAR 17R	VWR (Darmstadt, Germany)
Centrifuge HERAEUS MAGAFUGE 16R	Thermo Scientific (Waltham, USA)
Centrifuge HERAEUS MAGAFUGE 8	Thermo Scientific (Waltham, USA)
ChemiDoc™ MP Imaging System	Bio-Rad Laboratories (Feldkirchen, Germany)
CO_2-Inkubator Hera Cell 240i	Thermo Scientific (Waltham, USA)
Counting chamber	LO Laboroptik (Friedrichsdorf, Germany)
Electrical stimulator Isolated pulse stimulator model 2100	A-M Systems
Electrophoresis chamber Mini-PROTEAN® Tetra System with PowerPac™ Basic	Bio-Rad Laboratories (Feldkirchen, Germany)
Freezer (-20°C) Liebherr MediLine	Liebherr (Biberach an der Riss, Germany)
Freezer (-80°C) pHcbi hybrid	PHC Group (Neatherlands)
Fridge (4°C) Liebherr ProfiLine	Liebherr (Biberach an der Riss, Germany)
Heating plate with magnetic stirrer	VWR (Darmstadt, Germany)
Ice machine AF 80	Scotsman
Immunofluorescence imaging camera Prime BSI	Photometrics
Immunofluorescence light emitting diodes (LEDs) LedHUB	Thorlabs
Microcentrifuge 5415 R	Eppendorf (Hamburg, Germany)
Nikon ECLIPSE Ti2	Nikon (Tokyo, Japan)
Nikon Confocal	Nikon (Tokyo, Japan)
Multipipette E3	Eppendorf (Hamburg, Germany)
PCR Thermocycler Professional Trio	Biometra (Göttingen, Germany)
PH-Meter 765 Calimatic	Knick (Berlin, Germany)
Pipettes	Eppendorf (Hamburg, Germany)
Powermeter PM100 mit S130A Sensor	Thorlabs, (München, Germany)
Power supply for electrophoresis PowerPac™ HC	Bio-Rad Laboratories (Feldkirchen, Germany)
Powerlab 4/25 oder 16/30	ADInstruments (Spechbach, Germany)
NANODROP 2000C spectrometer	Thermo Scientific (Waltham, USA)
Sterile benches Hera Safe & Hera Safe KS	Thermo Scientific (Waltham, USA)
Ultrasonic bath	VWR (Darmstadt, Germany)
Vacuum pump with filter	Vacuubrand (Wertheim, Germany)
Vortex mixer	VWR (Darmstadt, Germany)
Western blot and DNA gel imager ChemiDoc™ MP Imaging System	Bio-Rad Laboratories (Feldkirchen, Germany)
Western Blot Trans-Blot Turbo	Bio-Rad Laboratories (Feldkirchen, Germany)
Water bath Typ WB 10	Memmert

Table 42: Microscope Nikon Eclipse Ti2 channel equipment

Name	Filter	LED	Company
DAPI	C-FL-C DAPI-U HQ Mirror: 425-∞ nm Excitation: 383-408 nm Emission: 435-485 nm	385+405 nm	AHF Analysentechnik: F36-500 HC-Set
GFP	C-FL-C GFP-B Mirror: 500- ∞ nm Excitation: 450-490 nm Emission: 510-560 nm	465 nm	AHF Analysentechnik: F46-002 ET-Set
Cy3	C-FL-C Cy3 HQ Mirror: 565-∞ nm Excitation: 515-555 nm Emission: 570-610 nm	555 nm Filter: ET525/50 M ↑ 330567	AHF Analysentechnik: F46-004 ET-Set Cy3
Cy5	C-FL-C Cy5 HQ Mirror: 660-∞ nm Excitation: 590-650 nm Emission: 663-738 nm	625 nm	AHF Analysentechnik: F46-009 ET-Set Cy5
X-Rhod	G-2B Mirror: 575-∞ nm Excitation: 510-560 nm Emission: 610-∞ nm	555 nm Filter: BP 572/28 nm BrightLine® Fluorescence Filter 572/28 ↑	AHF Analysentechnik: F36-504 HC-Set X-Rhod
EYFP	YFP HYQ Mirror: 515- ∞ nm Excitation: 490-510 nm Emission: 520-550 nm	488 nm Filter: ET500/20 X ↑ 364368	AHF Analysentechnik: F46-003 ET-Set YFP
Cal-630	G-2B Mirror: 575-∞ nm Excitation: 510-560 nm Emission: 610-∞ nm	625 nm Filter ET605/50 X ↑ 348155	AHF Analysentechnik: F46-015 ET-Set Alexa 633
Fura/Fluo	Fura/Fluo H488 LP XR 5200LP	Ultra red light 380 nm	AHF Analysentechnik
1% Filter	ND2.0	-	AHF Analysentechnik
10% Filter	ND1.0	-	AHF Analysentechnik

Table 43: (Confocal) Microscope Nikon Eclipse Ti2 objectives

Objective	Working distance	Company
4x S Fluor 4x NA= 0.20	WD= 15500 µm	Nikon (Tokyo, Japan)
10x S Fluor 10x DIC N1, NA= 0.50	WD= 1200 µm	Nikon (Tokyo, Japan)
20x S Fluor 20x DIC M N2 NA= 0.75	WD= 1000 µm	Nikon (Tokyo, Japan)
Plan Fluor **20x** DIC N2, NA= 0.50	WD= 2100 µm	Nikon (Tokyo, Japan)
S Fluor **40x** Oil DIC H N2, NA= 1.30	WD= 220 µm	Nikon (Tokyo, Japan)
Plan APO D **60x** oil OFN25 DIC N2	WD= 183 µm	Nikon (Tokyo, Japan)
Plan Fluor **100x** Oil Iris DIC H N2, NA= 1.30,	WD= 160 µm	Nikon (Tokyo, Japan)

Table 44: Confocal Microscope Nikon Eclipse Ti2 filter

Name	Filter	Company
DAPI	DM-Wheel: DAPI/FITC/Cy3/Cy5 Emission: 432 nm, range 36 nm Excitation: 405 nm, range 20 nm	AHF Analysentechnik: F68-400 AHF Analysentechnik: F39-432 AHF Analysentechnik: F49-406
EYFP	DM-Wheel: DAPI/FITC/Cy3/Cy5 Emission: 535 nm, range 30 nm Excitation: 472 nm, range 30 nm	AHF Analysentechnik: F68-400 AHF Analysentechnik: 535/30 AHF Analysentechnik: F39-472
Cy3	DM-Wheel: DAPI/FITC/Cy3/Cy5 Emission: 595 nm, range 31 nm Excitation: 554 nm, range 23 nm	AHF Analysentechnik: F68-400 AHF Analysentechnik: F39-595 AHF Analysentechnik: F39-553
Cy5	DM-Wheel: DAPI/FITC/Cy3/Cy5 Emission: 685 nm, range 40 nm Excitation: 635 nm, range 18 nm	AHF Analysentechnik: F68-400 AHF Analysentechnik: F37-685 AHF Analysentechnik: F39-638

Table 45: Assay kits used in this work

Assay kits used in this work	article number	Company
EndoFree® Plasmid Maxi Kit	12362	Qiagen (Hilden, Germany)
FuGENE®HD Transfection Reagent	E2311	Promega
Mini-Protean® TGX™ Precast Stain-Free Protein Gels (4-20%)	4568096	Bio-Rad Laboratories (Feldkirchen, Germany)
P3 Primary Cell Solution Box, XL	F-15200	Lonza (Cologne, Germany)
PierceTM BCA Protein Assay Kit	23225	Thermo Fisher Scientific (Waltham, USA)
PierceTM ECL Western Blotting	32106	Thermo Fisher Scientific (Waltham, USA)
Trans-Blot Turbo Transfer Pack	1704156	Bio-Rad Laboratories (Feldkirchen, Germany)
QIAprep® Spin Miniprep Kit	27104	Qiagen (Hilden, Germany)

Table 46: Software used in this work

Software	Company
Bio-Rad ImageTM Software version 5.2.1	BioRad (München, Germany)
Clone Manager 9 Sci-ed Software	(Westminster, USA)
Coral Draw 2020	Corel Corporation (München, Germany)
Cell Frequency Analysis 4.9	Custom-made Lab AG Sasse (Bonn, Germany)
Deep-L write and translate	DeepL SE (Köln, Germany)
Grammarly	Grammarly Inc. (San Francisco, USA)
GraphPad Prism 8	GraphPad Software (La Jolla, USA)
Image Lab 6.1	BioRad (München, Germany)
Labchart 7/8	ADInstruments (Spechbach, Germany)
Microsoft Office 2019	Microsoft (Unterschleißheim, Germany)
Nikon NIS Elements AR with GA3	Nikon Instruments Inc. (Tokyo, Japan)
Omicron control center v3	Omicron-Laserage
PyMol	Schrödinger
SnapGene	Dotmatics (Bosten, USA)

Table 47: Primary Antibodies used in this work

Antibody	Species specificity	article number	Company
Anti-α-Actinin	mouse monoclonal IgG1	A7811-.2ML	Sigma
Anti-α-Actinin	rabbit polyclonal IgG	ab137346	Abcam
Anit-SERCA2 ATPase	mouse monoclonal IgG2a	MA3-919	Thermo Fisher
Anti-GFP Living Colors® A.v. Monoclonal Antibody (JL-8)	mouse monoclonal IgG2a	632381	TAKARA
FKBP12.6 Antikörper (H-8): sc-376135	mouse monoclonal IgG1	sc-376135	SANTA CRUZ BIOTECHNOLOGY, INC.
L-type Ca^{++} CP α1C Antikörper (D-6)	Maus monoklonales IgG2a	sc-398433	SANTA CRUZ BIOTECHNOLOGY, INC.
Anti-CaV1.2(CACNA1C) Antibody	rabbit polyclonal IgG	ACC-003	Alomone Labs
L-type Ca^{++} Channel (Cav1.2) pSer1928 pAb	rabbit polyclonal IgG	A010-70	Badrilla
Phospholamban (PLN, PLB) mAb (clone A1)	mouse monoclonal IgG	A010-14	Badrilla
Phospholamban (PLN, PLB) (pser16) pAb	rabbit polyclonal IgG	A010-12AP	Badrilla
Phospho-PKA substrate (RRXS*/T*) (100g7E)	rabbit mAb IgG	5565S	Cell Signaling TECHNOLOGY
RyR2 monoclonal (C3-33)	mouse monoclonal IgG1	Ma3-916	Thermo Fisher Invitrogen
RyR2 (pSer2808) pAb	rabbit polyclonal IgG	A010-30AP	Badrilla
RyR2 (pSer2030) pAb	rabbit polyclonal IgG	A010-32	Badrilla
Anti-EYFP	rabbit polyclonal IgG	MB5800431	MyBioSource
Recombinant Anti-cAMP antibody	Rabbit monoclonal	ab134901	Abcam

Table 48: Secondary Antibodies used in this work

Antibody	Species specificity	Label (nm)	Source	article number	Company
IgG1	mouse	555	goat	A21127	Thermo Fisher Invitrogen
IgG1	mouse	647	goat	A21240	Thermo Fisher Invitrogen
IgG	rabbit	647	donkey	A31573	Thermo Fisher Invitrogen
IgG	mouse	555	donkey	A31570	Thermo Fisher Invitrogen
IgG	mouse	647	donkey	A31571	Thermo Fisher Invitrogen
IgG	rabbit	488	donkey	A21206	Thermo Fisher Invitrogen
IgG	rabbit	555	donkey	A31572	Thermo Fisher Invitrogen
IgG2a	mouse	555	goat	A21137	Thermo Fisher Invitrogen
HRP Anti-mouse	mouse IgG	-	goat	115-035-146	Jackson ImmunoResearch Laboratories, INC.
HRP Anti-rabbit	rabbit IgG	-	goat	111-035-144	Jackson ImmunoResearch Laboratories, INC.
HRP Anti-goat	goat	-	donkey	SA5-10089	Jackson ImmunoResearch Laboratories, INC.
Abberior STAR RED	mouse	STED 655	goat	STRED-1001-500UG	Abberior Instruments GmbH
Abberior STAR 580	rabbit	STED 607	goat	ST580-1002-500UG	Abberior Instruments GmbH

4 Results

4.1 Subcellular targeting of RyR2 and LTCC with optogenetic tools

Precise subcellular targeting and modulation of ion channels and regulatory proteins can help us better understand their regulation and function. Several sub-targets (proteins associated with or bound to the LTCC and RyR2) have been considered to localize the optogenetic tool to the LTCC and RyR2. AKAPs localized at the LTCC, such as AKAP18α[73] and AKAP5[74], or mAKAP[75], which is localized at the RyR2, were considered. However, we were searching for smaller proteins to fuse our optogenetic tools.

The present study employed the nanobody-based approach developed by Morgenstern et al. (2019),[76] wherein a nanobody (nb.F3) that specifically recognizes the $ß_{1-4}$ subunit of the LTCC was developed. Their approach enabled them to precisely deliver an LTCC inhibitor, as demonstrated in their study.[76] To target the RyR2, we used the FKBP12.6 protein, which role on RyR2 was already studied by Despa et al. (2014).[77] FKBP12.6 binds to RyR2 with a high affinity and stabilizes its closed state, thereby preventing excessive Ca^{2+} leakage from the SR.[77] Disruption of FKBP12.6-RyR2 interactions has been implicated in cardiac arrhythmias and heart failure, through Ca^{2+} leakage from the SR. The study by Despa and colleagues highlights the importance of FKBP12.6 in maintaining proper RyR2 function and the potential implications of targeting this interaction for therapeutic intervention.[77]

This study investigated the precise subcellular modulation of LTCC and RyR2 to understand their impact on standard cardiac excitation-contraction coupling and Ca^{2+} homeostasis, particularly the relative contribution to the overall inotropic and chronotropic effect. Dysregulation of these proteins contributes to cardiac arrhythmias, heart failure, and other cardiovascular diseases. **Figures 9** and **10** provide a schematic overview of LTCC and RyR2 targeting, utilizing the photo-activatable adenylyl cyclase (PAC) to activate cAMP locally (**Fig. 9**) and the photoactivated protein kinase A inhibitor (LOV-PKI) to locally inhibit PKA (**Fig. 10**). Both were additionally fused with fluorescent markers for identification. This work is divided into two main parts: the first, where experiments were conducted with PACs for cAMP generation, and the second, where LOV-PKI is used to inhibit the catalytic function of PKA.

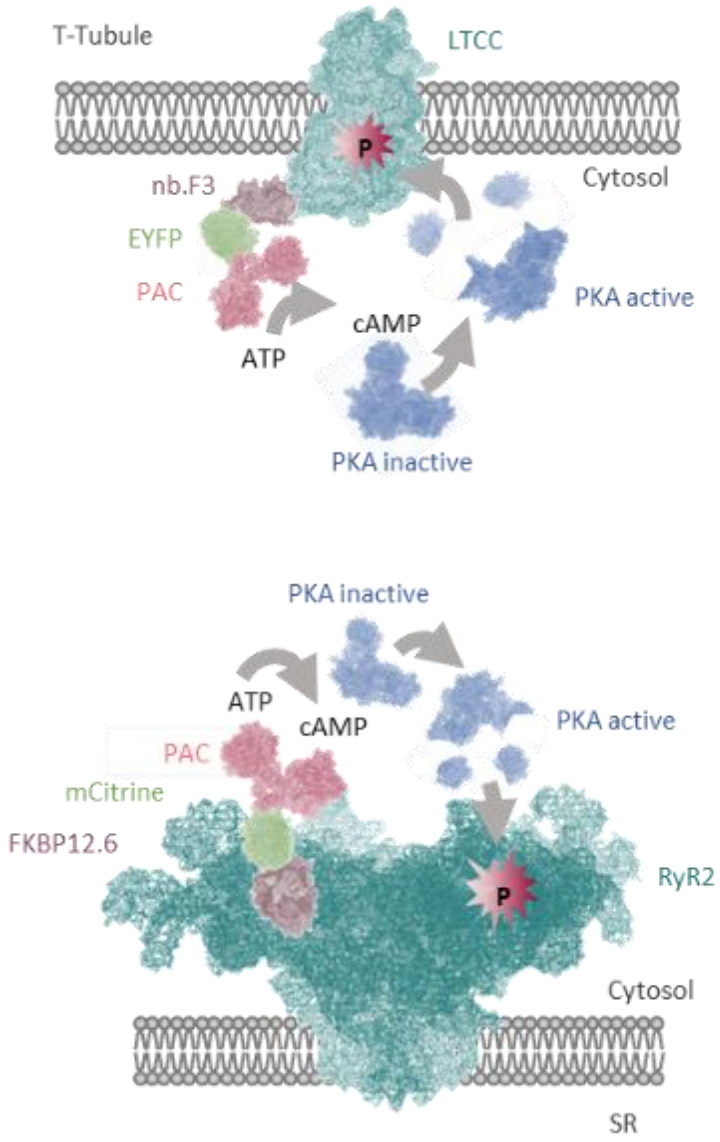

Fig. 9: Local activation of cAMP at LTCC and RyR2
The photoactivatable adenylyl cyclases (PACs) were fused to a nanobody nb.F3 to target the LTCC, and EYFP as a marker. To target the RyR2, the PACs were fused to the FKBP12.6 protein and mCitrine as a marker. Protein structures generated using PyMol. PDB numbers: LTCC (8E5B), RyR2 (5GOA), PKA (6NO7), EYFP/mCitrine (6ZQO), nb.F3 (8E0E), FKBP12.6 (4IQC) and OaPAC (8QFE).

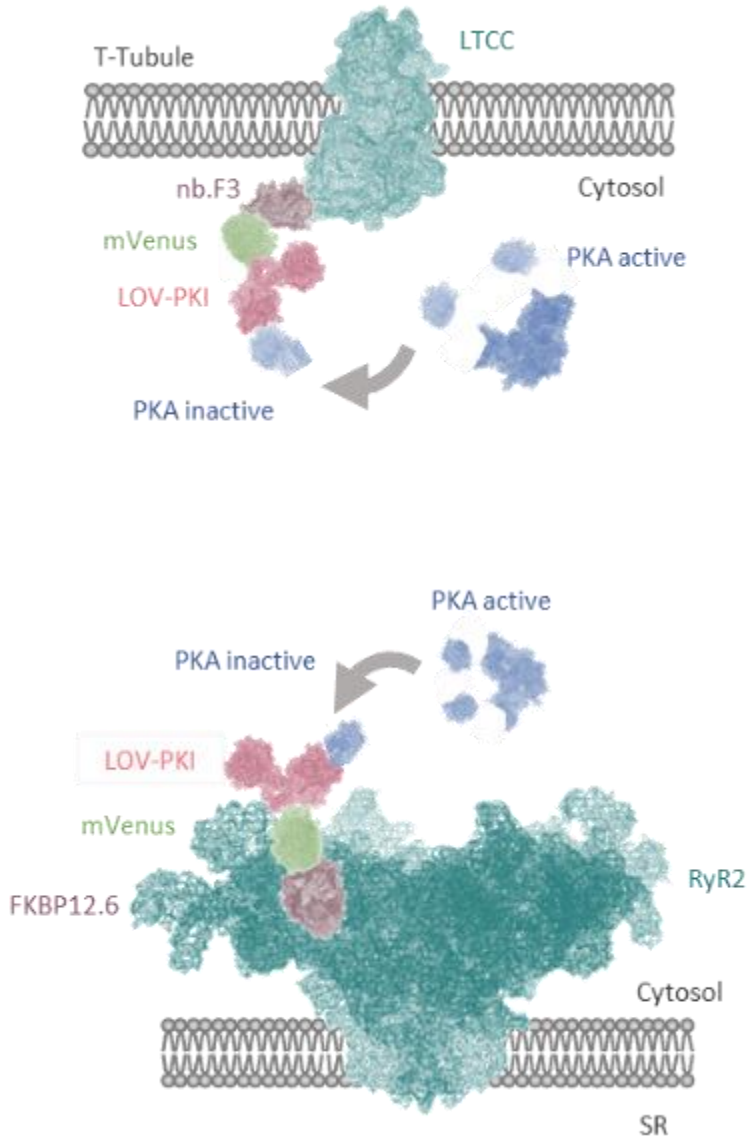

Fig. 10: Local inhibition of PKA at LTCC and RyR2
The LOV-PKI was fused to a nanobody nb.F3 to target the LTCC, and mVenus was used as a marker. To target the RyR2, the PACs were fused to the FKBP12.6 protein and mCitrine as a marker. Protein structures generated using PyMol. LOV-PKI construct from Yi et al., 2014. PDB numbers: LTCC (8E5B), RyR2 (5GOA), PKA (6NO7), EYFP/mCitrine (6ZQO), nb.F3 (8E0E), FKBP12.6 (4IQC).

4.2 Construct and target validation of PACs

The first cloned constructs were the three different PACs (bPAC,[69] bPAC-S27A[69], and TpPAC[70]). They were cloned into a plasmid with a cytomegalovirus early enhancer/chicken β-actin/rabbit β-globin (CAG) promoter, a fluorescent marker, and for LTCC targeting with the nb.F3[76] nanobody and RyR2 targeting with the FKBP12.6[77] protein (**Fig. 11**). Non-targeted PACs were used as controls for global cytosolic cAMP modulation. The constructs were cloned using overhang primers, and the DNA fragments of nb.F3 and FKBP12.6 were produced by GeneArt (Thermo Fisher).

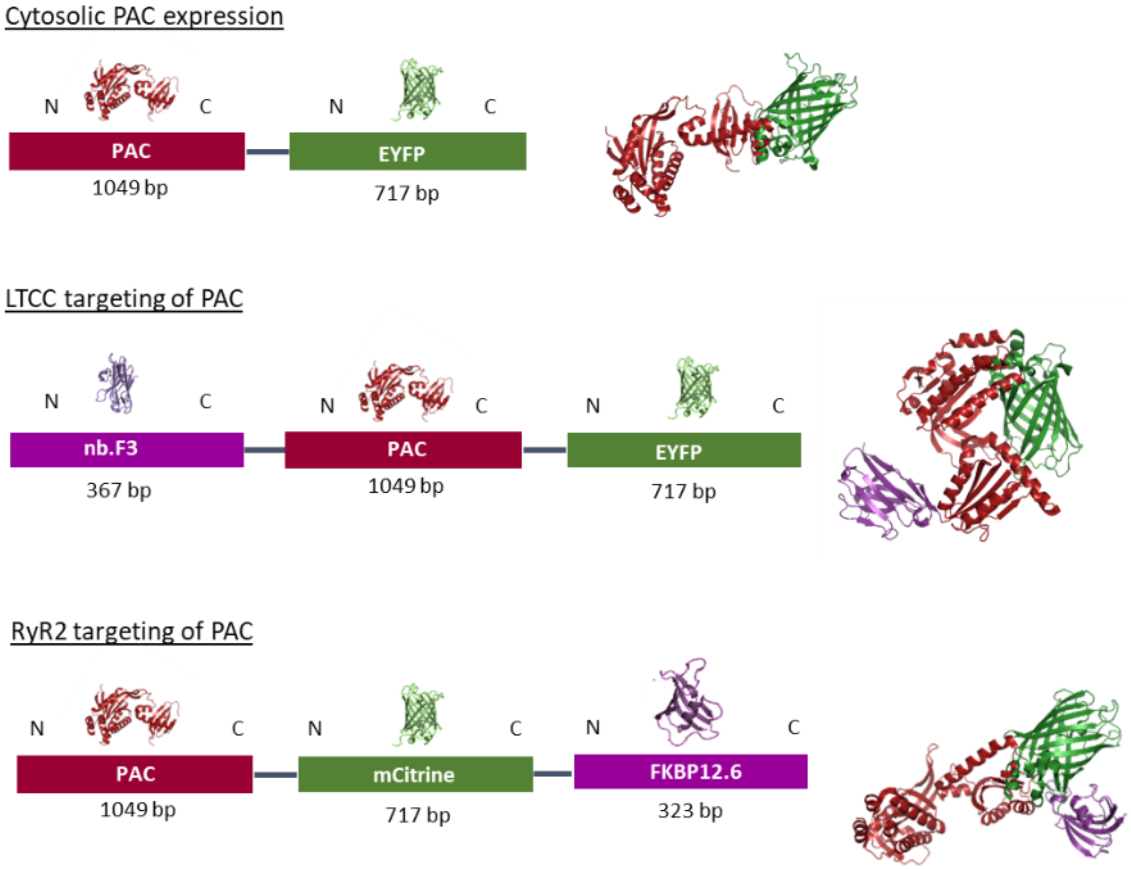

Fig. 11: Targeting design and predicted protein structure
For cytosolic expression, the various PACs were cloned to EYFP. For LTCC targeting, the nanobody nb.F3 was cloned to the PACs and EYFP. The FKBP12.6 protein was used to target RyR2. The marker mCitrine was fused to the PACs, and then the FKBP12.6 protein was fused to mCitrine. Predicted protein structures of the fusion proteins were generated using PyMol. PDB numbers: EYFP/mCitrine (6ZQO), nb.F3 (8E0E), FKBP12.6 (4IQC), and OaPAC (8QFE).

First, the functionality of the light-activated proteins was validated after fusing them with other proteins. Human embryonic kidney 293 (HEK293)[78] cells were used as a proof of principle because they are generally easy and inexpensive to handle compared to cardiomyocytes, and their culturing is well-established in the laboratory. HEK293 cells do not express LTCCs and RyR2s; this cell line was used solely as a model to validate the construct fusion and functionality, but not the targeting ability of the nanobody nb.F3 or the FKBP12.6 protein. Thus, all different constructs expressed in HEK293 cells were

located in the cytosol (**Fig. 12**). To verify that the protein fusion did not abolish the PAC function to generate cAMP upon blue light illumination, the constructs were transfected into HEK293 cells expressing the cAMP-sensitive luminescence-based GloSensor construct (Promega).[79]

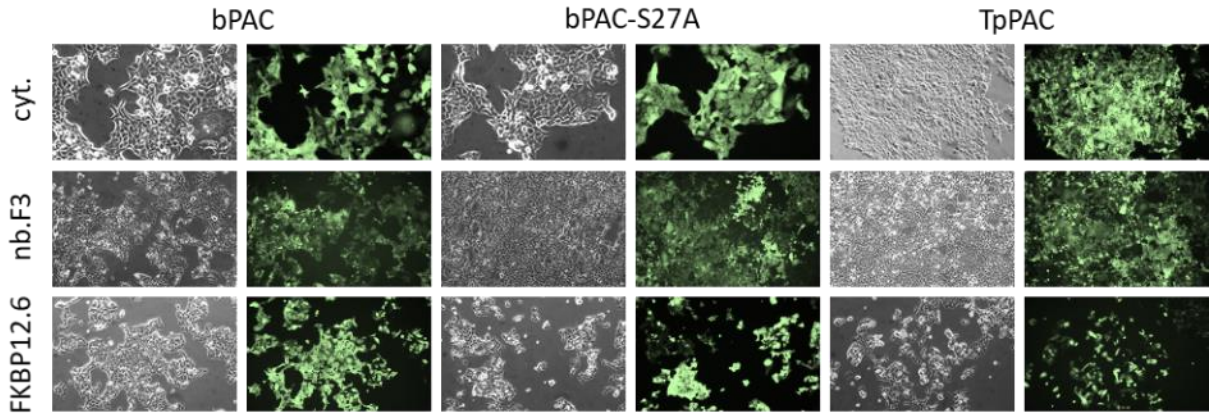

Fig. 12: HEK293 cells transfected with PACs
Transfected HEK293 cells co-expressing the GloSensor (no marker) and PAC-EYFP, nb.F3-PAC-EYFP and PAC-mCitrine-FKBP12.6 (PACs: bPAC, bPAC-S27A and TpPAC) constructs showing EYFP/mCitrine signal (green). Images taken with a Nikon Eclipse Ti2 fluorescence microscope using a 10x objective, with brightfield images compared to YFP (488 nm) in green.

Blue light (465 nm) flashes of increasing duration were applied through the injector port in a multi-plate reader. Luminescence was continuously monitored to establish a dose-response curve (**Fig. 13**). All nine constructs demonstrated a dose-dependent increase in cAMP (area under the curve), which was enhanced with longer light flashes (**Fig. 13, 14**), indicating intact and fine-tunable PAC function (**Fig. 13 C, blue**). WT HEK293 cells containing only the GloSensor were used to validate the GloSensor function, measure cAMP concentrations, and demonstrate that illumination does not lead to an increase in cAMP. These cells did not respond to light but showed a positive forskolin (FSK) control response (**Fig. 13 red**). FSK activates the AC and induces cAMP generation (see Chapter **1.4**). The PAC GloSensor lines also responded to FSK, demonstrating a functional GloSensor response in analyzed cells (**Fig. 13, blue**). The pure HEK293 WT cells (**Fig. 13, gray**) served as a negative control and did not exhibit any signal, as they did not express the GloSensor for cAMP measurement.

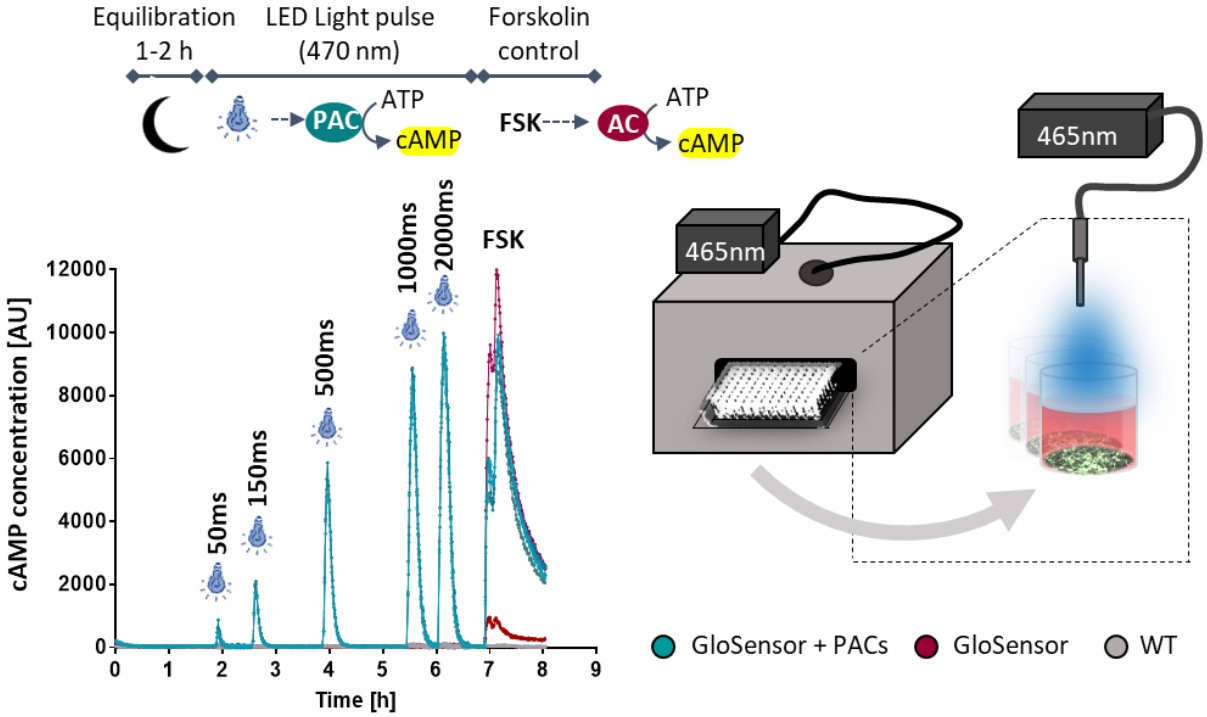

Fig. 13: Intact and gradual light-induced cAMP generation of PAC fusion constructs
Example of nb.F3-bPAC-EYFP (blue), showing a light-induced cAMP increase in a dose-dependent manner, with the schematic explanation provided above. Cells were incubated for 1-2 h in a GloSensor assay medium containing luciferin. Right: Schematic of the TECAN reader with light guide built into the injector port to activate PACs. Negative control of HEK cells with GloSensor (red) didn't respond to light but showed increased cAMP compared to FSK and HEK WT cells (gray), which showed no signal.

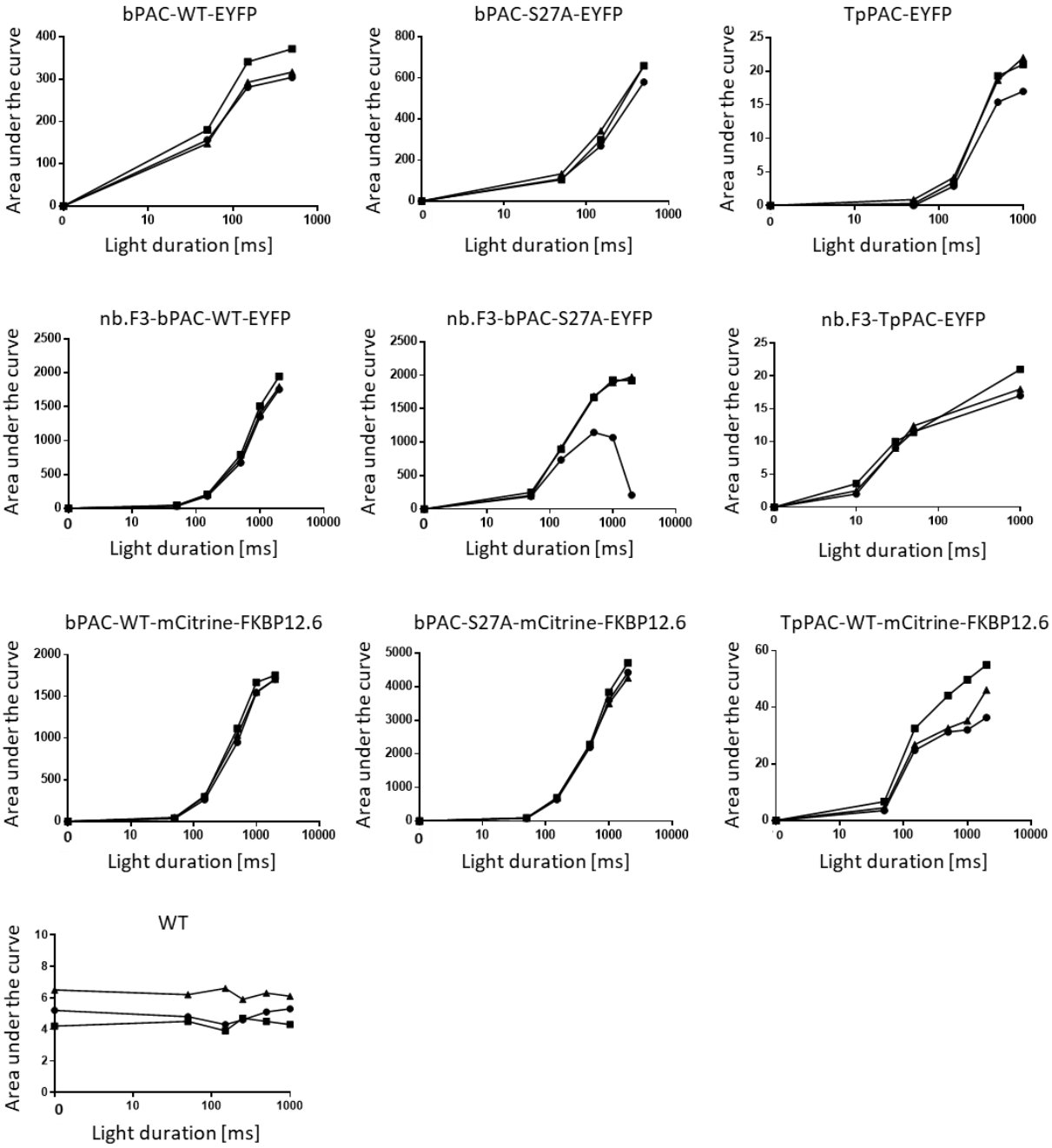

Fig. 14: Dose-dependent light-induced cAMP generation of PAC fusion constructs
Functional cAMP generation by PAC fusion constructs in HEK293 cells was validated by co-expression of the cAMP-sensitive, luminescence-based GloSensor construct. Blue light illumination of different durations resulted in cAMP accumulation in a dose-dependent manner. To quantify the cAMP response, the area under the curve was analyzed for each light pulse and showed a dose-dependent increase (n = 3) in cells expressing PACs, but no effect in wild-type (WT) cells.

The fusion proteins were further validated by analyzing the correct protein sizes in stable HEK293 cells expressing the proteins using Western blot analysis (**Fig. 15**) with a GFP antibody. The expected sizes of the fusion constructs are approximately 67 kDa for PAC-EYFP (**1**), 81 kDa for nb.F3-PAC-EYFP (**2**), and 79 kDa for PAC-mCitrine-FKBP12.6 (**3**). A HEK293 cell line with GFP (27 kDa) was used as a positive control for the GFP antibody, and HEK293 WT cells were used as a negative control. Clear bands with no sign of degradation were detected, and protein sizes were measured with the BioRad ImageLab software, showing approximately the expected protein size (**Fig. 15**).

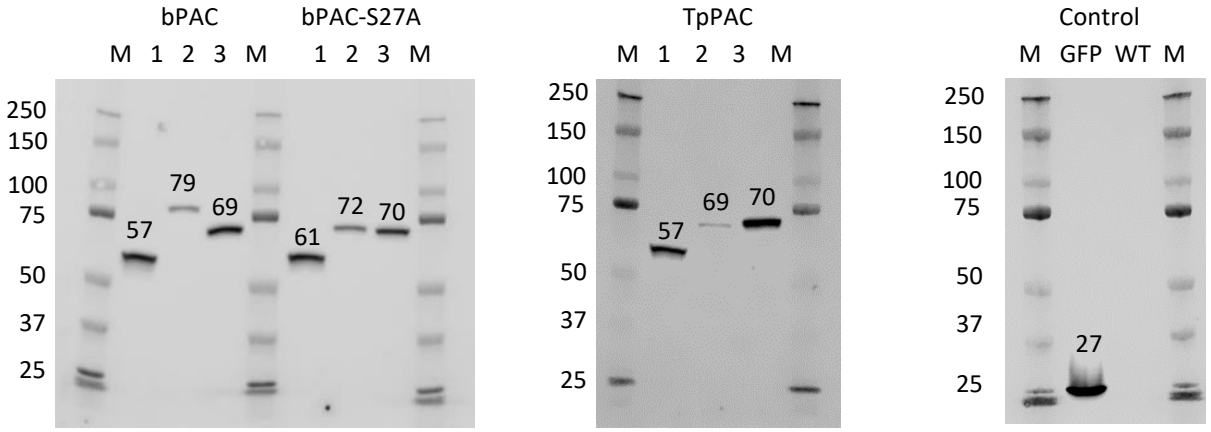

Fig. 15: Western blot analysis of constructs in HEK 293 cells
*The fusion constructs **1**) PAC-EYFP (expected size: 67 kDa), **2**) nb.F3-PAC-EYFP (expected size: 81 kDa) and **3**) PAC-mCitrine-FKBP12.6 (expected size: 79 kDa) were cloned, expressed in HEK293 cells and analyzed by Western blots (left) using a GFP antibody (1:3000). GFP-expressing HEK293 cells (30 kDa) and wild-type (WT) cells were used as controls (right). Using a Bio-Rad protein marker (**M**) as a size standard, we observed a slightly smaller size than predicted but no degradation.*

4.3 Establishing the best cell line and transfection method for functional analysis

Several cardiac cell lines and different transfection protocols were tested to find a suitable system for functional analysis of local LTCC and RyR2 cAMP modulation with the targeted optogenetic constructs.

Initially, the Heart Line-1 (HL-1) cells were selected for consideration due to their status as a well-characterized, immortalized mouse cardiomyocyte cell line, defined by their proliferative and spontaneous contractile capabilities.[80, 81]

To test the RyR2 function in HL-1 cells, Ca^{2+} imaging was performed with the red-shifted Ca^{2+} dye Cal630. Caffeine activates RyR2 by increasing its opening probability, resulting in a Ca^{2+} release from the SR. RyR2 activation with 10 mM caffeine increased cytosolic Ca^{2+} (**Fig. 16**), confirming the functional role of RyR2 in HL-1 cells.

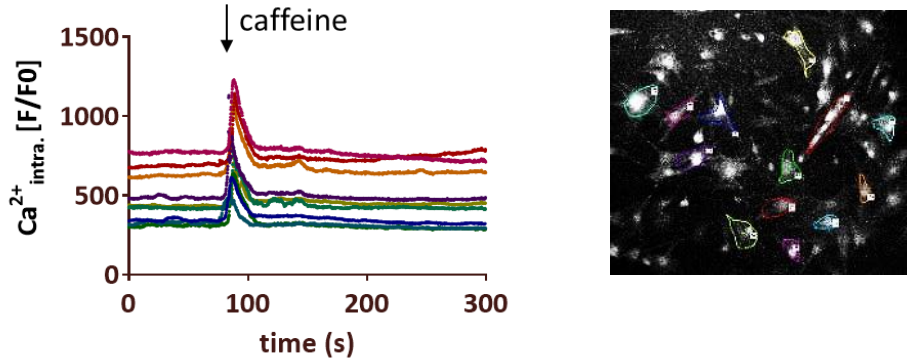

Fig. 16: Testing RyR2 function in HL-1 cells using Ca2+ imaging
HL-1 cells were plated on glass coverslips, and two days later, the cells were stained with Cal-630 and imaged on a microscope equipped with a perfusion system. The HL-1 cells were perfused with DEMEM F12 solution, and after baseline measurement, they were perfused with 10 mM caffeine, resulting in an increase in the Ca^{2+} signal. Images were captured using a Nikon Eclipse Ti2 fluorescence microscope equipped with a 20x objective, a Cal-630 filter, and a 625 nm LED.

While culturing HL-1 WT cells, we observed an insufficient contractile capacity to study changes in excitation–contraction coupling (ECC), particularly inotropy and chronotropy. Furthermore, immunohistological stainings against α-actinin, a crucial component of the Z-lines in the sarcomere, were performed. The primary role of α-actinin is to cross-link actin filaments from adjacent sarcomeres, thereby maintaining the alignment of sarcomeres for stable contraction. Additionally, antibodies against LTCC, RyR2, FKBP12.6, and PLN were used to investigate whether the Ca^{2+} handling in HL-1 cells was sufficient. Staining with the cardiac-specific marker α-actinin did not reveal a clear α-actinin striation pattern, indicating impaired contractility (**Fig. 17, red**). LTCC and RyR2 stainings confirmed the presence of these channels but also lacked the typical membrane localization (LTCC) or striation pattern (RyR2). PLN exhibited a specific localization around the nuclear envelope (**Fig. 17**).

FKBP12.6 staining did not display the same staining pattern as RyR2, but rather showed colocalization with α-actinin at the Z-lines. Although the Ca^{2+} imaging experiments reveal a functional RyR2, due to the insufficient contractility observed by the eye and the absence of distinctive α-actinin staining characteristic of cardiomyocytes, we concluded that we could not perform a functional analysis of localized cAMP modulation using HL-1 cells. Nevertheless, we continued to use HL-1 cells to establish an efficient transfection method for cardiomyocytes.

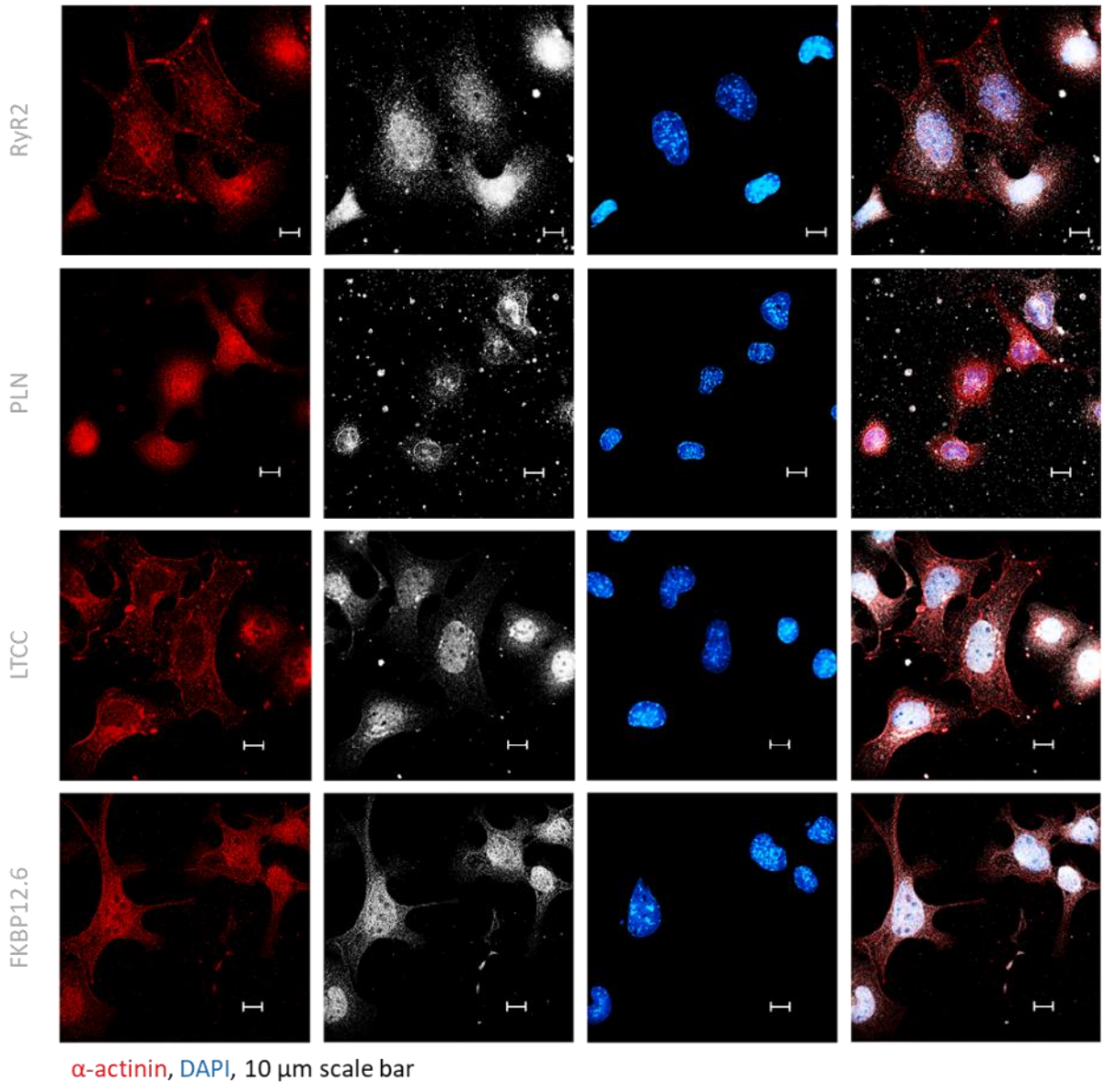

Fig. 17: HL-1 WT morphological testing in immunohistological staining
HL-1 cells were stained and images were taken with a Nikon Eclipse Ti2 fluorescence microscope with 40x oil objective and following channels: Hoechst (DAPI: 405 nm) in blue, α-actinin (Cy3: 505 nm) in red and either RyR2, PLN-P, LTCC, or FKBP12.6 (Cy5: 625 nm) in white. The scale bar is 10 µm.

Different transfection methods were tested for HL-1 cells with a GFP plasmid. First, Lipofectamine 3000 and FUGENE were tested as lipofection methods. In addition, two nucleofection methods were tested and developed: the Neon Transfection System (Invitrogen) and the 4D-Nucleofector™ System (Lonza). Examples of the different transfection methods are shown in **Figure 18**. Due to its highest transfection efficiency, the 4D-Nucleofector System™ (Lonza) was selected for further development.

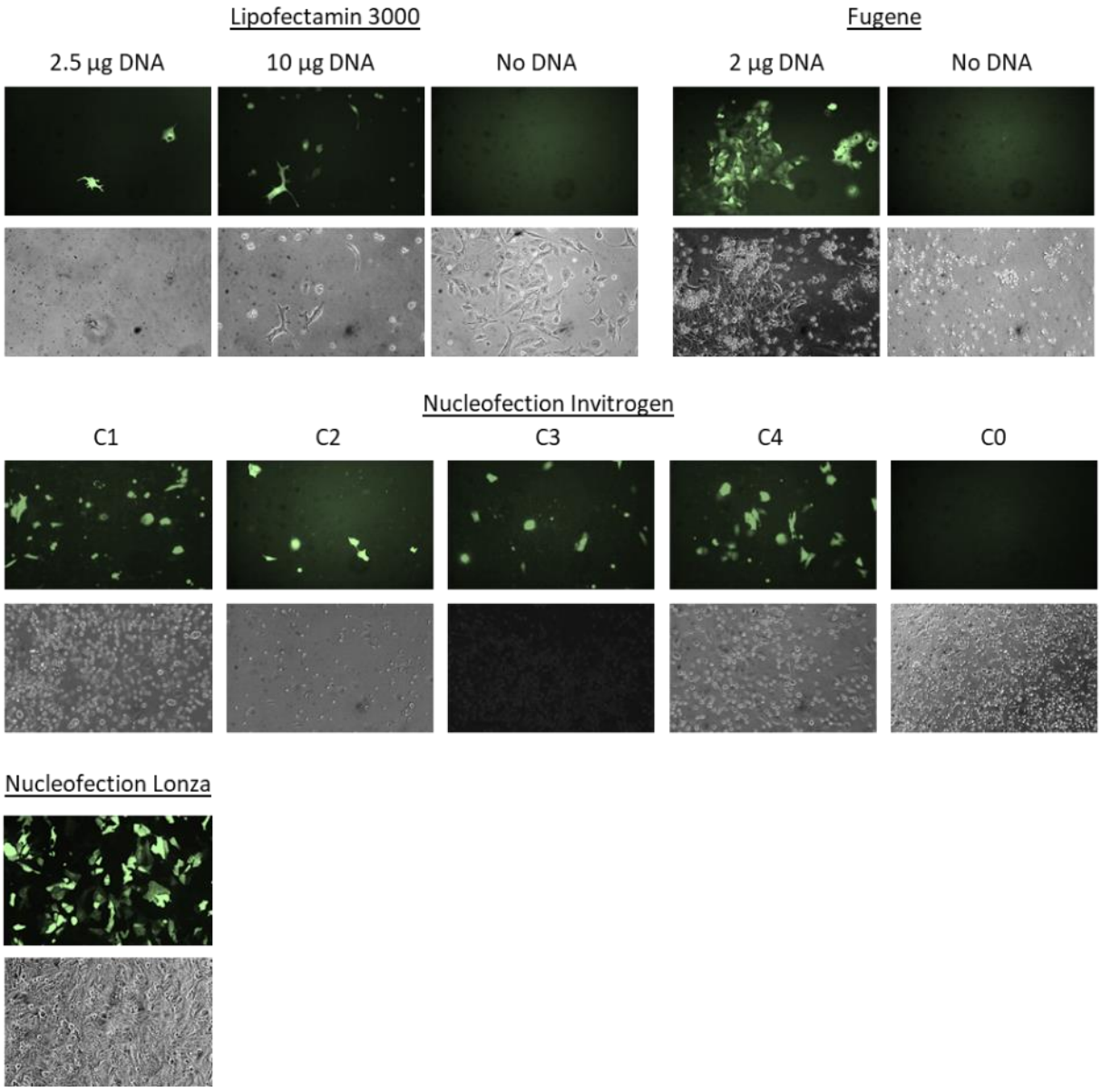

Fig. 18: HL-1 lipofection and nucleofection transfection methods
HL-1 cells were cultured, and lipofection and nucleofection protocols were tested to determine the most efficient transfection method. The Lipofectamine 3000 protocol was tested with 2.5 µg and 10 µg GFP-DNA. The FUGENE lipofection method was tested with 2 µg GFP-DNA. The nucleofection methods were tested with 0.1 µg GFP-DNA. The Neon Transfection System (Invitrogen) was tested with four different conditions: C 1: 1600 V, 10 ms, 3 pulses, C 2: 1500 V, 30 ms, 1 pulse, C 3: 1700 V, 20 ms, 1 pulse and C 4: 1400 V, 20 ms, 2 pulses. The nucleofection method 4D-Nucleofector™ System (Lonza), was tested with P3 buffer and the CM-150 program. For control, the protocols were performed without (-) GFP-DNA. Images taken with a Nikon Eclipse Ti2 fluorescence microscope using a 10x objective in brightfield and GFP (465 nm) illumination.

To test the impact of global and local PAC activity on cardiomyocyte inotropy and chronotropy, transgenic D3 mouse embryonic stem cells (ESCs) were generated stably expressing cytosolic or targeted PAC fusion constructs.

Between 6 and 15 clones of each line were screened for their ability to undergo proper cardiac differentiation. The best clones were differentiated into spontaneously beating embryoid bodies (EBs) using the hanging drop method (**Fig. 19**). Immunohistological stainings of D3 EBs (**Fig. 20**) revealed low levels of cross-striation in the α-actinin signal (**Fig. 20, red**).

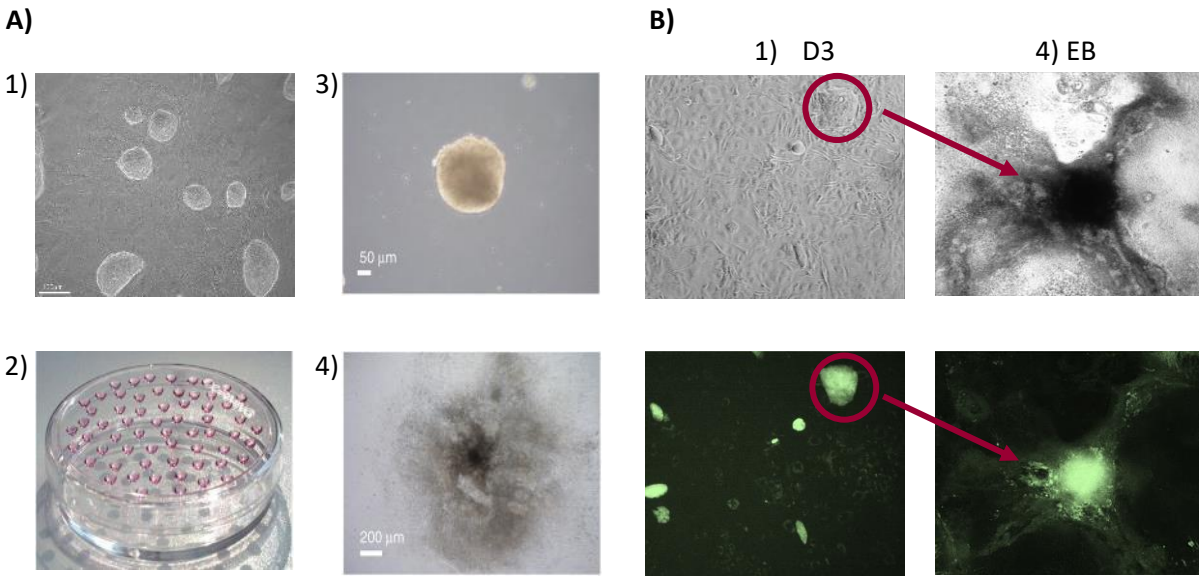

Fig. 19: D3 mouse embryonic stem cell differentiation
A*) D3 mouse embryonic stem cells (ESCs) were cultured on feeder cells (**1**) and transfected by nucleofection using the 4D-Nucleofector™ System from Lonza and the P3 buffer with the CM-150 program and 10 µg of DNA. The differentiation into cardiomyocytes was performed via the hanging drop method. **2)** Cell suspension was formed into drops to generate embryoid bodies (EBs). **3**) EBs were then grown in suspension under shaking. **4**) EBs were plated, and beating could be observed. **B)** Brightfield and YFP (488 nm, green) images of step **1)** cultured on feeder cells and step **4)** beating EBs.*

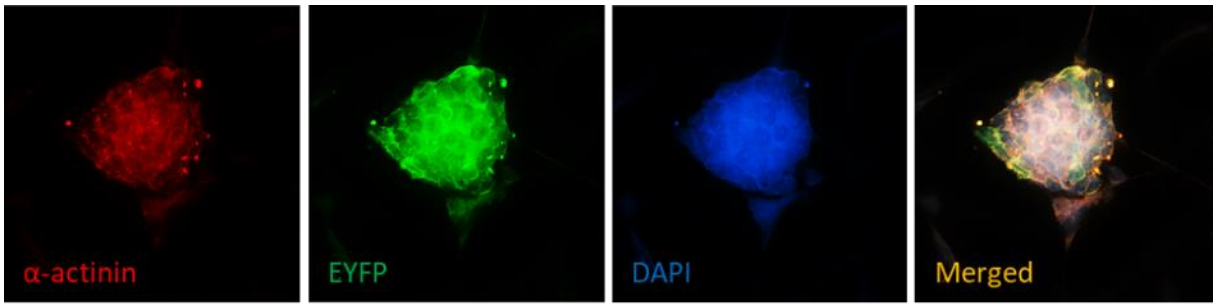

Fig. 20: D3 EBs immunohistological staining
D3 EBs generated, as shown in Figure 18, were fixed and stained with α-actinin (red) and the nuclear stain Hoechst (blue). The EYFP (green) signal was detected in transfected cells. Representative example of D3 EB with TpPAC-mCitrine-FKBP12.6. A Nikon Eclipse Ti2 fluorescence microscope with a 20x objective and the following filters was used: Hoechst (DAPI: 405 nm), α-actinin (Cy5: 625 nm), and EYFP (488 nm).

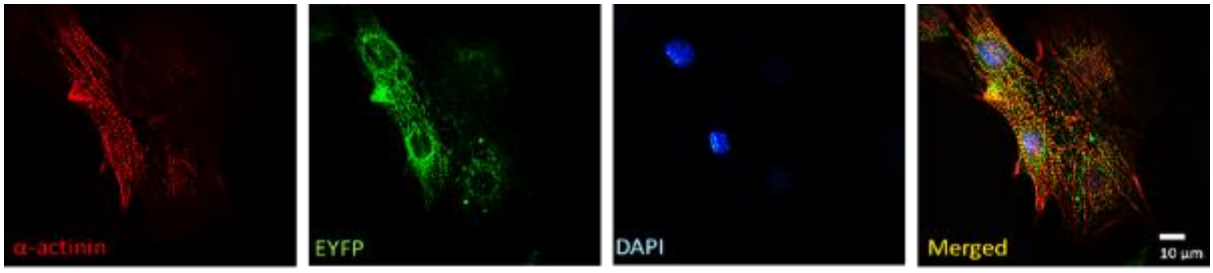

Fig. 21: Immunohistological staining of dissociated D3 EBs
EBs were dissociated by incubation with collagenase B and triple E for 30 min and then transferred and plated as single cells. Cells were fixed and stained with α-actinin (red) and the nuclear stain Hoechst (blue). The EYFP (green) signal was detected in transfected cells. Representative example of D3 EBs transfected with TpPAC-mCitrine-FKBP12.6. A Nikon Eclipse Ti2 fluorescence microscope with a 60x oil objective and the following filters was used: Hoechst (DAPI: 405 nm), α-actinin (Cy5: 625 nm), and EYFP (488 nm).

After dissociation of the EBs, some cells with clear α-actinin cross-striation were found (**Fig. 21, red**). Beating rate changes of dissociated cells were analyzed using video microscopy (**Fig. 22**), where they were screened for an EYFP-positive signal and a stable beating frequency to ensure a stable baseline for accurate light response. Brief flashes of blue light (465 nm) caused an instantaneous acceleration of beating frequency in a dose-dependent manner (**Fig. 22, 23**), demonstrating cAMP-dependent chronotropy. Beating EBs were successfully generated and measured in bPAC-EYFP, nb.F3-bPAC-EYFP, bPAC-mCitrine-FKBP12.6, TpPAC-EYFP, and TpPAC-mCitrine-FKBP12.6, but with a low sample size (n). A lower cAMP concentration was observed in TpPACs than in bPACs. Unfortunately, only a few cells of the D3 EBs differentiated into cardiomyocytes. In screened EBs that were beating, the beating areas were smaller than expected for this method. This could be due to the optogenetic modulation of cAMP, which interferes with the development of cell differentiation in cardiomyocytes. Nevertheless, the

resulting cardiomyocytes could be used to provide initial proof of principle for both the dose-dependent effect of the PACs and the method validation of beating rate measurement.

Due to its lower dark activity and smaller cAMP signal (**Fig. 23**), we chose to work with TpPAC for further functional experiments to ensure local activation rather than widespread cAMP generation, which might occur under bPAC.

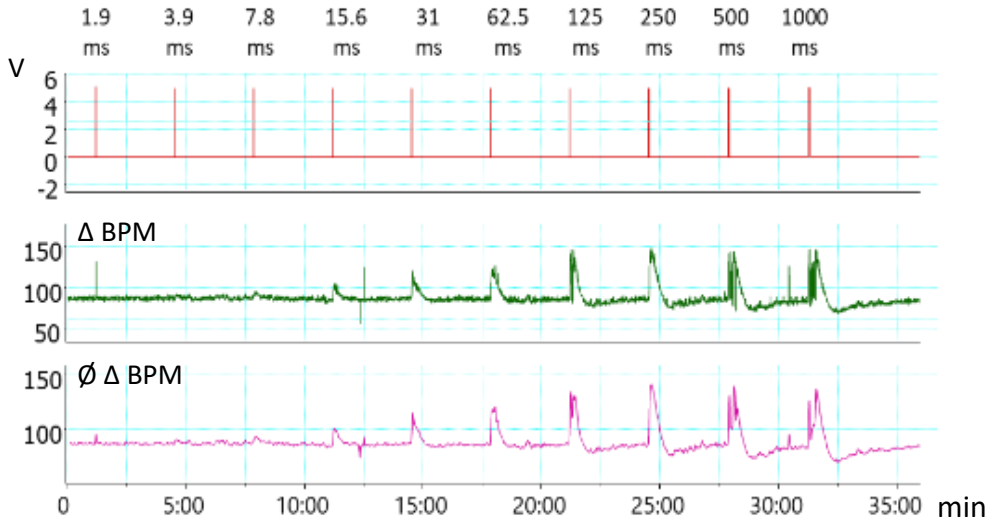

Fig. 22: Representative raw data of light-induced frequency acceleration
Frequency changes after short light flashes (465 nm, 0.11 mW/mm^2) of different durations (1.9 -1000 ms) in beating EBs of ESCs. Example of nb.F3-bPAC-EYFP. Note the frequency effect as a function of logarithmic light duration. A Nikon Eclipse Ti2 fluorescence microscope was used, equipped with red light imaging using a Fura/Fluo filter (380 nm) and blue light optogenetic stimulation with a blue light (465 nm) source, combined with a 1% ND2.0 filter.

Due to the difficulties encountered with the EBs, neonatal mouse cardiomyocytes (nCMs) were selected as the model system for the functional analysis of global and local PAC activity on cardiomyocyte inotropy and chronotropy. The decision to use nCMs as the model system was based on several factors. First, nCMs exhibit more organized α-actinin formation, enhancing contractile ability. Secondly, nCMs contain RyR2, LTCC, and other critical systems, such as the Gs signaling pathway and SERCA2a/PLN.[82] In the next step, a nucleofection protocol was developed to express cytosolic and targeted TpPAC in nCMs, using the nucleofection method of the 4D-Nucleofector™ System (Lonza). Different programs were tested and screened for nCM nucleofection, using the X-Unit (**Fig. 24**) and the Y-Unit (**Fig. 26**). In the X-unit method, cells were nucleofected in suspension in transfection cuvettes, and in the Y-unit method, cells were adherent in a 24-well plate and a transfection lid was placed on top of the cells.

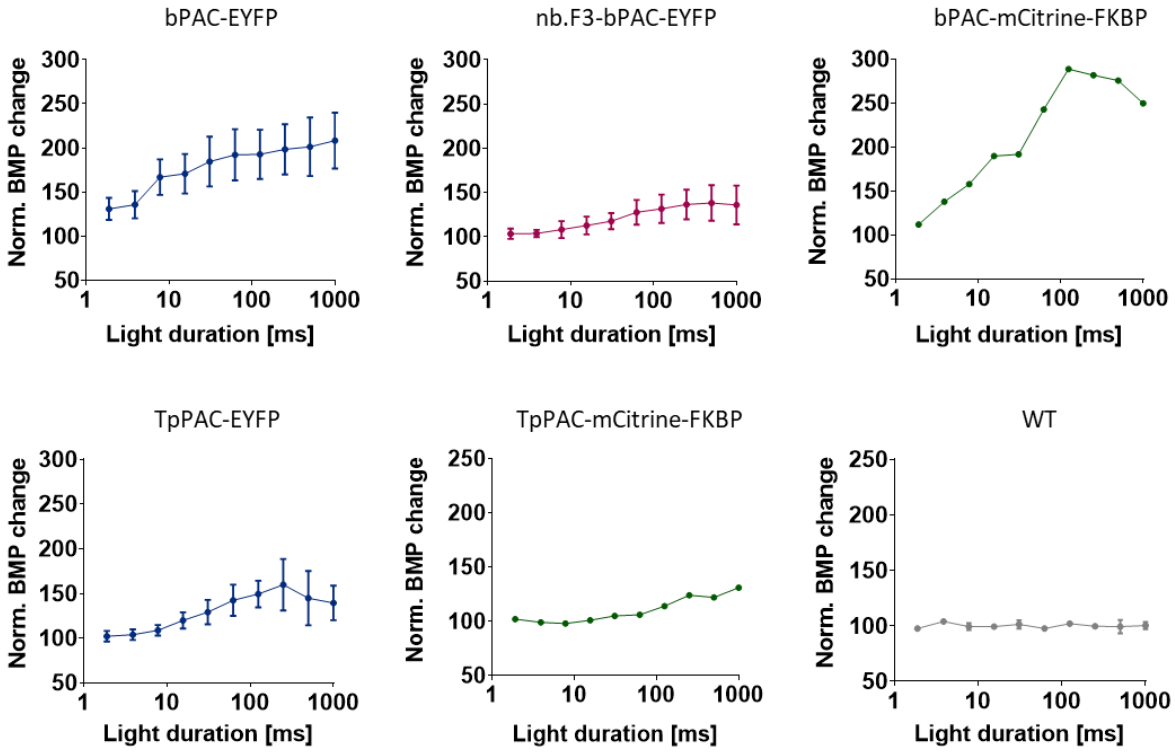

Fig. 23: Light-induced frequency acceleration in ESC-derived cardiomyocytes with targeted PACs *Frequency change after brief light flashes (465 nm, 0.11 mW/mm²) of different durations (1.9 -1000 ms) in beating embryoid bodies of ESCs expressing cytosolic (cyt), nb.F3-fused or FKBP12.6-fused proteins bPAC or TpPAC, n=1-5. Note the frequency effect as a function of logarithmic light duration. Cytosolic =blue, nb.F3 =red, FKBP = green, WT = gray.*

The X-unit method (**Fig. 24**) was selected due to its cost-effectiveness and straightforward implementation, whereas the Y-unit method (**Fig. 26**) did not yield in significantly higher expression levels. The X-unit and the CM-150 program were used as the standard for transfection of nCMs, resulting in approximately 11% transfected cardiomyocytes (**Fig. 25**).

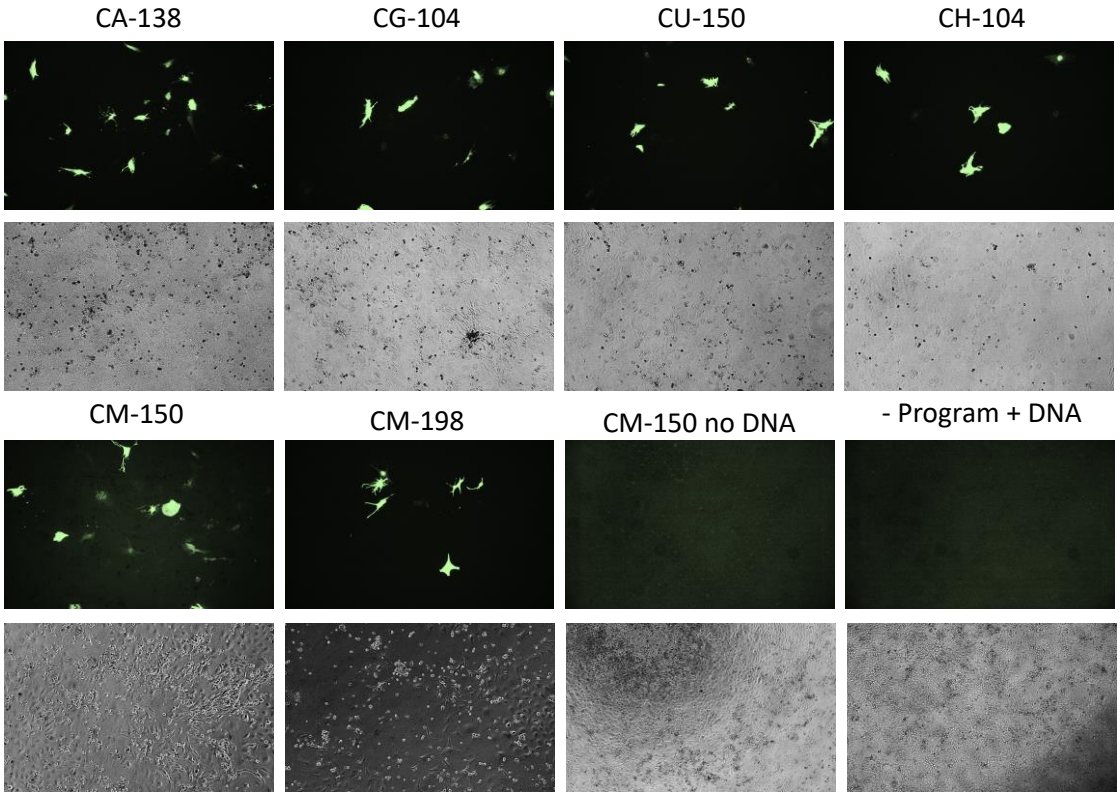

Fig. 24: nCMs nucleofection with different 4D-Nucleofector™ System (Lonza) X-Unit programs *P1-P3 nCMs were prepared, and 1.000.000 cells were dissolved in 100 µL of P3 buffer and placed in a cuvette with 10 µg of TpPAC-EYFP DNA and nucleofection was tested using various programs provided by LONZA. Images taken with a Nikon Eclipse Ti2 fluorescence microscope using a 10x objective and brightfield and YFP (488 nm) filters in green.*

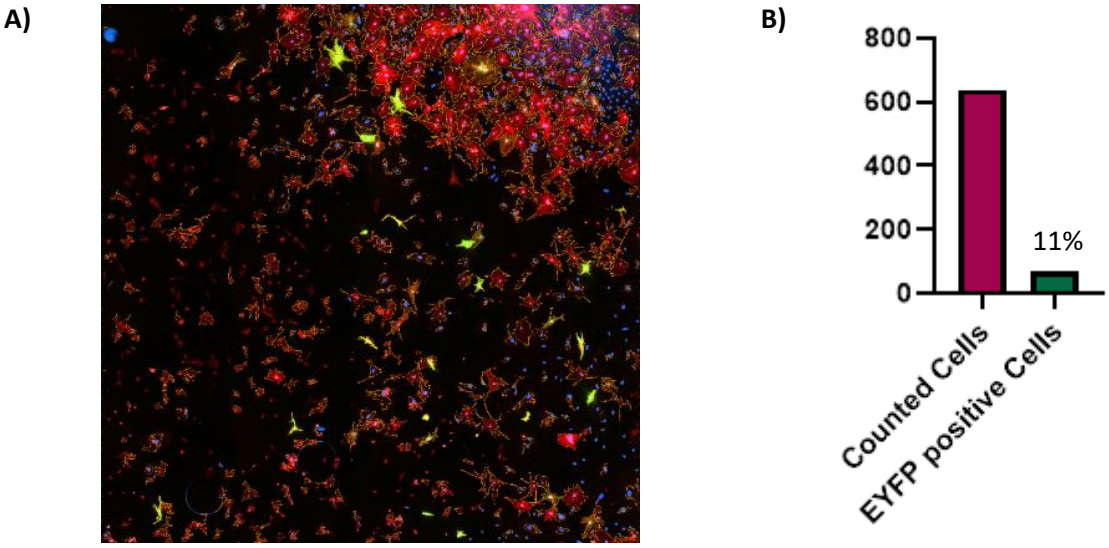

Fig. 25: nCMs nucleofection with 4D-Nucleofector™ System (Lonza) X-Unit CM-150 programs *1.000.000 P1-P3 nCMs were dissolved in 100 µL P3 buffer and placed in a cuvette with 10 µg DNA (TpPAC-EYFP) and nucleofected with the CM-150 program.* ***A)*** *Five days later, the cells were fixed and stained with α-actinin (red) and Hoechst (blue), and the EYFP (green) signal was used to detect transfected cells.* ***B)*** *The number of transfected nCMs (11%) was determined using a custom-made General Analysis 3 (GA3) system from NIS-Elements. A Nikon Eclipse Ti2 fluorescence microscope was used with Hoechst (DAPI: 405 nm), α-actinin (Cy5: 625 nm), and EYFP (488 nm) detection.*

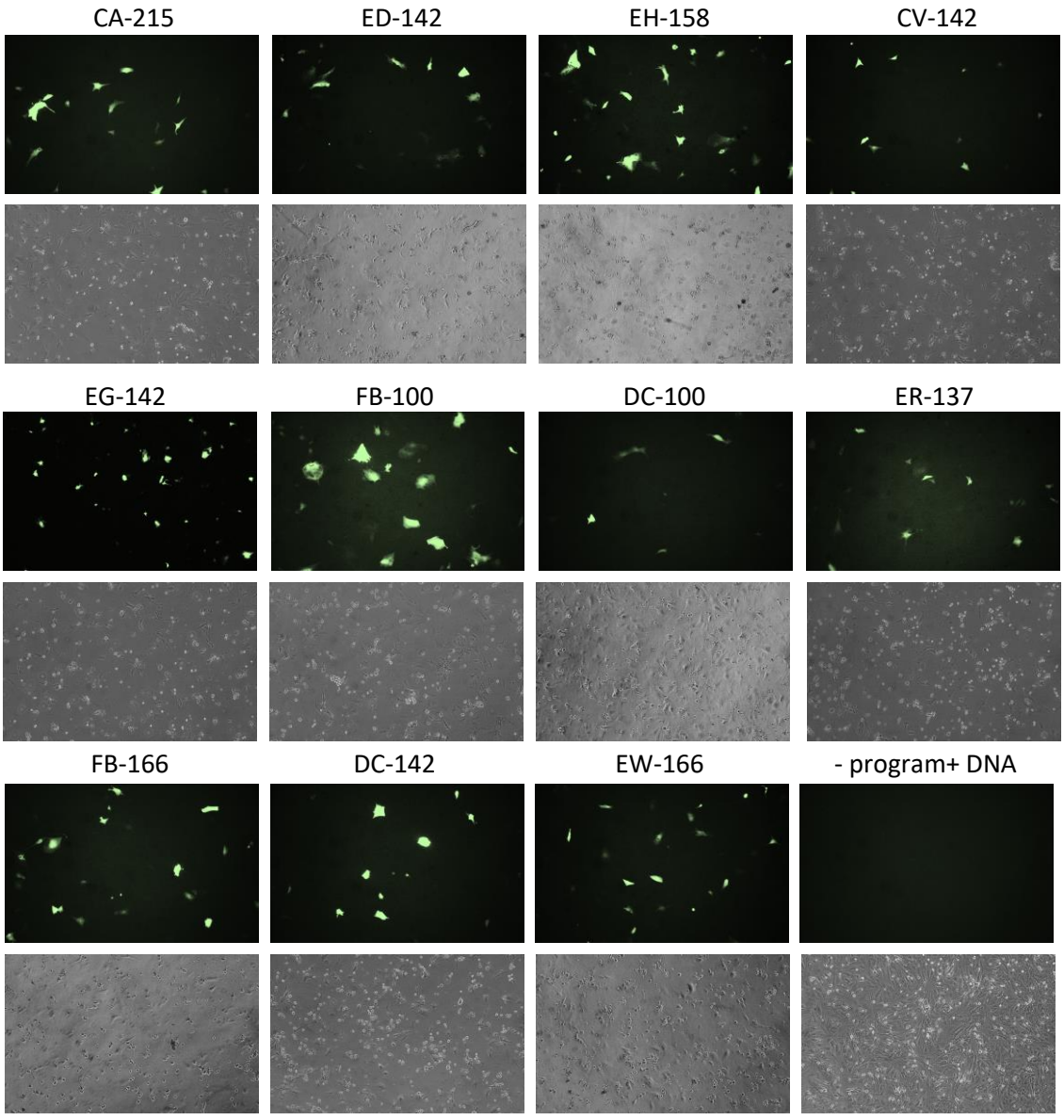

Fig. 26: nCMs nucleofection with different 4D-Nucleofector™ System (Lonza) Y-Unit programs *P1-P3 nCMs were prepared, and 1.000.000 cells were dissolved in 100 µL of P3 buffer and placed in a cuvette with 10 µg of DNA (TpPAC-EYFP) and nucleofection was tested using various programs provided by LONZA. Images taken with a Nikon Eclipse Ti2 fluorescence microscope using a 10x objective and brightfield and YFP (488 nm) filters in green.*

To determine whether the nanobody nb.F3 and the FKBP12.6 protein result in the intended local targeting of LTCC and RyR2, immunohistological stainings were conducted and observed via confocal microscopy (**Fig. 27**). The subcellular distribution of the fusion proteins was analyzed by their EYFP signal within the cardiac-specific marker α-actinin-positive cardiomyocytes.

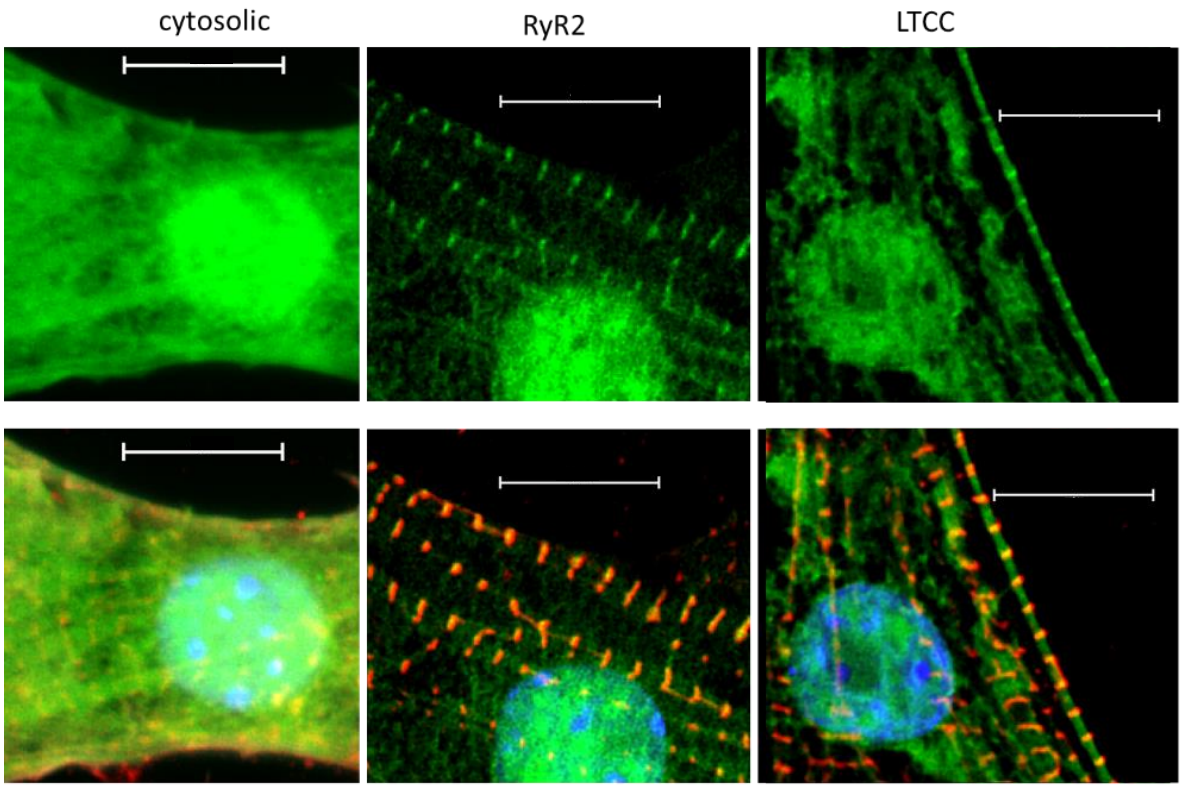

Hoechst, EYFP, α-actinin, 100x

Fig. 27: Localization of PAC fusion constructs in neonatal cardiomyocytes
P1-3 nCMs were transfected by nucleofection (Lonza) with TpPAC-EYFP, TpPAC-mCitrine-FKBP12.6, and nb.F3-TpPAC-EYFP. Cells were stained 5 days later with the cardiac-specific marker α-actinin (red) and the nuclear stain Hoechst (blue). Images were captured using a Nikon Eclipse Ti2 confocal microscope with a 60x oil objective and post-processed by deconvolution (Nikon NIS Elements). The following filters were used: Hoechst (DAPI: 405 nm), α-actinin (Cy5: 625 nm), and EYFP (488 nm). Scale bar: 10 µm.

Cells with non-targeted PACs had a homogeneous EYFP distribution with no evidence of aggregation, indicating cytosolic expression. In contrast, FKBP12.6-containing fusion proteins were localized around the nuclear envelope and Z-disc, indicating localization in the SR by RyR2 targeting. Cells with nb.F3 for LTCC targeting also localized around the nuclear envelope and exhibited membrane targeting (**Fig. 27**). Generally, it was possible to distinguish between the differently localized constructs by observing EYFP expression with a 20x objective. In addition, colocalization was investigated using a RyR2 and an LTCC antibody, and the localized TpPACs, which are shown in **Fig. 28**. The TpPAC-mCitrine-FKBP12.6 colocalized clearly with the RyR2 antibody (**Fig. 28 A**). The nb.F3-TpPAC-EYFP showed a clear membrane signal, but the LTCC antibody was not clearly membrane-bound (**Fig. 28 B**).

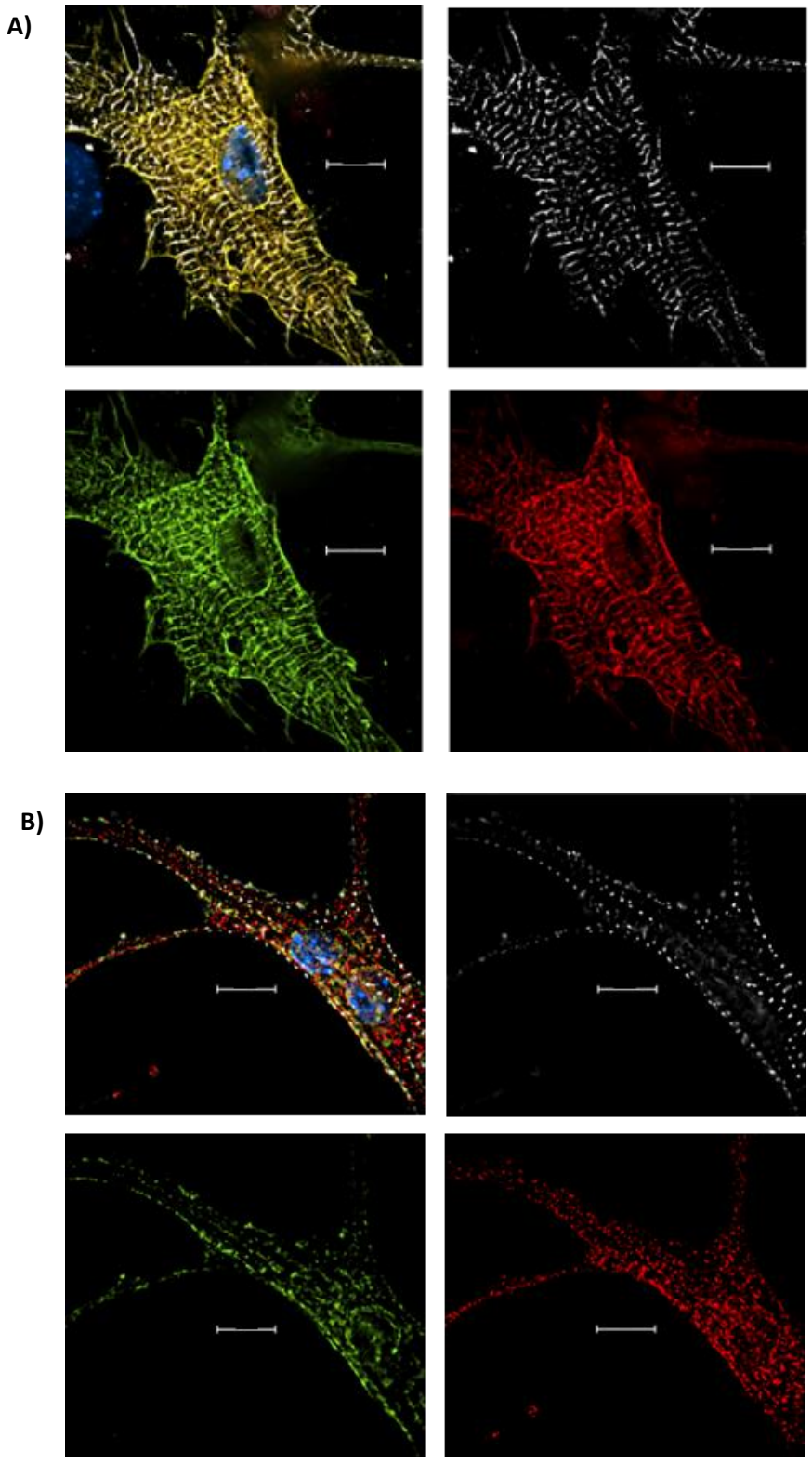

Fig. 28: Colocalization of targeted PAC fusion constructs in nCMs with RyR2 and LTCC antibody *P3 nCMs were transfected with* ***A)*** *TpPAC-mCitrine-FKBP12.6 and* ***B)*** *nb.F3-TpPAC-EYFP with the construct marker EYFP (green), by nucleofection and stained 6 days later with the cardiac-specific marker α-actinin (red) and the nuclear staining Hoechst (blue).* ***A)*** *was co-stained with RyR2 and* ***B)*** *with LTCC antibody (white). Images were captured using a Nikon Eclipse Ti2 confocal microscope with a 60x oil objective and post-processed by deconvolution (Nikon NIS Elements). The following filters were used: Hoechst (DAPI: 405 nm), α-actinin (Cy3: 505 nm), EYFP (488 nm), RyR2, and LTCC (Cy5: 625 nm). Scale bar: 10 µm.*

4.4 Changes in beating frequency upon localized cAMP generation

With the establishment of a standard nCM transfection method and validation of construct function (**Fig. 22, 23**) and location (**Fig. 27, 28**), functional analysis of localized cAMP generation on inotropy and chronotropic could be pursued in nCMs, which show highly developed striated α-actinin in the stainings (**Fig. 27, 28**).

The effect of light-dependent cAMP production on beating frequency was analyzed using infrared video microscopy, as previously described for EBs, to avoid activation of TpPAC. The transfected nCMs were screened for EYFP-positive cells and stable baseline beating frequency. Subsequent brief illumination with blue light (465 nm) accelerated the beating frequency in a dose-dependent manner, similar in nCM with all TpPAC constructs (**Fig. 29**), but with different kinetics. The negative control with WT nCMs, without TpPAC, showed no changes in beating frequency in response to light (**Fig. 29 B**). Differences in the kinetics of the beating frequency induced by global or local TpPAC were observed in the formation of a prolonged increase in frequency, manifesting as a plateau (**Fig. 30 F**), or in the duration of the light effect (**Fig. 30 E**). A comparison of the maximum beating frequency after illumination showed no differences between the different locations of TpPAC (**Fig. 30 G, J**).

The production of cAMP globally in the cytosol or locally at RyR2 by short light pulses of 250 ms results in a long-lasting constant plateau (> 50 s) of the increased beating rate effect, indicating the generation of a "large" cAMP pool (**Fig. 30 D, F, I, L**). In contrast, the effect of cAMP generation locally at the LTCC declined after its peak without a clear plateau and was subsequently longer-lasting (**Fig. 30 E**). These differences suggest an altered cAMP degradation machinery, presumably due to differences in PDE isoform expression or PDE activation mechanisms in LTCC, RyR2, and cytosolic microdomains, which should be investigated in the future using specific PDE blockers and activators. A pre-test with the PDE4 blocker rolipram was performed on nCMs expressing TpPAC-EYFP, and the effect of light was assessed before and after PDE4 inhibition (**Fig. 31**). Therefore, 10 µM rolipram was added. An increase in the height and duration of the increased beating frequency was observed (**Fig. 31**), as expected in response to a PDE4 inhibitor, which decreases cAMP degradation.

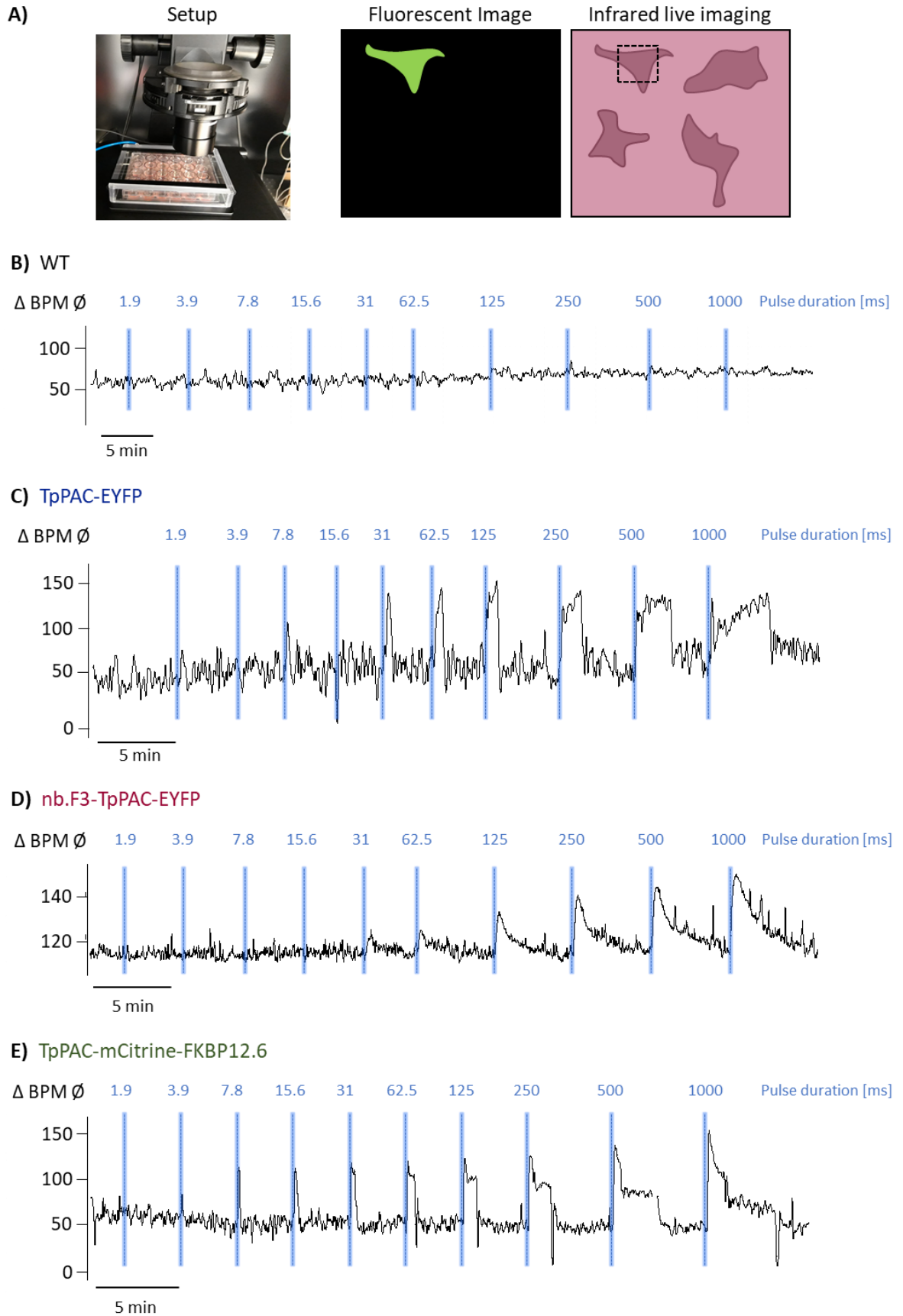

Fig. 29: Effect of global and local light-dependent cAMP production on beating frequency
A) *The effect of global and localized microdomain cAMP generation on* ***nCMs'*** *beating rate was analyzed by observing changes in spontaneous beating frequency using video microscopy.* ***B-E)*** *Blue*

light (465 nm) flashes were applied (102 µW/mm²) with increasing pulse durations, and the beating frequency was recorded online using custom software and displayed as beats per minute (BPM). Nikon Eclipse Ti2 fluorescence microscope with red light imaging using a Fura/Fluo filter (380 nm), blue light optogenetic stimulation with a blue light (465 nm) filter, and a 1% ND2.0 filter and EYFP filter (488 nm) for screening TpPAC-positive nCMs. ***B)*** *is an example of WT control nCMs, that do not show any light effect,* ***C)*** *is an example of an nCM transfected with TPPAC-EYFP,* ***D)*** *is an example of an nCM transfected with nb.F3-TpPAC-EYFP and* ***E)*** *is an example of an nCM transfected with TpPAC-mCitrine-FKBP12.6.*

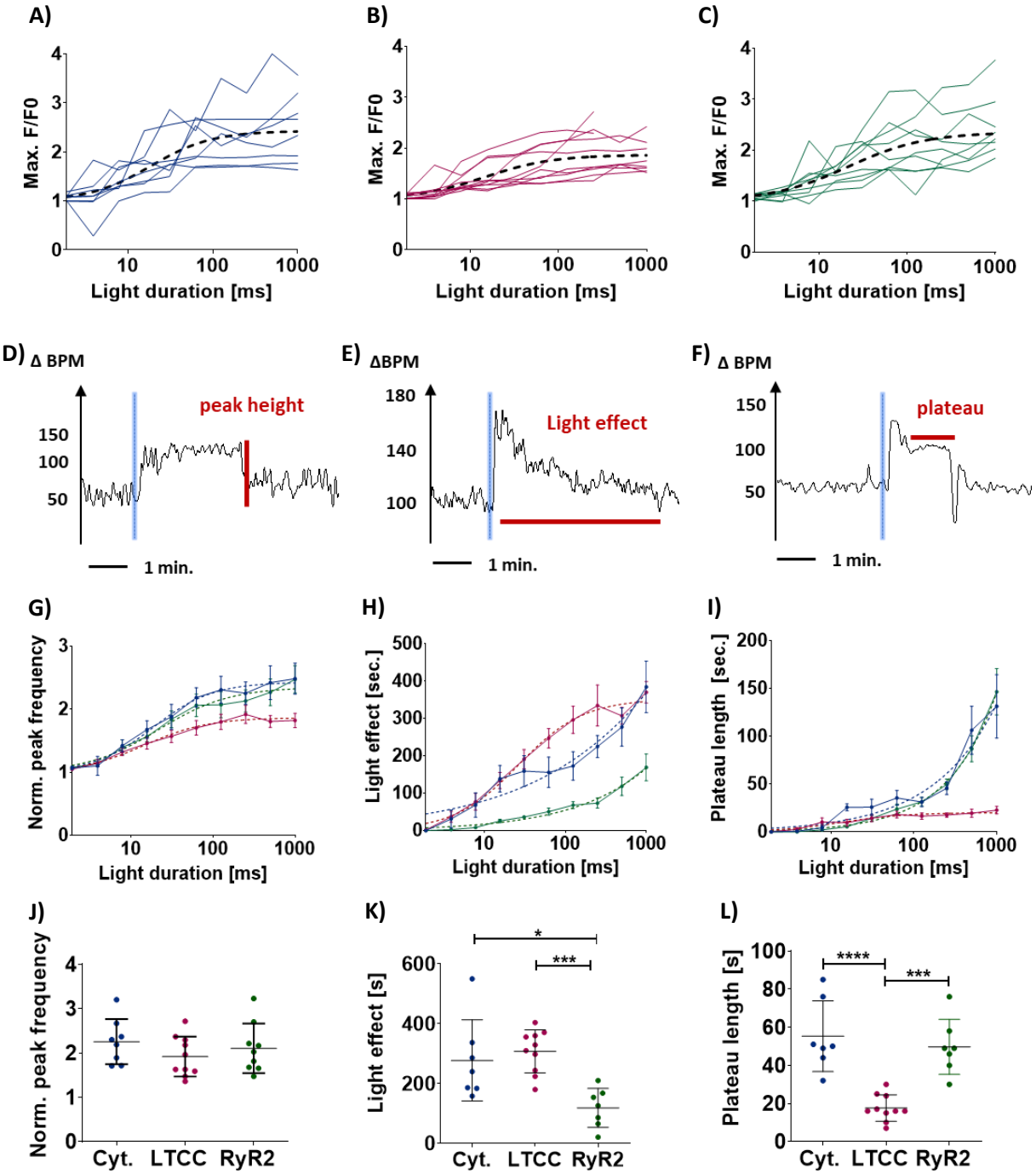

Fig. 30: Effect of global and localized cAMP generation on beating rate of nCMs

The effect of global and local microdomain cAMP generation on the beating rate of nCMs was analyzed by observing changes in spontaneous beating frequency using video microscopy. Blue light (465 nm)

flashes were applied at a fixed intensity (102 µW/mm²) with increasing pulse durations, and the beating frequency was recorded online using custom software and displayed as beats per minute (BPM). ***A-C)*** *peak frequency with increasing light duration* ***A)*** *TpPAC-EYFP (blue),* ***B)*** *nb.F3-TpPAC-EYFP (red),* ***C)*** *TpPAC-mCitrine-FKBP12.6 (green). Representative frequency responses at 250 ms pulse duration of nCM* ***D)*** *expressing TpPAC-EYFP,* ***E)*** *nb.F3-TpPAC-EYFP and* ***F)*** *TpPAC-mCitrine-FKBP12.6; note the differences in the kinetic profiles. Analysis of* ***G)*** *and* ***J)*** *peak frequency,* ***H)*** *and* ***K****) maximum duration of the cAMP effect, and* ***I)*** *and* ***J)*** *duration of a plateau with increased constant frequency. Analysis of the peak frequency after illumination, normalized to the baseline frequency at the beginning of the experiments, as a function of pulse duration* ***G)****, and statistical analysis of the response to 250 ms pulses* ***J)****, which showed no difference between constructs. The duration of cAMP effect as a function of pulse duration* ***H)*** *showed a longer effect of LTCC-targeted nb.F3-TpPAC-EYFP than RyR2-targeted TpPAC-mCitrine-FKBP12.6, which was also statistically significant at 250 ms pulse durations* ***K)****. Duration of a plateau with increased constant frequency as a function of pulse duration* ***I)*** *and statistical analysis at 250 ms pulse duration* ***J)*** *showing a significantly shorter plateau of LTCC-targeted nb.F3-TpPAC-EYFP compared to RyR2-targeted TpPAC-mCitrine-FKBP12.6 or non-targeted TpPAC-EYFP. Statistics by ANOVA with Tukey's multiple comparison test: TpPAC-EYFP, n = 8; nb.F3-TpPAC-EYFP, n = 10; TpPAC-mCitrine-FKBP12.6, n = 9. ns = not significant; *: p < 0.05.*

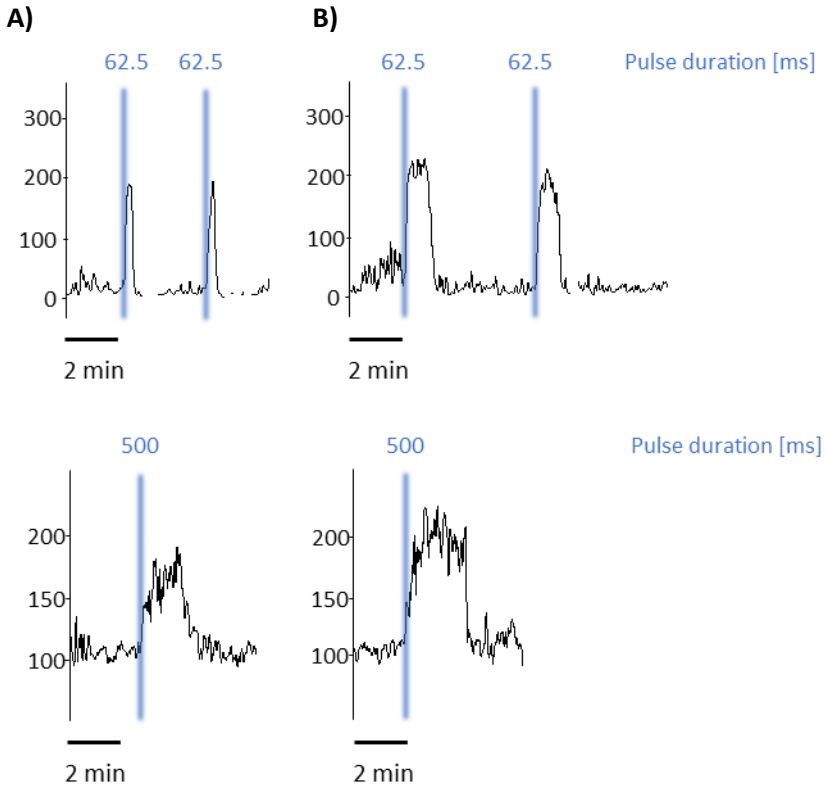

Fig. 31: Effect of rolipram on light-dependent cAMP production on beating frequency
The effect of rolipram on light-dependent cAMP generation on the beating rate of nCMs transfected with TpPAC-EYFP was analyzed by observing changes in spontaneous beating frequency using video microscopy. Blue light (465 nm) flashes were applied at 102 µW/mm², and the beat frequency was recorded online using custom software and displayed as beats per minute (BPM) before and after the addition of 10 µM rolipram. Representative examples: ***A)*** *Before rolipram, 62.5 ms light and 500 ms light.* ***B)*** *5 min after 10 µM rolipram with 62.5 ms and 500 ms light.*

4.5 Changes in Ca^{2+} transients upon localized cAMP generation

To gain further insight into the cAMP-dependent regulation of intracellular Ca^{2+} handling, Ca^{2+} imaging experiments were established using TpPAC-transfected nCMs (**Fig. 32**). Changes in Ca^{2+} transients provide insight into the efficiency of ECC and CICR as they reflect the release and reuptake of Ca^{2+} during each heartbeat. For this purpose, large EYFP-stitched images were generated to identify and locate transfected cells, which were subsequently imaged with the Ca^{2+} Cal630 dye (excitation: 600-620 nm) to avoid interference with optogenetic activation (465 nm). To ensure stable SR Ca^{2+} loading, a homemade electrical pacing device was constructed for 24-well plates. An Arduino microcontroller was programmed to synchronize the pacing of the cells, the imaging camera, and the optogenetic stimulation (see **S. 1** for Arduino code).

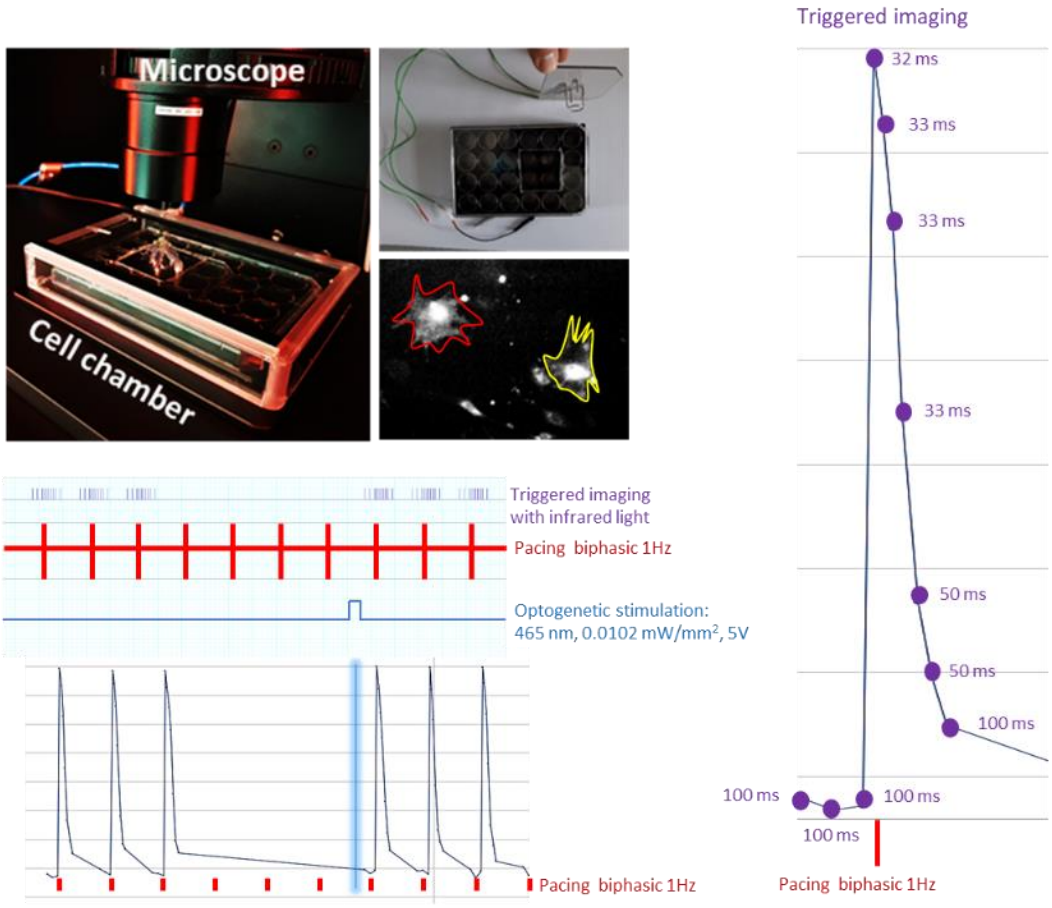

Fig. 32: Triggered Ca^{2+} transient imaging system
The effect of localized cAMP generation in microdomains was analyzed in nCMs stained with Cal630 (excitation: 600-620 nm) to record Ca^{2+} transients without PAC activation. Live microscopic imaging was performed in a cell chamber with a gas and heat control system (ibidi). An Arduino-controlled system for triggered pacing, imaging, and optogenetic stimulation was used to minimize bleaching from imaging. A Nikon Eclipse Ti2 fluorescence microscope with red light imaging using a Fura/Fluo filter (380 nm), blue light optogenetic stimulation with a blue light (465 nm) filter, and a 1% ND2.0 filter and EYFP filter (488 nm) for screening TpPAC-positive nCMs.

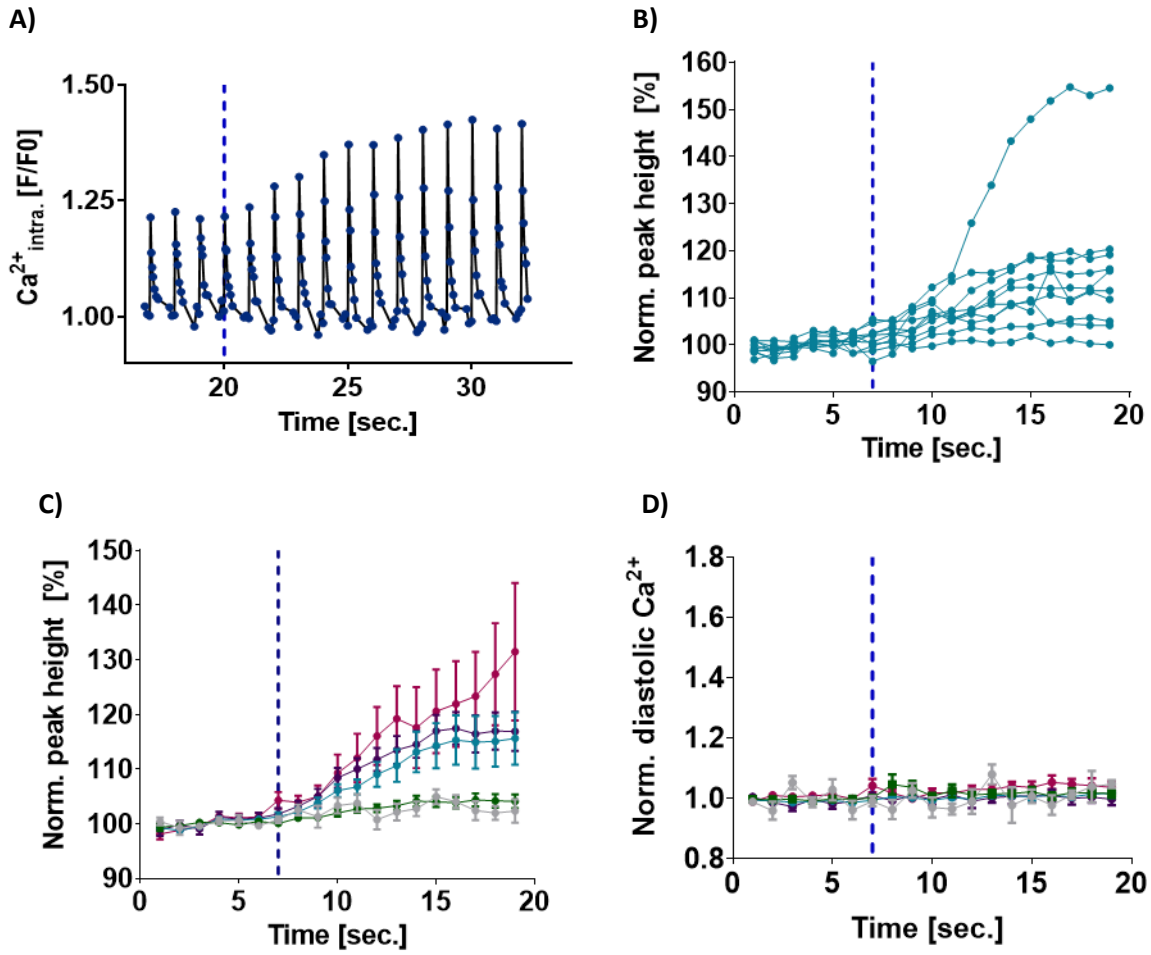

Fig. 33: The effect of global cAMP generation on Ca^{2+} transients

Neonatal cardiomyocytes transfected with TpPAC-EYFP were stained with Cal630 (excitation 600-620 nm) to record Ca^{2+} transients without PAC activation. ***C)*** *Blue light flashes (blue line) were applied for 1 s with increasing intensities (0.5- 23.4 µW/mm²),* ***A)*** *Representative example of Ca^{2+} transients from TpPAC-EYFP stimulated at 10 µW/mm².* ***B)*** *Single-cell data of Ca^{2+} transient peak height from TpPAC-EYFP stimulated at 10 µW/mm².* ***C)*** *Analysis of Ca^{2+} transient height,* ***D)*** *and diastolic Ca^{2+} levels. Light intensities* ***C)*** *and* ***D)****: 0.5 µW/ mm²x s, 1.5 µW/mm²x s, 4.1 µW/mm²x s, 10.0 µW/mm²x s, 23.4 µW/mm²x s.* *n= 10.*

All nCMs expressing the TpPAC constructs exhibited an increase in Ca^{2+} transients after illumination in a dose-dependent manner, with respect to light intensity, with no significant differences observed between the different constructs regarding peak height (**Fig. 36 A, B**). Interestingly, nCMs expressing TpPAC-mCitrine-FKBP12.6 (**Fig. 35 D**), but not those with the cytosolic or LTCC-targeting constructs (**Fig. 33 D, 34 D**), transiently elevated diastolic Ca^{2+} levels after illumination. Indicating a diastolic Ca^{2+} leak from the SR through the RyR2 upon cAMP generation and pointing towards cAMP pools that do

not affect the RyR2 microdomain from the LTCC and cytosol, and *vice versa*. This difference was also statistically significant, as indicated by ANOVA with Tukey's multiple comparison test (**Fig. 36 C, D**).

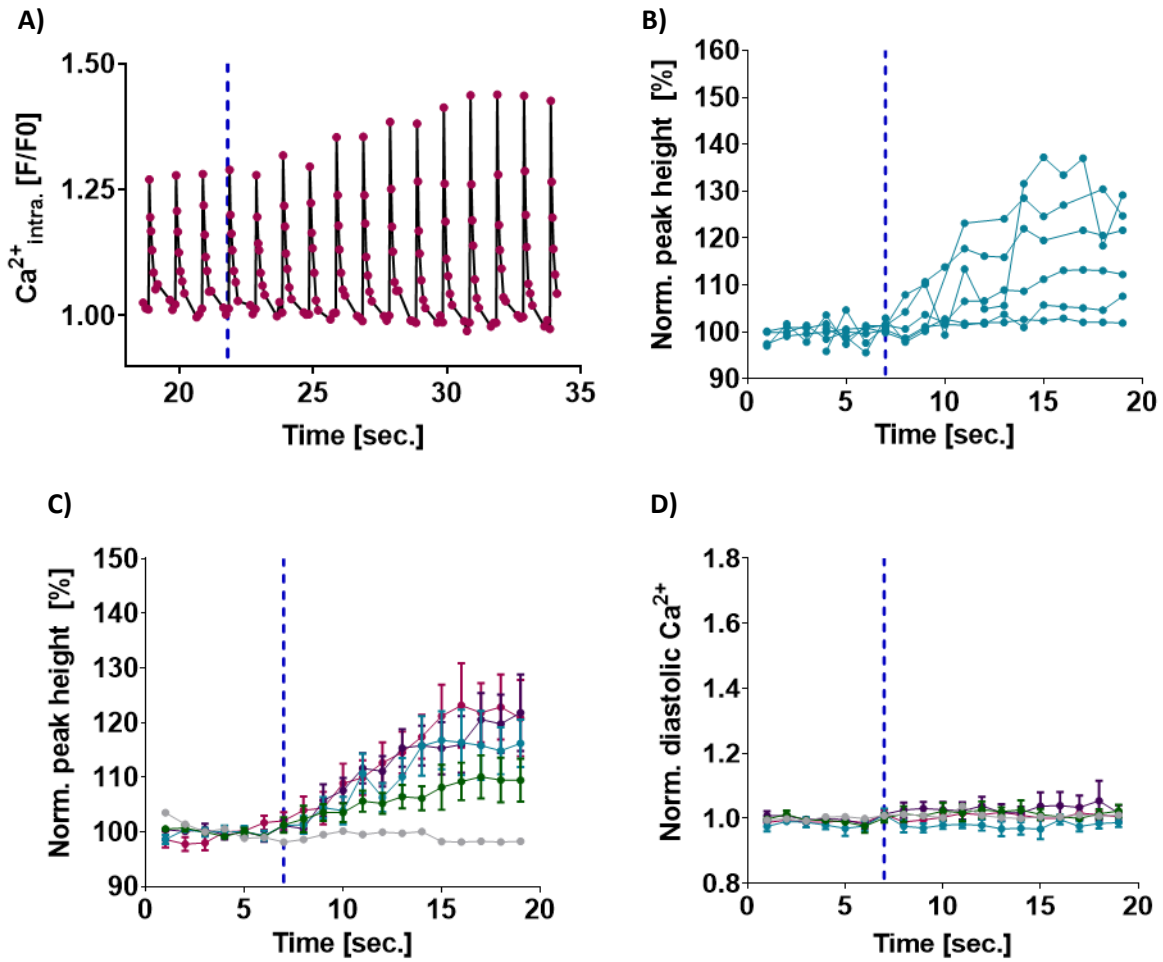

Fig. 34: The effect of local cAMP generation at the LTCC on Ca^{2+} transients
Neonatal cardiomyocytes transfected with nb.F3-TpPAC-EYFP were stained with Cal630 (excitation 600-620 nm) to record Ca^{2+} transients without PAC activation. ***C)*** *Blue light flashes (blue line) were applied for 1 s with increasing intensities (0.5- 23.4 µW/mm²).* ***A)*** *Representative example of Ca^{2+} transients from nb.F3-TpPAC-EYFP stimulated at 10 µW/mm².* ***B)*** *Single-cell data of Ca^{2+} transient peak height from nb.F3-TpPAC-EYFP stimulated at 10 µW/mm².* ***C)*** *Analysis of Ca^{2+} transient height,* ***D)*** *and diastolic Ca^{2+} levels. Light intensities* ***C)*** *and* ***D)****: 0.5 µW/ mm²x s, **1.5 µW/mm²x s**, **4.1 µW/mm²x s**, **10.0 µW/mm²x s**, **23.4 µW/mm²x s.** n=6.*

A slightly lower and earlier transient peak height was also observed for TpPAC-mCitrine-FKBP12.6 compared to TpPAC-EYFP and nb.F3-TpPAC-EYFP. Still, this difference was not statistically significant and may require a larger sample size (n-value) for clarification. But we can summarize that the RyR2 is more prone to dysregulation (diastolic Ca^{2+} leak, plateau of elevated beating frequency) upon cAMP production than the LTCC. The fact that we observe functional differences in the different locations of cAMP production points suggests that these microdomains are differently regulated and seperated.

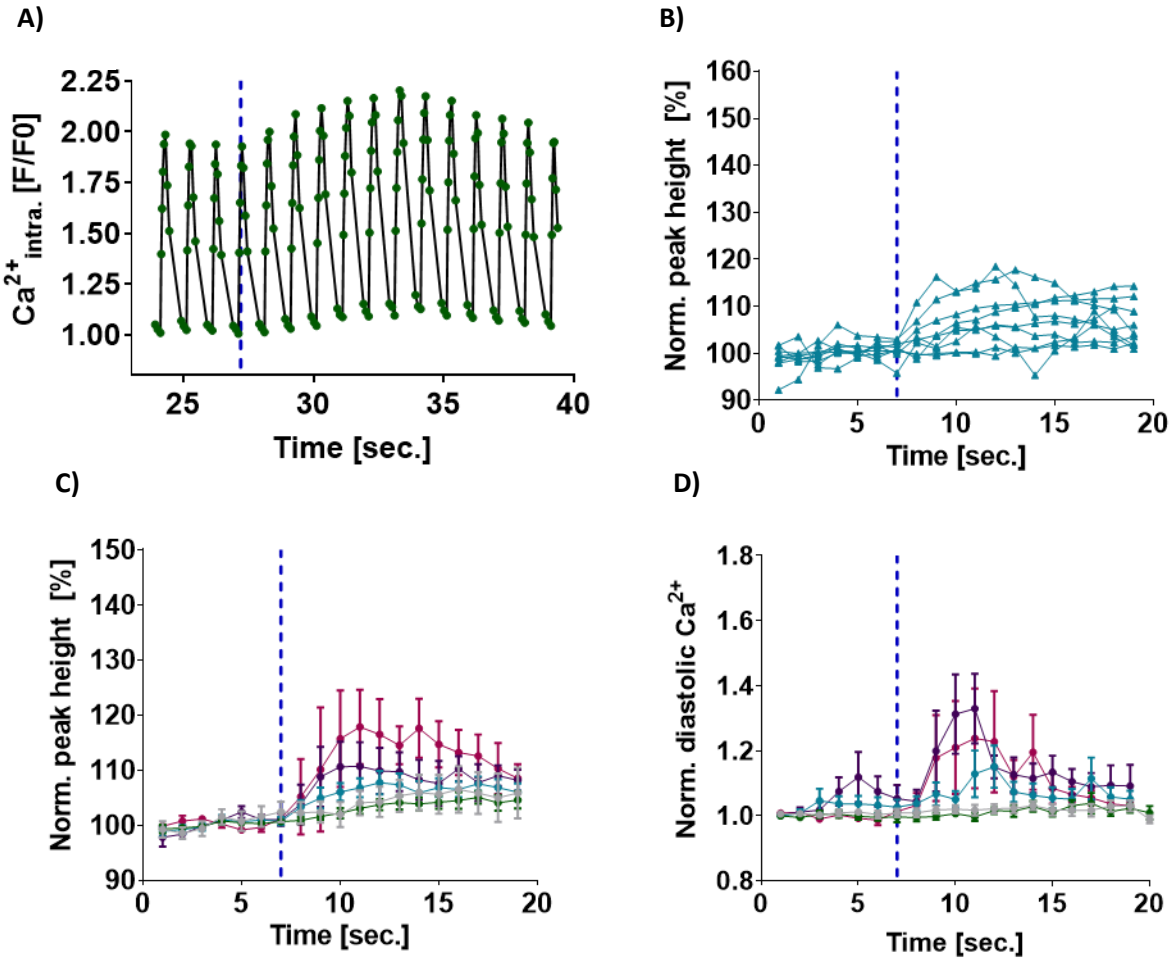

Fig. 35: The effect of local cAMP generation at the RyR2 on Ca^{2+} transients
Neonatal cardiomyocytes transfected with TpPAC-mCitrine-FKBP12.6 were stained with Cal630 (excitation 600-620 nm) to record Ca^{2+} transients without PAC activation. ***C)*** *Blue light flashes (blue line) were applied for 1 s with increasing intensities (0.5- 23.4 µW/mm²),* ***A)*** *Representative example of Ca^{2+} transients from TpPAC-mCitrine-FKBP12.6 stimulated at 10 µW/mm². **B)** Single-cell data of Ca^{2+} transient peak height from TpPAC-mCitrine-FKBP12.6 stimulated at 10 µW/mm². **C)** Analysis of Ca^{2+} transient height, **D)** and diastolic Ca^{2+} levels. Light intensities **C)** and **D)**: 0.5 µW/ mm²x s, **1.5 µW/mm²x s**, **4.1 µW/mm²x s**, **10.0 µW/mm²x s**, **23.4 µW/mm²x s.** n=8.*

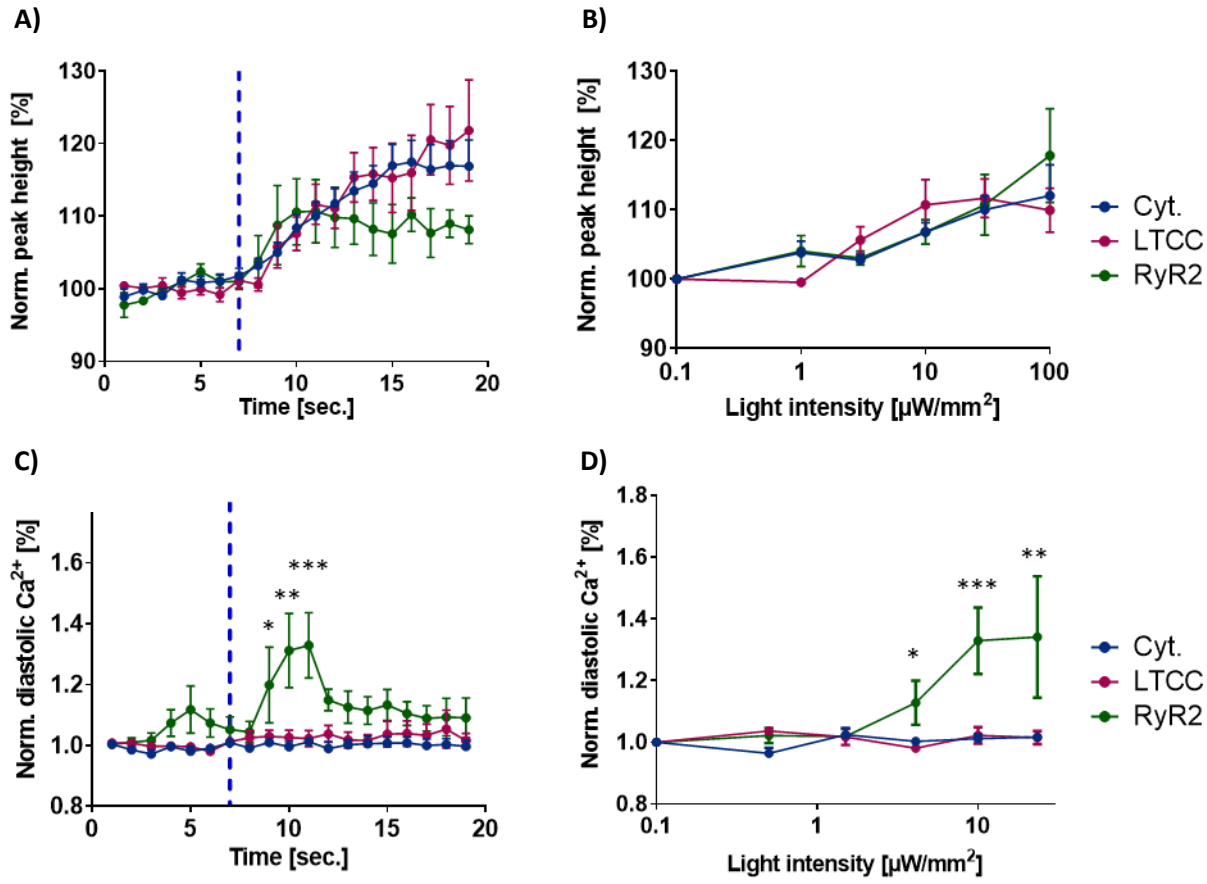

Fig. 36: Comparing the effect of global and local cAMP generation on Ca^{2+} transients
*Neonatal cardiomyocytes transfected with TpPAC-EYFP (**blue**), nb.F3-TpPAC-EYFP (**red**), and TpPAC-mCitrine-FKBP12.6 (**green**) were stained with Cal630 (excitation 600-620 nm) to record Ca^{2+} transients without PAC activation. **A)** Mean peak height of Ca^{2+} transients with SD normalized to baseline from TpPAC-EYFP, nb.F3-TpPAC-EYFP, and TpPAC-mCitrine-FKBP12.6 stimulated with 10 µW/mm². **B)** Dose-response curve of the peak height of TpPAC-EYFP, nb.F3-TpPAC-EYFP, and TpPAC-mCitrine-FKBP12.6 with increasing light intensity. Data normalized to baseline mean with SD. **C)** Analysis of Ca^{2+} transient diastolic Ca^{2+} levels from TpPAC-EYFP, nb.F3-TpPAC-EYFP, and TpPAC-mCitrine-FKBP12.6 stimulated at 10 µW/mm². Data normalized to baseline mean with SD. **D)** Dose-response curve of diastolic Ca^{2+} levels 5 s after illumination with increasing light intensities of TpPAC-EYFP, nb.F3-TpPAC-EYFP, and TpPAC-mCitrine-FKBP12.6. Data normalized to baseline mean with SD. Statistics by ANOVA with Tukey's multiple comparison test, n = 6-13; ***: p < 0.001, **: p < 0.01, *: p < 0.05.*

4.6 Changes in phosphorylation upon localized cAMP generation

After analyzing the changes in beating rate and Ca^{2+} transients following localized cAMP production, we observed that cAMP activation around the RyR2 is more prone to dysfunction. This is why the effect of global and local cAMP generation on alterations in phosphorylation was investigated next.

Therefore, the PKA phosphorylation site-specific antibody (RRXS*/T* from Cell Signaling)[83] (**Fig. 37 A**) was used in two different approaches. First, Western blot analysis was performed on nCMs transfected with TpPACs that were illuminated compared to nCMs kept in dark as control. Western blot analysis was already well established with the PKA phosphorylation site-specific antibody (RRXS*/T*). An increase in RRXS*/T* signal intensity was observed in the illuminated samples compared to the dark control (**Fig. 38**). However, in the Western blot experiment, all cells from a well were analyzed as one sample, which included non-transfected and non-cardiomyocyte cells, such as fibroblasts. Therefore, a second approach enabled the specific analysis of cardiomyocytes, separating transfected and non-transfected cells through immunohistological stainings. This approach captured images of single nCMs after transfection using the RRXS*/T* antibody to measure PKA phosphorylation and the α-actinin antibody for cardiomyocyte recognition. An illumination setup for a 24-well plate (**Fig. 37 B**) was used for optogenetic stimulation, controlled by an Arduino program (see **S. 2** for Arduino code). After stimulation, the cells were fixed and stained, and images were captured. The images were analyzed using a custom-made program in the general analysis 3 (GA3) tool of NIS-Elements (**Fig. 39 A, B**), which detects cells by nuclear staining with DAPI and cardiomyocytes by staining for the cardiomyocyte marker α-actinin. Illumination resulted in an increase in RRXS*/T* signals in EYFP-positive (TpPAC-positive) nCM, but not in EYFP-negative (WT) nCM (**Fig. 40**).

A) RRXS*/T* = PKA phosphorylation-specific antibody

B)

Fig. 37: Experimental setup to analyze the effect of cAMP generation on phosphorylation A) *Amino acid sequence of PKA phosphorylation site-specific antibody: RRXS*/T* (Cell Signaling): https://media.cellsignal.com/product/image/5565_fig02___20210423082539.jpg.* ***B)*** *A 24-well plate illumination system controlled by an Arduino program (**S. 2**) for adjusting light intensity, duration, and plate position.*

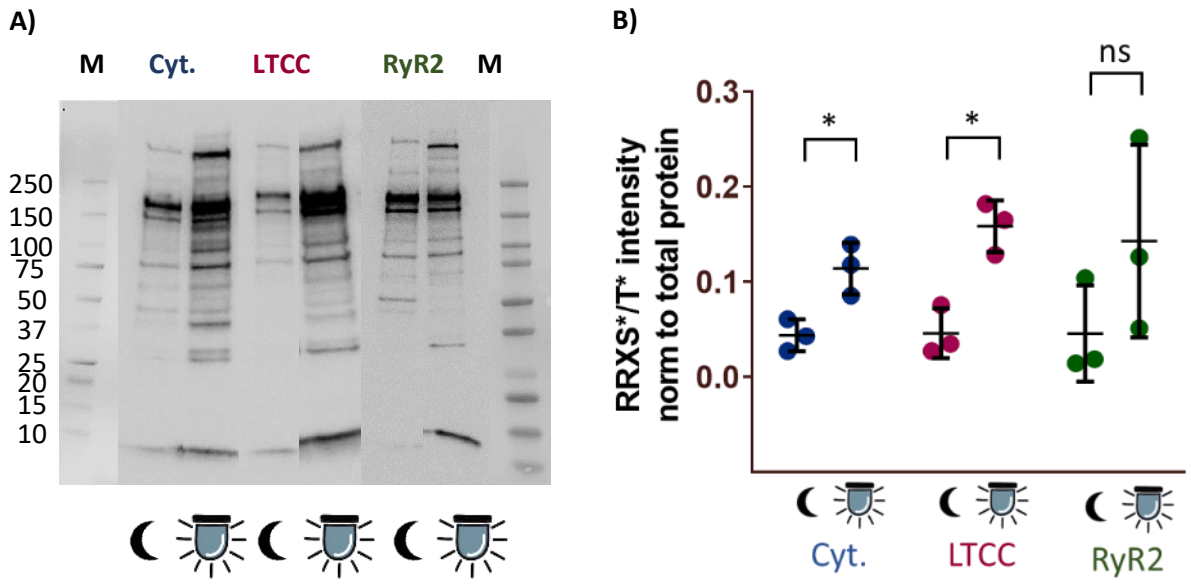

Fig. 38: Western blot analysis of TpPAC effect on phosphorylation in nCMs
A) *TpPAC-EYFP (**Cyt.**) nb.F3-TpPAC-EYFP (**LTCC**) and TpPAC-mCitrine-FKBP12.6 (**RyR2**) were transfected into nCMs and analyzed by Western blots using a PKA phosphorylation-specific antibody (RRXS*/T*). A Bio-Rad protein marker (**M**) was used as a size standard. Cells were kept either dark or illuminated 12 times with 1 s of blue light every 10 s at 100 µW/mm². Phosphorylation was fixed with titin lysis buffer and a phosStop cocktail 30 s after the last illumination. Cells were harvested, collected, and frozen at -80°C. A total of 10 µg protein was used in a volume of 15 µL. Western blot was performed using the Mini-PROTEAN Tetra Cell System for protein separation and the Trans-Blot Turbo Transfer System for transfer. RRXS*/T* antibody staining was performed at a concentration of 1:1000. Gel documentation was performed using the Bio-Rad ChemiDoc™ MP Imaging System.* ***B)*** *Statistical analysis of PKA phosphorylation intensities in nCMs expressing TpPAC-EYFP (**Cyt.**) nb.F3-TpPAC-EYFP (**LTCC**) and TpPAC-mCitrine-FKBP12.6 (**RyR2**), comparing illuminated (light) or unilluminated (dark) by ANOVA with Tukey's multiple comparison test, *: p<0.05, n=3.*

A) Custom-made analysis with Nikon GA3 analysis program

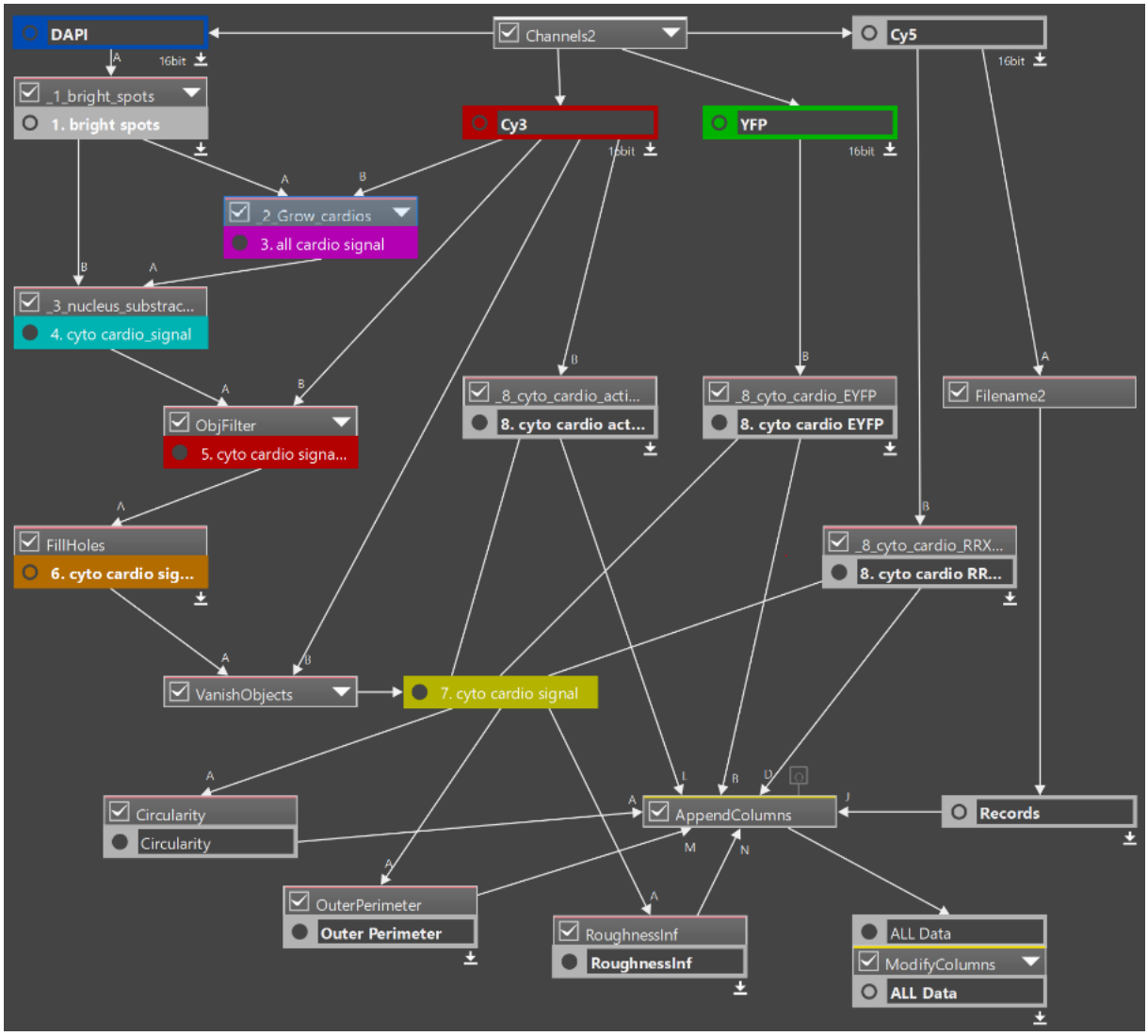

B)

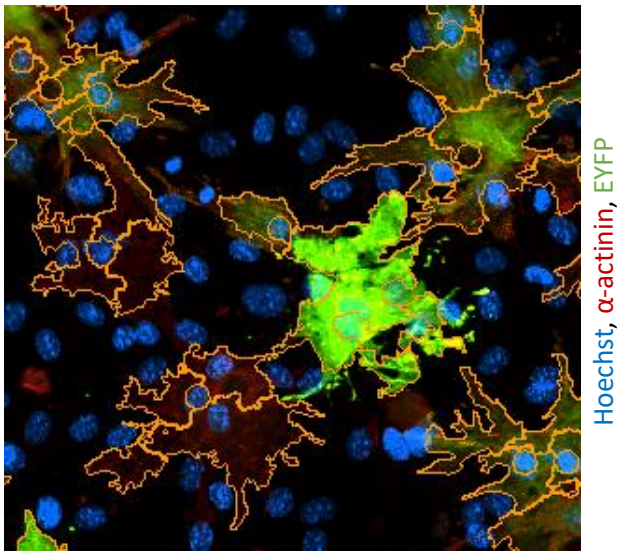

Fig. 39: GA3 to analyze the effect of cAMP generation on phosphorylation

A) *Showing the General Analysis 3 (GA3) command. The analysis is based on detecting nuclei (Hoechst) and subsequently identifying the cardiomyocyte marker α-actinin for recognizing the cell borders of cardiomyocytes. The intensity of EYFP and RRXS*/T* can eventually be measured in cardiomyocytes.* ***B)*** *shows an example of the cell recognition system of GA3.*

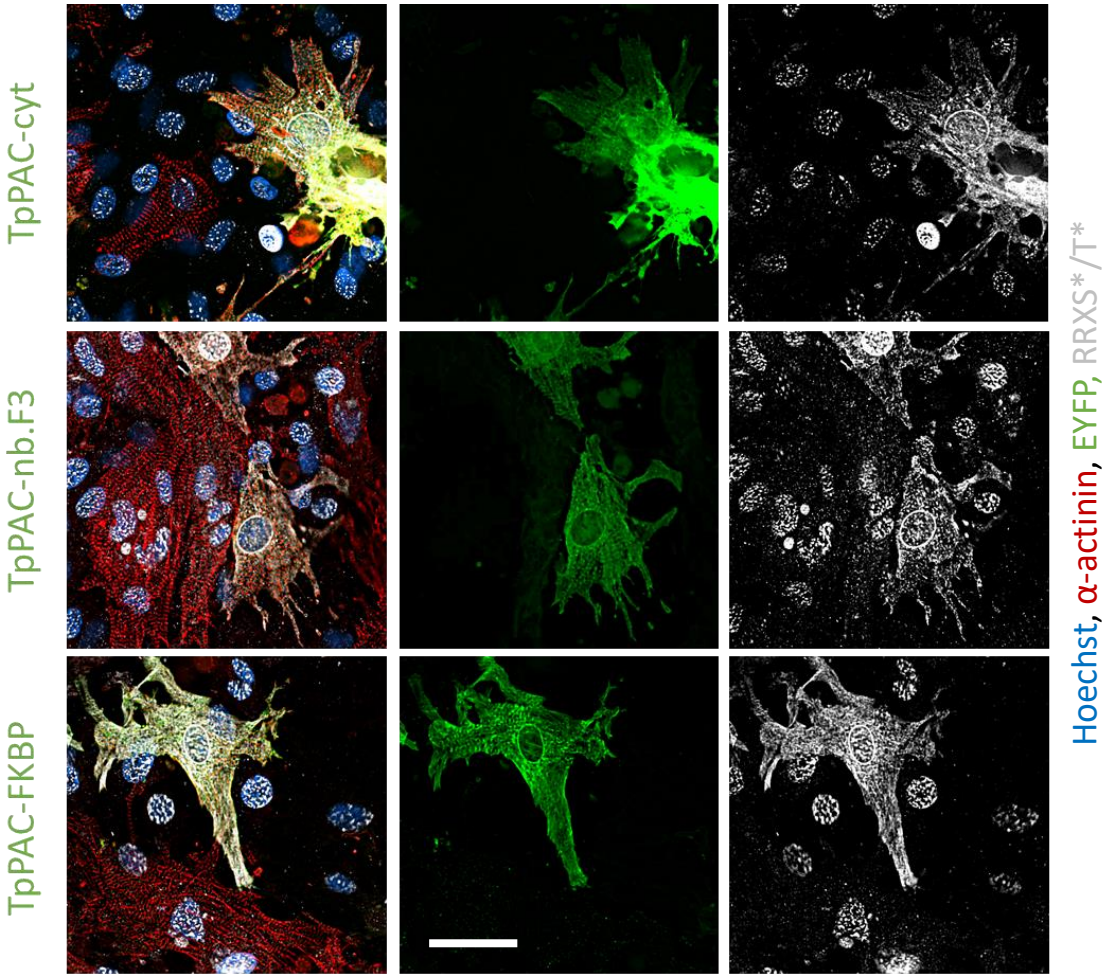

Fig. 40: The effect of cAMP generation on phosphorylation
Phosphorylation by localized cAMP generation in microdomains was analyzed by imaging in nCMs. Cells were stained with α-actinin, EYFP, DAPI, and a PKA phosphorylation-specific antibody (RRXS/T*). Representative example of TpPAC-EYFP, nb.F3-TpPAC-EYFP, and TpPAC-mCitrine-FKBP12.6-expressing (EYFP-positive) and non-expressing (EYFP-negative) cardiomyocytes illuminated with blue light: repetition of 1 s. with 100 µW/mm² blue light within 2 min and 10 s. breaks. Illumination was controlled by an Arduino program (**S. 2**). After the cells were fixed and stained, images showed a high RRXS*/T* signal in TpPAC-positive cells compared to WT cells. A Nikon Eclipse Ti2 fluorescence microscope with a 20x objective and the following filters was used to capture the images: Hoechst (DAPI, 405 nm), α-actinin (Cy3, 505 nm), EYFP (488 nm), and RRXS*/T* (Cy5, 625 nm).*

By analyzing all TpPAC-expressing single nCMs from three wells from a single experiment, we found that illumination resulted in a significant increase in RRXS*/T* signals of 2.7-fold for TpPAC-EYFP, 3.7-fold for TpPAC-nb.F3 and 1.8-fold for TpPAC-FKBP12.6 (**Fig. 41 F**), when comparing dark control to illuminated cells. The cytosolic signal was used for analysis as the nucleus showed a high RRXS*/T* baseline staining (**Fig. 40**). EYFP-negative cells that were in the same well as EYFP-positive cells showed higher RRXS*/T* signals than WT cells from wells without transfected cells, but significantly lower than EYFP-positive cells (**Fig. 41 C-E** ****: $p<0.0001$), indicating a certain signal transfer between the cells in a well and baseline activity of TpPAC also in dark control.

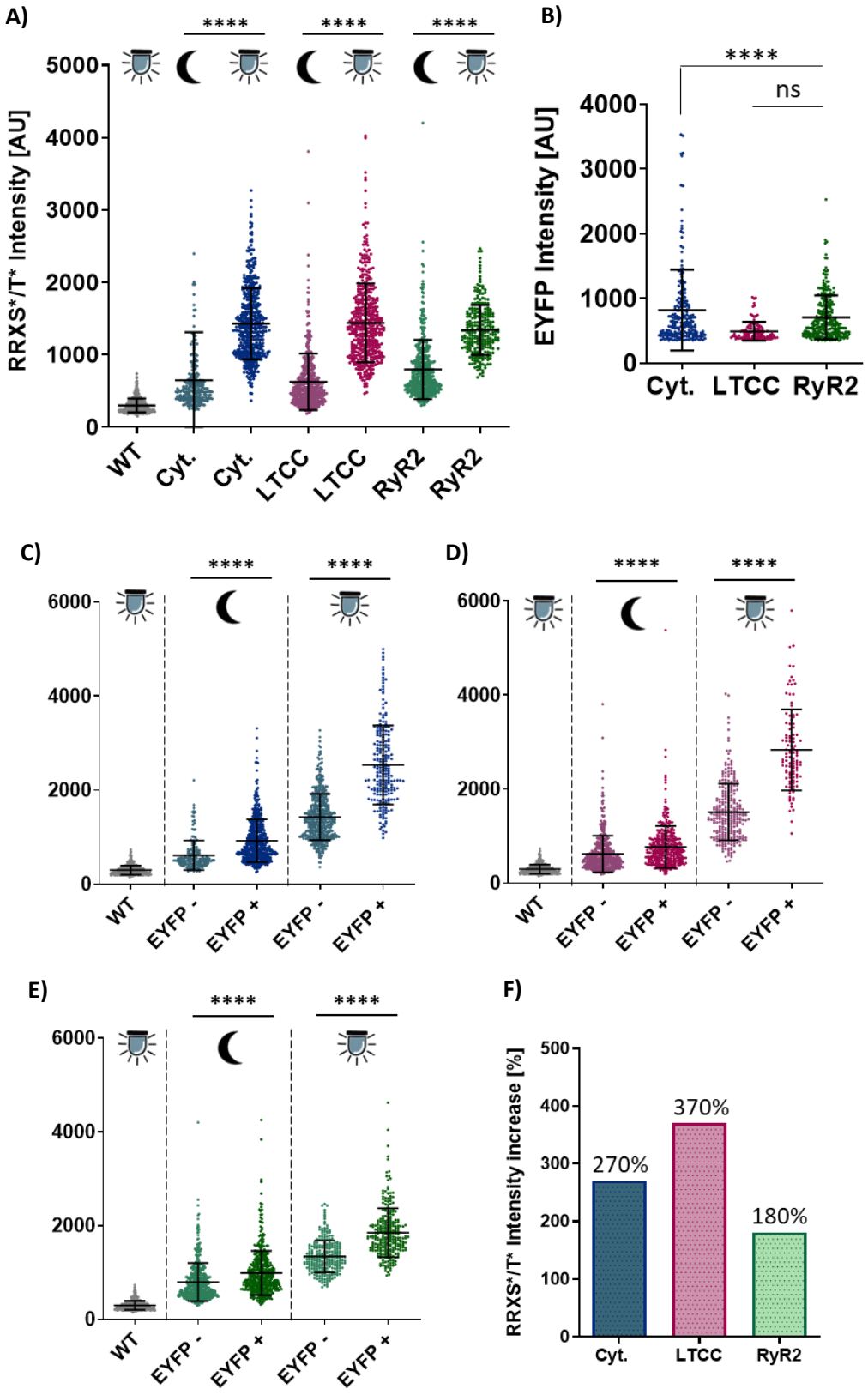

Fig. 41: Effect of cAMP generation on phosphorylation

Phosphorylation by localized cAMP generation in microdomains was analyzed in nCMs using imaging. Cells were kept in the dark or illuminated 12 x with 1 s of blue light every 10 s at 100 µW/mm². Phosphorylation was fixed with PFA and a phosStop cocktail 30 s after the last illumination. Cells were stained against α-actinin, EYFP, and with Hoechst and a PKA phosphorylation specific antibody (RRXS/T*). **A**) Average with SD of PKA phosphorylation intensity in WT and wells with transfected cells*

expressing TpPAC-EYFP, F3-TpPAC-EYFP, and TpPAC-mCitrine-FKBP12.6 after illumination or dark control. ***B****) EYFP intensity of TpPAC-EYFP, nb.F3-TpPAC-EYFP and TpPAC-mCitrine-FKBP12.6.* ***C****) Average with SD of PKA phosphorylation intensity in WT and wells with transfected cells, separated by EYFP-positive and negative cells expressing TpPAC-EYFP after illumination.* ***D****) Average with SD of PKA phosphorylation intensity in WT and wells with transfected cells, separated by EYFP-positive and negative cells expressing nb.F3-TpPAC-EYFP after illumination.* ***E****) Average with SD of PKA phosphorylation intensity in WT and wells with transfected cells separated by EYFP-positive and negative cells expressing TpPAC-mCitrine-FKBP12.6 after illumination.* ***F)*** *RRXS*/T* intensity increase of TpPAC-EYFP, F3-TpPAC-EYFP, and TpPAC-mCitrine-FKBP12.6-positive cells after illumination compared to the dark control. Statistical analysis of PKA phosphorylation intensities in EYFP-positive single cardiomyocytes expressing TpPAC-EYFP, TpPAC-nb.F3 and TpPAC-FKBP12.6, illuminated (light) or without illumination (dark) compared to wild-type illuminated cells (WT light) using ANOVA with Tukey's multiple comparison test, ****: p<0.0001.*

To investigate the effect of expression intensity on the RRXS*/T* signal, the EYFP expression was correlated (**Fig. 42)** in illuminated and dark control samples, revealing a higher RRXS*/T* signal in lower-expressed nb.F3-TpPAC-EYFP compared to TpPAC-EYFP and TpPAC-mCitrine-FKBP12.6 under illuminated conditions (**Fig. 42 D**). The effect on the dark control was similar in all cardiomyocytes expressing TpPAC-EYFP, TpPAC-nb.F3, and TpPAC-mCitrine-FKBP12.6 (**Fig. 42 A-C**).

This experiment was then repeated three times with three different illumination protocols (**Fig. 43**). An increase in RRXS*/T* signal was observed in a dose-dependent manner with increasing illumination for TpPAC-EYFP (**Fig. 43 A, B**), nb.F3-TpPAC-EYFP (**Fig. 43 C, D**) and TpPAC-mCitrine-FKBP12.6 (**Fig. 43 E, F**) positive cells.

Comparing global and local cAMP generation in microdomains (**Fig. 44**), it was observed that low light illumination induced an 85% RRXS*/T* signal compared to maximal illumination in TpPAC-mCitrine-FKBP12.6, while in TpPAC-EYFP and nb.F3-TpPAC-EYFP, the RRXS*/T* signal was 45% and 43%, respectively, compared to maximal illumination. This is further underlied in **Fig. 44,** where for TpPAC-mCitrine-FKBP12.6, 100 ms light and 1 s light, the RRXS*/T* signal is not significantly different, while for TpPAC-EYFP it is ****: $p < 0.0001$ significantly different and for nb.F3-TpPAC-EYFP it is ***: $p < 0.001$ significantly different. This supports the other results that the RyR2 is more susceptible to cAMP dependant phosphorylation.

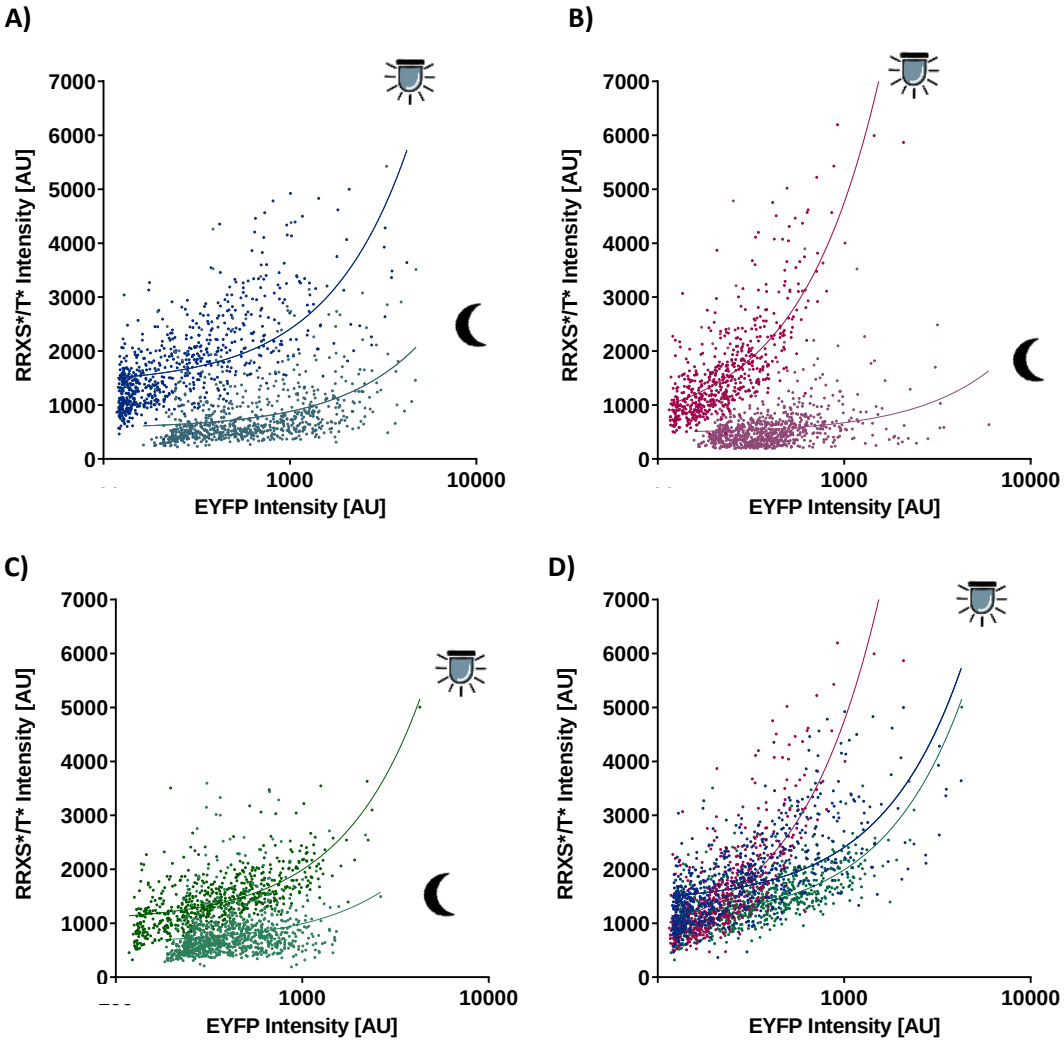

Fig. 42: The effect of cAMP generation on phosphorylation related to EYFP expression *Phosphorylation by localized cAMP generation in microdomains was analyzed in neonatal cardiomyocytes using imaging. Cells were kept in darkness or illuminated 12 times with 1 s of blue light every 10 s at 100 µW/mm². Phosphorylation was fixed with PFA and a phosStop cocktail 30 s after the last illumination. Cells were stained for α-actinin, EYFP, and with DAPI, as well as a PKA phosphorylation-specific antibody (RRXS*/T*). Data were collected from three 24-well plates, with each point representing the EYFP expression and the corresponding RRXS*/T* signal of a single cell.* ***A****) WT nCMs and nCMs transfected cells expressing TpPAC-EYFP after illumination or dark control with a fitted curve.* ***B****) WT nCMs and nCMs transfected cells expressing nb.F3-TpPAC-EYFP after illumination or dark control with a fitted curve.* ***C****) WT nCMs and nCMs transfected cells expressing TpPAC-mCitrine-FKBP12.6 after illumination or dark control with a fitted curve.* ***D****) Summary of illuminated WT nCMs and nCMs transfected cells expressing TpPAC-EYFP, nb.F3-TpPAC-EYFP and TpPAC-mCitrine-FKBP12.6 with fitted curves.*

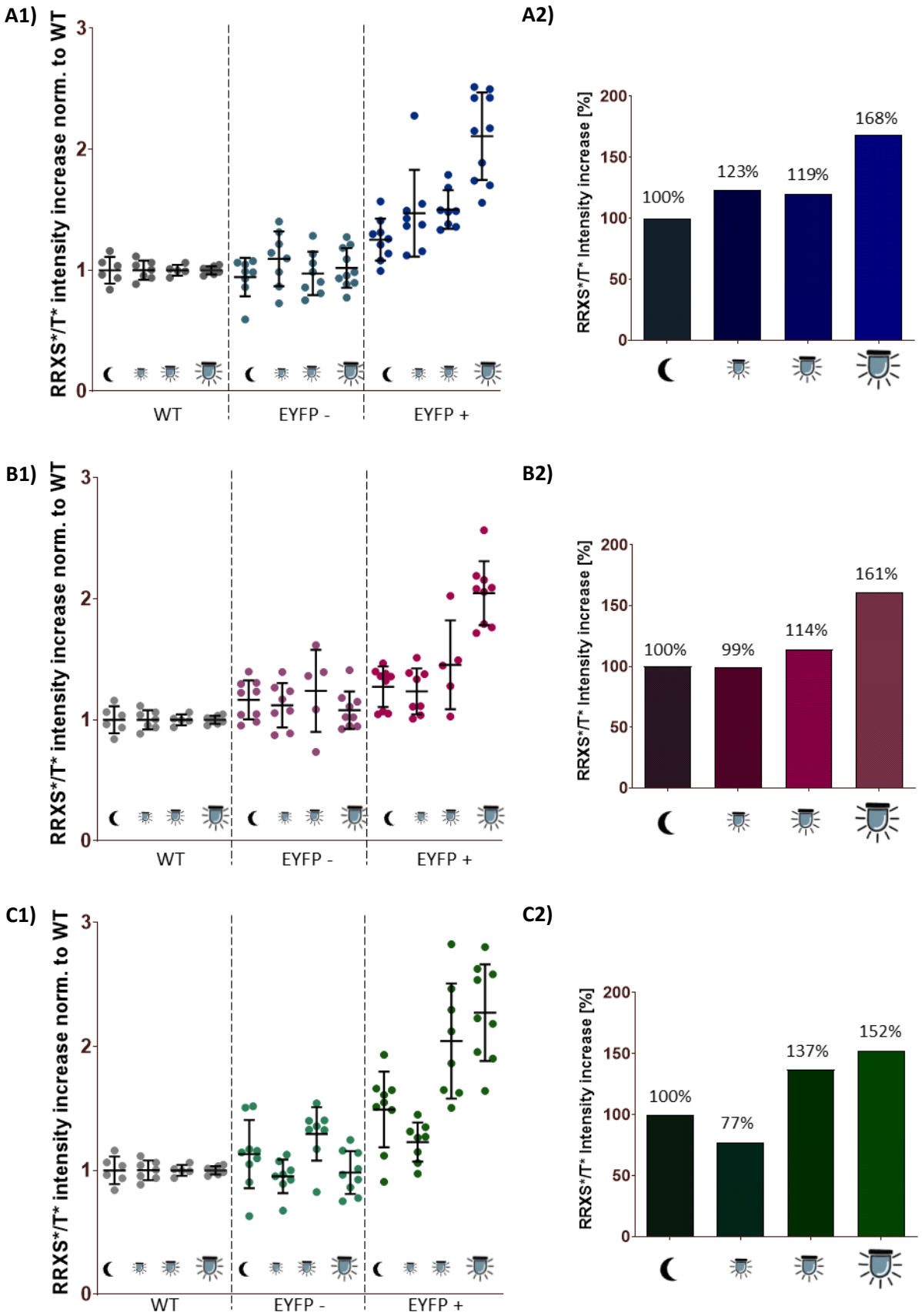

Fig. 43: The dose-dependent effect of cAMP generation on phosphorylation

Phosphorylation by localized cAMP generation in microdomains was analyzed in neonatal cardiomyocytes using imaging. Cells were kept in the dark or illuminated with 12 pulses of 1 s, 100 ms, or 10 ms of blue light at 100 µW/mm² every 10 s. Phosphorylation was fixed with PFA and a phosStop

cocktail 30 s after the last illumination. Cells were stained with antibodies against α-actinin, EYFP, and DAPI, as well as a PKA phosphorylation-specific antibody (RRXS/T*).* ***A1****) Average with SD of PKA phosphorylation intensity in WT and wells with transfected cells expressing TpPAC-EYFP after increasing illumination or dark control. Cells were separated into EYFP-positive and EYFP-negative cells.* ***A2****) RRXS*/T* signal increases after illumination compared to dark control (100%).* ***B1****) Average with SD of PKA phosphorylation intensity in WT and wells with transfected cells expressing nb.F3-TpPAC-EYFP after increasing illumination or dark control. Cells were separated into EYFP-positive and EYFP-negative cells.* ***B2****) RRXS*/T* signal increases after illumination compared to dark control (100%).* ***C1****) Average with SD of PKA phosphorylation intensity in WT and wells with transfected cells expressing TpPAC-mCitrine-FKBP12.6 after increasing illumination or dark control. Cells were separated into EYFP-positive and EYFP-negative cells.* ***C2****) RRXS*/T* signal increases after illumination compared to dark control (100%). Data normalized to WT RRXS*/T* signal.*

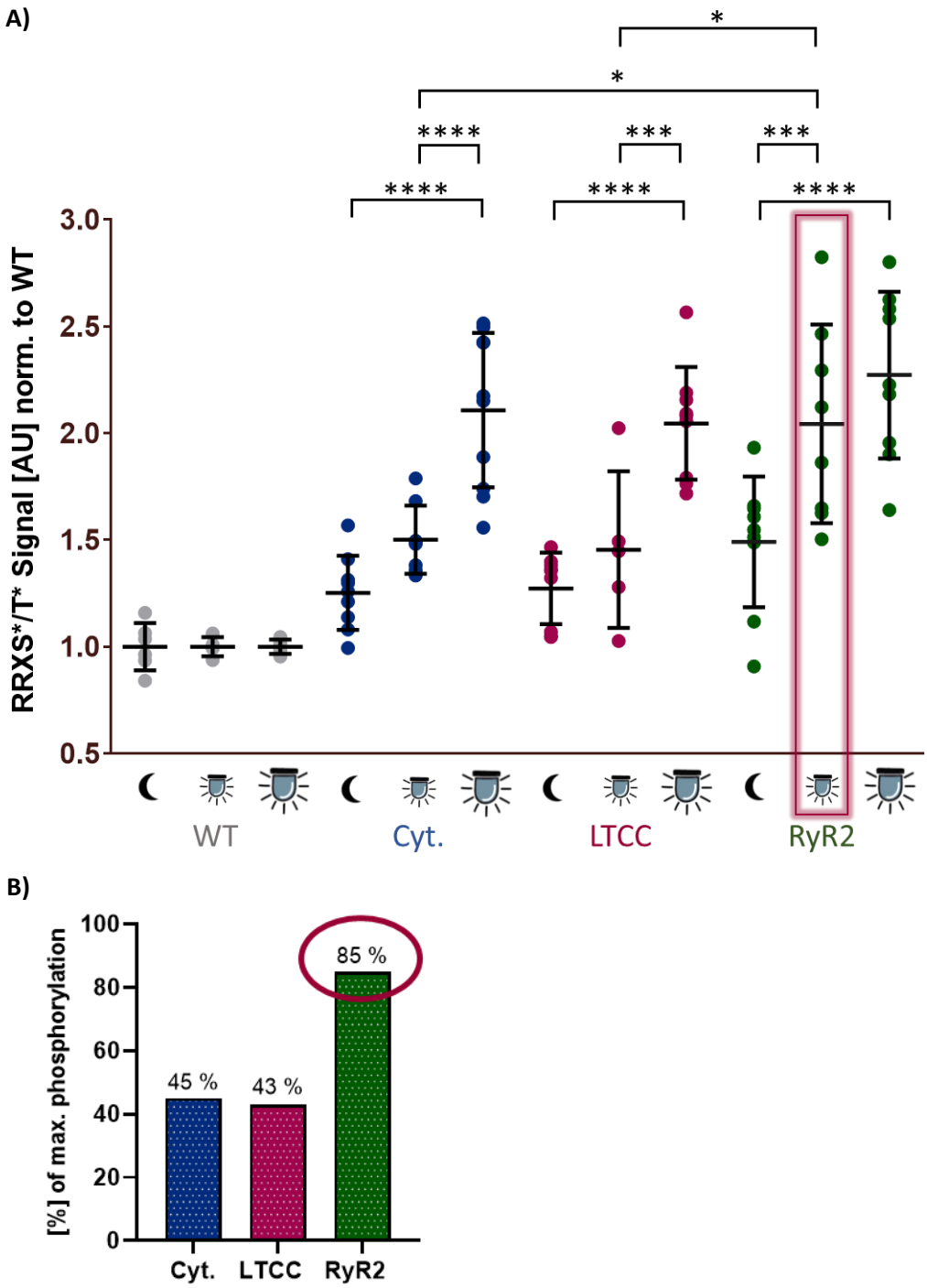

Fig. 44: Statistical analysis of the effect of global and local cAMP generation on phosphorylation *Phosphorylation by localized cAMP generation in microdomains was analyzed in nCMs by imaging. Cells were kept either dark or illuminated 12 times with 1 s or 100 ms of blue light at 100 µW/mm² every 10 s. Phosphorylation was fixed with PFA and a phosStop cocktail 30 s after the last illumination. Cells were stained with antibodies against α-actinin, EYFP, and DAPI, as well as a PKA phosphorylation-specific antibody (RRXS*/T*).* ***A****) Average with SD of PKA phosphorylation intensity in WT and wells with transfected cells expressing TpPAC-EYFP, nb.F3-TpPAC-EYFP and TpPAC-mCitrine-FKBP12.6 after increasing illumination or dark control.* ***B****) RRXS*/T* intensity increase of TpPAC-EYFP, nb.F3-TpPAC-EYFP and TpPAC-mCitrine-FKBP12.6 at low light illumination compared to maximum illumination. Statistical analysis was performed using analysis of variance (ANOVA) with the Tukey multiple comparison test. ****: p < 0.0001, ***: p < 0.001, **: p < 0.01, *: p < 0.05.*

4.7 Local and global PKA inhibition

In addition to the previous work on global and local cAMP generation using PACs, a second approach utilizing optogenetic tools to inhibit global and local PKA activity was employed to study microdomains surrounding the LTCC and the RyR2. A photoactivated protein kinase A inhibitor (LOV-PKI),[71] containing a light-oxygen-voltage sensing (LOV) domain, was used to decrease PKA phosphorylation with light. For the global and subcellular localization of LOV-PKIs, three constructs were generated using a fluorescent marker and either nb.F3[76] for LTCC targeting or FKBP12.6[77] for RyR2 targeting (**Fig. 45**). Non-targeted LOV-PKIs served as a control for global cytosolic PKA modulation (**Fig. 45**). The constructs were cloned using overhang primers. The DNA fragments of nb.F3 and FKBP12.6 were produced by GeneArt (Thermo Fisher).

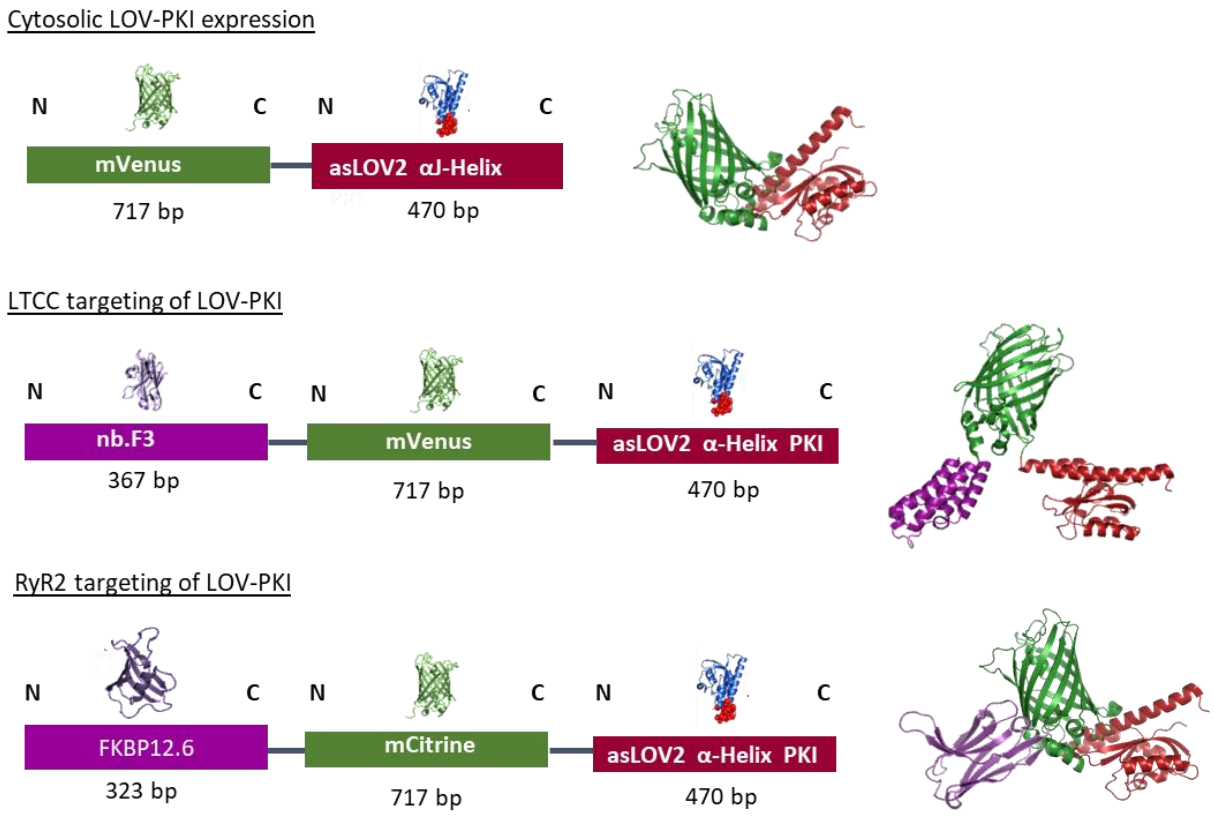

Fig. 45: Cloning strategy and predicted protein structure

For cytosolic expression, LOV-PKIs were fused to the marker mVenus. For LTCC targeting, the nanobody nb.F3 was cloned the LOV-PKIs and mVenus. The FKBP12.6 protein was used to target RyR2. The FKBP12.6 protein was fused to mCitrine and the LOV-PKI.

Fusion proteins were validated by analyzing the correct protein sizes in stable HEK293 cells using Western blot analysis (**Fig. 46**) with a GFP antibody. The expected size of the fusion constructs LOV-PKI-mVenus (**1**) is approximately 40 kDa. The sizes of nb.F3-LOV-PKI-mVenus (**2**) and LOV-PKI-mCitrine-FKBP12.6 (**3**) are expected to be 59 kDa and 57 kDa, respectively. A HEK293 cell line expressing GFP (27 kDa) was used as a positive control for the GFP antibody, while HEK293 WT cells served as a negative control. Clear bands with no sign of degradation were detected, and protein sizes were measured with the BioRad ImageLab software, showing approximately the expected protein size (**Fig. 46**).

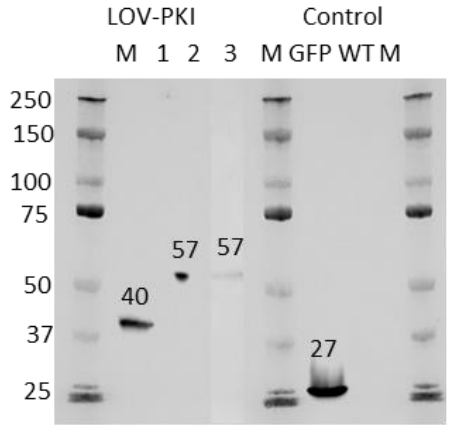

Fig. 46: HEK 293 cells stably expressing LOV-PKIs
*The fusion constructs **1**) LOV-PKI-mVenus (expected size: 40 kDa), **2**) nb.F3-LOV-PKI-mVenus (expected size: 59 kDa) and **3**) LOV-PKI-mCitrine-FKBP12.6 (expected size 57 kDa) were cloned, expressed in HEK293 cells and analyzed by Western blots (left) using a GFP antibody (1:3000). GFP-expressing HEK293 cells (30 kDa) and cells were used as controls (right). Using a Bio-Rad protein marker (**M**) as a size standard, we observed a slightly smaller size than predicted but no degradation. Cells were harvested, collected, and frozen at -80°C. Proteins were extracted with RIPA buffer. A total of 10 µg protein was used in a volume of 15 µL. Western blot was performed using the Mini-PROTEAN Tetra Cell System for protein separation and the Trans-Blot Turbo Transfer System for transfer. GFP antibody staining was performed at a concentration of 1:1000. Gel documentation was performed using Li-COR Odyssey FC.*

To investigate whether nb.F3 and FKBP12.6 indeed lead to the local targeting of LTCC and RyR2, immunohistological stainings were performed and observed by confocal microscopy (**Fig. 47**). The subcellular distribution of the fusion proteins was analyzed by their EYFP signal in α-actinin-positive cardiomyocytes, which served as a cardiac-specific marker. Most cells with non-targeted LOV-PKI exhibited a homogeneous EYFP distribution with no evidence of aggregation, indicating cytosolic expression. In contrast, FKBP12.6-containing fusion proteins were localized around the nuclear envelope and Z-disc, indicative of the SR, where RyR2 is localized.

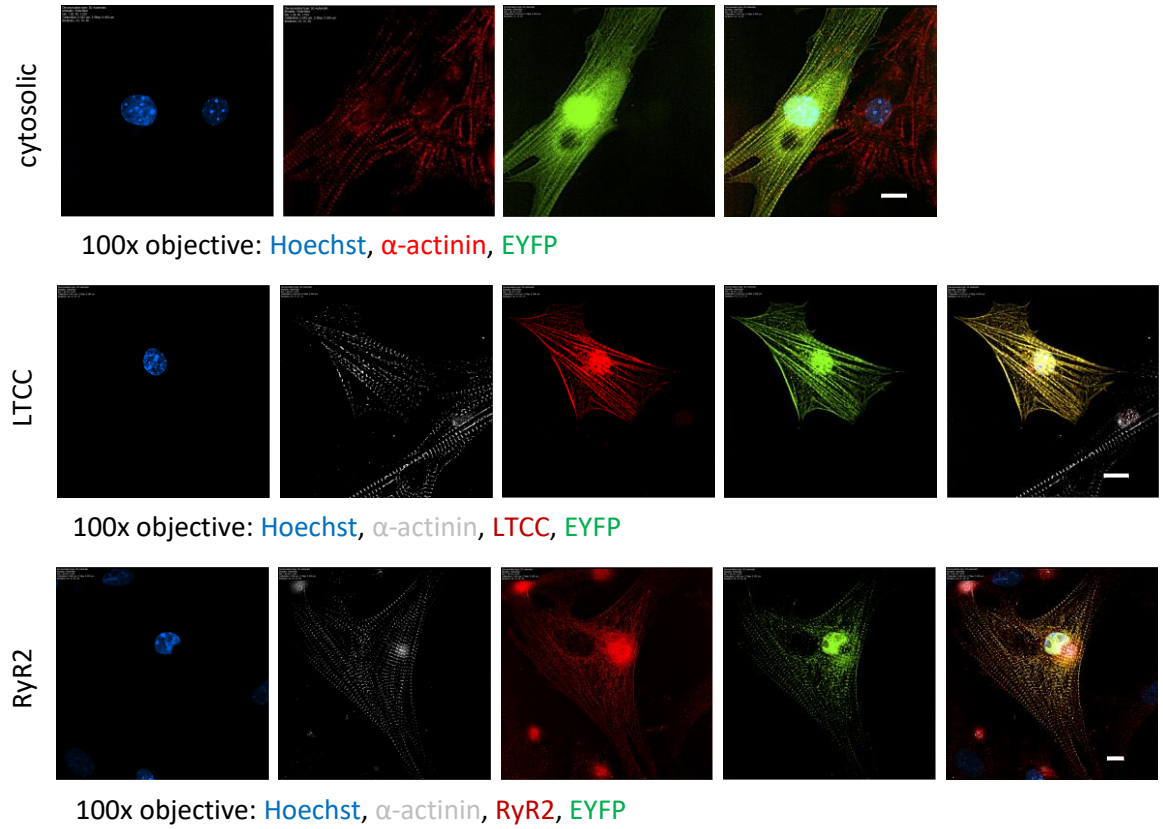

Fig. 47: Localization of LOV-PKI fusion constructs in neonatal cardiomyocytes
P1-3 neonatal cardiomyocytes were transfected with constructs for expression of the cytosolic (cyt), nb.F3-fused or FKBP12.6-fused and EYFP (green) containing proteins LOV-PKI (green) by nucleofection (Lonza) and stained 5 days later with the cardiac-specific marker α-actinin (red or white) and the nuclear marker Hoechst (blue). The second raw (LTCC) was co-stained with LTCC, and the third raw (RyR2) was co-stained with the RyR2 antibody. Images were captured using a Nikon Eclipse Ti2 confocal microscope with a 60x oil-immersion objective and post-processed by deconvolution using Nikon NIS Elements. The following filters were used: Hoechst (DAPI, 405 nm), α-actinin (Cy3, 505 nm), EYFP (488 nm), RyR2, and LTCC (Cy5, 625 nm). Scale bar: 10 µm.

Cells with nb.F3 for LTCC targeting showed membrane targeting and some signals around the nuclear envelope. In general, it was possible to distinguish between the differently locatized constructs by observing EYFP expression with a 20x objective. Colocalization of LOV-PKI-mCitrine-FKBP12.6 (green) with the RyR2 (red) and nb.F3-LOV-PKI-mVenus (green) with the LTCC (red) antibody showed clear colocalization (yellow) (**Fig. 47**).

The functionality of global and local PKI inhibition by the LOV-PKI constructs was tested by frequency analysis (**Fig. 48**). The changes in beating rate of nCMs transfected with global and local LOV-PKI constructs were observed before and after illumination for three examples per construct (**Fig. 48**). Illumination decreased the beating rate and irregular beating was observed for all constructs. Validating the light-activated PKA inhibition by LOV-PKI.

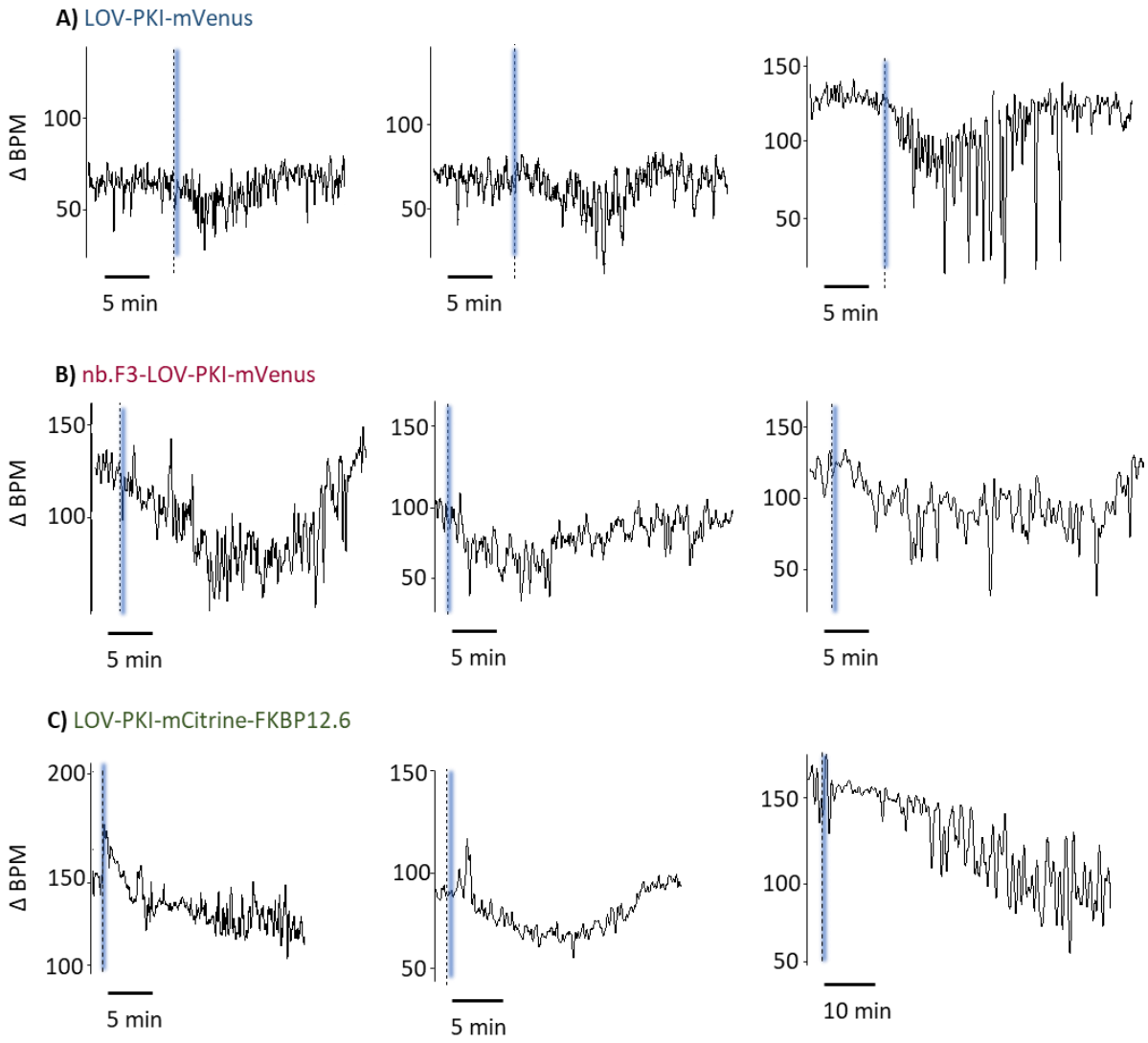

Fig. 48: Effect of global and local light-dependent PKA inhibition on beating frequency
The effect of global and local microdomain PKA inhibition on the beating rate of nCMs was analyzed by observing changes in spontaneous beating frequency using video microscopy. Blue light (465 nm) flashes were applied at 102 µW/mm², and the beating frequency was recorded online using custom software and displayed as beats per minute (BPM). ***A)*** *three examples for LOV-PKI-mVenus,* ***B)*** *three examples for nb.F3-LOV-PKI-mVenus,* ***C)*** *three examples for LOV-PKI-mCitrine-FKBP12.6.*

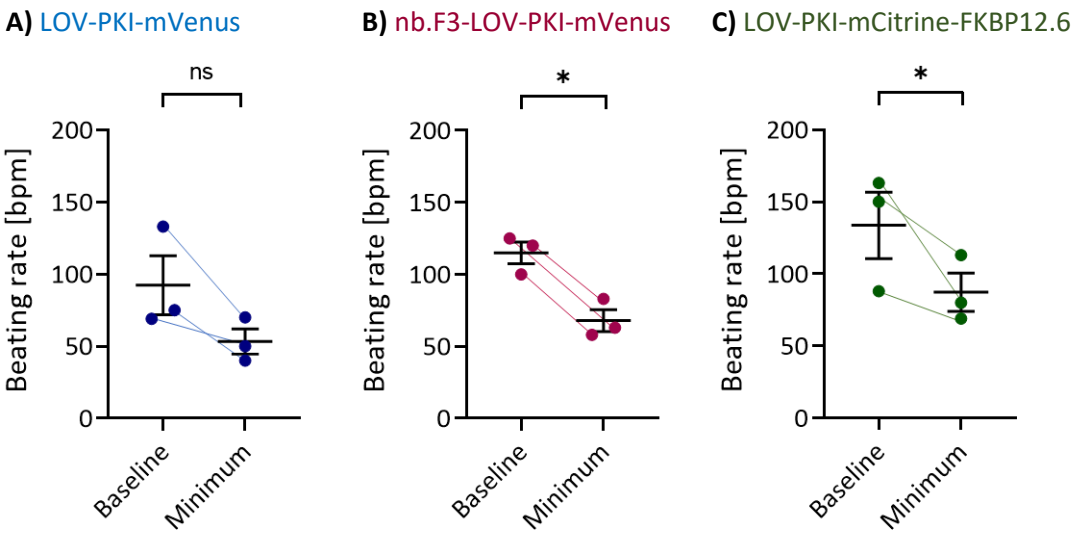

Fig. 49: Decrease in beating rate after global and local light-dependent PKA inhibition
Quantification of beating frequency in nCMs expressing LOV-PKI constructs. 1 s blue light (465 nm, 102 µW/mm²) was applied to trigger PKA inhibition. Statistical analysis comparing the average of 10s baseline and the minimum after-illumination (Minimum) was performed using one-way ANOVA with Tukey's multiple comparisons test. ***A)*** *LOV-PKI-mVenus (ns),* ***B)*** *nb.F3-LOV-PKI-mVenus (*: p = 0.0450), and* ***C)*** *LOV-PKI-mCitrine-FKBP12.6 (*: p = 0.0477).*

While the reduction in beating rate was not significant for LOV-PKI-mVenus, it reached statistical significance for nb.F3-LOV-PKI-mVenus (*: p = 0.0450) and LOV-PKI-mCitrine-FKBP12.6 (*: p = 0.0477) (**Fig. 49**). Most of the time, the beating rate recovered to the baseline rate after a while. Interestingly, in 2 of 3 samples of LOV-PKI-mCitrine-FKBP12.6, an increase in the beating rate was observed immediately after illumination, followed by a decrease. In addition, the beating frequency of nCMs transfected with LOV-PKI-mCitrine-FKBP12.6 was tested before and after the application of rolipram, a PDE4 inhibitor (**Fig. 50**). After 5 min incubation with 10 µM rolipram, illumination resulted in a higher and more prolonged initial increase in beating frequency before the decrease in frequency occurred, compared to before rolipram treatment. To gain further insight into the kinetics of frequency changes in beating rate, additional experiments are needed to increase the number of samples and to perform rolipram experiments with LOV-PKI-mVenus and nb.F3-LOV-PKI-mVenus, as well as other specific PDE inhibitors and activators.

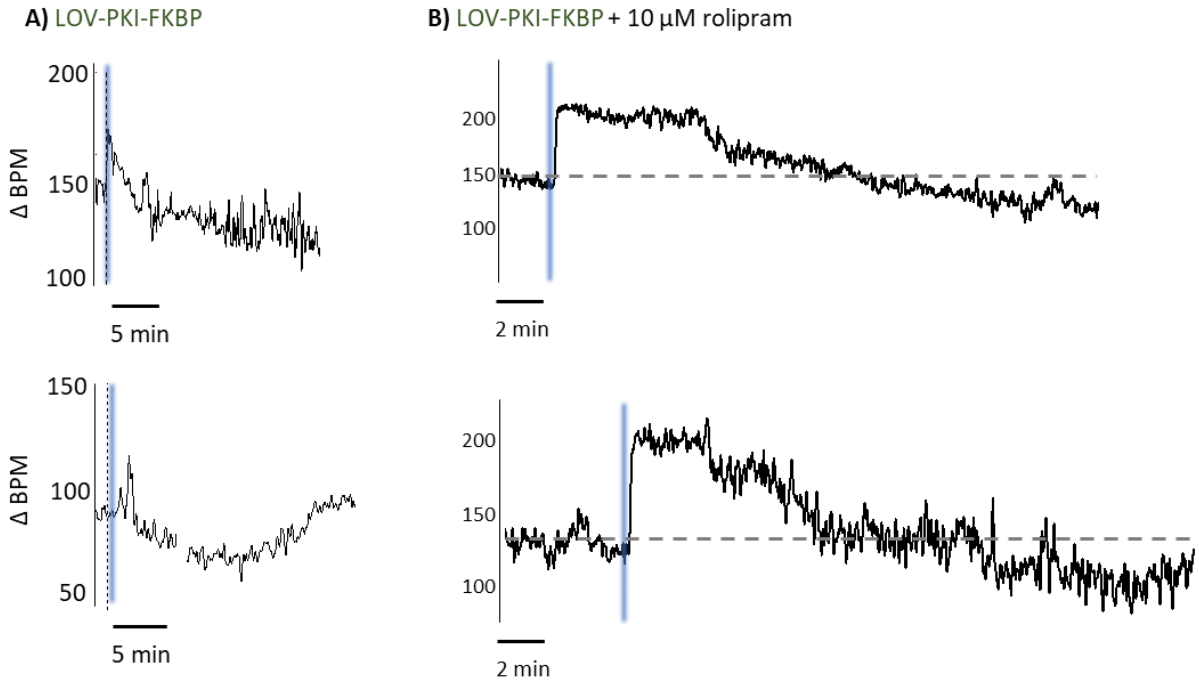

Fig. 50: Effect of rolipram on light-dependent PKA inhibition on beating frequency
*The effect of rolipram on light-dependent PKA inhibition on the beating rate of nCM transfected with LOV-PKI-FKBP12.6 was analyzed by observing changes in spontaneous beating frequency using video microscopy. Blue light (465 nm) flashes were applied at 102 µW/mm², and the beat frequency was recorded online using custom software and displayed as beats per minute (BPM) before **A)** and after **B)** the addition of 10 µM rolipram*.

Furthermore, the effect of local PKA inhibition on phosphorylation at RyR2 was observed in nCMs using immunohistological staining with a PKA phosphorylation site-specific antibody: RRXS*/T*. Comparing the phosphorylation (RRXS*/T* signal) of nCMs with LOV-PKI-mCitrine-FKBP12.6 illuminated versus dark control, a significant decrease (****: $p < 0.0001$) was observed (**Fig. 51 A**). This changes when cells are incubated with the PDE4 inhibitor rolipram for 5 min. A slightly higher phosphorylation signal (**: $p = 0.0093$) was observed after illumination compared to the dark control (**Fig. 51 B**). **Fig. 54 C**) and **D**) show examples of nCMs transfected with LOV-PKI-mCitrine-FKBP12.6 under illumination **C**) without rolipram and **D**) with rolipram. In **C**)**,** the EYFP-positive cells exhibit a lower RRXS*/T* signal than WT, which is not observed after rolipram incubation in **D**). Again, for further insights, more experiments are needed to increase the n number and investigate the effects of rolipram and other specific PDE isoform inhibitors and activators for all localizations.

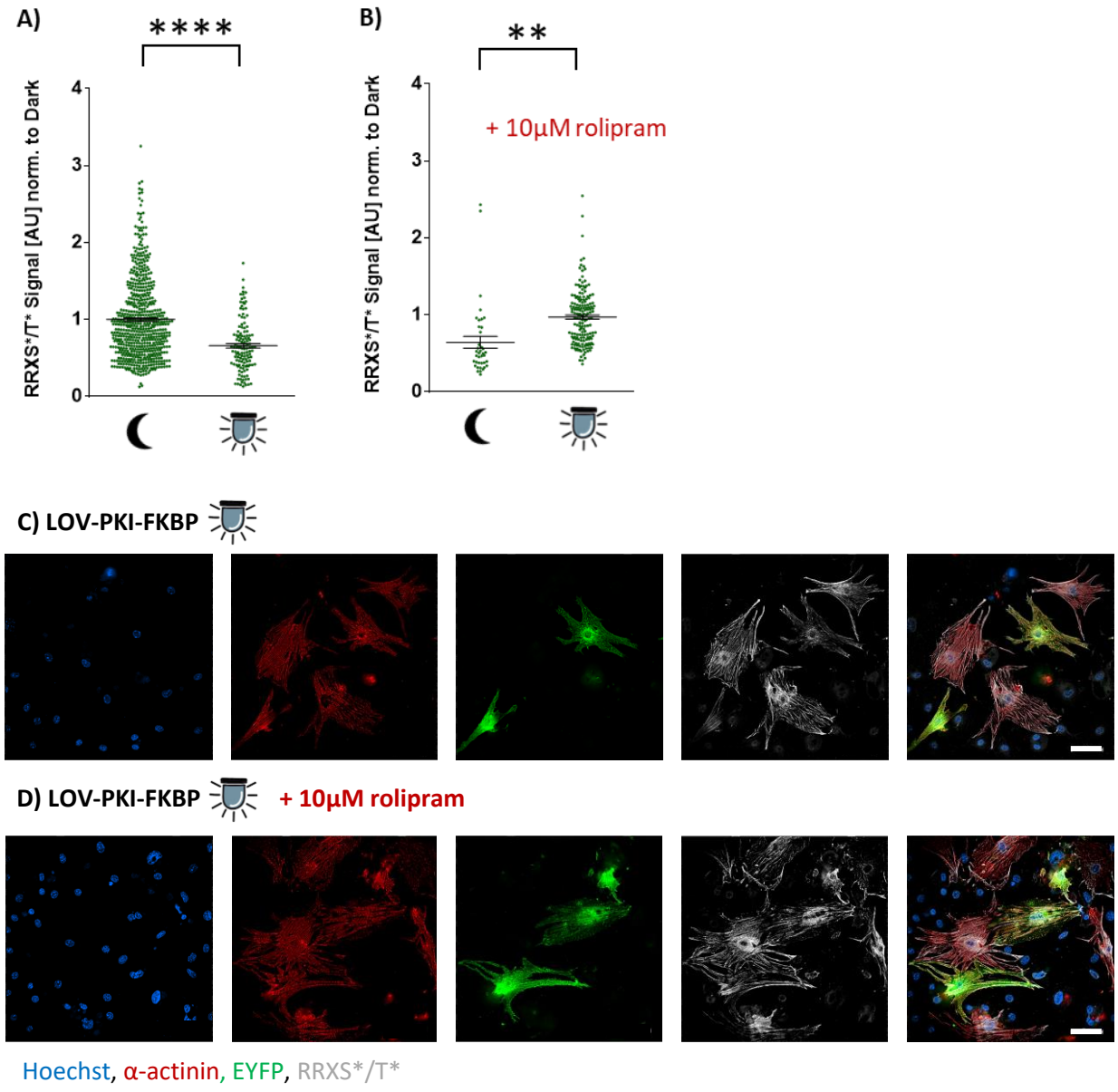

Fig. 51: The effect of PKA inhibition on RyR2 phosphorylation

Phosphorylation by local PKI inhibition in the RyR2 microdomain was analyzed in neonatal cardiomyocytes using imaging. Cells were kept in the dark or illuminated 12 x with 1 s blue light every 10 s. Phosphorylation was fixed with PFA and a phosStop cocktail 30 s after the last illumination. Cells were stained for α-actinin, EYFP, and DAPI, as well as a PKA phosphorylation-specific antibody (RRXS/T*).* ***A)*** *Signal of PKA phosphorylation sites with antibody RRXS*/T* from nCMs transfected with LOV-PKI-mCitrine-FKBP12.6 in dark and illuminated samples, showing ****: $p < 0.0001$ by t-test. Each data point represents the signal from one cell.* ***B)*** *Signal of PKA phosphorylation sites with the antibody RRXS*/T* from nCMs transfected with LOV-PKI-FKBP and incubated with 10 µM rolipram for 5 min in dark or illuminated samples, showing **: $p = 0.0093$ in a t-test. Each data point represents the signal from one cell.* ***C)*** *Representative example of LOV-PKI-mCitrine-FKBP12.6-expressing (EYFP-positive) and non-expressing (EYFP-negative) cardiomyocytes, illuminated with blue light, showing a lower RRXS*/T* signal compared to WT cells.* ***D)*** *Representative example of LOV-PKI-mCitrine-FKBP12.6-expressing (EYFP-positive) and non-expressing (EYFP-negative) cardiomyocytes, illuminated with blue light and preincubated with 10 µM rolipram for 5 min, showing a high RRXS*/T* signal. Nikon Eclipse Ti2 fluorescence microscope with 20x objective and the following filters: Hoechst (DAPI: 405 nm), α-actinin (Cy3: 505 nm), EYFP (488 nm) and RRXS*/T* (Cy5: 625 nm). Scale bar = 50 µm.*

4.8 Outlook

Further experiments with specific PDE inhibitors and activators should be performed in the future for the frequency, Ca^{2+} imaging, and phosphorylation experiments to:

1. induce kinetic changes in beating frequency and induce and diminish the plateau effect of elevated beating frequency
2. induce elevated diastolic Ca^{2+} also in TpPAC-EYFP and nb.F3-TpPAC-EYFP by resolving the signaling microdomains, as well as to diminish elevated diastolic Ca^{2+} in TpPAC-mCitrine-FKBP12.6 to proof the microdomain formation further
3. induce higher sensitivity to low light in TpPAC-EYFP and nb.F3-TpPAC-EYFP, as well as to diminish the sensitivity to low light in TpPAC-mCitrine-FKBP12.6 to prove the microdomain formation further

The Western blot experiment and immunohistological staining with the RRXS*/T* antibody showed a light-induced increase in phosphorylation for nCMs with TpPAC. However, we cannot determine which specific proteins were phosphorylated under global and local cAMP generation at the LTCC or RyR2, nor whether this phosphorylation is specifically localized. Therefore, samples of nCMs WT and transfected nCMs with TpPAC-EYFP, nb.F3-TpPAC-EYFP, and TpPAC-mCitrine-FKBP12.6 were collected for phosphoproteomic analysis under increasing illumination (12 times with 1 s, 100 ms, or 10 ms of blue light at 100 µW/mm² every 10 s). For control samples, cells were keept in dark. Additionally, WT samples were treated with isoprenaline, FSK, and IBMX as a positive control. Phosphoproteome analysis is yet to be performed in the future.

Since all of the experiments described were performed in nCMs, TpPAC-EYFP, nb.F3-TpPAC-EYFP, and TpPAC-mCitrine-FKBP12.6 proteins were also expressed in HEK293 cells and purified for transfer into aCMs for future experiments. To collect TpPAC-EYFP, nb.F3-TpPAC-EYFP, and TpPAC-mCitrine-FKBP12.6 proteins from HEK293 cells, immunoprecipitation of GFP-tagged proteins was performed using ChromoTek GFP-Trap® Magnetic Agarose. It is planned to transfer these proteins into aCMs using either a patch pipette or saponin permeabilization.

5.0 Discussion

5.1 Relevance of investigating cAMP microdomain signaling at LTCC and RyR2

Cardiovascular diseases have become a major burden in modern society. Sudden cardiac death is a significant global health problem, accounting for an estimated 15-20% of all reported deaths.[84] It is typically associated with fatal ventricular arrhythmias in hearts affected by structural abnormalities, such as those occurring after myocardial infarction or in heart failure, as well as in hereditary arrhythmia syndromes (see Chapter **1.4**).

Implantable cardioverter defibrillators (ICDs) and ß-blockers (see Chapter **1.6.2**) are the most common therapeutic interventions against ventricular arrhythmias in high-risk individuals. The previously described treatments in **1.6.2** are accompanied by a wide range of adverse effects, necessitating more targeted therapies.[84] In particular, impaired Ca^{2+} handling leads to various diseases, including Ca^{2+} leak through the RyR2 from the SR and increased Ca^{2+} influx through the LTCC and NCX. Therefore, it is essential to understand the precise contribution of LTCC and RyR2 to cardiac arrhythmias. Previous research has highlighted the significance of cAMP microdomains in cardiomyocyte function, e.g., the group of Prof. Viacheslav O. Nikolaev has been investigating the localized role of cyclic nucleotides (cAMP and cGMP), GPCRs, and PDEs in cardiomyocytes by mainly using FRET biosensors to detect changes under different conditions (see Chapter **1.4** and **1.5**).[62, 100, 103] Similarly, the group of Prof. Andreas Bock investigates GPCRs and their signaling pathways, particularly in the context of cAMP microdomains, GPCR signaling specificity, and the role of PDEs in cardiomyocytes, utilizing cutting-edge techniques, including advanced biosensors and imaging methods.[64]

These approaches provide detailed insights into cAMP regulation within heart cells; however, local modulation and the corresponding functional readout were not possible with these methods. Building on these previous works, this study focuses on modulating cAMP signaling locally, providing novel insights into the spatial and functional organization of LTCC and RyR2 microdomains. In particular, to investigate the function and control of the LTCC and RyR2 in relation to cardiac arrhythmias using targeted optogenetics. This study focuses on whether the LTCC and RyR2 are modulated by the same cAMP pool or separate cAMP pools via PDEs or other regulatory mechanisms. Understanding the contributions of the PKA phosphorylation on LTCC and RyR2 to arrhythmias can help confirm whether one is a suitable drug target.

5.2 Which is the right model for functional experiments?

After successful cloning of the optogenetic tools for global and local expression, which was verified by Western blot in HEK cells (**Fig. 15, 46**), it was confirmed that the fusion of the optogenetic tools still resulted in functional light-dependent cAMP production in a light-dose dependent manner (**Fig. 13, 14**). Initially, the main challenge was finding a suitable cell line for functional analysis to study the local and global cAMP generation and PKA inhibition in cardiomyocytes. Therefore, several cell lines and transfection methods were tested. Ideally, the aim was not to use primary cells but cell lines, which could not be achieved.

First, the HL-1 cell line, which is derived from atrial cardiomyocytes, was tested. The advantages of HL-1 cardiomyocytes include their ability to continuously divide, spontaneously contract, and maintain a differentiated adult cardiac phenotype through indefinite passages in culture.[80] It has been shown that the HL-1 cell line exhibits well-organized sarcomeres, essential for contraction, and contains intracellular atrial natriuretic factor (ANF) granules, typical of atrial myocytes.[81, 85] The gene expression profile of these cells closely resembles that of adult cardiomyocytes.[81] Moreover, HL-1 cells express specific atrial markers, including atrial natriuretic peptide (ANP).[80, 81] This finding has been corroborated by immunohistochemical staining, which revealed a distribution of cardiac-specific markers, including ANP, that is analogous to that observed in cultured atrial cardiomyocytes. [80, 81] Furthermore, the cells spontaneously depolarize and express ion channels necessary for AP generation, thus mimicking primary cardiomyocytes.[81] Pharmacological studies confirm the cells' responsiveness to inotropic and chronotropic agonists, thereby demonstrating the presence of functional receptors and signaling proteins involved in these pathways. [80, 81] Indeed, a caffeine-induced Ca^{2+} release from the SR (**Fig. 16**), indicating functional RyR2 activity, could be reproduced. However, in culture, the HL-1 cells did not exhibit sufficient and stable contractile capacity, as indicated by insufficient α-actinin staining (**Fig. 20**). To conduct a functional analysis of the local cAMP microdomains, stable contractility was necessary; consequently, the use of HL-1 cells was not a viable option.

Additionally, the generation of stable D3 mESC lines with global and local PAC constructs and their subsequent differentiation into cardiomyocytes using the hanging drop method did not result in a pure or highly enriched population of cardiomyocytes. Also, the dissociation into single cells was challenging (**Fig. 20, 21**). However, a preliminary analysis of the PAC constructs in mESCs differentiated into cardiomyocytes (**Fig. 22, 23**) revealed a light-dependent increase in beating frequency, which was dose-dependent. D3 mESC-derived cardiomyocytes were considered because they exhibited spontaneous contractions, functional Ca^{2+} cycling, and APs, and expressed key cardiac markers such as

α-actinin, cardiac troponin T (cTnT), Nkx2.5, GATA4, and HCN4, consistent with early cardiomyocyte identity.[143]

The poor differentiation into cardiomyocytes may be due to the ubiquitous expression of PACs with the CAG promoter and the background activity of the optogenetic tools, which may have perturbed some vital signaling pathways for cardiomyocyte differentiation. For example, the activation of cAMP response element-binding protein (CREB) affects gene transcription and long-term cellular responses.[86] The culture and differentiation of mESCs into cardiomyocytes consumed a significant amount of materials, such as FCS and time, which was inefficient in terms of cardiomyocyte yield. It would have been possible to differentiate into cardiomyocytes and then transfect the cells to avoid the interference of cAMP modulation in differentiation; however, this approach would also result in a low number of transfected cardiomyocytes, and a suitable transfection method would have had to be established.

The transfection and culturing of nCMs were established and used further to investigate cAMP microdomains at the LTCC and RyR2. These cells share more physiological properties with cardiomyocytes in the heart, including the spontaneous pacemaking activity, Ca^{2+}-clock, and functional RyR2 and LTCC. They are of particular value in studies that require a high degree of physiological relevance, including investigations of Ca^{2+} regulation, signal transduction, and the effects of drugs.[82] It is essential to note that in nCMs, the T-tubule system and the rod-shaped structure are either immature or absent, resulting in a less organized distribution of LTCCs and RyR2. This results in less efficient excitation-contraction coupling than adult cardiomyocytes (aCMs).[87] As the heart matures, there is an increase in the expression of junctophilin-2, a protein essential for T-tubule maturation, which facilitates the proper coupling between LTCCs on the sarcolemma and RyR2 on the SR located in close proximity, forming a cardiac dyad.[84] This maturation enhances the efficiency of CICR and restricts Ca^{2+} entry from $I_{Ca,\,L}$ to a smaller region.[87-90] A study revealed that the functional coupling between LTCC and RyR2 is weaker in nCMs than in aCMs.[87] This was achieved by conducting a series of experiments, including Ca^{2+}-imaging, patch-clamp, Ca^{2+}-spark analysis, gene and protein analysis, and morphological analysis.[88, 89] The study suggests that the development of cardiomyocytes involves intricate processes during the early stages of cardiac development and that their maturation continues postnatally.[90] Nevertheless, the α-actinin formation resulting in a sufficient contractility ability and the presence of RyR2 and LTCC, spontaneous pacemaker activity, as well as other vital systems like the Gs signaling pathway and SERCA2a/PLN, led to the decision to use nCMs as a model system for the functional analysis of cAMP microdomains around LTCC and RyR2.[87-90]

Initially, three different PACs were used: bPAC[69], bPAC-S27A[72] (red-shifted bPAC), and TpPAC[70]. bPAC-S27A was considered due to its red-shifted activation; however, it was only 10 nm shifted to the red

light and did not significantly improve the imaging conditions. Optogenetic tools activated by red light would be a valuable asset for future applications due to the deeper tissue penetration of red light, facilitating therapeutic applications. Since TpPAC had the lowest dark activity and generally lower cAMP production (**Fig. 14**), it was chosen for further investigation because it would allow a more specific subcellular/local response than the bPACs. bPACs have a higher baseline (dark) activity and an overall higher cAMP production, which would lead to a cAMP "spillover" effect.[70]

In nCMs, local targeting of TpPAC was observed, with some cytosolic background, primarily around the nuclear envelope, but with an overall higher signal intensity at specific locations (**Fig. 27, 47**). It is unclear whether the background expression could be due to newly synthesized proteins being transported to their correct location and thus not being functional, and therefore not contributing to untargeted cAMP signaling, or if it is due to overexpression, thereby contributing to background non-targeted cAMP signaling. Overexpression of optogenetic proteins leads to saturation of their intended binding sites, resulting in excess proteins localizing nonspecifically within the cytosol. A solution for overexpression could be to express the optogenetic tool under the control of a doxycycline-activated promoter, thereby inducing the expression of the optogenetic tool for a limited time.

Co-localization of TpPAC-mCitrine-FKBP12.6 and LOV-PKI-mCitrine-FKBP12.6 with the RyR2 antibody showed a good overlap (**Figs. 27, 47**), indicating the correct localization. Staining of nCMs with the LTCC antibody did not show a precise membrane localization of the antibody. Still, the expression of nb.F3-TpPAC-EYFP and nb.F3-mVenus-LOV-PKI was mainly localized at the membrane, with some less prominent intracellular signals, primarily around the nuclear envelope, similar to the RyR2 targeting constructs (**Fig. 28, 47**).

5.3 Different targeting of TpPAC alters the modulation of beating frequency

The beating rate of the heart is regulated in vivo by SAN cells through two key mechanisms: the M-clock, involving HCN channels and LTCCs, and the Ca^{2+}-clock, driven by rhythmic Ca^{2+} release from the SR via RyR2. Both clocks are modulated by cAMP through PKA-mediated phosphorylation. Since PDEs degrade cAMP, they play a critical role in controlling the rhythmicity of pacemaker activity.[29]

In this work, the beating rate of nCMs was analyzed following local cAMP generation at LTCC by nb.F3-TpPAC-EYFP and at the RyR2 by TpPAC-mCitrine-FKBP12.6, as well as after global cAMP generation by TpPAC-EYFP. Illumination of TpPAC-expressing nCMs resulted in a dose-dependent increase in beating rate, with a similar magnitude and light sensitivity but different kinetics based on microdomain location. Global or local cAMP production at the RyR2 showed a prolonged plateau in beating rate, indicating a sustained cAMP/Ca^{2+} signal compared to local cAMP production at the LTCC. Conversely, the beating rate after cAMP generation at LTCC declined gradually without a clear plateau. The overall impact of cAMP production was the shortest at the RyR2 compared to global and local cAMP production at the LTCC.

The prolonged plateau effect of increased beating rate, after illumination upon global and local cAMP generation at RyR2, might be due to different concentrations of Ca^{2+} released into the cytosol. The activation of the LTCCs allows a small amount (10-20%) of Ca^{2+} to enter the cytosol from the extracellular space. This Ca^{2+} binds to RyR2 on the SR, triggering a significant (80-90%) release of Ca^{2+} from the SR stores into the cytosol (CICR).[4, 114] Other reasons for the absence of a plateau in the elevated beating frequency rate at the LTCC might be due to a negative feedback mechanism of the LTCC, which is inhibited by intracellular Ca^{2+}.[3] Alternatively, activating Ca^{2+}-activated K^+ (K_{Ca}) channels, such as the big potassium channel ($K_{Ca}1.1$), might accelerate repolarization and thus reduce the Ca^{2+} entry through the LTCC.[142] Furthermore, an explanation could also be that SERCA is only activated by global or local cAMP production at the RyR2. This would allow the prolonged plateau of beating rate, which cannot be maintained without increased Ca^{2+} reuptake into the SR. For this reason, the prolonged beating rate plateau is not seen under LTCC cAMP activation (this will be discussed further in Section **5.4**). Another highly speculative explanation for the generation of the prolonged plateau of elevated beating rate could be a higher concentration of PKA or ATP at these sites. It is known that mitochondria are highly concentrated near the SR and thereby provide more ATP for cAMP generation.[115]

Additionally, the differences in kinetics suggest an altered and separated cAMP degradation and signaling machinery, resulting from differences in PDE isoforms within local LTCC or RyR2 microdomains and globally (**Fig. 29, 30**). Different PDE isoforms are regulated by various molecules, resulting in different activation times and efficiencies (**Table 49**).

Table 49: Cardiac PDE isoforms and their kinetics and localization

PDE-Isoform	Regulation	Localization and Association	Reference
PDE1C	Activation: ↑Ca^{2+}/ Calmodulin	Z-/M-lines (striated) in SAN	Fischmeister 2006,[18] Perra 2013,[100]
PDE2A	Activation: cGMP	RyR2 (indirect), cytosolic	Fischmeister 2006,[18] Nikolaev 2006,[103] Perra 2013[100]
PDE3A	Inhibition: cGMP	LTCC, SERCA, ß-AR, cytosolic	Fischmeister 2006,[18] Perra 2013,[100]
PDE4D	Activation: PKA	LTCC, RyR2, HCN, AKAPs	Nikolaev 2006,[103] Perra 2013,[100] Fischmeister 2006[18]
PDE4B	Activation: PKA	RyR2, HCN, SAN	Nikolaev 2006,[103] Kraft 2024[102]
PDE5A	Activation: PKG/cGMP	RyR2 (indirect)	Fischmeister 2006,[18] Nikolaev 2006[103]
PDE8B	Activation: PKA	LTCC (indirect), ß-AR, mitochondria	Pavlidou 2022,[101] Perra 2013, [100] Qasim 2024[140]

Since TpPACs modulate cAMP levels, PDEs regulated by PKA and Ca^{2+} may contribute to the differences observed in beating rate kinetics. The widespread distribution of PKA-activated PDE4D across multiple cardiac signaling microdomains (LTCC, RyR2, HCN) suggests that it alone cannot account for the location-specific differences observed in beating rate kinetics. Instead, two other PDEs: PDE8B and PDE1C, are likely responsible for the distinct cAMP degradation patterns explicitly observed at the LTCC microdomain. [13, 101, 107] Studies in ventricular cardiomyocytes have shown that PDE8B regulates Ca^{2+} transients and $I_{Ca,L}$ currents, in patch clamp experiments with an PDE8B inhibitor (PF-04957325).[101, 104, 105] PDE1C is located near the LTCC and is activated by Ca^{2+}/calmodulin, as demonstrated by its striated distribution along the Z-lines and M-lines of cardiomyocytes.[107, 110-112] PDE8B and PDE1C, which have a negative feedback through PKA and Ca^{2+}, likely account for gradual and instantaneous decreases in beating frequency observed following cAMP generation at the LTCC, effects not seen after cAMP generation at the RyR2 or in the cytosol (**Fig. 29, 30**).

To answer the question of which PDEs are responsible for the gradual and instantaneous decrease in beat frequency at the LTCC, systematic testing of different selective PDE inhibitors such as PDE1: IC295, PDE2: BAY 60-7550, PDE3: amrinone, PDE4: rolipram and PDE8: PF-04957325, as well as global PDE inhibition by IBMX, should be performed in the future.[29,3] Specific PDE inhibition would provide insight into whether the same kinetics are observed at different sites when dissolving the PDE microdomains, thus providing further support for the microdomain hypothesis. Specifically, blocking PDEs would eliminate location-specific differences in beating frequency, such as the prolonged elevation (plateau), confirming that PDE microdomains (not just uncontrolled cAMP diffusion) shape response kinetics. Another approach would be to use PDE activators to reverse the prolonged elevated beating frequency, possibly.

In this work, Rolipram, a well-established PDE4 inhibitor that plays a crucial role in regulating the LTCC and RyR2 under increased cAMP levels, was used as an example to establish the principle of testing PDE inhibitors in beating rate measurements with TpPAC.[103] After adding 10 µM rolipram, the impact of TpPAC-EYFP upon illumination showed a prolonged increase in heart rate compared to the untreated. In particular, an increased duration and peak height in response to light were observed with rolipram (**Fig. 31**). The prolonged TpPAC-EYFP effect after rolipram was expected, as PDE4 inhibition reduced cAMP degradation and led to a subsequent prolonged PKA effect, among other effects, including increased LTCC and RyR2 phosphorylation.[116, 117] The increased beating rate returned to the baseline level, even after prolongation, showing that other PDE isoforms, that are not inhibited by Rolipram, degrade cAMP with an overall delay. It is important to consider that PDE4 accounted for only approximately 15% of the total PDE activity, implying that the remaining 85% was attributable to other factors (PDE isoforms).[117] In the future, a systematic testing of specific PDE inhibitors and activators should be conducted to gain insights into the local microdomains.

5.4 Regulation of Ca^{2+} signaling by local cAMP microdomain generation

To further investigate the role of LTCC and RyR2 microdomains in heart arrhythmia mechanisms, the Ca^{2+} transients were analyzed. Changes in the amplitude or shape of the Ca^{2+} transients provide information about the function of LTCC and RyR2, especially by examining changes in cytosolic Ca^{2+} concentration during systole and diastole.

The effect of global and local cAMP generation at LTCC and RyR2 with TpPAC on Ca^{2+} transients was examined, revealing dose-dependent increases in Ca^{2+} transients with a similar magnitude and light sensitivity at all subcellular locations (**Fig. 36 A, B**). Importantly, local generation of cAMP at the RyR2 with TpPAC-mCitrine-FKBP12.6 results in an increase in diastolic Ca^{2+} levels, possibly by increasing Ca^{2+} leak from the SR, which was not observed with global cAMP generation TpPAC-EYFP or local cAMP generation at the LTCC with nb.F3-TpPAC-EYFP (**Fig. 36 C, D**). These observations suggest that cAMP signaling within the microdomains of LTCC and the cytosol does not significantly influence diastolic Ca^{2+} leak. If such an effect were present, one would also expect to observe a Ca^{2+} leak during cAMP elevation at the LTCC or in the cytosolic compartment, which was not the case. Future experiments could use specific PDE inhibitors to determine whether disrupting local cAMP degradation causes the microdomain structure to break down, potentially allowing a RyR2-mediated Ca^{2+} leak to be triggered by cAMP generated at the LTCC or throughout the cytosol. In contrast, activating PDEs may reveal whether increased cAMP breakdown can suppress or even reverse the observed Ca^{2+} leak.

Additionally, it was observed that the Ca^{2+} transient peaked more rapidly and declined faster during cAMP generation at the RyR2 compared to global or LTCC-targeted cAMP production (see **Fig. 36 A**). Although this trend was not statistically significant, a larger sample size may be needed to confirm the observation (see **Fig. 36 B**). Interestingly, the RyR2-associated Ca^{2+} leak terminated approximately 10 seconds after illumination at 10 µW/mm², suggesting that different regulatory mechanisms control the activation and termination of this leak. A likely explanation for this delay might be that, while RyR2 responds rapidly to local cAMP generation, initiating the Ca^{2+} leak, the subsequent activation of SERCA may depend on the slower diffusion or amplification of the cAMP signal necessary for PLB phosphorylation. Investigating the generation of Ca^{2+} leak is important, because it can promote extrasystoles and impair myocardial relaxation by leaving myofibrils partially activated during diastole. Additionally, elevated cytosolic Ca^{2+} increases the energetic demand on the cell, as more ATP is required for SERCA to return Ca^{2+} to the SR.

The FKBP12.6 protein plays a critical role in regulating Ca^{2+} leak from the SR in cardiac cells.[118] FKBP12.6 binds with a high affinity to the central cytosolic domain of RyR2, forming a complex that helps maintain the structural integrity of the channel, prevents unwanted conformational changes, and supports proper protein folding. Furthermore, this interaction is essential for regulating the gating

properties of RyR2. Under resting conditions, FKBP12.6 maintains the RyR2 channels in a closed state, thereby preventing inappropriate Ca^{2+} release during diastole (Ca^{2+} leak). PKA-mediated phosphorylation of RyR2 results in the temporary dissociation of FKBP12.6, thereby increasing the channel's open probability. By maintaining this balance, FKBP12.6 helps protect against potentially life-threatening arrhythmias. [10, 118, 119, 120, 121]

Studies in FKBP12.6-deficient (FKBP12.6$^{-/-}$) mice have revealed an increased susceptibility to AF/VF and AT/VT. This highlights the link between impaired SR Ca^{2+} leak, which contributes to diastolic Ca^{2+} overload and/or activates the NCX, resulting in DADs. These DADs can subsequently trigger premature atrial or ventricular contractions, leading to arrhythmias such as VT/AT or VF/AF.[120] An impaired interaction between RyR2 and FKBP12.6 has been demonstrated in diseases such as CPVT or arrhythmogenic right ventricular cardiomyopathy (ARVC), thereby increasing susceptibility to VT and VF.[118, 121]

The development of arrhythmias is further facilitated by hyperphosphorylation of Ca^{2+} handling proteins such as LTCCs, RyR2, and PLN. Hyperphosphorylation can result from various mechanisms, including the disruption of PDE function, overactivation of protein kinases such as PKA, PKC, or CaMKII, impaired protein phosphatase activity like PP1 or PP2A, altered adrenergic signaling, oxidative stress, as well as mutations or genetic disorders.[6, 29,126, 127] In PDE4D knockout mice, hyperphosphorylation of RyR2 by PKA has been observed to result in SR Ca^{2+} leak, increased arrhythmia sensitivity, dilated cardiomyopathy, and accelerated progression of heart failure.[121, 125]

Increased phosphorylation of LTCCs, particularly at specific sites such as Ser1928, can lead to enhanced Ca^{2+} entry during each AP. This prolonged or excessive Ca^{2+} influx prolongs the plateau phase (phase 2) of the AP, delaying repolarization and extending the QT interval, and thereby can contribute to arrhythmias, LQTS, and altered contractility by increasing CICR.[127, 128] Additionally, it has been shown that increased PDE2 activity is associated with alterations in cAMP dynamics within LTCC microdomains in heart failure with reduced ejection fraction (HFrEF), including a redistribution of LTCC to the crest and uncoupling from RyR2 as well as altered SERCA activity. These alterations affect Ca^{2+} entry and, again, the opening of RyR2.[128]

In general, hyperphosphorylation disrupts the interplay of Ca^{2+} handling proteins, exacerbating contractile dysfunction and promoting myocardial damage in HF. Chronic Ca^{2+} dysregulation can induce structural changes, such as fibrosis, creating arrhythmogenic substrates that perpetuate AF and ventricular arrhythmias.[126, 127] The result of the Ca^{2+} transient experiment indicates that RyR2 phosphorylation, due to the increased diastolic Ca^{2+}, has a higher impact on arrhythmias than LTCC phosphorylation.

Promising therapeutic strategies targeting FKBP12.6 dysfunction have been developed to restore its binding to RyR2 or stabilize RyR2 channels. Rycals have demonstrated efficacy in mitigating Ca^{2+} leak and averting arrhythmias in experimental models.[122, 137] One example is the Rycal: S107, which stabilizes the interaction between FKBP12.6 and RyR2, preventing FKBP12.6 dissociation and reducing Ca^{2+} leak. It has been shown to improve cardiac function in experimental models of heart failure and CPVT.[123, 140] Another Rycal: ARM210 specifically stabilizes dysfunctional RyR channels without interfering with normal physiological Ca^{2+} release.[141] Ongoing clinical trials will provide valuable insights into its effectiveness, safety, and potential to transform the management of Ca^{2+} handling disorders.

Addressing the Ca^{2+} leak through the RyR2 via cAMP/PKA-mediated phosphorylation would significantly reduce the risk of arrhythmias and heart failure, and improve patient outcomes. Using TpPAC-mCitrine-FKBP12.6 to induce Ca^{2+} leak in cardiomyocytes and subsequently test for Ca^{2+} leak blockers is a promising screening tool for identifying new potential medications such as Rycals.

5.5 Higher phosphorylation sensitivity to low light in TpPAC-mCitrine-FKBP

In light of the well-documented severe effects of hyperphosphorylation on cardiac function,[125, 126, 136] as well as the findings from the previous analyses of beating rate and Ca^{2+} transients at the local level of LTCC, RyR2, and global cAMP generation, it is important to investigate the differences in phosphorylation at these microdomain locations.

The PKA phosphorylation site-specific antibody RRXS*/T*[83] was used to investigate the phosphorylation effect after global and local cAMP generation in nCMs. First, the antibody was used in Western blot analysis. Then, it was used in single-cell imaging of immunohistological stainings, establishing a newly developed method for investigating phosphorylation status.

Western blot analysis with the RRXS*/T* antibody of nCMs with global and local cAMP generation showed an increase in total RRXS*/T* signal intensity compared to dark control (**Fig. 38**). However, since the samples for Western blot analysis contain all cells, including many non-transfected CMs (transfection rate about 11% **Fig. 25**) and fibroblasts, a second approach was established to examine single cell immunohistological staining. This immunohistological staining method enabled us to automatically analyze thousands of cells regarding their phosphorylation level, combined with the detection of cell type and fluorescent marker using a newly developed analysis routine, GA3 from Nikon.

Only the cytosolic signal was used for immunohistological staining analysis with the RRXS*/T* antibody because the nucleus showed high basal staining. Illumination of nCMs with TpPAC-EYFP, nb.F3-TpPAC-EYFP, and TpPAC-mCitrine-FKBP12.6 resulted in a significant increase in RRXS*/T* signals in a dose-dependent manner. At maximal illumination, a 2.7-fold increase in RRXS*/T* signal was observed for TpPAC-EYFP, a 3.7-fold increase for nb.F3-TpPAC-EYFP, and a 1.8-fold increase for TpPAC-mCitrine-FKBP12.6, compared to the dark control (**Fig. 41 F**).

Interestingly, nCMs with TpPAC-mCitrine-FKBP12.6 showed a higher sensitivity to low light compared to TpPAC-EYFP and nb.F3-TpPAC-EYFP nCMs (**Fig. 44**). It was observed that low light illumination induced an RRXS*/T* signal intensity of 85% of maximal illumination intensity in TpPAC-mCitrine-FKBP12.6, while in TpPAC-EYFP and nb.F3-TpPAC-EYFP it was only 45% and 43% of the maximal effect of illumination intensity, respectively.

The increased sensitivity to low levels of cAMP production observed with TpPAC-mCitrine-FKBP12.6 at the RyR2 (**Fig. 44**) may be linked to elevated local PKA activity, resulting in enhanced RyR2 phosphorylation. Alternatively, a higher mitochondrial density within this microdomain could increase ATP availability, thereby supporting greater cAMP synthesis.[115] This hypothesis is consistent with the observations made in the frequency results section.

Alternatively, the observed differences may stem from variations in how phosphorylation signals, particularly those mediated by PKA and CaMKII, are regulated. Both LTCC and RyR2 are essential components of cardiac excitation–contraction coupling and are targets of PKA-mediated phosphorylation. However, RyR2 exhibits a greater phosphorylation response to cAMP compared to LTCC.[6, 126] This difference is likely due to the presence of multiple phosphorylation sites on RyR2 (e.g., PKA sites Ser2808 and Ser2030; CaMKII site Ser2814), which enable more complex and finely tuned regulatory control.[125, 126, 130] In contrast, LTCC has fewer major phosphorylation sites, such as Ser1928 and Ser1700 for PKA and Thr1704 for CaMKII, resulting in a more straightforward and limited regulatory pattern. [6, 126] The greater number and diversity of RyR2 phosphorylation sites enable it to integrate multiple signaling pathways, thereby contributing to its heightened sensitivity to cAMP/PKA signaling compared to LTCC.[3]

Additionally, an insufficient degradation of cAMP by phosphodiesterases (PDEs) in the RyR2 microdomain may lead to excessive local cAMP accumulation, resulting in RyR2 hyperphosphorylation and subsequent Ca^{2+} leak (see Chapters **5.3** and **5.4**). In contrast, hyperphosphorylation at the LTCC appears to be more effectively regulated, as evidenced by the absence of sustained increases in beating frequency or Ca^{2+} leak following cAMP elevation via TpPAC activation. This could be due to better PDE regulation or feedback mechanisms, such as the inactivation of the LTC by Ca^{2+}, or the activation of Ca^{2+}-activated K^+ (K_{Ca}) channels (see discussion in Chapter **5.3**).

The RyR2 microdomain shows increased sensitivity to light-induced cAMP production, demonstrated by a Ca^{2+} leak, a plateau in the elevated beating rate, and a stronger response at lower light intensities compared to the LTCC. This distinct responsiveness indicates that RyR2 is more susceptible to cAMP/PKA-mediated modulation, likely due to differences in local PDE activity or AKAP-anchored signaling complexes. Consequently, RyR2's heightened phosphorylation sensitivity poses a significant risk for pathological Ca^{2+} leak and arrhythmia development.

5.6 Local and global PKA inhibition in cardiomyocytes by LOV-PKI

A second approach to studying the modulation of LTCC and RyR2 microdomains involved inhibiting PKA globally and locally. To investigate global and local PKA inhibition, the optogenetic tool LOV-PKI, which releases the PKA inhibitor peptide PKI upon illumination, was fused to nb.F3 and FKBP12.6 for subcellular location. Western blot analysis (**Fig. 46**) and immunohistological staining (**Fig. 47**) showed that the distribution was similar to that previously seen with TpPAC fusion constructs.

To confirm the functional light-dependent inhibition of PKA by the optogenetic fusion constructs, changes in beating frequency following illumination were analyzed (**Fig. 48**). Light activation of global and local-targeted PKA inhibition at the LTCC and the RyR2, resulted in a sustained reduction in beating frequency (lasting 5–30 minutes), accompanied by irregular beating rates, across all constructs, confirming PKI function upon illumination. The decrease in beating rate (minimum after illumination compared to baseline) was not significant for LOV-PKI-mVenus, but nb.F3-LOV-PKI-mVenus (*: $p = 0.0450$) and LOV-PKI-mCitrine-FKBP12.6 (*: $p = 0.0477$) reached statistical significance. Notably, local PKA inhibition at RyR2 via LOV-PKI-mCitrine-FKBP12.6 induced a transient increase in frequency, before the sustained decrease in 2 out of 3 experiments. This initial rise was further amplified and prolonged by 10 µM rolipram, a PDE4 inhibitor that prevents cAMP degradation through PDE4 (**Fig. 50**). Immunohistological stainings using the RRXS*/T* PKA phosphorylation-site-specific antibody confirmed that LOV-PKI-mCitrine-FKBP12.6 reduced PKA-dependent phosphorylation, validating its inhibitory function. Moreover, in the presence of 10 µM rolipram, the decrease in phosphorylation caused by LOV-PKI-mCitrine-FKBP12.6 was reversed (**Fig. 51**), supporting the role of enhanced cAMP levels in the transient frequency increase.

As we observed only an initial increase in frequency with LOV-PKI-mCitrine-FKBP12.6, but not with LOV-PKI-mVenus or nb.F3-LOV-PKI-mVenus, this may suggest different regulatory microdomains. One explanation could be that the soluble ACs surrounding the RyR2 may be more sensitive and susceptible to regulation by the PKA feedback mechanism (**Fig. 52 A**) than those ACs surrounding the LTCC and cytosol. ACs generate cAMP, activating PKA, which in turn inhibits AC activity as a negative feedback mechanism. The transient frequency increase after LOV-PKI-mCitrine-FKBP12.6 activation can be related to the absence of PKA inhibition of local ACs; therefore, cAMP increases from the basal level (**Fig 52 A**). Consequently, the absence of this inhibition leads to elevated cAMP levels, which likely activate HCN channels. At the same time, the effects on LTCC and RyR2 are expected to remain limited due to ongoing PKA inhibition by LOV-PKI. Rolipram, a PDE4 inhibitor, increases cAMP levels in cardiomyocytes, thereby sustainably increasing the beating rate by enhancing HCN activity (**Fig. 52 B**).

Among AC isoforms, the transmembrane ACs tmAC5 and tmAC6 are predominant in cardiomyocytes and primarily localized to the plasma membrane, where they regulate the LTCC microdomain via cAMP

production in response to GPCR signaling.[130] And both are modulated by Ca^{2+} and PKA.[131, 132, 133] In contrast, soluble ACs (sACs) are cytosolic enzymes found in organelles such as mitochondria and have been implicated in local cAMP production at RyR2.[134] sAC activity may contribute to the enhanced cAMP sensitivity at RyR2, supporting more extensive phosphorylation required for Ca^{2+} release, but potentially promoting hyperphosphorylation and arrhythmogenesis under pathological conditions.[129–136]

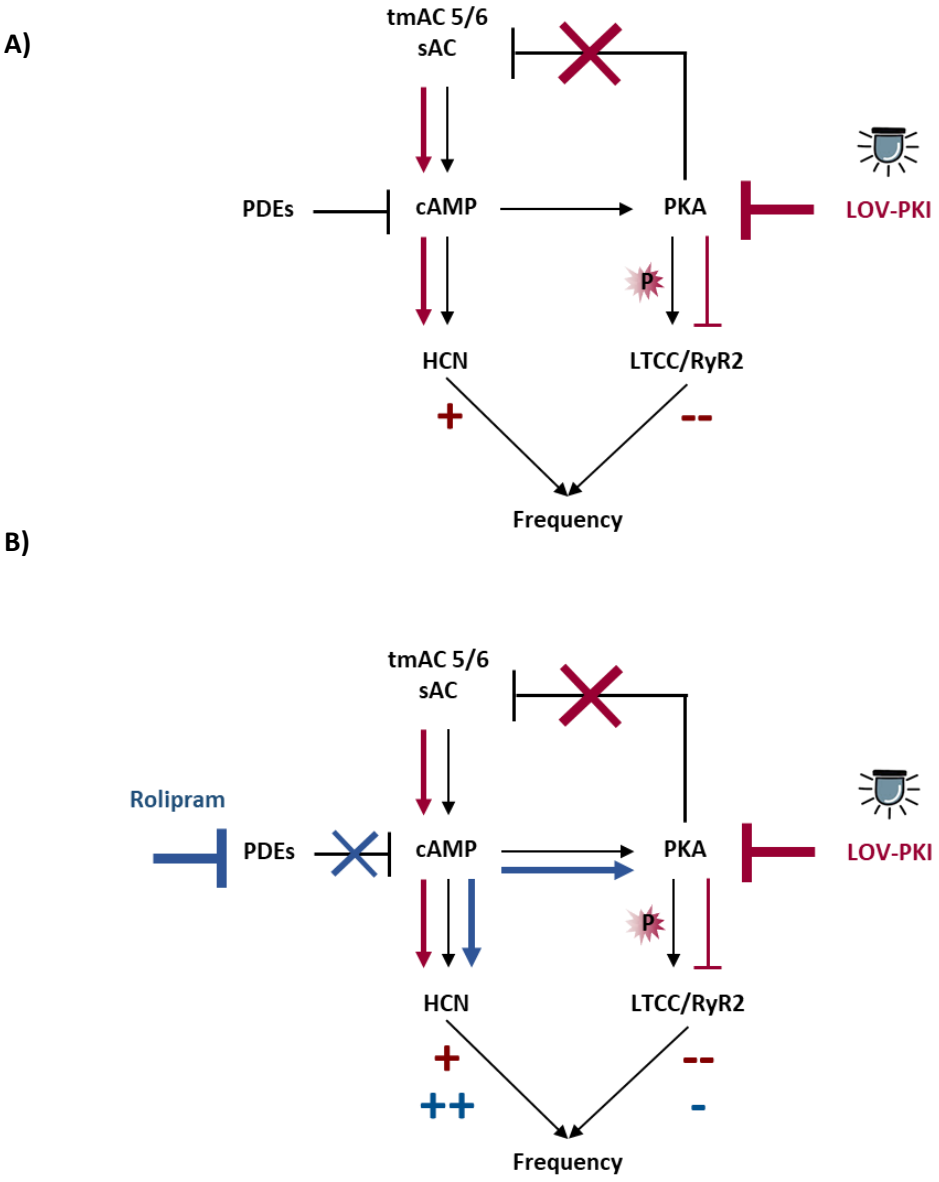

Fig. 52: Feedback loop of the cAMP/PKA signaling pathway
ACs generate cAMP, which activates PKA and can inhibit AC activity as a feedback mechanism. Increased cAMP and PKA activity enhance the beating frequency in cardiomyocytes by activating HCN, LTCC, and RyR2. LOV-PKI inhibits PKA phosphorylation, resulting in a decrease in the beating rate. Still, in some cases, it can lead to a temporary increase in frequency because the feedback mechanism that inhibits ACs is missing; therefore, more cAMP is present, which activates the HCNs. This was only observed with LOV-PKI-FKBP and might indicate a different AC regulation. Rolipram, a PDE4 inhibitor, increases cAMP levels in cardiomyocytes, increasing HCNs activity. Red = LOV-PKI effect, blue = Rolipram effect, black = normal.

5.7 Therapeutic potential of targeted cAMP microdomains and their outlook

In summary, the findings of this study demonstrate that the production of cAMP, both globally and locally at the RyR2, results in a constant plateau (>50 s) of the increased beating rate effect, indicative of the generation of a "large" cAMP pool. The RyR2 has a greater vulnerability to the effect of cAMP than the LTCC, as evidenced by the absence of a plateau in the increase of beating rate after LTCC light-activation. Furthermore, the observed increase in diastolic Ca^{2+} levels resulting from local cAMP generation at the RyR2, may be due to enhanced Ca^{2+} leak from the SR. This phenomenon was not observed with local cAMP generation at the LTCC or with global cAMP generation. The heightened sensitivity of RyR2 to low light (low cAMP generation), in contrast to the LTCC or the cytosol, further supports the idea that RyR2 plays a more significant role in cAMP/PKA dependant arrhythmias than the LTCC. Factors contributing to RyR2 deregulation and increased arrhythmia risk may include hyperphosphorylation, insufficient PDE activity, and disruption of FKBP12.6 stabilisation.

These mechanistic insights into RyR2's heightened sensitivity to local cAMP signaling not only establish its central role in pathological Ca^{2+} handling but also point toward actionable molecular targets for therapeutic intervention. Building on these findings, several strategies emerge that could address the underlying causes of RyR2 dysfunction and restore Ca^{2+} homeostasis in cardiac disease.

To address dysregulated cAMP signaling and RyR2 hyperphosphorylation, several pharmacological interventions show promise. One key strategy involves restoring local PDE activity to prevent cAMP accumulation and downstream overactivation of kinases. Specifically, activating Ca^{2+}/CaM-activated PDE1 or PKA-activated PDE4 may reduce cAMP levels and suppress diastolic Ca^{2+} leak. In parallel, inhibition of PKA and CaMKII may prevent excessive phosphorylation of RyR2 and LTCCs. Enhancing phosphatase activity (e.g., PP1, PP2A) could help reestablish balance in phosphorylation dynamics. Oxidative stress, which contributes to RyR2 hyperphosphorylation and FKBP12.6 dissociation, represents another therapeutic target. Antioxidant strategies may indirectly stabilize RyR2 function and improve EC coupling. TpPAC-based localized optogenetic cAMP modulation provides a powerful platform for investigating compartment-specific signaling and drug responses, including the screening of compounds like Rycals that stabilize RyR2–FKBP12.6 interactions and reduce Ca^{2+} leak. This platform could be extended to other subcellular domains, such as the PLN microdomain. However, the PLN-targeted construct presented technical challenges due to protein aggregation and was therefore not further investigated in this study. Nevertheless, TpPAC-based methods are highly valuable for the functional screening of therapeutic compounds, including Rycals, which stabilize the RyR2–FKBP12.6 interaction.

Although pharmacological therapies are promising, they must be tightly regulated to avoid off-target effects. Gene therapy offers a solution for tissue-specific treatments. Although the CUPID 1 (Calcium

Up-Regulation by Percutaneous Administration of Gene Therapy in Cardiac Disease) trial targeting SERCA2a did not improve outcomes in heart failure, the concept of enhancing SR Ca^{2+} uptake remains valid. However, SERCA2a overexpression may increase the risk of Store-Overload-Induced Calcium Release (SOICR) and should be approached cautiously.[124, 125] Future gene therapy efforts may focus instead on AAV-mediated delivery of PDEs, such as PDE1C or PDE4, as well as the FKBP12.6 protein, directly to RyR2 microdomains to restore RyR2 stabilization and reduce arrhythmogenic Ca^{2+} leak. This targeted approach may provide more effective and precise correction of local cAMP signaling defects than global SERCA2a overexpression.

To overcome the tissue specificity and off-target challenges of systemic drugs, a cardiac-targeted optogenetic approach using AAV-mediated delivery of light-controlled tools may offer unparalleled precision. By modulating subcellular signaling domains in a cell-type- and light-dependent manner, such strategies could precisely correct pathological signaling with minimal side effects.

Furthermore, techniques such as phospho-proteome analysis provide valuable insights into local phosphorylation patterns under various conditions (e.g., normal vs. diseased heart), helping to elucidate cardiac pathophysiology and identify new therapeutic targets.

Generating mouse models of TpPAC-EYFP, nb.F3-TpPAC-EYFP, and TpPAC-mCitrine-FKBP12.6, and testing these models in aCMs to investigate patch clamp and Ca^{2+} sparks, as well as drug screening by reversing diastolic Ca^{2+} leak, will be essential for a comprehensive understanding and the development of therapeutic strategies.

Ultimately, translating these findings into the clinic may enable precision medicine approaches in cardiology, tailoring interventions based on individual subcellular signaling fingerprints to improve efficacy while minimizing adverse effects.

6 Study limitations

This study was primarily conducted on nucleofected nCMs that expressed the PAC constructs. Using mouse nCMs as a model to study LTCC and RyR2 modulation and regulation has significant limitations. While mouse nCMs are a valuable model for studying LTCC and RyR2 modulation, they present several limitations. First, experiments in isolated single cells do not replicate the physiological context of the intact heart and its syncytial electrical conduction. However, this reductionist approach is necessary for dissecting specific signaling and ion channel mechanisms. Second, there are significant species differences in calcium handling. In humans, approximately 70% of cytosolic Ca^{2+} is released into the cytosol from the SR, whereas in mice, this proportion reaches up to 90%. In addition, the expression profiles of ion channels, particularly repolarizing K^+ channels, differ significantly between mice and humans. Mouse nCMs also lack T-tubules, resulting in altered spatial organization of LTCCs and RyR2s compared to adult ventricular cardiomyocytes. These developmental and structural differences may affect excitation-contraction coupling and localized cAMP signaling.[83-87] Despite these limitations, mouse nCMs remain a robust and widely accepted system for investigating SR/RyR2 Ca^{2+} leak-induced arrhythmias, given their strong reliance on SR Ca^{2+} release for Ca^{2+} transients.

Another limitation of this study is the technical variability; the nucleofection leads to variable TpPAC expression levels between cells due to the differing amounts of DNA integrated. The gold standard would be a knock-in of TpPACs into the endogenous genome, which is only possible for TpPAC-mCitrine-FKBP12.6, as FKBP12.6 is endogenously expressed. Obtaining a high number of samples for the frequency and Ca^{2+} imaging experiments was challenging, as the cells had to meet several strict criteria: they needed to be confirmed nCMs, successfully transfected, exhibit regular spontaneous beating for frequency measurements, and for Ca^{2+} imaging, respond reliably to external pacing and tolerate the Ca^{2+} dye well.

Optogenetic tools, such as TpPACs, allow for precise spatial and temporal control of intracellular cAMP generation without activating broader β-adrenergic pathways. However, limitations persist. Blue light activation can be technically restrictive to working under far red light when used with other imaging techniques (e.g., Ca^{2+} imaging or beating frequency measurements). Heterogeneous light intensities across the field of view may also lead to uneven stimulation, complicating data interpretation.

From a translational perspective, while optogenetics represents a powerful approach for dissecting subcellular signaling, its therapeutic application still faces major challenges. These include the engineering of light-sensitive proteins with optimized kinetics and spectral properties, improving light delivery to deep tissue, and achieving efficient and cell-type-specific expression of optogenetic constructs.

7.1 Summary

In cardiomyocytes, cAMP/PKA-dependent phosphorylation of LTCC and RyR2 increases Ca^{2+} transient and contractile force. Due to the proximity of both proteins, it remains unclear whether their cAMP/PKA microdomains are functionally separated or cross-talk. To investigate differences in selective phosphorylation, localized cAMP microdomains were selectively generated at the LTCC and RyR2 using a novel optogenetic approach that subcellularly targets photo-activated adenylate cyclase from *Turneriella parva* (TpPAC). TpPAC was targeted together with EYFP or mCitrine to RyR2 by fusion with the high-affinity protein FKBP12.6 and to the LTCC ß-subunit by fusion with a specific nanobody (nb.F3). TpPAC-EYFP was used as a control for global cytosolic cAMP generation. Intact light-dependent cAMP generation by TpPAC fusion proteins was detected in HEK293 cells co-expressing the cAMP-sensitive GloSensor, where blue light increased cAMP levels dose-dependently.

After expression in nCMs, TpPAC-EYFP showed a homogeneous distribution. TpPAC-mCitrine-FKBP12.6 localized near the Z-discs, indicating RyR2 targeting, while nb.F3-TpPAC-EYFP showed cell membrane targeting. However, both targeted TpPACs also exhibited some background cytosolic expression. Brief flashes of blue light induced a transient increase in spontaneous beating rate in all constructs in a light dose-dependent manner. The global production of cAMP in the cytosol and the local production at RyR2 by brief light pulses resulted in a long-lasting, constant plateau of the increased beating rate effect. In contrast, the effect of cAMP generation locally at the LTCC declined after its peak, without a clear plateau. The kinetic differences suggest the light-induced generation of a "large" cAMP pool in the cytosol and the RyR2 microdomain, as well as a rapid PDE activation or feedback mechanism in the LTCC microdomain. Ca^{2+} imaging of cardiomyocytes revealed a dose-dependent light-induced increase in the Ca^{2+} transient height with all three constructs. Interestingly, only the local generation of cAMP at RyR2 increased diastolic Ca^{2+} levels. Furthermore, low-intensity light stimulation of cAMP production at RyR2 resulted in PKA phosphorylation levels reaching 85% of the maximum observed with high-intensity illumination. In contrast, the same low-light conditions resulted in only 45% of maximal phosphorylation with cytosolic cAMP production and 43% at the LTCC, indicating that RyR2 exhibits a higher sensitivity to cAMP phosphorylation. The higher vulnerability of the RyR2 microdomain to cAMP may be an important mechanism in developing cardiac arrhythmias.

In a second preliminary approach, the inhibition of PKA with the optogenetic LOV-PKI protein was analyzed. A decrease in beating rate and phosphorylation levels was observed upon LOV-PKI illumination globally and locally at the LTCC and RyR2. These subcellular targeted optogenetic tools present a promising concept for further investigating the complex regulatory mechanisms of microdomains, compared to pharmacological or FRET-based research and present a platform for drug screenings.

7.2 Zusammenfassung

In Kardiomyozyten steigert die cAMP/PKA-abhängige Phosphorylierung von LTCC und RyR2 die Ca^{2+}-Transienten und die kontraktile Kraft. Da beide Proteine räumlich nah beieinander liegen, ist unklar, ob ihre cAMP/PKA-Mikrodomänen funktionell getrennt sind oder miteinander kommunizieren. Zur Untersuchung selektiver Phosphorylierung wurde ein neuartiger optogenetischer Ansatz eingesetzt, bei dem die photoaktivierte Adenylatzyklase aus Turneriella parva (TpPAC) gezielt subzellulär lokalisiert wurde, um cAMP-Mikrodomänen an LTCC und RyR2 zu erzeugen. TpPAC wurde mit EYFP oder mCitrine fusioniert – entweder mit dem hochaffinen Protein FKBP12.6 zur RyR2-Bindung oder mit dem spezifischen Nanokörper nb.F3 zur Bindung an die β-Untereinheit des LTCC. TpPAC-EYFP diente als Kontrolle für globale zytosolische cAMP-Produktion. Die funktionelle, lichtabhängige cAMP-Erzeugung konnte in HEK293-Zellen mithilfe des cAMP-sensitiven GloSensors nachgewiesen werden, wobei blaues Licht dosisabhängig den cAMP-Spiegel erhöhte.

Nach Expression in neonatalen Kardiomyozyten zeigte TpPAC-EYFP eine homogene Verteilung, während TpPAC-mCitrine-FKBP12.6 an den Z-Scheiben lokalisiert war, was eine gezielte Lokalisierung am RyR2 nahelegt. nb.F3-TpPAC-EYFP zeigte eine Membranlokalisation und damit eine Lokalisierung am LTCC. Beide Konstrukte wiesen jedoch auch zytosolische Hintergrundexpression auf. Kurze Lichtpulse führten bei allen Konstrukten zu einem dosisabhängigen Anstieg der Spontanschlagrate. Während globale cAMP-Produktion im Zytosol und lokale Produktion am RyR2 zu einem stabilen Frequenzplateau führten, fiel die Wirkung am LTCC nach einem Peak wieder ab, vermutlich durch schnelle PDE-Aktivierung oder Rückkopplungsmechanismen.

Ca^{2+}-Bildgebung zeigte bei allen drei Konstrukten einen licht- und dosisabhängigen Anstieg der Transientenhöhe. Interessanterweise führte nur die lokale cAMP-Erzeugung an RyR2 zu einem Anstieg des diastolischen Ca^{2+}-Spiegels. Zudem bewirkte geringe Lichtintensität (geringe cAMP Produktion) am RyR2 bereits 85% der maximalen PKA-Phosphorylierung (im Vergleich zur starken Beleuchtung), während unter denselben Bedingungen nur 45% bei zytosolischer und 43% bei LTCC-gerichteter cAMP-Produktion erreicht wurden. Dies weist auf eine besonders hohe Phosphorylierungsempfindlichkeit von RyR2 gegenüber cAMP hin und einen möglichen Mechanismus in der Entstehung von Arrhythmien.

In einem zweiten, vorläufigen Ansatz wurde die optogenetische Hemmung der PKA durch LOV-PKI untersucht. Lichtaktiviertes LOV-PKI reduzierte die Schlagfrequenz sowie die Phosphorylierungsniveaus global und lokal am LTCC und RyR2. Diese gezielten optogenetischen Werkzeuge bieten eine vielversprechende Alternative zur pharmakologischen oder FRET-basierten Analysen und eine Plattform zur Untersuchung subzellulärer Signalwege und zum Medikamentenscreening.

8. References

1. Von Skramlik, E. Die Regelung der Strömungsrichtung des Blutes [The regulation of direction of the blood flow]. *Experientia* 10, 441–454 (**1954**).
2. Klinke, R., Pape, H.-C. & Silbernagel, S. *Physiologie* (Georg Thieme Verlag, **2005**).
3. Zipes, D. P., Jalife, J. & Stevenson, W. G. *Cardiac Electrophysiology: From Cell to Bedside* (Elsevier, **2018**).
4. Capogrossi, M. C. et al. Synchronous occurrence of spontaneous localized calcium release from the sarcoplasmic reticulum generates action potentials in rat cardiac ventricular myocytes at normal resting membrane potential. *Circ. Res.* 61, 498–503 (**1987**).
5. Bers, D. M. Cardiac excitation–contraction coupling. *Nature* 415, 198–205 (**2002**).
6. Wei, J. et al. RyR2 Serine-2030 PKA Site Governs Ca2+ Release Termination and Ca2+ Alternans. *Circ. Res.* 132, e59–e77 (**2023**).
7. Wei, J. et al. Ca2+-CaM Dependent Inactivation of RyR2 Underlies Ca2+ Alternans in Intact Heart. *Circ. Res*. 128, e63–e83 (**2021**).
8. Sasse, P et al. Intracellular Ca2+ oscillations, a potential pacemaking mechanism in early embryonic heart cells. *J Gen Physiol*. 130, 133-44 (**2007**).
9. Lakatta, E. G. et al. A coupled SYSTEM of intracellular Ca2+ clocks and surface membrane voltage clocks controls the timekeeping mechanism of the heart's pacemaker. *Circ Res.* 106, 659-73 (**2010**).
10. Marx, S. O. et al. PKA phosphorylation dissociates FKBP12.6 from the calcium release channel (ryanodine receptor): defective regulation in failing hearts. *Cell* 101, 365–376 (**2000**).
11. Baker, J. G. & Hill, S. J. Multiple GPCR conformations and signalling pathways: implications for antagonist affinity estimates. *Trends Pharmacol. Sci.* 28, 374–381 (**2007**).
12. Gilchrist, A. Modulating G-protein-coupled receptors: from traditional pharmacology to allosterics. *Trends Pharmacol. Sci.* 28, 431–437 (**2007**).
13. Bristow, M. R., Hershberger, R. E., Port, J. D., Minobe, W. & Rasmussen, R. Beta 1- and beta 2-adrenergic receptor-mediated adenylate cyclase stimulation in nonfailing and failing human ventricular myocardium. *Mol. Pharmacol.* 35, 295–303 (**1989**).
14. De Jong, K. A. & Nikolaev, V. O. Multifaceted remodelling of cAMP microdomains driven by different aetiologies of heart failure. *FEBS J.* 288, 6603–6622 (**2021**).
15. Kobilka, B. K. & Deupi, X. Conformational complexity of G-protein-coupled receptors. *Trends Pharmacol. Sci.* 28, 397–406 (**2007**).

16. Timofeyev, V. *et al.* Adenylyl cyclase subtype–specific compartmentalization: differential regulation of L-type Ca^{2+} current in ventricular myocytes. *Circ. Res.* 112, 1567–1576 (**2013**).
17. Isensee, J. *et al.* PKA-RII subunit phosphorylation precedes activation by cAMP and regulates activity termination. *J. Cell Biol.* 217, 2167–2184 (**2018**).
18. Fischmeister, R. *et al.* Compartmentation of cyclic nucleotide signaling in the heart: the role of cyclic nucleotide phosphodiesterases. *Circ. Res.* 99, 816–828 (**2006**).
19. Diviani, D. & Scott, J. D. AKAP signaling complexes at the cytoskeleton. *J. Cell Sci.* 114, 1431–1437 (**2001**).
20. Feliciello, A. *et al.* The biological functions of A-kinase anchor proteins. *Cell. Signal.* 13, 21–35 (**2001**).
21. Mauban, J., O'Donnell, M., Warrier, S., Manni, S. & Bond, M. AKAP-scaffolding proteins and regulation of cardiac physiology. *Physiology (Bethesda)* 24, 78–87 (**2009**).
22. Nichols, C. B. *et al.* Sympathetic stimulation of adult cardiomyocytes requires association of AKAP5 with a sub-population of L-type calcium channels. *Circ. Res.* 107, 747–756 (**2010**).
23. Sacchetto, R., Damiani, E. & Margreth, A. Clues to calcineurin function in mammalian fast-twitch muscle. *J. Muscle Res. Cell Motil.* 22, 545–559 (**2001**).
24. Wang, L. *et al.* UCR1C is a novel activator of phosphodiesterase 4 (PDE4) long isoforms and attenuates cardiomyocyte hypertrophy. *Cell. Signal.* 27, 908–922 (**2015**).
25. Kapiloff, M. S., Schillace, R. V., Westphal, A. M. & Scott, J. D. mAKAP: an A-kinase anchoring protein targeted to the nuclear membrane of differentiated myocytes. *J. Cell Sci.* 112, 2725–2736 (**1999**).
26. Dodge-Kafka, K. L. *et al.* The protein kinase A anchoring protein mAKAP coordinates two integrated cAMP effector pathways. *Nature* 437, 574–578 (**2005**).
27. Dodge, K. L. et al. mAKAP assembles a protein kinase A/PDE4 phosphodiesterase cAMP signaling module. *EMBO J.* 20, 1921–1930 (**2001**).
28. Lygren, B. et al. AKAP complex regulates Ca^{2+} re-uptake into heart sarcoplasmic reticulum. *EMBO Rep.* 8, 1061–1067 (**2007**).
29. Essayan, D. M. Cyclic nucleotide phosphodiesterases. *J. Allergy Clin. Immunol.* 108, 671–680 (**2001**).
30. Engelhardt, S., Hein, L., Wiesmann, F. & Lohse, M. J. Progressive hypertrophy and heart failure in beta1-adrenergic receptor transgenic mice. *Proc. Natl Acad. Sci. USA* 96, 7059–7064 (**1999**).
31. Schäfer, M. et al. Hypertrophic effect of selective beta(1)-adrenoceptor stimulation on ventricular cardiomyocytes from adult rat. *Am. J. Physiol. Cell Physiol*. 279, C495–C503 (**2000**).

32. Schäfer, M., Frischkopf, K., Taimor, G., Piper, H. M. & Schlüter, K. D. Hypertrophic effect of selective beta(1)-adrenoceptor stimulation on ventricular cardiomyocytes from adult rat. *Am. J. Physiol. Cell Physiol.* 279, C495–C503 (**2000**).
33. Nikolaev, V. O., Bünemann, M., Schmitteckert, E., Lohse, M. J. & Engelhardt, S. Cyclic AMP imaging in adult cardiac myocytes reveals far-reaching beta1-adrenergic but locally confined beta2-adrenergic receptor-mediated signaling. *Circ. Res.* 99, 1084–1091 (**2006**).
34. Milano, C. A. et al. Enhanced myocardial function in transgenic mice overexpressing the β2-adrenergic receptor. *Science* 264, 582–586 (**1994**).
35. Kuschel, M. et al. β2-adrenergic cAMP signaling is uncoupled from phosphorylation of cytoplasmic proteins in canine heart. *Circulation* 99, 2458–2465 (**1999**).
36. Piscione, F. et al. Effects of Ile164 polymorphism of beta2-adrenergic receptor gene on coronary artery disease. *J. Am. Coll. Cardiol.* 52, 1381–1388 (**2008**).
37. Patterson, A. J. et al. Protecting the myocardium: a role for the beta2 adrenergic receptor in the heart. *Crit. Care Med*. 32, 1041–1048 (**2004**).
38. Lyon, A. R. et al. Loss of T-tubules and other changes to surface topography in ventricular myocytes from failing human and rat heart. *Proc. Natl Acad. Sci. USA* 106, 6854–6859 (**2009**).
39. Fu, Y. et al. Deletion of the distal C terminus of CaV1.2 channels leads to loss of β-adrenergic regulation and heart failure in vivo. *J. Biol. Chem.* 286, 12617–12626 (**2011**).
40. Hulme, J. T. et al. Beta-adrenergic regulation requires direct anchoring of PKA to cardiac CaV1.2 channels via a leucine zipper interaction with A kinase-anchoring protein 15. *Proc. Natl Acad. Sci. USA* 100, 13093–13098 (**2003**).
41. Orrenius, S. et al. Role of Ca^{2+} in toxic cell killing. *Trends Pharmacol. Sci.* 10, 281–285 (**1989**).
42. Stølen, T. O. et al. Interval training normalizes cardiomyocyte function, diastolic Ca^{2+} control, and SR Ca^{2+} release synchronicity in a mouse model of diabetic cardiomyopathy. *Circ. Res.* 105, 527–536 (**2009**).
43. McGrath, K. F. et al. Morphological characteristics of cardiac calcium release units in animals with metabolic and circulatory disorders. *J. Muscle Res. Cell Motil*. 30, 225–231 (**2009**).
44. Kapiloff, M. S. et al. mAKAP and the ryanodine receptor are part of a multi-component signaling complex on the cardiomyocyte nuclear envelope. *J. Cell Sci*. 114, 3167–3176 (**2001**).
45. Kerfant, B.-G. et al. PI3Kγ is required for PDE4, not PDE3, activity in subcellular microdomains containing the sarcoplasmic reticular calcium ATPase in cardiomyocytes. *Circ. Res*. 101, 400–408 (**2007**).
46. Ghigo, A. & Harvey, R. D. Illuminating cAMP dynamics at ryanodine receptors in arrhythmias. *Circ. Res*. 129, 95–97 (**2021**).

47. Haghighi, K. et al. Human phospholamban null results in lethal dilated cardiomyopathy revealing a critical difference between mouse and human. *J. Clin. Invest.* 111, 869–876 (**2003**).
48. Sprenger, J. U. et al. In vivo model with targeted cAMP biosensor reveals changes in receptor–microdomain communication in cardiac disease. *Nat. Commun*. 6, 6965 (**2015**).
49. World Health Organization. Global Health Estimates 2021: Deaths by Cause, Age, Sex, by Country and by Region, 2000–2021. (World Health Organization, Geneva, **2024**).
50. Priori, S. G. et al. ESC guidelines for the management of patients with ventricular arrhythmias and the prevention of sudden cardiac death: the task force for the management of patients with ventricular arrhythmias and the prevention of sudden cardiac death of the European Society of Cardiology (ESC). *Eur. Heart J*. 36, 2793–2867 (**2015**).
51. Xie, L.-H. & Weiss, J. N. Arrhythmogenic consequences of intracellular calcium waves. Am. J. Physiol. *Heart Circ. Physiol*. 297, H997–H1002 (**2009**).
52. Dobrev, D. & Nattel, S. New antiarrhythmic drugs for treatment of atrial fibrillation. *Lancet* 375, 1212–1223 (**2010**).
53. Clancy, C. E. et al. Deranged sodium to sudden death. *J. Physiol*. 593, 1331–1345 (**2015**).
54. Farzam, K. & Jan, A. Beta blockers. in StatPearls (StatPearls Publishing, Treasure Island, FL, **2024**).
55. Arunachalam, K. & Alzahrani, T. Flecainide. in StatPearls (StatPearls Publishing, Treasure Island, FL, **2025**).
56. Savio-Galimberti, E. & Knollmann, B. C. Channel activity of cardiac ryanodine receptors (RyR2) determines potency and efficacy of flecainide and R-propafenone against arrhythmogenic calcium waves in ventricular cardiomyocytes. *PLoS ONE* 10, e0131179 (**2015**).
57. Fahie, S. & Cassagnol, M. Verapamil. in *S*tatPearls (StatPearls Publishing, Treasure Island, FL, **2025**).
58. Mujović, N. et al. The role of amiodarone in contemporary management of complex cardiac arrhythmias. *Pharmacol. Res*. 151, 104521 (**2020**).
59. Fortea, J. I. *et al.* Carvedilol vs. propranolol for the prevention of decompensation and mortality in patients with compensated and decompensated cirrhosis. *J. Hepatol.* S0168-8278, 02772–7 (**2024**).
60. Wehrens, X. H. T. et al. Protection from cardiac arrhythmia through ryanodine receptor-stabilizing protein calstabin2. *Science* 304, 292–296 (**2004**).
61. Calebiro, D. & Maiellaro, I. cAMP signaling microdomains and their observation by optical methods. *Front. Cell. Neurosci.* 8, 1–10 (**2014**).
62. Froese, A. & Nikolaev, V. O. Imaging alterations of cardiomyocyte cAMP microdomains in disease. *Front. Pharmacol.* 6, 1–8 (**2015**).

63. Zaccolo, M. & Pozzan, T. Discrete microdomains with high concentration of cAMP in stimulated rat neonatal cardiac myocytes. *Science* 295, 1711–1715 (**2002**).
64. Bock, A. *et al.* Optical mapping of cAMP signaling at the nanometer scale. *Cell* 182, 1519–1530.e17 (**2020**).
65. Richards, M. et al. Intracellular tortuosity underlies slow cAMP diffusion in adult ventricular myocytes. *Cardiovasc. Res.* 110, 395–407 (**2016**).
66. De Arcangelis, V. et al. Equilibrium between adenylyl cyclase and phosphodiesterase patterns adrenergic agonist dose-dependent spatiotemporal cAMP/protein kinase A activities in cardiomyocytes. *Mol. Pharmacol.* 78, 340–349 (**2010**).
67. Deisseroth, K. & Hegemann, P. The form and function of channelrhodopsin. *Science* 357, eaan5544 (**2017**).
68. Makowka, P. et al. Optogenetic stimulation of Gs-signaling in the heart with high spatio-temporal precision. *Nat. Commun.* 10, 1281 (**2019**).
69. Stierl, M. et al. Light modulation of cellular cAMP by a small bacterial photoactivated adenylyl cyclase, bPAC, of the soil bacterium Beggiatoa. *J. Biol. Chem.* 286, 1181–1188 (**2011**).
70. Penzkofer, A. et al. Photo-dynamics of photoactivated adenylyl cyclase TpPAC from the spirochete bacterium Turneriella parva strain HT. *J. Photochem. Photobiol. B Biol.* 153, 90–102 (**2015**).
71. Iuliano, J. N. et al. Unraveling the mechanism of a LOV domain optogenetic sensor: A glutamine lever induces unfolding of the Jα helix. *ACS Chem. Biol.* 15, 2752–2765 (**2020**).
72. Stierl, M. et al. Key residues for the light regulation of the blue light-activated adenylyl cyclase from Beggiatoa sp. *Biochemistry* 53, 5121–5130 (**2014**).
73. Redden, J. M. & Dodge-Kafka, K. L. AKAP phosphatase complexes in the heart. *J. Cardiovasc. Pharmacol.* 58, 354 (**2011**).
74. Surdo, N. C. et al. FRET biosensor uncovers cAMP nano-domains at β-adrenergic targets that dictate precise tuning of cardiac contractility. *Nat. Commun*. 8, 15031 (**2017**).
75. Dodge-Kafka, K. L. & Kapiloff, M. S. The mAKAP signaling complex: Integration of cAMP, calcium, and MAP kinase signaling pathways. *Eur. J. Cell Biol*. 85, 593–602 (**2006**).
76. Morgenstern, T. J., Park, J., Fan, Q. R. & Colecraft, H. M. A potent voltage-gated calcium channel inhibitor engineered from a nanobody targeted to auxiliary CaVβ subunits. *eLife* 8, e49253 (**2019**).
77. Despa, S. et al. Junctional cleft $[Ca^{2+}]i$ measurements using novel cleft-targeted Ca^{2+} sensors. *Circ Res* 18; 339-47 (**2015**).
78. Kavsan, V. M., Iershov, A. V. & Balynska, O. V. Immortalized cells and one oncogene in malignant transformation: old insights on a new explanation. *BMC Cell Biol*. 12, 23 (**2011**).

79. GloSensor™ Technology. Available at: https://www.promega.de/products/cell-signaling/gpcr-signaling/glosensor-camp-cgmp-protease-biosensors/.

80. White, S. M. et al. Cardiac physiology at the cellular level: use of cultured HL-1 cardiomyocytes for studies of cardiac muscle cell structure and function. *Am. J. Physiol. Heart Circ. Physiol*. 286, H823–H829 (**2004**).

81. Claycomb, W. C. et al. HL-1 cells: A cardiac muscle cell line that contracts and retains phenotypic characteristics of the adult cardiomyocyte. *Proc. Natl. Acad. Sci. U.S.A.* 95, 2979–2984 (**1998**).

82. Cardoso, A. C. et al. Mechanisms of neonatal heart regeneration. *Curr. Cardiol. Rep*. 22, 33 (**2020**).

83. Cell Signaling Technology. Phospho-PKA Substrate (RRXS*/T*) (100G7E) Rabbit mAb. Available at: https://www.cellsignal.com/products/primary-antibodies/phospho-pka-substrate-rrxs-t-100g7e-rabbit-mab/9624.

84. Hayashi, M. et al. The spectrum of epidemiology underlying sudden cardiac death. *Circ. Res*. 116, 1887–1906 (**2015**).

85. Atlas, S. A. et al. Atrial natriuretic factor (auriculin): structure and biological effects. *J. Clin. Hypertens.* 1, 187–198 (**1985**).

86. Ichiki, T. Role of cAMP response element binding protein in cardiovascular remodeling: Good, bad, or both? *Arterioscler. Thromb. Vasc. Biol.* 26, 3 (**2005**).

87. Poindexter, B. J. et al. Calcium signaling mechanisms in dedifferentiated cardiac myocytes: comparison with neonatal and adult cardiomyocytes. *Cell Calcium* 30, 373–382 (**2001**).

88. Reynolds, J. O. et al. Junctophilin-2 is necessary for T-tubule maturation during mouse heart development. *Cardiovasc. Res*. 100, 44–53 (**2013**).

89. Gu, Y. et al. High-resolution scanning patch-clamp: new insights into cell function. *FASEB J.* 16, 748–750 (**2002**).

90. Montero, A. M. & Huang, A. H. The regenerative capacity of neonatal tissues. *Development* 149, dev199819 (**2022**).

91. Liu, J. et al. A full range of mouse sinoatrial node AP firing rates requires protein kinase A-dependent calcium signaling. *J. Mol. Cell. Cardiol*. 51, 730–739 (**2011**).

92. Dodge, K. L. et al. mAKAP assembles a protein kinase A/PDE4 phosphodiesterase cAMP signaling module. *EMBO J.* 20, 1921–1930 (**2001**).

93. Houslay, M. D. & Adams, D. R. PDE4 cAMP phosphodiesterases: modular enzymes that orchestrate signalling cross-talk, desensitization and compartmentalization. *Biochem. J.* 370, 1–18 (**2003**).

94. St. Clair, J. R. et al. Phosphodiesterases 3 and 4 differentially regulate the funny current, If, in mouse sinoatrial node myocytes. *J. Cardiovasc. Dev. Dis*. 4, 10 (**2017**).

95. Vandecasteele, G. et al. Cyclic GMP regulation of the L-type Ca^{2+} channel current in human atrial myocytes. *J. Physiol*. 533, 329–340 (**2001**).

96. Sun, B. et al. Role of phosphodiesterase type 3A and 3B in regulating platelet and cardiac function using subtype-selective knockout mice. *Cell. Signal*. 19, 1765–1771 (**2007**).

97. Vinogradova, T. M. et al. Constitutive phosphodiesterase activity restricts spontaneous beating rate of cardiac pacemaker cells by suppressing local Ca^{2+} releases. *Circ. Res.* 102, 761–769 (**2008**).

98. Osadchii, O. E. Myocardial phosphodiesterases and regulation of cardiac contractility in health and cardiac disease. *Cardiovasc. Drugs Ther*. 21, 171–194 (**2007**).

99. Leroy, J. et al. Phosphodiesterase 4B in the cardiac L-type Ca^{2+} channel complex regulates Ca^{2+} current and protects against ventricular arrhythmias in mice. *J. Clin. Invest*. 121, 2651–2661 (**2011**).

100. Perera, R. K. & Nikolaev, V. O. Compartmentation of cAMP signalling in cardiomyocytes in health and disease. *Acta Physiol*. 209, 12077 (**2013**).

101. Pavlidou, G. N. et al. Phosphodiesterase 8 governs cAMP/PKA-dependent reduction of L-type calcium current in human atrial fibrillation: a novel arrhythmogenic mechanism. *Eur. Heart J.* 44, 2483–2494 (**2023**).

102. Kraft, A. E. et al. Phosphodiesterases 4B and 4D differentially regulate cAMP signaling in calcium handling microdomains of mouse hearts. *Cells* 13, 476 (**2024**).

103. Shannon T. R. et al. Subcellular Propagation of Cardiomyocyte β-Adrenergic Activation of Calcium Uptake Involves Internal β-Receptors and AKAP7. *Function* 3, zqac020 (**2022**).

104. Patrucco, E. et al. Phosphodiesterase 8A (PDE8A) regulates excitation-contraction coupling in ventricular myocytes. *J. Mol. Cell Cardiol.* 49, 330–333 (**2010**).

105. Qasim, H. et al. AKAP12 upregulation associates with PDE8A to accelerate cardiac dysfunction. *Circ. Res.* 134, 1006–1022 (**2024**).

106. Rybalkin, S. D. et al. Cyclic GMP phosphodiesterases and regulation of smooth muscle function. *Circ. Res*. 93, 280–291 (**2003**).

107. Miller, C. L. et al. Role of Ca^{2+}/calmodulin-stimulated cyclic nucleotide phosphodiesterase 1 in mediating cardiomyocyte hypertrophy. *Circ. Res*. 105, 956–964 (**2009**).

108. Sadek, M. S. et al. Therapeutic implications for PDE2 and cGMP/cAMP mediated crosstalk in cardiovascular diseases. *Int. J. Mol. Sci*. 21, 7462 (**2020**).

109. Ho S. A. et al. Effects of selective inhibitors on cyclic nucleotide phosphodiesterases of rabbit aorta. *Biochem. Pharmacol*. 38, 3331–3339 (**1989**).

110. Nagel, D. J. et al. Role of nuclear Ca^{2+}/calmodulin-stimulated phosphodiesterase 1A in vascular smooth muscle cell growth and survival. *Circ. Res*. 98, 777–784 (**2006**).

111. Lukyanenko, Y. O. et al. Ca^{2+}/calmodulin-activated phosphodiesterase 1A is highly expressed in rabbit cardiac sinoatrial nodal cells and regulates pacemaker function*. J. Mol. Cell Cardiol*. 98, 73–82 (**2016**).

112. Vandeput, F. et al. Cyclic nucleotide phosphodiesterase PDE1C1 in human cardiac myocytes. *J. Biol. Chem.* 282, 32749–32757 (**2007**).

113. Yano, M. et al. Altered intracellular Ca^{2+} handling in heart failure. *J. Clin. Invest*. 115, 556–564 (**2005**).

114. Fabiato, A. Calcium-induced release of calcium from the cardiac sarcoplasmic reticulum. *Am. J. Physiol.* 245, C1–C14 (**1983**).

115. Pasqualini, F. S. et al. Mechanotransduction and metabolism in cardiomyocyte microdomains. *Biomed. Res. Int*. 4081638 (**2016**).

116. Molina, C. E. et al. Cyclic adenosine monophosphate phosphodiesterase type 4 protects against atrial arrhythmias. *J. Am. Coll. Cardiol*. 59, 2182–2190 (**2012**).

117. Lehnart, S. E. et al. Phosphodiesterase 4D deficiency in the ryanodine-receptor complex promotes heart failure and arrhythmias. *Cell* 123, 25–35 (**2005**).

118. Wehrens, X. H. T. et al. FKBP12.6 deficiency and defective calcium release channel (ryanodine receptor) function linked to exercise-induced sudden cardiac death. *Cell* 113, 829–840 (**2003**).

119. Zhao, Y.-T. et al. Sensitized signalling between L-type Ca^{2+} channels and ryanodine receptors in the absence or inhibition of FKBP12.6 in cardiomyocytes. *Cardiovasc. Res.* 113, 332–342 (**2017**).

120. Sood, S. et al. Intracellular calcium leak due to FKBP12.6 deficiency in mice facilitates the inducibility of atrial fibrillation. *Heart Rhythm* 5, 1047–1054 (**2008**).

121. Shan, J. et al. Calcium leak through ryanodine receptors leads to atrial fibrillation in three mouse models of catecholaminergic polymorphic ventricular tachycardia. *Circ. Res*. 111, 708–717 (**2012**).

122. Hidisoglu, E. et al. The ryanodine receptor-calstabin interaction stabilizer S107 protects hippocampal neurons from GABAergic synaptic alterations induced by Abeta42 oligomers. *J. Physiol.* 600, 5295–5309 (**2022**).

123. Jessup, M. et al. Calcium upregulation by percutaneous administration of gene therapy in cardiac disease (CUPID): a phase 2 trial of intracoronary gene therapy of sarcoplasmic reticulum Ca^{2+}-ATPase in patients with advanced heart failure. *Circulation* 124, 304–313 (**2011**).

124. Greenberg, B. et al. Calcium upregulation by percutaneous administration of gene therapy in patients with cardiac disease (CUPID 2): a randomised, multinational, double-blind, placebo-controlled, phase 2b trial. *Lancet* 387, 1178–1186 (**2016**).

125. Dobrev, D. & Wehrens, X. H. T. Role of RyR2 phosphorylation in heart failure and arrhythmias. *Circ. Res*. 114, 1311–1319 (**2014**).

126. Shan, J. et al. Role of chronic ryanodine receptor phosphorylation in heart failure and β-adrenergic receptor blockade in mice. *J. Clin. Invest*. 120, 4375–4387 (**2010**).

127. Feng, T. et al. L-type calcium channels: structure and functions. in Ion Channels in Health and Sickness. *InTech* (**2018**).

128. Marks, A. R. Calcium cycling proteins and heart failure: mechanisms and therapeutics. *J. Clin. Invest.* 123, 46–52 (**2013**).

129. Taussig, R. & Gilman, A. G. Mammalian membrane-bound adenylyl cyclases. *J. Biol. Chem*. 270, 1–4 (**1995**).

130. Braun, T. The effect of divalent cations on bovine spermatozoal adenylate cyclase activity. *J. Cyclic Nucleotide Res*. 1, 271–281 (**1975**).

131. Braun, T. & Dods, R. F. Development of a Mn^{2+}-sensitive, 'soluble' adenylate cyclase in rat testis. *Proc. Natl Acad. Sci. USA* 72, 1097–1101 (**1975**).

132. Litvin, T. N. et al. Kinetic properties of 'soluble' adenylyl cyclase. Synergism between calcium and bicarbonate*. J. Biol. Chem.* 278, 15922–15926 (**2003**).

133. Kleinboelting, S. et al. Expression, purification, crystallization and preliminary X-ray diffraction analysis of a mammalian type 10 adenylyl cyclase. *Acta Crystallogr. F Struct. Biol. Commun*. 70, 467–469 (**2014**).

134. Conti, M. & Beavo, J. Biochemistry and physiology of cyclic nucleotide phosphodiesterases: essential components in cyclic nucleotide signaling. *Annu. Rev. Biochem*. 76, 481–511 (**2007**).

135. El-Armouche, A. et al. Molecular determinants of altered Ca^{2+} handling in human chronic atrial fibrillation. *Circulation* 114, 670–680 (**2006**).

136. Neef, S. et al. CaMKII-dependent diastolic SR Ca^{2+} leak and elevated diastolic Ca^{2+} levels in right atrial myocardium of patients with atrial fibrillation. *Circ. Res*. 106, 1134–1144 (**2010**).

137. Guo, W. et al. The ryanodine receptor stabilizer S107 ameliorates contractility of adult Rbm20 knockout rat cardiomyocytes. *Physiol. Rep.* 9, e15011 (**2021**).

138. Miotto, M. C. et al. Structural analyses of human ryanodine receptor type 2 channels reveal the mechanisms for sudden cardiac death and treatment. *Sci. Adv.* 8, eabo1272 (**2022**).

139. Omar, F. et al. Small-molecule allosteric activators of PDE4 long-form cyclic AMP phosphodiesterases*. Proc. Natl Acad. Sci. USA* 116, 13320–13329 (**2019**).

140. Qasim, H. & McConnell, B. K. AKAP12 Signaling Complex: Impacts of Compartmentalizing cAMP-Dependent Signaling Pathways in the Heart and Various Signaling Systems. *J Am Heart Assoc.* 9(13):e016615 (**2020**).

141. Li, T et al. Targeting RyR2 with a phosphorylation site–specific nanobody reverses dysfunction of failing cardiomyocytes in rats. *The FASEB Journal*, 33: 7467-7478 (**2019**).

142. Dong, D.L. et al. Calcium-Activated Potassium Channels: Potential Target for Cardiovascular Diseases. *Adv Protein Chem Struct Biol*., 104:233-261 (**2016**).

143. Soleimani, E. et al. Cardiomyocytes differentiated in vitro from pluripotent embryonic stem cells exhibit specific ion channel expression and electrophysiological properties. *Circ. Res.* 75, 233–244 (**1994**).

9. List of publications

- Selective optogenetic control of Gq signaling using human Neuropsin
  Ahmed Wagdi, Daniela Malan, Udhayabhaskar Sathyanarayanan, Janosch S. Beauchamp, Markus Vogt, David Zipf, Thomas Beiert, **Berivan Mansuroglu**, Vanessa Dusend, Mark Meininghaus, Linn Schneider, Bernd Kalthof, J. Simon Wiegert, Gabriele M. König, Evi Kostenis, Robert Patejdl, Philipp Sasse & Tobias Bruegmann. Nature Communications volume 13, Article number: 1765 (**2022**). DOI: https://doi.org/10.1038/s41467-022-29265-w.
- Reductive stress triggers ANAC017-mediated retrograde signaling to safeguard the endoplasmic reticulum by boosting mitochondrial respiratory capacity
  Philippe Fuchs, Finja Bohle, Sophie Lichtenauer, José Manuel Ugalde, Elias Feitosa Araujo, **Berivan Mansuroglu**, Cristina Ruberti, Stephan Wagner, Stefanie J Müller-Schüssele, Andreas J Meyer, Markus Schwarzländer. The Plant Cell, Volume 34, Issue 4, Pages 1375–1395 (**2022**). DOI: https://doi.org/10.1093/plcell/koac017.
- Mitochondria-derived reactive oxygen species are the likely primary trigger of mitochondrial retrograde signaling in Arabidopsis
  Kasim Khan, Huy Cuong Tran, **Berivan Mansuroglu**, Pinar Önsell, Stefano Buratti, Markus Schwarzländer, Alex Costa, Allan G. Rasmusson, Olivier Van Aken. Current Biology, ISSN 0960-9822 (**2024**). DOI: https://doi.org/10.1016/j.cub.2023.12.005.

10. Selected symposia and meeting contributions

- International Symposium of the Research Training Group 1873, Pharmacology of the 7-TM receptors and downstream signaling pathways, Bonn, Germany, **2019** (*attended*)
  The Cardiovascular Disease Symposium “CaVaD” from the Heinrich Heine University Düsseldorf, **2021** online (*attended*)
- International Symposium of the Research Training Group 1873, Pharmacology of the 7-TM receptors and downstream signaling pathways, Bonn, Germany, **2021** (*Chair, organizer, poster presentation, poster prize*)
- SSP, Vollpriehausen, Germany ,**2021** (*attended*)
- Deutsche Physiologische Gesellschaft (DPG), **2021**, Frankfurt, Germany, and **2023** Berlin, Germany (*poster presentations*)
- Junge Physiologen (JP), Essen, Germany, **2022** (*poster presentation*)
- Europhysiology, The Physiological Society, Copenhagen, Denmark, **2022** (*poster presentation*)
- International Society for Heart Research (ISHR), **2023** online (*attended*)

11. Supplement

Arduino codes were written by Prof. Philipp Sasse

S.1 Triggered Ca imaging

```
//https://roboticsbackend.com/arduino-millis-vs-micros/
//#define Sprintln(a) (Serial.println(a))
//#define Sprint(a) (Serial.print(a))
#define Sprintln(a)
#define Sprint(a)
#include <LiquidCrystal.h>
LiquidCrystal lcd(22, 24, 26, 28, 30, 32);
int cameraPin = 3;
int pulseCamera = 1; // ms
int pacePin = 5;
int pacePinNeg = 4;
int pulsePace = 1; // ms total biphasic pulse
int optoPin = 6;
int grassPin = 7;
unsigned long optoDelay = 50; // how many ms off before next pulse imaging episolde
unsigned long optoDuration = 500; // in ms make sure that there is long enough delay
int pacingIntensity = 128;
int optoIntensity = 255;
unsigned long frequencyPace = 1000000; // 1000000; // in µsec 1000000 = 1 sec, must not be shorter than optoDelay + optoDuration (in ms) not shorter then 750000
unsigned long transientTimes[][3] = {
  {0, 100, 0}, // imaging, delay 100, unused
  {0, 100, 0},
  {0, 32, 0}, //
  {1, 1 , 0}, // pacing, no delay till next image
  {0, 33, 0}, //
  {0, 33, 0}, //
  {0, 33, 0}, //
  {0, 40, 0}, //
  {0, 50, 0}, //
  {0, 50, 0}, //
  {0, 60, 0}, //
```

```
  {0, 70, 0}, //
  {0, 100, 0}, //
  //{0, 100, 0}, //
 // {0, 200, 0}, //
  };
int transientCount = sizeof(transientTimes) / sizeof(transientTimes[0]);
int episodes[][2] = {
  {0, 0}, // 0 no image, 0 = no optogentic
  {0, 0}, //
  {0, 0}, //
  {0, 0}, // 0 no image, 0 = no optogentic
  {0, 0}, //
  {0, 0}, // 0 no image, 0 = no optogentic
  {0, 0}, //
  {0, 0}, // 0 no image, 0 = no optogentic
  {0, 0}, //
  {1, 0}, // 1 image, 0 = no optogentic
  {1, 0}, //
  {1, 0}, //
  {0, 0}, // 0 no image, 0 = no optogentic
  {0, 0}, //
  {0, 0}, //
   {1, 0}, // 1 image, 0 = no optogentic
  {1, 0}, //
  {1, 0}, //
  {1, 1}, // 1 image, 1 = optogenetic on in next loop
  {1, 2}, //
  {1, 0}, //
  {1, 0}, //
  {1, 0}, //
  {1, 0}, //
  {1, 0}, //
  {1, 0}, //
  {1, 0}, //
  {1, 0}, //
  {1, 0}, //
  {1, 0}, //
  {1, 0}, //
  {1, 0}, //
  {1, 0}, //
  {1, 0}, //
  {1, 0}, // 1 image, 2 = optogentic off in next loop
```

```
  {1, 0}, //
  {1, 0}, //
  {1, 0}, //
  {1, 0}, //
  {1, 0}, //
  {1, 0}, //
  {1, 0}, //
  {1, 0}, //
  {1, 0}, //
  {1, 0}, //
 /*  {0, 0}, //
   {0, 0}, //
   {1, 0}, //
   {1, 0}, //
   {1, 0}, //
   {1, 0}, //
   {1, 0}, //
   {1, 0}, //
   {1, 0}, //*/
 };
int episodesCount = sizeof(episodes) / sizeof(episodes[0]);
unsigned long lastPace = 0;
unsigned long currentTime;
bool imagingBit = false;
bool optoBit = false;
bool optoLEDon = false;
int currentTransient =0;
int currentEpisode = 0;
unsigned long paceTime = 0;
unsigned long optoOn;
unsigned long optoOff;
void setup()
{
 Serial.begin(115200);
 digitalWrite(pacePin, LOW);
 digitalWrite(pacePinNeg, LOW);
 digitalWrite(optoPin, LOW);
 digitalWrite(cameraPin, LOW);
 pinMode(pacePin, OUTPUT);
 pinMode(pacePinNeg, OUTPUT);
```

```
 pinMode(optoPin, OUTPUT);
 pinMode(cameraPin, OUTPUT);
 pinMode(grassPin, OUTPUT);
 digitalWrite(pacePin, LOW);
 digitalWrite(pacePinNeg, LOW);
 digitalWrite(optoPin, LOW);
 digitalWrite(cameraPin, LOW);
 digitalWrite(grassPin, LOW);
lastPace = micros();
 //pinMode(interruptPin1, INPUT_PULLUP); // müssen wir noch testen ob der pullup wichtig
 Sprintln("Ready");
 //  digitalWrite(outputPin, HIGH);   // uncomment to thest LED at beginning
 delay(1000);
 lcd.begin(16, 4);
 lcd.setCursor(0, 0);
 lcd.print("Ready");
 lcd.setCursor(0, 0);
//  lcd.print("Intensity: "); lcd.print(light_intensity);
 lcd.setCursor(0, 1);
   currentTime = micros();
}
void loop() {
while (currentEpisode<episodesCount){
 if (episodes[currentEpisode][0] == 1) {
   imagingBit = true;
   }
 else {
   imagingBit = false;
    }
 if ((episodes[currentEpisode][1] == 1) && (optoBit == false)) {  // optogenetic now
   optoBit = true;
   Sprintln("Opto this loop");
    Sprint("last pace ");
   Sprintln(lastPace);
   optoOn =  lastPace + frequencyPace - (1000 * optoDelay);
   Sprint("lightOn: ");
   Sprintln(optoOn);
   unsigned long temp = optoOn-currentTime;
   episodes[currentEpisode][1] = 0;   //to avoid second switch in tis loop
   }
```

```
  if ((episodes[currentEpisode][1] == 2) && (optoBit == false)) {  // optogenetic off now
  optoBit = true;
  Sprintln("Opto this loop");
    Sprint("last pace ");
  Sprintln(lastPace);
  optoOn =  lastPace + frequencyPace - (1000 * optoDelay);
  Sprint("lightOff: ");
  Sprintln(optoOn);
  unsigned long temp = optoOn-currentTime;
  episodes[currentEpisode][1] = 0;   //to avoid second switch in tis loop
  }
 // now time comparisons
 currentTime = micros();
 if ((currentTime > optoOn) && (optoBit == true) && (optoLEDon == false)) {
  digitalWrite(optoPin, HIGH);  // need to switch opto on?
   optoLEDon= true;
   optoBit = false;
   Sprint(" current time:");
  Sprint(currentTime);
  Sprintln("------------------------OptoOn");
  }
 if ((currentTime > optoOn) && (optoBit == true) && (optoLEDon == true)) {     // need to switch opto
off?
  digitalWrite(optoPin, LOW);
    Sprint(" current time:");
    optoBit = false;
  Sprint(currentTime);
  Sprintln("------------------------OptoOff");
    optoLEDon=false;
  optoBit = false;
 }
 if (currentTime - lastPace > frequencyPace) { // now next pace
  //Sprintln("Pace loop");
  lastPace = currentTime;
  currentTransient = 0;
  Sprint(" current time:");
  Sprint(currentTime);
  while (currentTransient < transientCount) { // loop over images
    paceTime = micros();
        if (transientTimes[currentTransient][0] == 0) {  //imaging event
```

```
      if (imagingBit == true) {
        digitalWrite(cameraPin, HIGH);  // do imaging only if active
         Sprint(" On: ");
      }
      delay(pulseCamera);
      //while (micros() < (paceTime + (100000*pulseCamera))); // pulse duration in ms
      digitalWrite(cameraPin, LOW);
      Sprint(" Loop:");
      Sprint(currentTransient);
     delay (transientTimes[currentTransient][1]-pulseCamera);
          //while (micros() < (paceTime + 1000*transientTimes[currentTransient][1]));  // delay anyway
till next pulse in ms
    }
    if ((transientTimes[currentTransient][0] == 1)) {  // this is a pace pulse
      digitalWrite(pacePin, HIGH);
      digitalWrite(grassPin, HIGH);
      //delay(pulsePace);
      delayMicroseconds(500);  //duration pos pulse in ms pace stärke negativ
      digitalWrite(pacePin, LOW);
      digitalWrite(grassPin, LOW);
      delayMicroseconds(50);
      digitalWrite(pacePinNeg, HIGH);
      delayMicroseconds(500); //duration neg pulse in ms pace stärke negativ
      //delay(pulsePace);
      digitalWrite(pacePinNeg, LOW);
     /* analogWrite(pacePin, pacingIntensity);
      delay(pulsePace);
      analogWrite(pacePin, 0);
      delayMicroseconds(50);
      analogWrite(pacePinNeg, pacingIntensity);
      delay(pulsePace);
      analogWrite(pacePinNeg, 0);*/
      delay(transientTimes[currentTransient][1] - pulsePace);
           Sprint(" pace:");
      Sprint(currentTransient);
    }
   currentTransient++;
  }
 Sprint(" episode:");
 Sprintln(currentEpisode);
```

```
  currentEpisode++;
}
}
// done
 Sprintln("End");
delay(20000);
  while(1){
    digitalWrite(cameraPin, HIGH);  // do imaging only if active
    delay(pulseCamera);
    digitalWrite(cameraPin, LOW);
    delay(100);
  }
}
/*
if (digitalRead(interruptPin1) == LOW) {
  if (pulse == 1) {
    Serial.print("Trigger No: "); Serial.print(count);
    delay(List[count][0]);
    Serial.print("     HIGH    ");
    if ((List[count][1]) > 0) digitalWrite(outputPin, HIGH);
    delay(List[count][1]);
    digitalWrite(outputPin, LOW);
    Serial.println("LOW");
    pulse = 0;
    Serial.print("pulse 0");
  }
  if (loopwait == List[count][2]) { // waited long enough
    count ++;
    pulse = 1;
    loopwait = 0;
    Serial.print("pulse 0");
    if ((List[count][0]) == 1111) count = 0;
    Serial.print("next pulse No: "); Serial.println(count);
    Serial.print("       next delay: "); Serial.print(List[count][0]);
    Serial.print("       next pulse: "); Serial.println(List[count][1]);
    Serial.print("       next loopwait "); Serial.println(List[count][2]);
  }
  else {
    Serial.print("loop "); Serial.println(loopwait);
    loopwait ++;
```

```
  }
  while (digitalRead(interruptPin1) == LOW) {
    delay (1);
  }
}
delay(1);
}
*/
```

Fig. S1: Arduino code for triggering pacing, imaging and optogenetic stimulation

The programmed code processes an input file containing time and signal information and performs triggered electrical pacing, imaging and optogenetic stimulation.

S.2 24-well-plate illumination

```
Enter x ms illumination
void setup() {
  analogWrite(2, 0);
  analogWrite(4, 0);
  analogWrite(6, 0);
  analogWrite(8, 0);
  analogWrite(10, 0);
  analogWrite(12, 0);
  delay(1000);
  for (int i = 0; i <= 12; i++) {
    analogWrite(12, 255);  //420
    analogWrite(6, 255);   //1660
    analogWrite(10, 255);  //160
    analogWrite(4, 255);   //180
    analogWrite(2, 255);   //420
    analogWrite(8, 255);   //166
    delay(x);
    analogWrite(2, 0);
    analogWrite(4, 0);
    analogWrite(6, 0);
    analogWrite(8, 0);
    analogWrite(10, 0);
    analogWrite(12, 0);
    delay(9990);
  }
}
void loop() {
  // put your main code here, to run repeatedly:
}
```

Fig. S2: Arduino code for illumination protocol

The programmed code processes an input file containing illumination duration and intensity.